

Universität
Rostock



Traditio et Innovatio

Investigation and Development of a Transverse Deflecting
Structure: A Beam Separator for ELBE

DISSERTATION

to attain the academic degree of
Doctor of Engineering (Dr.-Ing.)
from the Faculty of Computer Science and Electrical Engineering
at the University of Rostock

Submitted by
Gowrishankar Thalagavadi Hallilingaiah,
born on 29.09.1985 in Maddur, India
from Dresden, Germany

Dresden, 30 November 2022

Reviewers:

Prof. Dr. Ursula van Rienen, Institute of General Electrical Engineering, University of Rostock, Germany

Prof. Dr. Herbert De Gerssem, Department of Electrical Engineering and Information Technology, Technical University of Darmstadt, Germany

Dr. André Arnold, Institute of Radiation Physics, Helmholtz-Zentrum Dresden-Rossendorf, Germany

Day of submission: 30 November 2022

Day of defense: 08 June 2023

This work is licensed under a Creative Commons “Attribution 4.0 International” license.



To view a copy of this license, visit: <https://creativecommons.org/licenses/by/4.0/deed.en>

Acknowledgement

I want to take this opportunity to thank everyone who has supported me during my thesis. My sincere thanks go to my guide, Prof. Ursula van Rienen, for giving me an opportunity to work on the topic. She has always supported me in all my aspects, beginning with my Master's studies, and her help and encouragement have been the key factor in completing the thesis.

I am grateful to my supervisor, Dr. André Arnold. I have immensely benefited from his theoretical knowledge and gained a lot of practical experience from him. Despite his busy and tight schedule, he has always listened to my ideas (sometimes crazy!) and problems and come up with a practical solutions. Furthermore, he motivated me to complete writing this thesis when I was about to give up.

I also like to take this opportunity to thank Prof. Peter Michel, who, as a leader of the ELBE group, takes care of all the problems of his colleagues and has a vision for the future. I really appreciate his effort in getting me funding for an extended time. My Master's studies at the University of Rostock gave me a solid foundation to pursue this work. I want to thank Thomas Flisgen and Johann Heller for their help and coordination extended during my Master's thesis. Their teaching and problem-solving skills have immensely benefited me.

Fabrication of the cavity was only possible with the effort of Sebastian Köppen. I thank his help in making all the technical drawings, working on details of the machining and fabrication, procuring the necessary parts, and travelling with me for frequency pre-tuning. I thank him for introducing me to Billiards.

I also want to thank Dr G. Sugilal, who inspired and motivated me to choose a new career path. He assessed my situation and addressed my ambiguity during my work in India, and his suggestion to pursue higher studies has been pivotal to my success. I am greatly indebted to him.

During the first phase of the thesis work, I was at the University of Rostock, and

I like to thank my former colleagues Eden, Farooqi, Julius, Yogesh, Shahnam, and Revathi. I also thank Kathrin and Maya Gudat for helping me to navigate the German bureaucracy.

In the second phase of my work, I moved to HZDR, Dresden, and I would like to thank my colleagues Michael Kunstch, Rong, Andre Malberg, Pavel, Ulf, and other colleagues of FWK who have been kind and supportive to me. I especially thank Rico, Michel Freitag, Eno, and the operator crew of ELBE for helping me set up the RF test facility and conditioning the cavity. I thank Petra and Kathrin for helping me with all the paperwork.

During my stay in Dresden, I enjoyed the lunchtime discussion with Anton and sometimes with Mike. I thank Anton for forcing me to get on to the bike, which has helped to keep me in shape and reduce my carbon footprint. I also thank Mike for correcting the first chapter of my thesis; his writing advice has helped a lot in this thesis. I also like to thank Jana and Shuai for having a discussion during morning coffee times.

I believe my achievements have been a proud moment for my parents. In certain instances, my decision and action have disappointed them. Despite the dissatisfaction, I thank my mother for her support and love. I acknowledge my dad's contribution here for being critical of my decisions. I am grateful for my brother's constant moral and financial support during my Master's.

I want to thank my friends, Anush, Deepak, Kunal, Sanjeev, Shyam and Adriana, for giving company to me. I also want to thank my friends in India who have supported me for all these years.

Last but not least, I want to thank my wife, **LavanYa**, for being supportive, patient, caring, and understanding towards me.

Abstract

The linear electron accelerator, ELBE (Electron Linac for beams with high Brilliance and low Emittance) at Helmholtz-Zentrum Dresden-Rossendorf, Dresden, Germany, is a versatile machine that drives six distinct secondary particle and radiation sources used in a wide range of experiments related to health, matter, transmutation, and accelerator development. The accelerator can efficiently handle 1 mA beam current at a 13 MHz bunch repetition rate in continuous-wave mode with a maximum beam energy of 40 MeV. Currently, it is not possible to simultaneously operate more than one ELBE secondary source. In this work, a suitable beam separator device for ELBE was developed to overcome the limitation of single beamline operation. The developed kicker can distribute the bunches from the existing single beam into two or more beamlines, which will enable the simultaneous operation of multiple downstream secondary sources, significantly enhancing the accelerator's capabilities. The state-of-the-art transverse deflecting structures suitable for beam separation were reviewed. Subsequently, pulsed magnet, stripline kicker, and radio-frequency (RF) cavity designs were adapted for the current requirements, and RF cavities were found suitable. Furthermore, the cavity operating frequency was set to 273 MHz, reducing both the differential kick voltage error and projected emittance growth and providing a better field homogeneity. The cavity can be easily integrated into the ELBE's existing low-level RF control system. Six deflecting cavity designs were shortlisted, and the cavity geometries were scaled and adapted to match the requirements. Then, a cavity design was selected based on lower power loss, peak electric field and surface power loss density, as well as better field homogeneity.

Subsequent to the cavity design, the cavity components were adapted from the existing designs. Next, beam loading and multipacting in the cavity were analyzed, and the effect of higher-order modes on the cavity was studied. A multiphysics analysis was carried out to aid in the engineering design of the cavity. Thereafter, the copper cavity parts were machined, and the cavity frequency was pre-tuned before the final vacuum brazing was performed.

Finally, RF measurements were performed to validate the simulation. A thorough investigation was carried out to determine the cause of the low intrinsic quality factor

of the cavity. Consequently, the quality factor was improved by eliminating the RF filter present at the vacuum port. A bead-pull measurement setup was built, and the measured field profiles matched the simulation results. Further, the cavity was driven up to 1 kW using the modified pick-up antenna, and eventually, the vacuum conditioning of the cavity was accomplished. The cavity's performance meets the design requirements and is ready to be installed in the beamline for further testing.

Zusammenfassung

Der lineare Elektronenbeschleuniger ELBE (Electron Linac for beams with high Brilliance and low Emittance) am Helmholtz-Zentrum Dresden-Rossendorf, Dresden, Deutschland, ist eine vielseitige Maschine, welche sechs verschiedene sekundäre Teilchen- und Strahlungsquellen antreibt, die in einer Vielzahl von Experimenten im Zusammenhang mit Gesundheit, Materie, Transmutation und Beschleunigerentwicklung eingesetzt werden. Der Beschleuniger ist in der Lage, einen Strahlstrom von 1 mA bei einer Wiederholfrequenz von 13 MHz im Dauerstrichbetrieb mit einer maximalen Strahlenergie von 40 MeV effizient zu verarbeiten. Derzeit ist es nicht möglich, mehr als eine ELBE-Sekundärquelle gleichzeitig zu betreiben. In dieser Arbeit wurde ein geeigneter Strahlseparator für ELBE entwickelt, um die Beschränkung des Betriebs an einer einzelnen Beamline zu überwinden. Der entwickelte Kicker kann die Strahlenbündel des vorhandenen Einzelstrahls auf zwei oder mehr Strahlführungen verteilen, was den gleichzeitigen Betrieb mehrerer nachgeschalteter Sekundärquellen ermöglicht und damit die Leistungsfähigkeit des Beschleunigers erheblich steigert. Die für die Strahlseparation geeigneten transversalen Ablenkstrukturen wurden nach dem Stand der Technik untersucht. Anschließend wurden gepulste Magnet, Stripline-Kicker und Hochfrequenz (HF) Resonatoren an die aktuellen Anforderungen angepasst, wobei sich die HF-Resonatoren als geeignet erwiesen. Darüber hinaus wurde die Betriebsfrequenz auf 273 MHz festgelegt, wodurch sowohl der Fehler der differentiellen Kick-Spannung, als auch das projizierte Emittanzwachstum reduziert und eine bessere Feldhomogenität erreicht wurde. Die Kavität kann problemlos in das bestehende Low-Level-HF-Steuerungssystem des ELBE integriert werden. Sechs Ablenkresonatoren wurden in die engere Wahl gezogen und die Resonatorgeometrien wurden entsprechend den Anforderungen skaliert und angepasst. Anschließend wurde ein Resonator-Design ausgewählt, das sich durch eine geringere Verlustleistung, ein geringeres elektrisches Spitzenfeld, eine höhere Verlustleistungsdichte an der Oberfläche und eine bessere Feldhomogenität auszeichnet. Im Anschluss an das Hohlraumdesign wurden die Komponenten des Resonators an die vorhandenen Designs angepasst. Anschließend wurden die Strahlenbelastung und die Mehrfachverdichtung in der Kavität analysiert und die Auswirkungen von

Moden höherer Ordnung auf die Kavität untersucht. Eine Multiphysik-Analyse wurde durchgeführt, um die technische Auslegung des Resonators zu unterstützen. Danach wurden die Kupferhohlraumteile bearbeitet und die Resonanzfrequenz wurde vor dem abschließenden Vakuumlöten abgestimmt.

Schließlich wurden HF-Messungen durchgeführt, um die Simulation zu validieren. Es wurde eine gründliche Untersuchung durchgeführt, um die Ursache für den niedrigen Eigengütefaktor des Hohlraums zu ermitteln. Daraufhin wurde der Qualitätsfaktor durch Beseitigung des HF-Filters am Vakuumanschluss verbessert. Ein Bead-Pull-Messaufbau wurde gebaut und die gemessenen Feldprofile stimmten mit den Simulationsergebnissen überein. Außerdem wurde der Hohlraum mit der modifizierten Pick-up-Antenne bis zu 1 kW betrieben, und schließlich wurde die Vakuumkonditionierung des Hohlraums durchgeführt. Die Leistung der Kavität entspricht den Konstruktionsanforderungen und ist bereit für weitere Tests in die Beamline eingebaut zu werden.

Contents

List of Acronyms	xiii
List of Symbols	xvi
List of Figures	xxi
List of Tables	xxxii
1 Introduction	1
1.1 ELBE Accelerator	1
1.2 Motivation	4
1.3 Aim and Outline of the Thesis	7
2 Theoretical Background	9
2.1 Maxwell's Equations	9
2.2 Deflection due to the Static Electric and Magnetic Fields	12
2.2.1 Static Electric Field	13
2.2.2 Static Magnetic Field	14
2.2.3 Static Electric and Magnetic Fields	14
2.3 Electromagnetic Field in a Closed Structure	16
2.3.1 Cylindrical Resonators	16
2.3.2 Coaxial Resonators	17
2.4 Identification of Transverse Deflecting Modes	20
2.5 Cavity Parameters	21
2.5.1 Integrated Longitudinal and Transverse Voltage	21
2.5.2 Quality Factor	23
2.5.3 Cavity Shunt Impedance	23
2.5.4 Geometrical Factor G and $R_{\perp}R_s$	24

Contents

2.5.5	Surface Power Loss in a Cavity	24
2.5.6	Peak Surface Power Loss Density	25
2.5.7	Peak Surface Electric Field	25
2.5.8	Kick Voltage Homogeneity	25
2.6	Power Coupling and Beam Loading	26
2.6.1	Power Coupling	26
2.6.2	Beam Loading	28
2.7	Multipacting	31
2.8	Higher Order Mode	34
3	Selection of the Deflecting Structure	35
3.1	Classification of Deflecting Structures	35
3.1.1	Electric Deflecting Structures	37
3.1.2	Magnetic Deflecting Structures	40
3.1.3	Electromagnetic Deflecting Structures	43
3.2	Feasibility Study of the Possible Deflecting Structures for Beam Sepa- ration	47
3.2.1	Pulsed Magnet	48
3.2.2	Stripline Kicker	52
3.2.3	Transverse Deflecting Cavity	56
3.2.4	Comparative Analysis	58
3.3	Choosing the Cavity Operating Frequency	62
3.3.1	Kick Voltage and Deflection Angle Errors	63
3.3.2	Projected Emittance Growth	66
3.3.3	RF Power Loss	67
3.3.4	Kick Voltage Homogeneity	70
3.3.5	Discussion	71
3.4	Criteria for the Selection of a Beam Separator	73
3.5	Identification of the Probable Cavity Designs	73
4	Scaling, Adaptation, and Comparison of the Probable Cavity Designs	76
4.1	Cavity Requirements	76

Contents

4.2	Cavity scaling and adaptation	77
4.2.1	Adaptation of a 4-rod Cavity Design: Design I and II	78
4.2.2	Design III and IV: Adaptation of the RF-dipole Crab Cavity	86
4.2.3	Design V: Adaptation of the Double-quarter-wave Crab Cavity	89
4.2.4	Evolution of Design VI	92
4.3	Comparison of the Cavity Designs	104
5	Development of the Cavity Components and Further Analysis	107
5.1	Pre-buncher Cavity	107
5.2	Fundamental Power Coupler	108
5.3	Pick-up Probe	111
5.4	Frequency Tuners	112
5.5	Multipacting Analysis	113
5.6	Required RF Power and Beam Loading	116
5.7	HOM Analysis	118
6	Multiphysics Analysis of the Cavity	120
6.1	Simulation Setup for Multiphysics	120
6.1.1	Eigenmode Analysis	122
6.1.2	Thermal Analysis	122
6.1.3	Structural Analysis	123
6.1.4	Eigenmode Sensitivity Analysis	124
6.2	Frequency Sensitivity of the Cavity Surfaces	125
6.3	Cavity Material and Wall Thickness	127
6.4	Effect of Ambient Temperature	130
6.5	Effect of RF Power and Coolant Temperature	131
6.6	Conclusion	134
7	Cavity Fabrication	136
7.1	Cavity Fabrication Methods	136
7.1.1	Fabrication Method I	137
7.1.2	Fabrication Method II	138
7.1.3	Comparison of the Fabrication Methods	138

Contents

7.2	Fabrication of the Cavity	138
7.3	Frequency Pre-tuning of the Cavity	140
7.4	Vacuum Brazing	142
7.5	Inspection of the Brazed Cavity	143
8	RF Testing of the Cavity	145
8.1	Initial RF Measurements	145
8.2	Investigation of the Low Quality Factor	147
8.2.1	Effect of the Cavity Surface Roughness	148
8.2.2	Influence of the Cavity Components	149
8.2.3	Conclusion	157
8.3	Bead-pull Measurement	159
8.3.1	Measurement Setup	160
8.3.2	Field Profile From the Simulation	161
8.3.3	Field Profile From the Measurements	162
8.4	Warm RF Test of the Cavity	166
8.4.1	RF Test Setup	166
8.4.2	Frequency Shift due to the Temperature Variation	168
8.4.3	Vacuum Conditioning	169
8.5	Steps to Improve the Cavity Performance	173
8.5.1	Quality Factor of the Cavity	173
8.5.2	Mechanical Design and Fabrication	175
9	Summary and Outlook	177
	Appendices	183
A	Numerical Techniques and Convergence Study	183
A.1	Numerical Techniques	183
A.2	Convergence Study	184
	Bibliography	186

List of Acronyms

AGS	Alternating Gradient Synchrotron, Brookhaven
ALS-U	Advanced Light Source upgrade
ANL	Argonne National Laboratory
ARIEL	Advanced Rare Isotope Laboratory
bERLinPro	Berlin Energy Recovery Linac Prototype
BNL	Brookhaven National Laboratory
CEBAF	Continuous Electron Beam Accelerator Facility
CERN	Conseil Européen pour la Recherche Nucléaire
CLIC	Compact Linear Collider
CNAO	Centro Nazionale di Adroterapia Oncologica
CST MWS	CST MICROWAVE STUDIO®
CTF3	CLIC Test Facility 3
CW	Continuous Wave
DAFNE	Double Annular Φ Factory for Nice Experiments
DALI	Dresden Advanced Light Infrastructure
ELBE	Electron Linac for beams with high Brilliance and low Emittance
ERL	Energy Recovery Linac
ESS	European Spallation Source
FEL	Free Electron Laser
FELBE	FEL station at the ELBE
FEM	Finite Element Method
FERMI	Fermi National Accelerator Laboratory
FIT	Finite Integration Technique
FRANZ	FRAnkfurt Neutron Source at the Stern-Gerlach-Zentrum
FOM	Figures of Merit
GANIL	Grand Accélérateur National d'Ions Lourds

List of Acronyms

gELBE	gamma ray experimental station at the ELBE
HOM	Higher Order Mode
HUST-PF	Huazhong University of Science and Technology-Proton Facility
HZDR	Helmholtz Zentrum Dresden-Rossendorf, Dresden
ILC	International Linear Collider
JELIC	Jefferson Lab Electron Ion Collider
J-PARC	Japan Proton Accelerator Research Complex
JLab	Thomas Jefferson National Accelerator Facility
LANL	Los Alamos National Laboratory
LHC	Large Hardon Collider
LOM	Lower Order Mode
LCLS	Linac Coherent Light Source
NCRF	Normal Conducting Radio-Frequency
nELBE	neutron station at the ELBE
OFHC	Oxygen Free High Conductivity
PEFP	Proton Engineering Frontier Project
pELBE	positron station at the ELBE
PS	Proton Synchrotron
PSI	Paul Scherrer Institute
RF	Radio-Frequency
RHIC	Relativistic Heavy Ion Collider
RMS	Root Mean Square
SACLA	Spring-8 Angstrom Compact free electron LAser
SLAC	Stanford Linear Accelerator Center
SOM	Same Order Mode
SPS	Super Proton Synchrotron
SRF	Superconducting Radio-Frequency
TCAV	Transverse deflecting CAVity
TE	Transverse Electric
TELBE	Terahertz lab at the ELBE

List of Acronyms

TEM	Transverse Electric and Magnetic
TESLA	TeV-Energy Superconducting Linear Accelerator
THz	Tera Hertz
TM	Transverse Magnetic
UHV	Ultra-High Vacuum
X-FEL	X-ray Free-Electron Laser Facility

List of Symbols

Symbol	Unit	Description
$a(t)$	m/s^2	acceleration of a particle
$\mathbf{B}(\mathbf{r}, t)$	Vs/m^2	magnetic flux density
B_x, B_y, B_z	Vs/m^2	magnetic flux density along the x , y and z -axis
c	m s^{-1}	speed of light in vacuum
C_c	F	capacitance of a magnet cell
C_{end}	F	end capacitance of a quarter-wave resonator
D	1	duty cycle of macro-pulse
$\mathbf{D}(\mathbf{r}, \mathbf{t})$	As/m^2	electric flux density
d_c	m	diameter of a cavity
Ef_s	m^{-1}	efficiency of a stripline kicker
$\mathbf{E}(\mathbf{r}, \mathbf{t})$	V/m	electric field strength
$\mathbf{E}_\perp, \mathbf{E}_\parallel$	V/m	tangential and parallel electric field
E_b	eV	beam energy
$E_{0,n}$	V m^{-1}	electric field magnitude for the n^{th} order multipacting
E_{pk}	V m^{-1}	peak electric field of the mode on the cavity surface
$E_z(0, 0, z)$	V m^{-1}	longitudinal electric field along the cavity axis
\mathbf{F}	kgm/s^2	Lorentz force
f_b	s^{-1}	bunch repetition rate of a beam
f_0	Hz	operating frequency of a cavity
f_p	s^{-1}	pulse repetition rate
f_{pr}	s^{-1}	resonance frequency of the perturbed cavity
G	Ω	Geometrical factor of a cavity
g_\perp	1	transverse geometry factor of a stripline
$\mathbf{H}(\mathbf{r}, t)$	A m^{-1}	magnetic field strength

List of Symbols

Symbol	Unit	Description
$\mathbf{H}_\perp, \mathbf{H}_\parallel$	A m ⁻¹	tangential and parallel magnetic field strength
h_{ap}	m	horizontal aperture
h_c	m	cavity height
h_{gap}	m	horizontal gap between the rods
h_{st}	m	stem height
I_b, I_c	A	beam current and coil current
j	1	complex unit
$\mathbf{J}(\mathbf{r}, t)$	A/m ²	current density
$J_m(x), J'_m(x)$	1	Bessel function of the first kind of m^{th} order and its derivative
$j_{m,n}, j'_{m,n}$	1	n^{th} zero of the $J_m(x)$ Bessel function and its derivative
k	1/m	wave number
k_d	Ω s ⁻¹	loss factor
K_n	eV	impact energy of the particle for the n^{th} order multipacting
l_c, l_s, l_r, l_{st}	m	length of a cavity, structure, rod and stem
L_c	H	cell inductance of a travelling wave kicker
m_e	eV/cm ²	rest mass of an electron
\mathbf{n}	1	normal vector
p_\parallel, p_\perp	kg m s ⁻¹	longitudinal and transverse momentum of a particle
P_c	W	power deposited by the operating mode
P_{av}, P_{pk}	W	average and peak power loss
P_g	W	total power fed into the cavity through FPC
P_{fwd}	W	total power transmitted into the cavity
P_{ref}	W	total power reflected from the cavity
P_{sg}	W	control power fed from the signal generator to the amplifier
q	A s	electric charge
q_b	A s	bunch charge
Q_0	-	unloaded or intrinsic quality factor of a cavity
Q_L	-	loaded quality factor of a cavity
Q_m	1	the quality factor measured from the S-parameters
Q_{in}, Q_{pu}	1	quality factor of the main coupler and pick-up probe

List of Symbols

Symbol	Unit	Description
Q_{pc}	1	quality factor of a plain cavity
Q_n	1	quality factor of a component at the cavity Port n
r_c, r_r	m	radius of a cavity and rod
r_{gf}	m	radius of the good field region required
R_s	Ω	surface resistance
$R/Q, R_{\perp}/Q$	Ω	longitudinal and transverse shunt impedance
R_z	m	RMS surface roughness
S_{pk}	W/cm ²	peak surface power loss density
S_{av}	W/cm ²	average surface power loss density
SF_r	1	scaling factor of the rods
t_f, t_r, t_w	s	pulse fall time, rise time, and pulse width
t_m	s	field fill time in a magnet
t_{of}	m	vertical offset between the construction and cutting ellipse
T_w	°C	temperature of the coolant water
U	J	energy stored in the cavity
\mathbf{v}	m/s	velocity of the charged particle
$v_n(t), v_n$	m/s	velocity of the charged particle for the n_{th} order multipacting
V_{acc}	V	integrated accelerating voltage
v_{ap}	m	vertical aperture
V_p	V	magnitude of the pulse
V_c	V	coil voltage
$V_{ }, V_{\perp}$	V	integrated longitudinal and transverse voltage
$V_{ ,qb}$	V	longitudinal induced voltage by a bunch with charge q_b
$V_{\perp,qb}$	V	transverse induced voltage by a bunch with charge q_b
$V_{b,r}$	V	the deflecting voltage induced by the beam at resonance
$\tilde{V}_g, \tilde{V}_c, \tilde{V}_b$	V	generator, cavity and beam induced voltage in phasor
V_c	V	the cavity voltage at resonance
$V_{g,r}$	V	the generator voltage at resonance
w_c, w_{st}	m	width of a cavity and stem
x, y, z	1	axis of the Cartesian coordinate system

List of Symbols

Symbol	Unit	Description
Z_{in}	Ω	input impedance of a transmission line
Z_L	Ω	load impedance of a transmission line
Z_0	Ω	characteristic impedance of a transmission line
β	1	ratio of the particle velocity to speed of light in vacuum
β_d	m	beta function at the deflector
β_{in}	1	input coupling factor of the main coupler
β_{pu}	1	output coupling factor of the pick-up probe
δ	m	skin depth
$\delta V_{\perp}(d, 0)$	1	relative V_{\perp} error at an offset d in the x -axis
$\delta V_{\perp}(0, d)$	1	relative V_{\perp} error at an offset d in the y -axis
Δd_{max}	m	maximum deformation in the cavity
Δf_0	s^{-1}	frequency change of the operating mode
Δf_{bw}	s^{-1}	bandwidth of a mode
Δf_{pr}	s^{-1}	frequency change due to perturbation
Δf_{tr}	s^{-1}	frequency range of the cavity tuning
$\Delta \phi$	rad	the phase shift of S_{21} parameter measured at f_0
ΔV_{\perp}	V	kick voltage error due to non-uniform kicking of a bunch
$\Delta \theta$	rad	deflection error due to non-uniform kicking of a bunch
Δp_{\perp}	$kg\ m\ s^{-1}$	change in the transverse momentum of a particle
ΔW	J	longitudinal energy gain by a particle
$\Delta x, \Delta y$	m	offset from the cavity center along the x and y -axis
$\Delta \epsilon_0$	mm rad	change in the emittance of the beam
$\Delta \psi$	rad	betatron phase advance from the cavity to the screen
ϵ_0, ϵ_N	mm rad	geometric and normalized emittance of a beam
ϵ, ϵ_0	As/Vm	absolute permittivity and permittivity of the free space
μ, μ_0	Vs/Am	absolute permeability and permeability of the free space
ϵ_r, μ_r	1	relative permittivity and permeability of the medium
Γ	1	reflection coefficient
ω	1/s	angular frequency
ϕ_0	rad	RF phase at which bunch is at the cavity center

List of Symbols

Symbol	Unit	Description
$\rho(\mathbf{r}, t)$	As/m ³	electric charge density
σ	S m ⁻¹	electrical conductivity
σ_t	s	bunch length in terms of time
σ_{Rz}	S m ⁻¹	electrical conductivity due to the surface roughness
θ	rad	deflection angle of a particle
$\theta_E, \theta_B, \theta_{EB}$	rad	deflection due to electric field, magnetic field and both
$\nabla \cdot$	1/m	divergence operator
∇_{\perp}	1/m	transverse divergence operator
$\nabla \times$	1/m	curl operator
η	Ω	wave impedance
ψ	rad	detuning angle due to off-resonance cavity operation
$\partial\Omega$	1	boundary of the problem domain
Ω	1	problem domain
τ	1	the time constant of a cavity
ζ	MV/m/MW ⁻²	efficiency factor of a TW disc-loaded cavity

List of Figures

1.1	Layout of the linear accelerator, ELBE, highlighting the main accelerator components and different experimental stations at the facility (image source: [2]).	2
1.2	An initial conceptual sketch of a proposed accelerator, DALI, at the HZDR. The beam from the acceleration section is split into multiple beams using beam separators, enabling the concurrent delivery of the beam to different user stations.	5
1.3	A schematic showing the basic working principle of a beam separator. Alternate bunches of the main beam (f_b) receive a transverse kick of opposite polarity in a beam separator, resulting in two separate beams, each with a bunch repetition rate of $f_b/2$	6
2.1	A sketch of the transverse deflection of a charged particle ($-q$) in the y plane due to the static electric field E_y (a) and the magnetic field B_x (b).	13
2.2	A schematic view of a stripline kicker of length l_s with the electrodes separated by a distance d , and the corresponding pulse structure applied on the strips.	15
2.3	Sketch of a coaxial transmission line and the distribution of the electric and magnetic field of a TEM mode in the xy -plane (red \rightarrow 1 and blue \rightarrow 0).	18
2.4	A cross-sectional sketch of the $\lambda/2$ and $\lambda/4$ coaxial resonator (top row). The graph shows the voltage on the inner conductor surface for the first three modes supported by the resonator (middle row). The bottom line shows the equivalent transmission line diagrams for the $\lambda/2$ and $\lambda/4$ coaxial resonator.	19

List of Figures

2.5	a) A sketch of two-point multipacting between parallel plates shown in 2D with an oscillating electric field (E_y) between the plates which are separated by a distance d . For the first half of the RF cycle (b), electrons travel from right to left plate, and in the second half cycle the electrons travel direction reverses (c).	32
3.1	Classification of deflecting structures based on the field components and their mode of operation with an example.	36
3.2	Illustration of the timing structure of a beam and the different operating modes of the deflecting structures: (a) beam structure with a bunch rate of f_b , (b) pulse structure with the uni-polarity pulses, (c) pulse structure with the alternate polarity pulses, (d) transverse force at the subharmonic frequency of the bunch rate in CW mode, (e) transverse force at the ultraharmonic frequency of the bunch rate in CW mode, and (f) transverse force at the ultraharmonic frequency of the bunch rate in quasi-CW mode.	37
3.3	A sample pulse structure scheme of a stripline kicker, where the input pulse is applied on electrodes at time t_1 for a duration of t_w , and t_r is the field rise time.	55
3.4	A sketch of the beam path of an ideal deflecting structure and an RF deflecting structure and the corresponding transverse kick voltage received by the bunches. The direction and length of an arrow corresponds to the polarity and magnitude of the transverse voltage.	63
3.5	The bunch length expressed in terms of RF phase for different frequencies (left), and the transverse kick voltage error at different RF phases for the two frequencies of interest (right).	64
3.6	The kick angle error for different RF phases for the three frequencies (left), and variation of the kick angle error at four RF phases at different frequencies (right). A bunch length of 5 ps and the kick angle of 3 mrad is considered.	65
3.7	The relative projected emittance growth for different RF frequencies at the zero-crossing and the on-crest phase. Here, σ_t is 2 ps, β_d is 2.5 m, beam energy is 100 MeV, θ is 3 mrad, and ϵ_N is 5 mm mrad.	67

List of Figures

3.8	The surface power loss and average surface power loss density in the single-cell pill-box cavity which delivers a V_{\perp} of 300 kV.	68
3.9	RF power loss per cell, total power loss in a multi-cell cavity, and the average surface loss density at various frequencies for the multi-cell pill-box cavity with a length of 1 m and a kick voltage gradient of 300 kV/m.	69
3.10	Distribution of the normalized magnetic field H_x in the xy -plane of the TM_{110} mode (left), and the normalized magnetic field H_x along the x and the y -axis (right).	70
3.11	The radius of the good field region along the x and y -axis of a pill-box cavity for the various resonance frequencies when the cavity is operated in TM_{110} mode.	71
4.1	Illustration of the electric field distribution in the four fundamental modes of a 4-rod cavity.	79
4.2	Distribution of the electric (a) and the magnetic field (b) in the deflecting mode (Mode 2) on the longitudinal cross section of the 4-rod cavity, and (c) shows the corresponding surface power loss distribution. The red and blue colors represent the maximum and minimum magnitude of a parameter.	79
4.3	The transverse electric and magnetic fields along the beam axis of a 4-rod TCAV (left), and the instantaneous transverse force due to the electric field, magnetic field, and both the fields (right). Also shows the development of the transverse voltage along the cavity.	80
4.4	Geometry of a complete 4-rod cavity and the rods with the important geometry parameters labeled.	80
4.5	Variation of the rod length and the FOM for the different rod radii of Design I with the deflecting mode frequency fixed at 273 MHz.	81
4.6	A comparison of the kick voltage homogeneity of the 4-rod scaled cavity and the Design I cavity of various rod radii. The relative kick voltage error variation along the x and y -axis are given by $\delta V_{\perp}(d, 0)$ and $\delta V_{\perp}(0, d)$, respectively.	82

List of Figures

4.7	Geometry of a 4-rod crab cavity with the dimensions labeled. Also shows the construction of the kidney shaped rods with the construction ellipses (yellow) for the rods and the cutting ellipse (red) which subtracts the construction ellipse.	83
4.8	Comparison of the kick voltage homogeneity of the scaled kidney-shaped rods and the flat rods. The relative kick voltage error variation along the x and y -axis are given by $\delta V_{\perp,(x,0)}$ and $\delta V_{\perp}(0, d)$, respectively. The scaled cavity values are multiplied by a factor of 10 for better visual representation.	84
4.9	FOM for different sizes of kidney-shaped rods and flat rods. V_{\perp} is calculated for the total energy of 1 J in the cavity, and the P_c , S_{pk} , and E_{pk} are calculated for a V_{\perp} of 300 kV.	85
4.10	Geometries of the RF-dipole crab cavity with the circular and rectangular outer cross section discussed in [33, p.99].	87
4.11	The transverse electric and magnetic fields along the beam axis of an RF-dipole TCAV (left), and the instantaneous transverse force due to the electric field, magnetic field, and both the fields (right). Also shows the development of the transverse voltage along the cavity. . .	88
4.12	The kick voltage homogeneity of RF-dipole cavities with a circular and rectangular outside conductor, as well as the respective adapted designs, Design III and IV. The relative kick voltage error variation along the x and y -axis are given by $\delta V_{\perp}(d, 0)$ and $\delta V_{\perp}(0, d)$, respectively.	89
4.13	Geometrical model of a double-quarter-wave crab cavity [171], with important dimensions labeled.	90
4.14	FOM for the different cavity aspect ratios (l_c/w_c) with the deflecting mode fixed at 273 MHz. The power loss, S_{pk} , and E_{pk} are calculated for the V_{\perp} of 300 kV. V_{\perp} is calculated for the total energy of 1 J in the cavity, and the P_c , S_{pk} , and E_{pk} are calculated for a V_{\perp} of 300 kV.	91
4.15	The kick voltage homogeneity of the scaled cavity, and also for the different aspect ratios (l_c/w_c) of the cavity. The relative kick voltage error along the x and y -axis are given by $\delta V_{\perp}(d, 0)$ and $\delta V_{\perp}(0, d)$, respectively.	92

List of Figures

4.16	The base geometry of the TCAV with a rectangular cross-section stem and outer conductor.	93
4.17	Variation of cavity height and FOM for different stem width and stem length for the deflecting mode frequency at 273 MHz. The V_{\perp} is calculated for the total energy of 1 J in the cavity, whereas the surface power loss, S_{pk} , and E_{pk} are calculated for the V_{\perp} of 300 kV.	94
4.18	Comparison of the kick voltage homogeneity for the different stem widths with the stem length fixed at 300 mm. The relative kick voltage error along the x and y -axis are given by $\delta V_{\perp}(d, 0)$ and $\delta V_{\perp}(0, d)$, respectively.	95
4.19	Distribution of the surface power loss density on the surface of the different cross-sectional stems.	96
4.20	FOM of the cavity for different stem blend radii with the stem length and frequency fixed at 300 mm and 273 MHz, respectively. The power loss, S_{pk} , and E_{pk} are calculated for the V_{\perp} of 300 kV.	96
4.21	FOM of the cavity for the different stem aspect ratios with the deflecting mode frequency fixed at 273 MHz. The power loss, S_{pk} , and E_{pk} are calculated for the V_{\perp} of 300 kV.	97
4.22	Comparison of the kick voltage homogeneity of the cavity for different stem blended radii and stem aspect ratios with the relative kick voltage error along the x and y -axis are given by $\delta V_{\perp}(d, 0)$ and $\delta V_{\perp}(0, d)$, respectively.	98
4.23	The side and top view of a stem highlighting the protrusion of the stem base.	98
4.24	The electric and magnetic field distribution in the cavity with a plain stem and a protrusion in the stem's base. The field values refers to the total energy of 1 J in the cavity.	99
4.25	Variation of the cavity height and FOM for different stem and protrusion lengths with the deflecting mode frequency fixed at 273 MHz. The V_{\perp} is calculated for an 1 J of energy in the cavity, whereas P_c , S_{pk} and E_{pk} are calculated for a V_{\perp} of 300 kV.	100

List of Figures

4.26	The kick voltage homogeneity for different protrusion lengths with the stem length and protrusion thickness fixed to 300 mm and 20 mm, respectively. The relative kick voltage error along the x and y -axis are given by $\delta V_{\perp}(d, 0)$ and $\delta V_{\perp}(0, d)$, respectively.	101
4.27	Variation of cavity height and FOM for different cavity length for the deflecting mode frequency at 273 MHz. The V_{\perp} is calculated for total energy of 1 J in a cavity and power loss is calculated for V_{\perp} of 300 kV.	102
4.28	Variation of cavity height and important FOM for Design VI for various cavity apertures with the deflecting mode frequency at 273 MHz. The V_{\perp} is calculated for total energy of 1 J in a cavity and power loss is calculated for V_{\perp} of 300 kV.	102
4.29	Comparison of the kick voltage homogeneity of Design VI for different cavity apertures. The relative kick voltage error along the x and y -axis are given by $\delta V_{\perp}(d, 0)$ and $\delta V_{\perp}(0, d)$, respectively.	103
4.30	Comparison of the kick voltage homogeneity of the probable TCAV designs. V_{\perp} is calculated for the total energy of 1 J in the cavity, and the P_c , S_{pk} , and E_{pk} are calculated for a V_{\perp} of 300 kV.	106
5.1	A cross-sectional view of the ELBE pre-buncher and the cavity components: fundamental power coupler, frequency tuner and pick-up probe.	108
5.2	The coupling strength, β_{in} , of the three coupling loop designs with the FPC placed at the corner and center of the cavity with different orientations of the loop.	110
5.3	A sketch showing the two options for the pick-up probe location in the cavity (right). The graph shows the variation of the pick-up quality factor, Q_{pu} , for the different antenna lengths for option II (left).	112
5.4	Graph shows the frequency shift (Δf_{tr}) due to single and dual tuners placed at the center and corner of the cavity and the cross-sectional view of the cavity showing different cavity components is also presented (right).	113

List of Figures

5.5	The magnitude of the electric field between the stems for different RF power levels and cavity apertures, and the dot refers to the maximum electric field above which 2-point multipacting can not sustain (left). A strong uniform electric field distribution between the stems is shown in the right picture.	114
5.6	The electric field at different RF phases and order of multipacting for which the resonance condition for multipacting is satisfied (left). The variation of impact energy of the electrons for various RF power levels and orders of multipacting in a cavity (right). The shaded region represents the multipacting region for copper. The cavity aperture under consideration is 30 mm.	115
5.7	Vector diagram for the deflecting cavity when the beam loading is purely active (a) and reactive (b). The beam current is aligned with the real part of the voltage, and \tilde{V}_b , \tilde{V}_g , \tilde{V}_c refers to the beam induced voltage, the generator voltage and the cavity voltage in phasor notation, respectively.	117
5.8	The shunt impedance of the longitudinal, horizontal, and vertical deflecting modes of the deflecting cavity.	119
6.1	Illustration of the two types of multiphysics coupling analysis: a) Strong (two-way) coupling between the physics process and b) Weak (one-way) coupling between the physics process. The connection or coupling between the sub-domain is between the boundaries in the surface-coupled case, whereas the interaction is in the same spatial domain in the volume-coupled case.	121
6.2	The process flow of the cavity multiphysics analysis carried out with CST Studio Suite® [36] considering a weakly coupled problem. The solvers included in the black dotted line were sequentially executed in the parametric analysis.	122
6.3	The cavity is symmetric in all three planes and the cavity surfaces split by the symmetric planes are assigned a fixed boundary condition normal to its surface. Also shows the $1/8^{th}$ of the cavity model considered in the structural analysis.	124

List of Figures

6.4	The important cavity faces considered for the frequency sensitivity analysis.	126
6.5	Copper cavity deformation due to the atmospheric pressure for three different wall thicknesses with the outline of the original cavity marked by a solid black line. For better visualization, the deformation in the model is scaled by a factor of 10, 100, and 500 times for the wall thickness of 5 mm, 15 mm, and 25 mm, respectively. The effect due to cavity is neglected.	128
6.6	Maximum deformation and frequency shift for various wall thicknesses of copper and stainless steel cavities with a pressure of 1 bar on the outer cavity surface.	129
6.7	Distribution of the von Mises stress on a 25 mm thick copper cavity in an evacuated state.	130
6.8	Maximum deformation in the cavity and resonance frequency shift of the copper cavity at different ambient temperatures.	131
6.9	Surface power loss density distribution across the inner cavity surface for an RF power loss of 800 W (a) and location of the coolant channels are highlighted in green (b).	132
6.10	Temperature distribution across the copper cavity for an RF power loss of 800 W, with a coolant and ambient temperature of 30 °C and 20 °C, respectively.	132
6.11	Deformation of the copper cavity with a wall thickness of 25 mm: a) due to the atmospheric pressure, (b) due to atmospheric pressure with the maximum deformation of the scale set to 10 μm, (c) due to P_c of 800 W with the coolant and ambient temperature of 30 °C and 20 °C, respectively, and (d) due to atmospheric pressure, P_c of 800 W with the coolant and ambient temperature of 30 °C and 20 °C, respectively. Outline of the original cavity is marked by a black line and the deformation of the model is scaled by 100 times.	133
6.12	Resonance frequency shift of the copper cavity for different RF power levels and coolant temperatures.	134

List of Figures

7.1	Cavity divided into three parts considering two different fabrication methods.	137
7.2	Three parts of the copper cavity were machined separately and the stainless steel base was used as a template for machining the parts. .	139
7.3	The cavity resonance frequency for different apertures and a quadratic fitted curve. The resonance frequency measured during the pre-tuning process and the corresponding extrapolated curve are plotted (in green). The values obtained during pre-tuning process are listed in Table 7.2.	140
7.4	A sketch of the cavity bottom surface highlighting the filler overflow region and the filler channel (left), and the photos of different regions captured with a telescopic camera. The distances mentioned are the approximate values.	143
8.1	Calculating loaded quality factor of a cavity Q_L from the measured S_{21} parameter (left) and representation of S_{11} on a Smith chart for three different coupling factors (right).	146
8.2	The variation of σ_{R_z}/σ and Q_{R_z}/Q for different ratios of the surface roughness to skin depth (R_z/δ) as predicted through the Hammerstand and Bekkadal model [179] (left). Extrapolation of the cavity quality factor obtained from the simulation using the model, including the measured quality factor and the RMS surface roughness (right). . . .	149
8.3	A sketch of the cavity showing all the cavity ports and the components associated with the ports (left), and the two over-coupled antennas are used at the Port 1 and Port 2 (right) for measuring the S-parameters.	150
8.4	A snapshot of the actual RF filter (a), pick-up probe (b), and main power coupler (c) of the cavity which are placed at Port A, Port B and Port C, respectively.	152
8.5	The cavity resonance frequency and the quality factor measured for different orientations of the coupler loop with and without the RF fingerstock. Here, at 0 the loop is directed towards the stem, at $\pi/2$ it is parallel to the stem, and at π it is oriented away from the stem. .	155

List of Figures

8.6	The actual bead-pull measurement setup built to measure the field profile along the cavity axis of a deflecting cavity. A small perturbing object (bead) tethered by a thin string (fishing wire) is moved along the cavity axis using a DC motor.	160
8.7	The on- and off-axis electric and magnetic field components of the deflecting mode along the longitudinal direction obtained through simulation. In this case, an offset distance Δy of 11 mm is considered.	161
8.8	The relative frequency change along the cavity axis measured with the metallic and the dielectric spherical bead. The graph represents the mean of 40 measurements, and the difference between the values of the scaled dielectric and those of the metallic sphere render $ \mathbf{H} ^2$.	163
8.9	The relative frequency shift measured on- and off-axis along the z -axis using a ceramic and a metallic cylinder with an offset along the y -axis (Δy of 11 mm). The longitudinal electric field at the off-axis is obtained by taking the difference between the on- and the off-axis measurement values (black).	165
8.10	The cavity and the associated components arranged for the warm RF test (left); the sketch shows the RF devices and the power measurement points.	167
8.11	Temperature readings during the cavity cooling down process and the location of the thermocouples in the cavity.	169
8.12	Variation of the input coupling factor of the main coupler and the resonance frequency shift at different cavity temperatures.	169
8.13	Snapshot of the pick-up probe surface captured through an infrared camera when 400 W of power was fed to the cavity. Variation of the power coupled out of the cavity through the pick-up probe for different antenna lengths with the input power to the cavity fixed at 800 W.	170
8.14	Temperature distribution on the pick-up and antenna for the input power of 800 W for a steel and copper pick-up. The graph shows the variation of maximum temperature on the pick-up cup and antenna for different power level.	172

List of Figures

8.15 Silver coated pick-up cup, the old and the modified antenna of the cavity. 173

8.16 Variation of the intrinsic quality factor of a plain copper cavity with the vacuum port partially closed with a set of rods at different orientations. 174

A.1 Mesh convergence study of the eigenmode simulation with and without symmetry plane using the tetrahedral mesh carried out in CST MWS® .185

List of Tables

- 1.1 A list of the experimental stations of the ELBE, the corresponding beam parameters and the properties of the radiation source [1, 6]. 3
- 2.1 The electric and magnetic field components of the TM and TE mode in a pill-box cavity [29] of radius r_c and length l_c . Here, m , n and p are the integers which characterize the field variations in the z , r , and θ directions of a cylindrical coordinate system, ω is the resonance frequency of a mode, k_{mn} is the angular wave number of the mode, and $j_{m,n}$ and $j'_{m,n}$ are the n^{th} root of the m^{th} order Bessel function ($J_m(x)$) and its first derivative ($J'_m(x)$), respectively. 17
- 3.1 Important parameters of the beam chopper structures. The chopper length and vertical aperture are denoted by l_s and v_{ap} , the pulse voltage, rise/fall time, width and repetition rate are denoted by V_p , t_r/t_f , t_w , and f_p , the duty cycle of the macro pulse is represented by D , and the deflection angle by θ 39
- 3.2 Important parameters of selected stripline kicker structures. The stripline length and vertical aperture are denoted by l_s and v_{ap} , the pulse voltage and width are denoted by V_p and t_w , the number of pulses in a pulse train is given by N_b , the repetition rate of the pulse train is given by f_p , V_{\perp} is the transverse kick voltage, P_{pk} and P_{av} are the peak and average power loss, and Ef_s is a constant that defines the efficiency of a stripline kicker ($Ef_s = V_{\perp}/(l_s \cdot V_p)$). Here, DR stands for Damping Ring, ATF for Accelerator Test Facility, and MBA for multi-bend achromat. 47

List of Tables

3.3	The approximate pulse characteristics expected from a deflecting pulsed structure of length 500 mm. Furthermore, the structure should deliver a transverse voltage V_{\perp} of 300 kV or an integrated transverse magnetic field of 1 mT m.	48
3.4	The properties of the preliminary design of the transmission line pulsed magnet of length 500 mm, and an integrated magnetic field of 1 mT m. Here, N , I_c , and V_c denote the number of coil turns, the current and voltage in a coil, respectively; t_r/t_f , t_w , and f_p the pulse's rise/fall time, width, and repetition rate, and Z and P_{av} are the value of the load impedance and the average power loss at the load, respectively.	52
3.5	The required pulse voltage, peak and average power loss at the 50 Ω load of the stripline kickers presented in Table 3.2 to deliver a V_{\perp} of 300 kV with the structure length (l_s) scaled to 50 cm and pulse width of 10 ns. Here, P_{av_1} and P_{av_2} are the average power loss at the load with the pulse rate at 13 MHz and 1 MHz, respectively.	54
3.6	The properties of the stripline kicker's basic design discussed with the electrode length of 500 mm and are separated by 30 mm, and delivers a transverse kick voltage of 300 kV. Here, V_p , t_r/t_f , t_w and f_p denotes the voltage, rise and fall time, width and repetition rate of pulses, whereas, Z , P_{pk} , and P_{av} are the load impedance, peak and the average power loss at the load, respectively.	56
3.7	Important properties of the selected TW and SW disc-loaded structures and the required RF power to achieve a V_{\perp} of 300 kV. Here, $P_{av,1}$ refers to the power required with the original cavity length, and $P_{av,2}$ is the normalized power loss with respect to the reference cavity length of 500 mm.	59
3.8	Important properties of selected TEM-class normal conducting deflecting cavities. The required RF power to achieve a V_{\perp} of 300 kV with the original cavity and the normalized power loss with respect to the reference cavity length of 500 mm are given as P_{av_1} and P_{av_2} , respectively.	60
3.9	A list of criteria for selecting the operating frequency of the TCAV and the corresponding values obtained in this section.	72

List of Tables

3.10	The possible use case scenarios of the TCAV as a beam separator and dark current kicker for ELBE and DALI [162].	73
3.11	Selection criteria for a beam separator based on the beam parameters, the kick voltage requirement, kick field homogeneity, and the ease of the design, fabrication, and CW operation of the device.	74
4.1	Main requirements of the TCAV being developed as a beam separator for the ELBE and the DALI.	77
4.2	Important dimensions of the 4-rod CEBAF cavity [105, 158], the scaled cavity, and the final adapted cavity, i.e Design I. The parameters are labeled in Figure 4.4.	81
4.3	FOM of the scaled 4-rod CEBAF cavity and the adapted cavity, Design I, with the deflecting mode frequency fixed at 273 MHz. V_{\perp} is calculated for the total energy of 1 J in the cavity, and the P_c , S_{pk} , and E_{pk} are calculated for a V_{\perp} of 300 kV.	82
4.4	Important dimensions of the 4-rod crab cavity [165, p.10], the scaled cavity, and the final adapted cavity i.e Design II. Here, ellipse width and breadth are denoted by w and b , and the subscripts b , t and c refer to the ellipse of the rod base, rod tip, and the cutting ellipse, and the vertical offset between the construction and cutting ellipse is denoted by t_{of} . The parameters are labeled in Figure 4.7.	84
4.5	FOM of the scaled 4-rod crab cavity and its adapted cavity, Design II, with the deflecting mode frequency at 273 MHz. V_{\perp} is calculated for the total energy of 1 J in the cavity, and the P_c , S_{pk} , and E_{pk} are calculated for a V_{\perp} of 300 kV.	86
4.6	Important dimensions of the RF-dipole cavity having a trapezoidal stem and an outer conductor with a circular and a rectangular cross section [33], and the corresponding scaled and the adapted cavity designs (Design III and IV). The parameters are labeled in Figure 4.10.	88

List of Tables

4.7	FOM of the scaled RF-dipole cavities with a trapezoidal stem and an outer conductor of a circular and a rectangular cross section, and the corresponding adapted cavity designs, Design III and IV. V_{\perp} is calculated for the total energy of 1 J in the cavity, and the P_c , S_{pk} , and E_{pk} are calculated for a V_{\perp} of 300 kV.	89
4.8	Important dimensions of the double-quarter wave crab cavity [172], the scaled cavity, and the final adapted cavity i.e. Design V. The parameters are labeled in Figure 4.13, and aspect ratio is the ratio of the cavity length to the cavity width.	91
4.9	FOM of the scaled double-quarter wave crab cavity and its adapted cavity, Design V, with the deflecting mode fixed at 273 MHz. V_{\perp} is calculated for the total energy of 1 J in the cavity, and the P_c , S_{pk} , and E_{pk} are calculated for a V_{\perp} of 300 kV.	92
4.10	Important FOM of Design VI. V_{\perp} is calculated for the total energy of 1 J in the cavity, and the P_c , S_{pk} , and E_{pk} are calculated for a V_{\perp} of 300 kV.	103
4.11	Comparison of the cavity dimensions and FOM of the six TCAV designs with the deflecting mode frequency at 273 MHz. V_{\perp} is calculated for the total energy of 1 J in the cavity, and the P_c , S_{pk} , and E_{pk} are calculated for a V_{\perp} of 300 kV.	105
5.1	Cutoff frequency of the beampipe and the vacuum connection port.	118
6.1	Comparison of the frequency sensitivity values obtained from CST MWS [®] and the Slater's theorem for the critical cavity faces highlighted in Figure 6.4.	127
6.2	The electrical, thermal, and mechanical properties of the materials used in the multiphysics analysis.	128
7.1	Procedure followed during the frequency pre-tuning of the cavity.	141
7.2	Measurement values obtained during the frequency pre-tuning of the cavity. The values need to be considered in combination with the contents of Table 7.1 and Figure 7.3	142

List of Tables

8.1	Cavity properties measured during pre- and post-brazing, and the design values.	147
8.2	Measurement and simulation values of the cavity resonance frequency and the quality factor. The measurements are carried out with the ports kept open and/or close using a stainless steel flange.	151
8.3	The cavity resonance frequency and the quality factor were measured with the RF filter and the pick-up probe placed at Port A, and the simulation results.	152
8.4	Results of the RF measurement carried out with the pick-up probe placed at Port B of the cavity, and the simulation results are presented for a comparison.	154
8.5	Results of the RF measurement carried out with the power coupler placed at Port C of the cavity with open and matched terminations.	154
8.6	Results of the RF measurement carried out with the tuners placed separately at their respective ports and in three different positions. Here, ‘-1’, ‘0’, and ‘+1’ refers to the tuner head completely moved out of the cavity (at -25 mm), nominal position (at 0 mm), and completely inside the cavity (at 25 mm), respectively.	156
8.7	Results of the RF measurement carried out with both tuners and RF fingerstock placed simultaneously at their respective ports at three different positions, and also the quality factor predicted from the values given in Table 8.6.	157
8.8	The quality factor of the individual cavity components obtained from the measurements and simulation.	158
8.9	The quality factor of the cavity calculated using equation 8.5 with the quality factor of the individual components listed in Table 8.8.	158
8.10	Geometrical dimensions of the needle and sphere made of dielectric and metal used in the bead-pull measurement experiment.	162
8.11	The surface power losses on the pick-up cup and antenna of different material for the cavity input power of 800 W obtained from the simulation.	171

1 Introduction

Particle accelerators have historically been the primary tool of particle physics research and photon science, but more recently, their use has expanded from the purely fundamental scientific fields to the health and industrial sectors. High energy accelerators like the Large Hardon Collider (LHC) at CERN, Geneva, Switzerland, and KEK at Tsukuba, Japan, for example, are two of the primary tools for particle research. In comparison, the linear accelerator ELBE (Electron Linac for beams with high Brilliance and low Emittance) at the Helmholtz-Zentrum Dresden-Rossendorf (HZDR), Dresden, Germany, is a low energy accelerator that drives several different secondary particle and radiation sources, which are utilized for many different types of scientific experiments. Currently, it is not possible to simultaneously operate more than one ELBE secondary source. In this thesis, a new radio-frequency (RF) kicker design is presented which overcomes this limitation. The new design operates at an ultraharmonic of the beam repetition rate to enable the simultaneous operation of multiple downstream secondary sources, thus significantly enhancing the capabilities of the ELBE accelerator.

In this first chapter, the first section provides a brief introduction to the ELBE facility and different experimental stations, as well as the beam parameters required by the different user stations. The motivation for the present work is discussed in the second section. The goal of this thesis and the structure of the thesis are outlined in the final section of this chapter.

1.1 ELBE Accelerator

The linear electron accelerator, ELBE, is a versatile machine which drives six distinct secondary particle and radiation sources that are used in investigating condensed matter (e.g. carrier-, lattice-, and magneto-dynamics; nonlinear and high-

1 Introduction

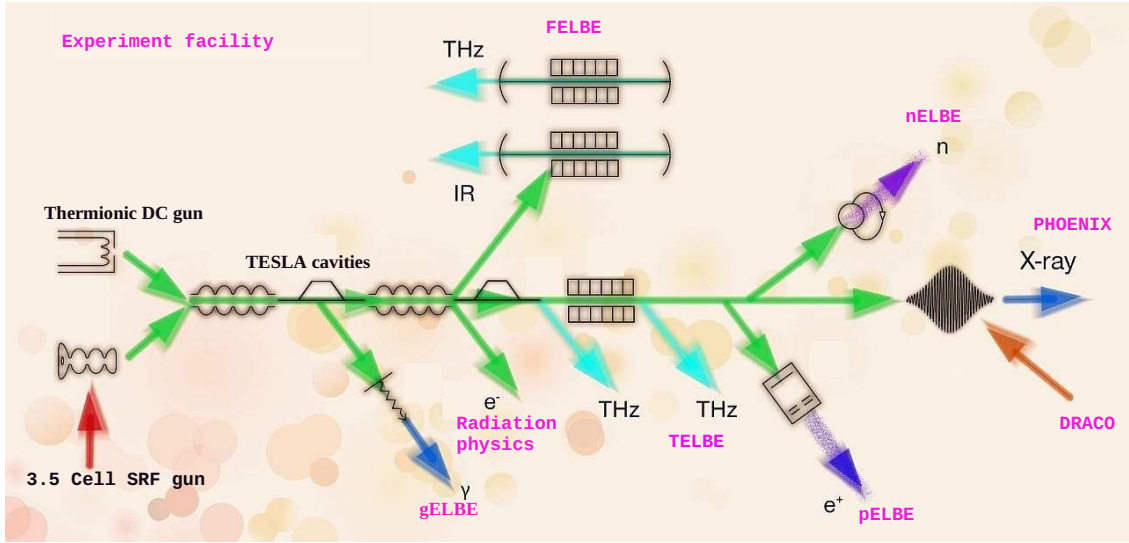


Figure 1.1: Layout of the linear accelerator, ELBE, highlighting the main accelerator components and different experimental stations at the facility (image source: [2]).

field phenomena; spectroscopy; nanophotonics; defect analysis; etc.), soft matter (biophysics, biochemistry, radiobiology, etc.), nuclear and astrophysics, detector testing, and accelerator development [1]. The layout of the ELBE, highlighting the important accelerator components and experimental stations is presented in Figure 1.1.

The accelerator has two electron sources, a thermionic direct current (DC) gun and a $3\frac{1}{2}$ cell superconducting radio-frequency (SRF) gun operating at 1.3 GHz. In the thermionic gun, electrons emitted from the hot cathode pass through a pulse control grid that releases the electrons in short bunches at a repetition rate of $26/2^n$ MHz (i.e., 26 MHz, 13 MHz, 6.5 MHz, 3.25 MHz, \dots) in continuous wave (CW) mode [3]. The anode is held at a potential of 250 kV, resulting in a beam of electron bunches with an energy of 250 keV and a bunch length of ≈ 500 ps. The control grid on the cathode can provide even more complex bunch repetition frequencies, including single bunches on demand. To setup the beam for the different types of experiments, the duty factor of the electron beam is reduced by a macropulsor which uses a set of steering magnets to sweep the electron beam across an aperture such that only a fraction of the beam passes from the injector into the accelerating cavities in “macropulses”. The individual electron bunches are compressed longitudinally to

1 Introduction

5 ps using a subharmonic pre-buncher followed by a harmonic buncher cavity. In the case of the SRF gun, a laser beam is flashed on a photocathode, and the emitted electrons are accelerated by the $3^{1/2}$ cell SRF cavity to 3.8 MeV [4]. The bunch length and bunch repetition rate are controlled by the laser pulse width and pulsing rate, respectively.

Electrons from either of the injector pass into the accelerating cavities present in the two linac cryomodules, with each module consisting of a pair of 9-cell TESLA cavities [5]. An acceleration gradient of 10 MeV per cavity has been achieved, and the beam can be accelerated up to a maximum of 40 MeV in CW mode [3].

The high energy electrons can be used directly for the experiments or passed through different devices to generate secondary radiation sources. Table 1.1 shows a list of the experimental stations of the ELBE, the required beam properties, and the features of the radiation sources. In the Bremsstrahlung (gamma ray) station at the ELBE (gELBE), an electron beam extracted after the first cryomodule strikes a niobium foil to generate γ rays which are used for experiments in nuclear astrophysics,

Table 1.1: A list of the experimental stations of the ELBE, the corresponding beam parameters and the properties of the radiation source [1, 6].

User station	ELBE electron beam		Radiation source		
	Energy	Bunch rate	Generated	Type	Properties
gELBE	6-20 MeV	Micro-pulse mode Pulse width: 1 ps to 5 ps	Bremsstrahlung	gamma ray	6-20 MeV
Radiation physics	10-31 MeV	CW mode Single pulse: kHz to Hz	ELBE beam	electron	10-31 MeV
TELBE	10-31 MeV	CW mode Single pulse: kHz to Hz	Undulator Diffraction radiator	infrared	0.1-2.5 THz 0.1-1.1 THz
FELBE	10-31 MeV	CW mode, macropulse Single pulse: kHz to Hz	Undulators	infrared	5-40 μm 18-250 μm
pELBE	10-16 MeV	CW mode: 1.625-13 MHz	Pair production	positron	0.5-15 keV
nELBE	10-35 MeV	CW mode: upto 406 kHz Single pulse	Photoneutron	neutron	0.01-15 MeV

1 Introduction

the investigation of material structure and defects, and the testing of high-energy photon detectors [1]. In the case of the radiation physics lab, the electron beam from the accelerator is used directly for the testing of the detectors and the irradiation of living cells. In the Terahertz lab at the ELBE (TELBE), the electron beam passing through a diffraction radiator or undulator generates THz pulses in a tunable range of 0.1-2.5 THz which are used for ultra-fast spectroscopy to investigate the dynamics of matter and also for the development of the advanced electron bunch diagnostic systems [7]. In the free-electron laser, the electron beam passing through an undulator produces light that gets confined in an optical resonator, and only a fraction of light is outcoupled for the user experiments. The FEL station at the ELBE (FELBE) has two undulators with individual laser systems to produce infrared radiation which is tunable from 5 μm to 250 μm and are used for the investigation of semiconductors, soft matter and biological materials, and THz spectroscopy [8]. At the positron station at the ELBE (pELBE), a tungsten target bombarded by the electron beam generates a monoenergetic positron beam due to pair production. The positron beam energy ranges from 0.5-15 keV and is used for positron spectroscopy of thin layers and the investigation of material defects [1]. In the case of the neutron station at the ELBE (nELBE), the electron beam hits a liquid-lead neutron radiator to produce neutrons in the energy range from 10 keV to 15 MeV [1]. The experimental station is used for the testing of materials used in nuclear fission and for experiments related to nuclear astrophysics and transmutation. A Petawatt laser system (DRACO) is used for the development of advanced compact and brilliant sources of energetic particle beams. A tunable source of intense ultra-short hard X-ray pulses are produced in PHOENIX using the electron beam of ELBE and laser pulse from DRACO.

1.2 Motivation

The ELBE linac can produce a 40 MeV electron beam with an average current of 1 mA at a bunch repetition rate of 13 MHz in CW mode [6]. Each experimental station has its own beam requirements which are based on the secondary radiation device and/or the needs of the user experiment. In the current beamline setup,

1 Introduction

the accelerated high energy beam can only be transported to a single experimental station at any given time. This limits the utilization of the accelerator to one user at a time. On the other hand, there is a high demand for user beamtime, with an average overbooking factor¹ for the different user beamlines ranging from 1.6 to 2.8 [9]. Furthermore, each experimental station has its own beam requirements which are based on the device that generates the secondary radiation and/or the needs of the user. Having the ability to operate multiple secondary sources concurrently in the existing accelerator would increase the available amount of user beam-time (i.e., increase the number of shifts awarded) and would improve the utilization of the facility. Furthermore, the multi-beamline operation is being actively considered for the proposed future accelerator facility Dresden Advanced Light Infrastructure (DALI) at the HZDR, Dresden (Figure 1.2).

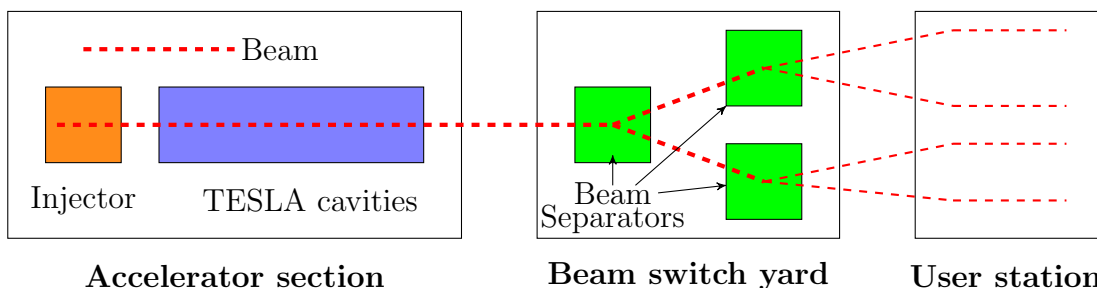


Figure 1.2: An initial conceptual sketch of a proposed accelerator, DALI, at the HZDR. The beam from the acceleration section is split into multiple beams using beam separators, enabling the concurrent delivery of the beam to different user stations.

The concept of utilizing multiple beamlines with a single primary beam is not a completely new concept. In 1961, Schnell proposed a deflecting cavity for the separation of the K mesons and anti-protons for the bubble chamber experiment at CERN [10]. Subsequently, similar techniques were implemented at the Alternating Gradient Synchrotron² (AGS), Brookhaven [11], the Stanford Linear Accelerator (SLAC) [12], and the Argonne National Laboratory (ANL) [13]. In 1982, Neil proposed a novel beam separator method for splitting a relativistic continuous beam into four pulsed

¹The average overbooking factor is the ratio of the shifts requested by the users to the shifts awarded to the users.

²At present, it is used as an injector to the Relativistic Heavy Ion Collider, Brookhaven

1 Introduction

beams [14]. The delivery of the beam to multiple experimental stations using a 3-way and 4-way beam splitting has been successfully achieved at the Continuous Electron Beam Accelerator Facility (CEBAF), Thomas Jefferson National Accelerator Facility (JLab) [15, 16]. Additionally, the multiple beamline concept has been proposed for and is at different stages of implementation/operation at the European X-Ray Free-Electron Laser Facility (**European X-FEL**), DESY, Hamburg, Germany [17], the **FERMI@Elettra** project³ [18], the Linac Coherent Light Source-II (**LCLS-II**), SLAC, the USA [19], the Spring-8 Angstrom Compact free electron LAsar (**SACLA**), RIKEN, Japan [20, 21], the Switzerland’s X-ray Free-Electron Laser (**SwissFEL**), Paul Scherrer Institute (PSI), Switzerland [22], the Next Generation Light Source (**NGLS**), Lawrence Berkeley National Laboratory (LBNL), Berkley, the USA [23], and the Advanced Rare Isotope Laboratory (**ARIEL**), TRIUMF, Vancouver, Canada [24]. Although the specifics of the techniques used in each application to achieve multiple beams may differ, the basic working principle remains the same: the use of a transverse deflecting structure/kicker, which delivers an alternating transverse kick to the sequence of bunches in the primary beam, thereby separating the bunches spatially to produce two or more secondary beams (Figure 1.3). An additional transverse kick from a septum or quadrupole magnet can be implemented to amplify the spatial separation of the deflected bunches [23] before the spatially separated beams are transported onward to different user stations.

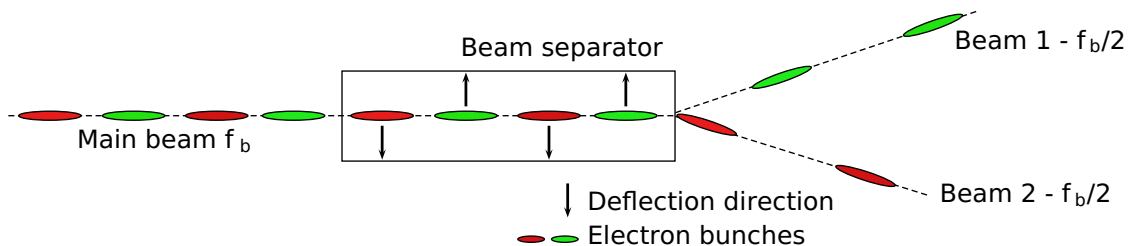


Figure 1.3: A schematic showing the basic working principle of a beam separator. Alternate bunches of the main beam (f_b) receive a transverse kick of opposite polarity in a beam separator, resulting in two separate beams, each with a bunch repetition rate of $f_b/2$.

³FERMI@Elettra stands for Free Electron laser Radiation for Multidisciplinary Investigations planned at Elettra- Sincrotrone Trieste, Italy

1.3 Aim and Outline of the Thesis

The multi-beamline operation of a linac significantly expands the research opportunity for user experiments by increasing the potential utilization of the facility. The distribution of bunches to multiple beamlines is achieved using a suitable transverse deflecting structure/kicker. This study aimed to investigate and develop a suitable deflecting structure that can be operated as a beam separator for the ELBE. Additionally, the structure is also capable of meeting the requirements of the DALI. This chapter presented a brief introduction to the ELBE, the user beam requirements, and motivation behind this work. The subsequent chapters provide detailed steps followed in developing the beam separator and they are structured as follows:

Chapter 2 briefly introduces the theoretical background necessary to follow this thesis. The transverse deflection due to the static magnetic and electric field is discussed before providing an overview of the theory of radio-frequency (RF) cavities. Concise information about the different types of cavities and their modes are described. Furthermore, the important cavity parameters are defined which are used to quantify the performance of the RF structure. Finally, the power required to drive the fundamental mode, the effect of high order modes, and the multipacting phenomena in a cavity are discussed.

Chapter 3 focuses on the review of the deflecting structures and their adaptation to the present application. First, the classification of the deflecting structures and their use cases are discussed. After that, adaptation of the pulsed magnet, stripline kicker and RF cavity as a beam separator are studied, and an RF cavity was found suitable as a beam separator for this work. Furthermore, the criteria followed to select the cavity operating frequency are discussed. Finally, the probable cavity designs determined in accordance with the selected frequency are shortlisted.

Chapter 4 describes the computation of the RF properties of the probable cavity designs. The cavity geometry is both scaled and adapted to match the current beam separator requirements, and optimized to achieve a lower surface loss. Thereafter, the cavity designs are compared in terms of the RF power, peak electric field and surface power loss density, and kick voltage homogeneity.

Chapter 5 presents the design of the fundamental power coupler, pick-up probe

1 Introduction

and frequency tuners. Additionally, the beam loading effect, the possibility of multipacting, and the impact of higher-order modes on the cavity are discussed.

In Chapter 6, the engineering design of the cavity is described. This includes a description of setting-up of the multiphysics analysis using the commercial simulation tool, and the estimation of the cavity resonance frequency due to the atmospheric pressure, RF power, and coolant temperature. Additionally, the required dimensional tolerances of the cavity using the frequency sensitivity analysis are discussed.

Chapter 7 is devoted to the fabrication of a copper cavity, which includes different methods of fabrication, a frequency pre-tuning procedure and the actual cavity fabrication process. This chapter also discusses the reason behind the filler material spillage and its effect on the cavity performance.

Chapter 8 is dedicated to the RF testing of the cavity. The chapter also includes an investigation carried out to determine the reason behind the low intrinsic quality factor of the cavity, followed by a brief introduction of the bead-pull measurement technique, the measurement setup and also the results. This chapter also describes the high power cavity test setup and steps taken to mitigate the higher temperature at the pick-up port. Based on the present development effort, a few recommendations are listed at the end of this chapter that will be beneficial for fabricating similar type of cavities in the future.

The concluding chapter, Chapter 9, provides a summary and outlook on the current work.

2 Theoretical Background

The essential theoretical background forming the basis of this work is reviewed in this chapter. The first section introduces the Maxwell's equations and the formulation of the Helmholtz equation. Next section deals with the transverse deflection of a particle due to the static electric, magnetic, and electromagnetic fields. Subsequent sections provide an insight into the workings of an RF cavity, which is a vital part of this work. The modes in a cylindrical resonator and a coaxial resonator are presented before discussing the suitability of these modes for the deflection of a particle are examined using the Panofsky-Wenzel Theorem. The important cavity parameters and the computation of cavity figures of merit are discussed in the following section. Basics of power coupling in a cavity and beam loading concepts are also addressed. At the end of this chapter, a brief introduction on the multipacting and the effects of higher-order modes excited in a cavity are discussed.

2.1 Maxwell's Equations

Maxwell's equations which were collected and completed by James Clark Maxwell [25], form the fundamental basis for the computing of the macroscopic electromagnetic fields in classical electrodynamics. They have been discussed thoroughly in [26]. The integral form of four Maxwell's equations are transferred into the differential form of Maxwell's equations

$$\nabla \times \mathbf{H}(\mathbf{r}, t) = \mathbf{J}(\mathbf{r}, t) + \frac{\partial}{\partial t} \mathbf{D}(\mathbf{r}, t), \quad (2.1)$$

$$\nabla \times \mathbf{E}(\mathbf{r}, t) = -\frac{\partial}{\partial t} \mathbf{B}(\mathbf{r}, t), \quad (2.2)$$

$$\nabla \cdot \mathbf{B}(\mathbf{r}, t) = 0, \quad (2.3)$$

$$\nabla \cdot \mathbf{D}(\mathbf{r}, t) = \rho(\mathbf{r}, t), \quad (2.4)$$

2 Theoretical Background

by using Stoke's and Gauss's theorem of vector analysis [26]. In the above equations, $\mathbf{E}(\mathbf{r}, t)$ denotes the electric field strength, $\mathbf{D}(\mathbf{r}, t)$ the electric flux density, $\mathbf{H}(\mathbf{r}, t)$ the magnetic field strength, $\mathbf{B}(\mathbf{r}, t)$ the magnetic flux density, $\rho(\mathbf{r}, t)$ the free charge density and $\mathbf{J}(\mathbf{r}, t)$ the current density. Here, \mathbf{r} and t represent the spatial and time dependency of the quantities. The curl operator $\nabla \times$ in (2.1) and (2.2) measures the circulation of the magnetic and electric field in an infinitely small test area, and the divergence operator $\nabla \cdot$ in (2.3) and (2.4) measures the outward magnetic and electric flux from an infinitely small test volume. In addition to these equations, the following constitutive relations correlate the flux densities to the field strength

$$\mathbf{D}(\mathbf{r}, t) = \varepsilon(\mathbf{r}, t) \mathbf{E}(\mathbf{r}, t) = \varepsilon_0 \varepsilon_r(\mathbf{r}, t) \mathbf{E}(\mathbf{r}, t), \quad (2.5)$$

$$\mathbf{B}(\mathbf{r}, t) = \mu(\mathbf{r}, t) \mathbf{H}(\mathbf{r}, t) = \mu_0 \mu_r(\mathbf{r}, t) \mathbf{H}(\mathbf{r}, t), \quad (2.6)$$

$$\mathbf{J}(\mathbf{r}, t) = \sigma(\mathbf{r}, t) \mathbf{E}(\mathbf{r}, t), \quad (2.7)$$

where $\varepsilon(\mathbf{r}, t)$, $\mu(\mathbf{r}, t)$, $\varepsilon_r(\mathbf{r}, t)$ and $\mu_r(\mathbf{r}, t)$ are the permittivity, permeability, relative permittivity and relative permeability of the material, respectively. The constants ε_0 and μ_0 are the permittivity and permeability of the vacuum, and $\sigma(\mathbf{r}, t)$ is the electrical conductivity of the material.

Furthermore, a particle with a charge q traveling at a velocity \mathbf{v} experiences a force due to both the electric field $\mathbf{E}(\mathbf{r}, t)$ and the magnetic field $\mathbf{B}(\mathbf{r}, t)$, and is given by the Lorentz force equation as

$$\mathbf{F}(\mathbf{r}, t) = q (\mathbf{E}(\mathbf{r}, t) + \mathbf{v} \times \mathbf{B}(\mathbf{r}, t)). \quad (2.8)$$

Only the electric field can impart force in the longitudinal direction, whereas both the electric and magnetic fields contribute to the transverse force.

Helmholtz Equation

Maxwell's equations (2.1) and (2.2) are the first-order partial differential equations which are mutually coupled by the electric and magnetic field quantities. It is convenient to solve these equations if they are combined such that only the electric field or the magnetic field quantities occur in an equation, and the same is discussed further.

2 Theoretical Background

In an homogeneous media¹ and in the absence of free charges ($\rho = 0$) and of free currents ($\mathbf{J}(\mathbf{r}, t) = 0$), the Maxwell's equations (2.1)-(2.4) reduce to

$$\nabla \times \mathbf{B}(\mathbf{r}, t) = \varepsilon \mu \frac{\partial}{\partial t} \mathbf{E}(\mathbf{r}, t), \quad (2.9)$$

$$\nabla \times \mathbf{E}(\mathbf{r}, t) = -\frac{\partial}{\partial t} \mathbf{B}(\mathbf{r}, t), \quad (2.10)$$

$$\nabla \cdot \mathbf{B}(\mathbf{r}, t) = 0, \quad (2.11)$$

$$\nabla \cdot \mathbf{E}(\mathbf{r}, t) = 0. \quad (2.12)$$

Taking the curl of equation (2.10) results in

$$\nabla \times (\nabla \times \mathbf{E}(\mathbf{r}, t)) = -\frac{\partial}{\partial t} (\nabla \times \mathbf{B}(\mathbf{r}, t)). \quad (2.13)$$

To eliminate the magnetic field component from (2.13), $\nabla \times \mathbf{B}(\mathbf{r}, t)$ is replaced with (2.9) to obtain

$$\nabla \times (\nabla \times \mathbf{E}(\mathbf{r}, t)) = -\varepsilon \mu \frac{\partial^2}{\partial t^2} \mathbf{E}(\mathbf{r}, t). \quad (2.14)$$

The harmonically oscillating field is given as

$$\mathbf{E}(\mathbf{r}, t) = \mathbf{E}(\mathbf{r})e^{-j\omega t}, \quad (2.15)$$

where ω is the oscillating frequency and j the imaginary unit. The second derivative of $\mathbf{E}(\mathbf{r}, t)$ with respect to time results in

$$\frac{\partial^2}{\partial t^2} \mathbf{E}(\mathbf{r}, t) = -\omega^2 \mathbf{E}(\mathbf{r}). \quad (2.16)$$

Substituting equation (2.16) in (2.14) gives

$$\nabla \times (\nabla \times \mathbf{E}(\mathbf{r})) - k^2 \mathbf{E}(\mathbf{r}) = 0, \quad (2.17)$$

where $k = \omega\sqrt{\mu\varepsilon}$ is known as wave number. Using the standard vector identity² in equation (2.17), yields in the Helmholtz equation

$$\nabla^2 \mathbf{E}(\mathbf{r}) - k^2 \mathbf{E}(\mathbf{r}) = 0. \quad (2.18)$$

¹The permittivity and permeability of the materials do not vary spatially or temporally. Thus, $\varepsilon(\mathbf{r}, t)$ and $\mu(\mathbf{r}, t)$ can be replaced by ε and μ , respectively.

² $\nabla \times \nabla \times \mathbf{P} = \nabla(\nabla \cdot \mathbf{P}) + \nabla^2 \mathbf{P}$ [26], where \mathbf{P} is any vector field

2 Theoretical Background

Similarly, an expression for the magnetic field $\mathbf{H}(\mathbf{r})$ can be obtained as

$$\nabla^2 \mathbf{H}(\mathbf{r}) - k^2 \mathbf{H}(\mathbf{r}) = 0. \quad (2.19)$$

The main focus of this work is to obtain the field values inside an evacuated region enclosed by a conducting surface. Therefore, in vacuum, $\mu_r \approx 1$, $\varepsilon_r \approx 1$, whereas the outer conducting surface is considered as an ideal conductor (perfect electric conducting (PEC)) with $\sigma \rightarrow \infty$. Thus the field values of the resonating modes in a resonator should also satisfy the boundary condition

$$\mathbf{n} \times \mathbf{E}(\mathbf{r}, t) = 0 \text{ and } \mathbf{n} \cdot \mathbf{H}(\mathbf{r}, t) = 0 \text{ on } \partial\Omega_{PEC}, \quad (2.20)$$

where \mathbf{n} is the unit vector normal to the boundary $\partial\Omega_{PEC}$. Similar to PEC boundary condition, a perfect magnetic conducting (PMC) is defined, for which the field values should satisfy the condition

$$\mathbf{n} \times \mathbf{H}(\mathbf{r}, t) = 0 \text{ and } \mathbf{n} \cdot \mathbf{E}(\mathbf{r}, t) = 0 \text{ on } \partial\Omega_{PMC}. \quad (2.21)$$

In this thesis, the resonator's metallic surface is considered PEC to compute the field values. Subsequently, in the post-processing, the obtained surface magnetic field values and the conductivity of the metallic surface are used to calculate the surface power loss.

2.2 Deflection due to the Static Electric and Magnetic Fields

The expression for the Lorentz force (2.8) shows that both the electric and magnetic fields contribute to the transverse force. If the transverse momentum gain p_{\perp} of a particle is smaller than its longitudinal momentum p_{\parallel} , the angle θ at which particle gets deflected is expressed as

$$\theta = \tan^{-1} \left(\frac{p_{\perp}}{p_{\parallel}} \right) \approx \frac{p_{\perp}}{p_{\parallel}} = \frac{eV_{\perp}}{E_b}, \quad (2.22)$$

where V_{\perp} is the integrated transverse voltage experienced by the particle and E_b is the total energy of the particle. For the pulse driven beam separator devices,

2 Theoretical Background

it can be assumed that the field contributing to the transverse deflection is static for the pulse duration. To comprehend these devices, one must first understand the transverse kick due to the static electric and magnetic fields, as well as their combination, which is explained further below.

2.2.1 Static Electric Field

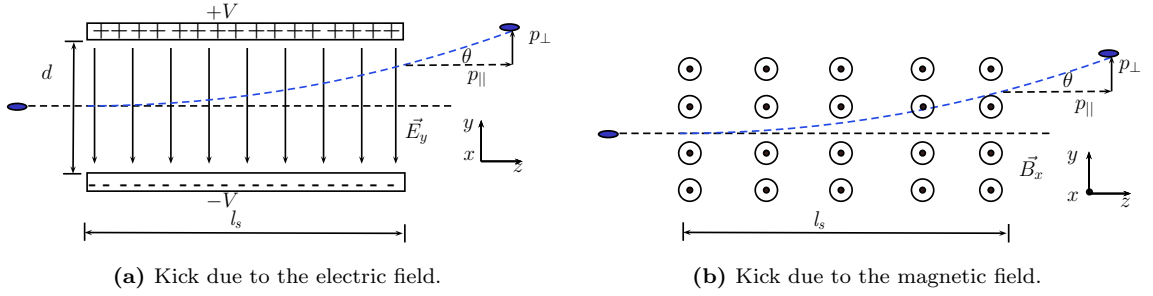


Figure 2.1: A sketch of the transverse deflection of a charged particle ($-q$) in the y plane due to the static electric field E_y (a) and the magnetic field B_x (b).

In an electrostatic kicker, a constant voltage V with opposite polarities is applied on the parallel electrode plates of length l_s which are separated by a distance d , resulting in a static electric field E_y between the electrodes (Figure 2.1 (a)). A charged particle with charge $-q$, energy E_b , and mass m_e passing through this constant electric field experiences a transverse force F_y along the y -axis, which increases the particle's transverse momentum by

$$p_{\perp} = q \frac{2V}{d} \frac{l_s}{\beta c} = q E_y \frac{l_s}{\beta c}, \quad (2.23)$$

where β is the ratio of the particle's velocity v^3 to the speed of light c . If we consider that the longitudinal momentum of the charged particle remains constant throughout the structure, then

$$p_{\parallel} = \gamma m_e \beta c, \quad (2.24)$$

where γ is the Lorentz factor ⁴ and m_e is the rest mass of an electron expressed. In

³ v is the absolute value of the particle's velocity.

⁴The Lorentz factor γ is given as $1/\sqrt{1-\beta^2}$, where β is the ratio of the particle's velocity to the speed of light in vacuum.

2 Theoretical Background

this case, the particle gets deflected by an angle

$$\theta_E = \frac{p_{\perp}}{p_{\parallel}} = q \frac{l_s E_y}{E_b} \frac{1}{\beta^2}. \quad (2.25)$$

2.2.2 Static Magnetic Field

A dipole magnet is the best example to explain the transverse kick due to a static magnetic field. A charged particle moving along the z -axis through a constant magnetic field B_x for a distance l_s experiences a transverse force along the y -axis (Figure 2.1 (b)). The transverse momentum p_{\perp} of the particle at the structure exit is

$$p_{\perp} = q\beta c B_x \cdot \frac{l_s}{\beta c} = q B_x l_s. \quad (2.26)$$

Therefore, the particle gets deflected by an angle

$$\theta_B = \frac{p_{\perp}}{p_{\parallel}} = \frac{q B_x l_s}{\gamma m_e \beta c} = q \frac{l_s c B_x}{E_b} \frac{1}{\beta}. \quad (2.27)$$

Considering that the length of the static electric and magnetic field structures are equal, then the ratio of the kick angle due to the electric field (2.25) to that of the magnetic field (2.27) results in

$$\frac{\theta_E}{\theta_B} = \frac{E_y}{B_x c} \cdot \frac{1}{\beta}. \quad (2.28)$$

The above expression suggests that electric field is preferable for deflecting a low energy beam ($\beta \ll 1$) and magnetic field for high energy ($\beta \approx 1$).

2.2.3 Static Electric and Magnetic Fields

A stripline kicker utilizes both the electric and the magnetic fields for the transverse deflection. The geometry of a stripline kicker is identical to that of the electrostatic kicker discussed previously. The stripline kicker consists of two parallel strips of length l_s which are separated by a distance d , as shown in Figure 2.2. Alternate polarity pulses are applied at the rear end of the strip, whereas the opposite end is terminated with a matching load to avoid pulse reflections. For an efficient kicking,

2 Theoretical Background

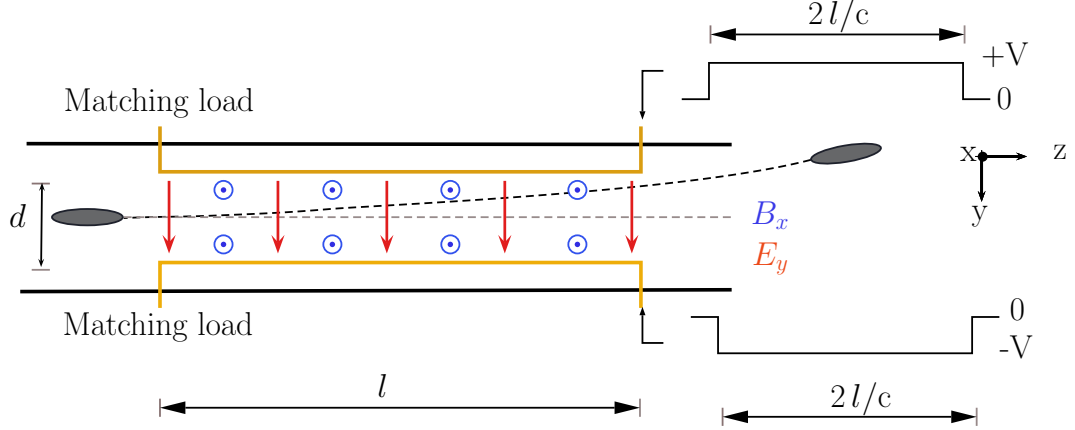


Figure 2.2: A schematic view of a stripline kicker of length l_s with the electrodes separated by a distance d , and the corresponding pulse structure applied on the strips.

the pulse width should be at least twice the time taken by a particle to travel the structure [27, 28].

Consider that a bunch arrives at $t = 0$ and exits the structure at $t = l_s/c$. The pulses have to be applied at time $t = -l_s/c$, so that they travel towards the structure entrance and meet the bunch at $t = 0$. Opposite polarity pulses create a transverse electric field E_y along the y -axis, whereas an anti-parallel current flow in the strips results in a magnetic field B_x along the x -axis. The field components remain steady during the transit of a bunch, and the force due to both the field components acts along the same direction (y -axis). In a travelling wave, the magnitude of field components are related by $|\mathbf{B}| = |\mathbf{E}|/c$, which demonstrates that both the field components exert an equal force on a bunch. Therefore, the expression for the net transverse force $F_y(0, 0, z)$ and transverse voltage V_\perp are derived as

$$F_y(0, 0, z) = qE_y(0, 0, z) + qcB_x(0, 0, z) = 2q\frac{2V_p}{d}, \quad (2.29)$$

$$V_\perp(0, 0) = \frac{1}{q} \int_{z=0}^{z=l_s} F_y(0, 0, z) dz = \frac{F_y(0, 0, z)}{q} \int_{z=0}^{z=l_s} dz = 2\frac{2V_p}{d}l_s, \quad (2.30)$$

where V_p is the magnitude of the pulse voltage. As a result, the bunch moving along the stripline kicker gets deflected by

$$\theta_{EB} = g_\perp \frac{eV_\perp}{E_b} = 2g_\perp \frac{2V_p l_s}{E_b d}, \quad (2.31)$$

where θ_{EB} is the deflection due to the presence of both the electric and the magnetic field, and g_{\perp} is the transverse geometry factor which depends on the field concentration along the particle's path due to the size and shape of the electrodes [28].

2.3 Electromagnetic Field in a Closed Structure

The field components of a mode present in a closed metallic structure (cavity) are used to accelerate or deflect a charged particle. A cylindrical cavity is one of these simple structures in which a standing wave eigenmode can sustain. The eigenvalue problem associated with this simple geometry can be solved analytically to obtain the resonance frequency and field distribution corresponding to an eigenmode.

2.3.1 Cylindrical Resonators

A cylindrical resonator with a radius r_c and length l_c is considered, with the particles travelling along the cylindrical axis⁵. An eigenmode in the cavity is referred to as *Transverse Magnetic* (TM) mode if the magnetic field along the z -axis is zero, i.e. $H_z(\mathbf{r}, t) = 0$, whereas, in the *Transverse Electric* (TE) mode the electric field along the z -axis is zero, i.e. $E_z(\mathbf{r}, t) = 0$. Furthermore, subscripts are used to define the spatial variation of the field profile in the cavity as TM_{mnp} or TE_{mnp} , where m , n and p are integers that characterize the field variation in the z , r , and θ directions of a cylindrical coordinate system. The modes with $m = 0$ are referred to as monopoles, $m = 1$ are called dipoles, $m = 2$ are defined as quadrupoles, etc. The general expression for the field components of the TM and TE mode of a pill-box cavity [29] are given in Table 2.1. In this table, E and H are the electric and magnetic field components and the subscript represents the field components in the z , r , and θ directions, ω is the resonance frequency of the eigenmode, and $j_{m,n}$ and $j'_{m,n}$ are the n^{th} root of the m^{th} order Bessel function ($J_m(x)$) and its first derivative ($J'_m(x)$), respectively.

⁵In accelerator physics, the z -axis is considered as the longitudinal direction in which the particle travels, and it is also known as cavity axis or beam axis.

2 Theoretical Background

Table 2.1: The electric and magnetic field components of the TM and TE mode in a pill-box cavity [29] of radius r_c and length l_c . Here, m , n and p are the integers which characterize the field variations in the z , r , and θ directions of a cylindrical coordinate system, ω is the resonance frequency of a mode, k_{mn} is the angular wave number of the mode, and $j_{m,n}$ and $j'_{m,n}$ are the n^{th} root of the m^{th} order Bessel function ($J_m(x)$) and its first derivative ($J'_m(x)$), respectively.

Field	TM mode	TE mode
E_z	$E_0 J_m(k_{mn}r) \cos\left(\frac{p\pi z}{l_c}\right) \cos(m\theta) \exp(j\omega t)$	0
E_r	$-E_0 \frac{p\pi}{l_c} \frac{r_c}{j_{m,n}} J'_m(k_{mn}r) \sin\left(\frac{p\pi z}{l_c}\right) \cos(m\theta) \exp(j\omega t)$	$j\omega B_0 \frac{mr_c^2}{j_{m,n}^2 r} J_m(k_{mn}r) \sin\left(\frac{p\pi z}{l_c}\right) \sin(m\theta) \exp(j\omega t)$
E_θ	$-E_0 \frac{p\pi}{l_c} \frac{mr_c^2}{j_{m,n}^2 r} J_m(k_{mn}r) \sin\left(\frac{p\pi z}{l_c}\right) \sin(m\theta) \exp(j\omega t)$	$j\omega B_0 \frac{r_c}{j'_{m,n}} J'_m(k_{mn}r) \sin\left(\frac{p\pi z}{l_c}\right) \cos(m\theta) \exp(j\omega t)$
B_z	0	$B_0 J_m(k_{mn}r) \sin\left(\frac{p\pi z}{l_c}\right) \cos(m\theta) \exp(j\omega t)$
B_r	$-j\omega E_0 \frac{mr_c^2}{j_{m,n}^2 r c^2} J_m(k_{mn}r) \cos\left(\frac{p\pi z}{l_c}\right) \sin(m\theta) \exp(j\omega t)$	$B_0 \frac{p\pi}{l_c} \frac{r_c}{j'_{m,n}} J_m(k_{mn}r) \cos\left(\frac{p\pi z}{l_c}\right) \cos(m\theta) \exp(j\omega t)$
B_θ	$-j\omega E_0 \frac{r_c}{j_{m,n} c^2} J'_m(k_{mn}r) \cos\left(\frac{p\pi z}{l_c}\right) \cos(m\theta) \exp(j\omega t)$	$-B_0 \frac{p\pi}{l_c} \frac{mr_c^2}{j_{m,n}^2 r c} J_m(k_{mn}r) \cos\left(\frac{p\pi z}{l_c}\right) \sin(m\theta) \exp(j\omega t)$
ω_{mnp}	$c \sqrt{\frac{j_{m,n}^2}{r_c^2} + \left(\frac{p\pi}{l_c}\right)^2}$	$c \sqrt{\frac{j_{m,n}^2}{r_c^2} + \left(\frac{p\pi}{l_c}\right)^2}$

2.3.2 Coaxial Resonators

In the coaxial resonators, TEM (Transverse Electric and Magnetic) modes exist where both the longitudinal electric and magnetic fields are absent, i.e $H_z(\mathbf{r}, t) = 0$ and $E_z(\mathbf{r}, t) = 0$. TEM modes are absent in cylindrical resonators because at least two conductors are required to sustain a TEM mode in a structure [30]. The field components of a TEM mode in an axis-symmetric coaxial transmission line are shown in Figure 2.3.

A coaxial resonator can be obtained by terminating the ends of a coaxial transmission line. There are two types of termination, short and open. In a half-wave resonator ($\lambda/2$ resonator), both the ends of the transmission line are shorted, whereas in a quarter-wave resonator ($\lambda/4$ resonator), one end of the line is open and the other end is terminated with a short circuit (Figure 2.4).

The analysis of the coaxial resonators starts with the calculation of the input

2 Theoretical Background

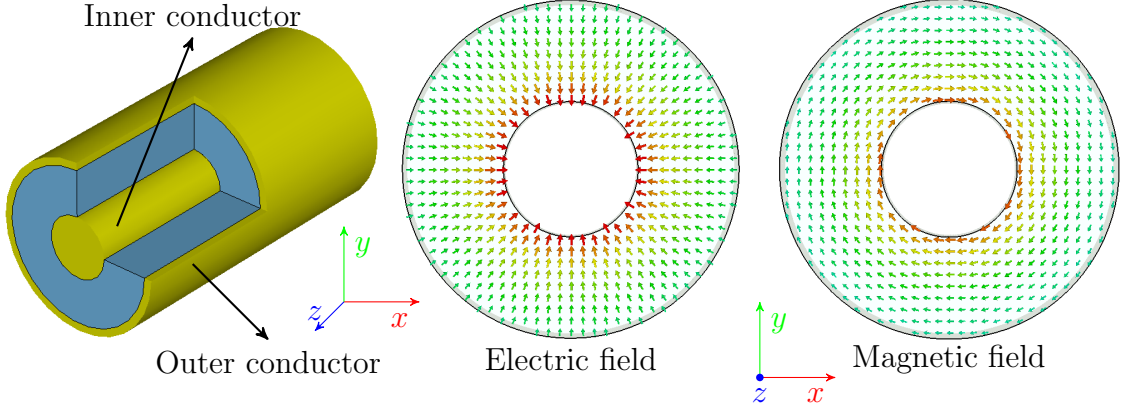


Figure 2.3: Sketch of a coaxial transmission line and the distribution of the electric and magnetic field of a TEM mode in the xy -plane (red \rightarrow 1 and blue \rightarrow 0).

impedance of a transmission line, Z_{in} , which is expressed as

$$Z_{in} = \frac{Z_L + jZ_0 \tan(\omega l_r/c)}{Z_0 + jZ_L \tan(\omega l_r/c)}, \quad (2.32)$$

where ω is the operating frequency, l_r is the length of the center rod, Z_0 , Z_{in} , and Z_L are the characteristic, input, and load impedance of a transmission line, respectively. Here, only a quarter-wave resonator is analyzed as this is important to this work. In a quarter-wave resonator, a load capacitance of C_{end} is formed between the surface of the open inner conductor with the outer conductor. This load impedance is given as

$$Z_L = \frac{-j}{\omega C_{end}}. \quad (2.33)$$

At resonance, the input impedance of the system reduces to zero. Then the equation (2.32) reduces to

$$Z_L = -jZ_0 \tan(\omega l_r/c). \quad (2.34)$$

Therefore, to satisfy the resonance criterion, the following condition should be satisfied:

$$\tan\left(\frac{\omega l_r}{c}\right) = \frac{1}{Z_0 C_{end} \omega}. \quad (2.35)$$

If the end capacitance is very large, the right hand side of (2.35) approaches to zero.

2 Theoretical Background

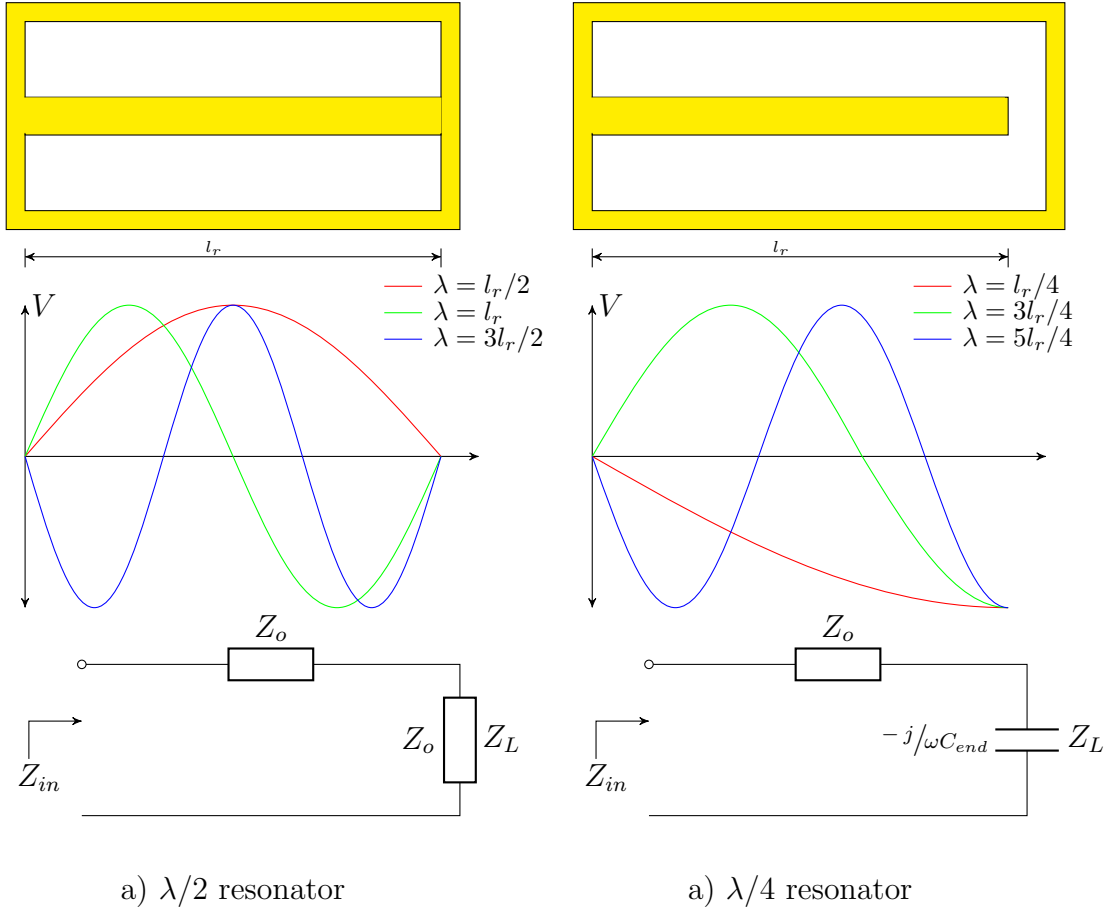


Figure 2.4: A cross-sectional sketch of the $\lambda/2$ and $\lambda/4$ coaxial resonator (top row). The graph shows the voltage on the inner conductor surface for the first three modes supported by the resonator (middle row). The bottom line shows the equivalent transmission line diagrams for the $\lambda/2$ and $\lambda/4$ coaxial resonator.

In this case, the possible frequencies supported by a resonator are given as

$$l_r = \frac{(2n + 1)\lambda_n}{4}, \quad (2.36)$$

where n can take any value $(0, 1, 2, 3, \dots)$. Similar to cylindrical resonators, the coaxial resonators can support an infinite number of eigenmodes. Mostly, the central rod length, l_r , decides the resonance frequency of a mode. The lowest mode in the coaxial resonator exists at $n = 0$, and the quarter-wavelength of this mode corresponds to the rod length. The resonance frequency of the other modes is higher than the fundamental mode, and these modes are spaced at the odd-integral multiple

2 Theoretical Background

of the quarter-wavelength of the fundamental mode. There are some fringe fields at the open end of the central conductor, which loads the cavity. Therefore, the frequency of the quarter-wave resonator is slightly lower than the one calculated using equation (2.36) for a given rod length [31]. In an ideal quarter-wave resonator, the frequency of the first higher-order mode ($n = 1$) is separated from the fundamental mode ($n = 0$) by three times the fundamental mode frequency. In reality, the end capacitance decreases the frequency gap between the modes. Compared to the cylindrical cavities, the coaxial resonators are compact at even low frequencies and they are used for the transverse kicking of the bunches [32, 33].

2.4 Identification of Transverse Deflecting Modes

As mentioned earlier, both the electric and the magnetic field impart transverse momentum to particles, whereas only the electric field can transfer energy to particles in the longitudinal direction. The absence of the longitudinal electric field in pure TE and TEM modes rules out their use in the acceleration of the particles, whereas the longitudinal acceleration could be achieved only by the TM mode, which has a non-zero longitudinal electric field along the cavity axis. Usually, the first TM monopole mode, TM_{010} , is used for acceleration. Naturally, one might expect that a TEM mode or the dipole modes (TM_{110} or TE_{111}) can kick the particles in the transverse direction. However, this is not the case, and whether a mode may be employed for the transverse deflecting of a particle can be determined using the Panofsky-Wenzel theorem [34].

In 1956, a note was published by Panofsky and Wenzel [34], which gave the relation between the transverse momentum gain p_{\perp} and the longitudinal electric field along the cavity \mathbf{E}_z as

$$p_{\perp} = -\frac{q}{\omega} \int_0^{l_c} (-j) \nabla_{\perp} \mathbf{E}_z dz, \quad (2.37)$$

where ∇_{\perp} denotes the transverse component of the gradient and l_c is the cavity length. The above relation states that if a resonant mode imparts a transverse kick to a bunch, the mode has a transversely varying longitudinal voltage which imparts an energy gradient across the transverse plane of the bunch. In other words, if the

2 Theoretical Background

longitudinal electric field component is absent in a mode, then this mode is not suitable for the transverse deflection. Thus, pure TE_{111} and TEM modes are not suitable for the transverse kicking of particles. In these modes, the magnitude of the transverse force due to the electric and magnetic field is identical but of an opposite sign. Therefore, the transverse forces cancel each other out, and the net transverse momentum gain by particles is zero. However, this may not be the case with the actual cavity, where small transverse fields are present due to the beam pipe, which gives a net transverse kick. Overall, a pure TE dipole or TEM mode can not be employed for the transverse deflection of particles. In contrast to these modes, only the magnetic field exerts transverse force in the TM_{110} mode and can deflect the beam in the transverse deflection. Additionally, the mode possesses a transversely varying longitudinal voltage, which imposes an energy gradient across the bunch's transverse plane. Thus, pure TM_{110} mode is a transverse deflecting mode. Note that this discussion applies only to the pure TM, TE and TEM modes.

2.5 Cavity Parameters

A number of cavity parameters are required to define the performance of RF cavities. Most importantly, these parameters assist in the comparison of the cavity designs that are operated at different frequencies and are introduced in this section. The content and notations used in this section closely follow that of Refs.[29, 33, 35].

2.5.1 Integrated Longitudinal and Transverse Voltage

The longitudinal energy gain/loss (ΔW) by a charged particle in a cavity is given as

$$\Delta W = \int_0^{l_c} F_z(0, 0, z) dz = \int_0^{l_c} q E_z(0, 0, z) e^{-jkz} dz, \quad (2.38)$$

where $F_z(0, 0, z)$ is the force experienced by a charged particle due to the longitudinal electric field $E_z(0, 0, z)$ present along the cavity axis. It is convenient to refer the energy change as a voltage (work done per unit charge). In a cavity, the electric field is oscillating harmonically, and the integrated longitudinal voltage (usually referred

2 Theoretical Background

to as longitudinal voltage) is given as

$$V_{\parallel}(0, 0) = \left| \int_0^{l_c} E_z(0, 0, z) e^{-jkz} dz \right|. \quad (2.39)$$

Similarly, the integrated transverse voltage can be defined along the x and y -axis as

$$\begin{aligned} V_{\perp,x}(0, 0) &= \left| \int_0^t (E_x(0, 0, z) + v \times B_y(0, 0, z)) e^{-jkz} dz \right| \\ &= \left| \int_0^t (E_x(0, 0, z) - \beta c B_y(0, 0, z)) e^{-jkz} dz \right|, \end{aligned} \quad (2.40)$$

$$\begin{aligned} V_{\perp,y}(0, 0) &= \left| \int_0^t (E_y(0, 0, z) + v \times B_x(0, 0, z)) e^{-jkz} dz \right| \\ &= \left| \int_0^t (E_y(0, 0, z) + \beta c B_x(0, 0, z)) e^{-jkz} dz \right|, \end{aligned} \quad (2.41)$$

where $E_x(0, 0, z)$, $E_y(0, 0, z)$, $B_x(0, 0, z)$, and $B_y(0, 0, z)$ are the electric and magnetic field components along the cavity axis, and $V_{\perp}(0, 0)$ is the integrated transverse voltage⁶. In the present work, unless explicitly mentioned, the estimated V_{\parallel} and V_{\perp} refer to the default field values obtained from CST MWS [36], where the field values are normalized such that the total energy in the problem domain is equal to 1 J. The equations (2.40) and (2.41) refer to the direct method of evaluating the transverse voltage V_{\perp} . Additionally, the Panofsky-Wenzel theorem can be used to calculate V_{\perp} solely based on the V_{\parallel} , and this is expressed as

$$V_{\perp} = c \frac{(V_{\parallel}(0, 0) - V_{\parallel}(0, d))}{\omega d}, \quad (2.42)$$

where $V_{\parallel}(0, 0)$ and $V_{\parallel}(0, d)$ are the longitudinal voltage along the cavity axis and at an offset of d in the deflecting direction, respectively. In case of a deflecting cavity, the longitudinal electric field along the cavity axis is absent, i.e $V_{\parallel}(0, 0)$ is zero. Therefore, equation (2.42) reduces to

$$V_{\perp} = -\frac{cV_{\parallel}(0, d)}{\omega d}. \quad (2.43)$$

⁶Usually, the notations V_{\perp} and V_{\parallel} are preferred instead of $V_{\perp}(0, 0)$ and $V_{\parallel}(0, 0)$.

2.5.2 Quality Factor

The unloaded quality factor of a cavity (Q_o) is the ratio of the stored energy to the RF power loss in one RF cycle and is expressed as

$$Q_0 = \frac{\omega U}{P_c}, \quad (2.44)$$

where P_c is the surface power loss and U is the total energy stored in the electromagnetic field of the eigenmode:

$$U = \frac{1}{2}\mu \iiint_{\Omega} \mathbf{H} \cdot \mathbf{H}^* dV = \frac{1}{2}\varepsilon \iiint_{\Omega} \mathbf{E} \cdot \mathbf{E}^* dV, \quad (2.45)$$

where V is the cavity volume.

2.5.3 Cavity Shunt Impedance

The shunt impedance of a cavity indicates how strongly the field couples to a charged particle moving along the cavity axis. The longitudinal and transverse shunt impedance⁷ of a cavity are given as

$$R_{\parallel} = \frac{V_{\parallel}^2}{P_c} \quad \text{and} \quad R_{\perp} = \frac{V_{\perp}^2}{P_c}. \quad (2.46)$$

An increase in the shunt impedance reduces the RF power required to achieve a given longitudinal or transverse voltage. Another important parameter of a cavity is the ratio of the transverse shunt impedance to the quality factor (R_{\perp}/Q)⁸, which is defined as

$$\frac{R_{\perp}}{Q} = \frac{V_{\perp}^2}{P_c} \cdot \frac{1}{\omega U/P_c} = \frac{V_{\perp}^2}{\omega U}. \quad (2.47)$$

An increase in R_{\perp}/Q of a mode increases the transverse momentum gained by a particle per unit of energy stored in that mode.

⁷The linac definition of the shunt impedance is used in this thesis. In the electrical circuits, the shunt impedance reduces by a factor of 2.

⁸As the thesis deals with a transverse deflecting cavity, only the transverse shunt impedance (R_{\perp}) and R_{\perp}/Q are discussed.

2.5.4 Geometrical Factor G and $R_{\perp}R_s$

A parameter that depends solely on the cavity geometry is known as the cavity geometry factor or geometrical factor (G), and is expressed as

$$G = R_s Q_0, \quad (2.48)$$

where R_s is the surface resistance of the cavity material. The geometrical factor is independent of the cavity material and the resonance frequency, and therefore, it aids in the comparison of the different cavity designs.

Another parameter which combines both the R_{\perp}/Q ratio and G is the product of the shunt impedance and surface resistance ($R_{\perp}R_s$) and is expressed as

$$R_{\perp}R_s = \frac{V_{\perp}^2}{P_c} \frac{G}{Q_0} = \frac{V_{\perp}^2}{\omega U} \frac{\omega U}{P_c} \frac{G}{Q_0} = \frac{R_{\perp}}{Q} G. \quad (2.49)$$

2.5.5 Surface Power Loss in a Cavity

The field strength in a cavity decays with time due to the deposition of RF power on the cavity surface. If we assume that the surface resistance is uniform all over the cavity, the total power loss is given as

$$P_c = -\frac{dU}{dt} = \frac{R_s}{2} \oint_S |\mathbf{H}_t|^2 dS, \quad (2.50)$$

where \mathbf{H}_t is the magnetic field tangential to the cavity surface and S is the total cavity surface. The surface resistance of a cavity at room temperature is defined as

$$R_s = \frac{1}{\sigma \delta}, \quad (2.51)$$

where σ is the electrical conductivity of the cavity surface and δ is the skin depth which is given as

$$\delta = \sqrt{\frac{2}{\sigma \mu \omega}}. \quad (2.52)$$

The RF power loss in a cavity is also defined in terms of $R_{\perp}R_s$ as

$$P_c = \frac{V_{\perp}^2}{R_{\perp}} = \frac{V_{\perp}^2 R_s}{R_{\perp} R_s} = \frac{V_{\perp}^2 R_s}{R_{\perp}/Q \cdot G}. \quad (2.53)$$

The main focus of a normal conducting cavity design is to maximize the R_{\perp} of a cavity so that the surface power losses is minimal.

2.5.6 Peak Surface Power Loss Density

The non-uniform distribution of the surface magnetic field of a mode results in the in-homogeneous power loss distribution on the cavity surface. A higher RF power is deposited in the region where the magnetic field gets concentrated, and this section of the cavity requires active cooling to remove the heat. Insufficient cooling leads to cavity deformation and shift in the mode resonance frequency. Moreover, at higher temperatures, the cavity vacuum breaks down due to degassing. Apart from the high power loss region, active cooling is required wherever a considerable RF power is deposited in a smaller area and these are the potential thermal hot spot regions. The peak surface power loss density S_{pk} in a cavity dictates the coolant flow rate and a lower values of S_{pk} relaxes the cooling requirement, which is one of the main requirements of the normal conducting cavity design.

2.5.7 Peak Surface Electric Field

A high electric field on a cavity surface may result in an RF breakdown. In [37], Kilpatrick conducted a series of experiments at different RF frequencies and field strengths and derived an empirical formula:

$$f_0[\text{MHz}] = 1.64 \cdot E_{pk}^2 \cdot e^{-(8.5/E_{pk})}. \quad (2.54)$$

Here, E_{pk} is the peak surface electric field below which the cavity can be operated reliably without breakdown, and f_0 is the cavity operating frequency. The Kilpatrick limit was based on old experimental results, and the limiting electric field from this expression can be considered a more conservative value. Advancements in vacuum systems and surface treatment techniques ensure that the peak electric field to be two times the Kilpatrick limit [29]. One of the constraints of the normal conducting cavity design is to maintain the peak surface electric field in the cavity below the Kilpatrick limit at maximum RF power.

2.5.8 Kick Voltage Homogeneity

Generally, we assume that the beam travels along the cavity axis and the transverse voltage is computed using the field values along this path. However, the beam may

2 Theoretical Background

travel off-axis due to the imperfections in the beam lattice or due to a finite transverse size of a bunch some of the particles in the bunch can travel off-axis. Therefore, a relatively homogeneous field is desired around the cavity axis to ensure that all the particles in the bunch receive a uniform kick. The relative kick voltage errors at an offset to the cavity axis in the x and y -axis are expressed as

$$\delta V_{\perp}(d, 0) = \frac{V_{\perp}(0, 0) - V_{\perp}(d, 0)}{V_{\perp}(0, 0)} \quad \text{and} \quad \delta V_{\perp}(0, d) = \frac{V_{\perp}(0, 0) - V_{\perp}(0, d)}{V_{\perp}(0, 0)}, \quad (2.55)$$

where $V_{\perp}(0, 0)$ is the kick voltage along the cavity axis, $V_{\perp}(d, 0)$ and $V_{\perp}(0, d)$ are the transverse voltages measured at an offset distance d in the direction of the x and y -axis, respectively. A low kick voltage error around the cavity axis indicates a good kick voltage homogeneity.

2.6 Power Coupling and Beam Loading

The microwave energy from a power amplifier is coupled into a cavity through a fundamental power coupler, and a loosely coupled pick-up probe samples the cavity field for measurement. The introduction of the couplers changes the cavity behavior at resonance. Further, the beam acts as an additional power source for the cavity, altering the RF power required to achieve the desired field strength in the cavity.

2.6.1 Power Coupling

The quality factor of a cavity defined with regard to the power loss on its surface is referred to as intrinsic quality factor, Q_0 . In addition to the surface losses, the field inside a cavity is coupled out through the fundamental power coupler and pick-up probe. A new term, loaded quality factor, Q_L , is introduced to account for this additional power loss. The loaded quality factor is expressed as

$$\frac{1}{Q_L} = \frac{1}{Q_0} + \frac{1}{Q_{in}} + \frac{1}{Q_{pu}}, \quad (2.56)$$

where Q_{in} and Q_{pu} are the external quality factors due to the input (fundamental power coupler) and output coupler (pick-up probe), respectively. In addition to the external equality factor, the couplers are also defined by the coupling factor, which

2 Theoretical Background

defines how strongly the cavity field gets coupled to the couplers. Thus, the coupling factors are defined as

$$\beta_{in} = \frac{Q_0}{Q_{in}} = \frac{P_{in}}{P_c} \text{ and } \beta_{pu} = \frac{Q_0}{Q_{pu}} = \frac{P_{pu}}{P_c}, \quad (2.57)$$

where β_{in} and β_{pu} are the coupling factors of the input and output couplers, P_c is the total power dissipated on the cavity surface, and P_{in} and P_{pu} are the RF power coupled into and out of the cavity, respectively. Consequently, the loaded quality factor is expressed in terms of the coupling factors as

$$Q_0 = Q_L (1 + \beta_{in} + \beta_{pu}). \quad (2.58)$$

The input coupling factor is also represented in terms of the transmitted and reflected power into and by the cavity. Consider P_g as the total RF power fed into the cavity through the fundamental power coupler, with P_{ref} and P_{fwd} as the power reflected and transmitted from or into the cavity. The reflection coefficient Γ is given as

$$\Gamma = \sqrt{\frac{P_{ref}}{P_g}}. \quad (2.59)$$

Consequently, the reflected and forward power are expressed as

$$P_{ref} = P_g \Gamma^2 \text{ and } P_{fwd} = P_g (1 - \Gamma^2). \quad (2.60)$$

Therefore, the input coupling factor β_{in} is described as

$$\beta_{in} = \frac{1 \pm \sqrt{\Gamma}}{1 \mp \sqrt{\Gamma}} = \frac{1 \pm \sqrt{P_{ref}/P_g}}{1 \mp \sqrt{P_{ref}/P_g}}, \quad (2.61)$$

where the upper sign is used in the overcoupled case ($\beta_{in} > 1$) and the lower sign is used in the undercoupled case ($\beta_{in} < 1$). If the reflected power is zero ($P_{ref} = 0$), then the coupler is said to be perfectly matched, and β_{in} reduces to unity. The factor β_{pu} is given as

$$\beta_{pu} = \frac{P_{pu}}{P_c}. \quad (2.62)$$

Therefore, the power P_{pu} measured at the pick-up probe is used to estimate the integrated transverse deflecting voltage in the cavity using

$$V_{\perp} = \sqrt{P_{pu} \cdot Q_{pu} \cdot \frac{R_{\perp}}{Q}}, \quad (2.63)$$

where R_{\perp}/Q refers to the transverse shunt impedance of the cavity.

2.6.2 Beam Loading

It is typically assumed that the beam absorbs energy from a cavity. However, the beam also acts as a power source by inducing a voltage back into the cavity. The beam-induced voltage might subtract or add to the generator voltage, which is known as beamloading. To understand this, the generator and beam-induced voltages are first computed separately. Later, the superposition of these voltages at different RF phases are discussed.

Usually, the pick-up probe is undercoupled and its influence on the cavity field can be neglected. Therefore, the power loss in a cavity is denoted by

$$P_c = P_g \frac{4\beta_{in}}{(1 + \beta_{in})^2}, \quad (2.64)$$

where β_{in} is the input coupling factor [29]. Using the expression for the shunt impedance (2.46) in equation (2.64), the generator deflecting voltage $V_{g,r}$ at resonance is given as

$$V_{g,r} = \frac{2\sqrt{\beta_{in}}}{1 + \beta_{in}} \sqrt{R_{\perp} P_g}. \quad (2.65)$$

If the cavity is driven at off-resonance, then the deflecting voltage reduces to

$$V_g = V_{g,r} \cos \psi e^{i\psi}, \quad (2.66)$$

where ψ is the detuning angle [35]. Due to the shift in resonance frequency by Δf_0 , the cavity gets detuned by an angle ψ and their relation is given by

$$\tan \psi = 2Q_L \frac{\Delta f_0}{f_0}. \quad (2.67)$$

The beam loads a cavity if it gains or loses energy while traversing through the cavity. In a deflecting cavity, the beam moving along the cavity axis does not encounter any longitudinal electric field, and there is no exchange of energy between the beam and the cavity. Hence, the beam loading is essentially zero for an on-axis travelling beam in the deflecting cavity. However, if the beam travels off-axis, the beam experiences a longitudinal electric field, resulting in the exchange of energy between the beam and the cavity, resulting in the beam loading of the cavity. A beam with a bunch charge q_b moving at an offset distance of Δy from the cavity axis couples to the

2 Theoretical Background

longitudinal electric field of the mode and the corresponding induced voltage $V_{\parallel, qb}$ is expressed as

$$V_{\parallel, qb} = -2k_d q_b, \quad (2.68)$$

where k_d denotes the loss factor and for a dipole mode this is expressed as $k_d = \left(\frac{\omega \Delta y}{c}\right)^2 \frac{\omega R_{\perp}}{4Q}$ [35]. The expression (2.43) obtained from the Panofsky-Wenzel theorem correlates the transverse and longitudinal voltages. Thus, the transverse voltage induced by a single bunch is rendered as

$$V_{\perp, qb} = -i \frac{\omega^2 \Delta y R_{\perp}}{2c Q} q_b. \quad (2.69)$$

If the bunches have a repetition rate of f_b , then the beam current I_b equals to $q_b f_b$. The voltage $V_{\perp, qb}$ induced by a bunch decays with a time constant of $\tau = 2Q_L/\omega$. Therefore, the voltage induced by each bunch adds up to

$$V_{\perp, I_b} = V_{\perp, q_0} + V_{\perp, q_1} e^{-1/f_b \tau} + V_{\perp, q_2} e^{-2/f_b \tau} + \dots = \sum_{n=0}^{\infty} V_{\perp, q_n} e^{-n/f_b \tau}, \quad (2.70)$$

where V_{\perp, I_b} is the total beam induced voltage and V_{\perp, q_n} represents the voltage induced by the n^{th} bunch. In the case of a highly damped cavity and a beam with a lower bunch repetition rate, $\tau f_b \ll 1$, the voltage induced by the previous bunch will decrease considerably before the arrival of the next bunch, and the bunch induced voltages do not add up. However, in a high quality factor cavity and at a higher bunch rate, $\tau f_b > 1$, the voltage induced by the previous bunches has an effect on the succeeding bunches, and the beam-induced voltage converges to

$$V_{\perp, I_b} = V_{\perp, qb} \tau f_b. \quad (2.71)$$

Substituting the voltage induced by a bunch (2.69) in (2.71), renders the deflecting voltage induced by the beam in the cavity as

$$V_{b,r} = -j \frac{\omega}{c} \frac{I_b R_{\perp}}{1 + \beta_{in}} \Delta y. \quad (2.72)$$

The factor j in the above equation implies that the voltage induced by the beam is offset to the bunch phase by 90° . Thus, the voltage induced by the beam arriving at the on-crest and zero-crossing phase influences the generator voltage differently. As

2 Theoretical Background

outlined when discussing the generator voltage, if the cavity is driven at off-resonance, the resulting induced deflecting voltage by the beam reduces to

$$V_b = V_{b,r} \cos \psi e^{i\psi}. \quad (2.73)$$

The total deflecting voltage in a cavity, V_c , is the sum of the generator and beam induced voltages, and is expressed in a phasor notation as

$$\tilde{V}_c = \tilde{V}_g + \tilde{V}_b, \quad (2.74)$$

where the voltages are represented in phasor form. The phasors rotate anti-clockwise in the complex plane at frequency ω , and the projection of this onto the real axis yields the cavity voltage which varies sinusoidally. The cavity voltage, \tilde{V}_c , is given as

$$\tilde{V}_c = V_c e^{j(\omega t + \phi)}, \quad (2.75)$$

where V_c and ϕ are the maximum cavity voltage and the RF phase, respectively. Since all the phasors rotate anti-clockwise in time at a frequency of ω , a new frame can be considered where the phasors are fixed in time. Then the cavity voltage in (2.75) can be written as

$$\tilde{V}_c = V_c e^{j\phi}. \quad (2.76)$$

Substituting the expression for the cavity voltage (2.76), the generator voltage (2.66), and the beam induced voltage (2.73) in (2.74) result in

$$V_c e^{j\phi} = V_{g,r} \cos \psi e^{j\psi} + V_{b,r} \cos \psi e^{j\psi}. \quad (2.77)$$

Splitting the above expression into real and imaginary terms, inserting values for $V_{g,r}$ and $V_{b,r}$ from the equations (2.65) and (2.69), and re-arranging the terms renders an expression for the required generator power, P_g , as

$$P_g = \frac{V_c^2 (1 + \beta_{in})^2}{R_{\perp} 4\beta_{in}} \left\{ \left(1 + \frac{R_{\perp} I_b}{V_c} \frac{\omega \Delta y}{c(1 + \beta_{in})} \cos \phi \right)^2 + \left(\tan \psi - \frac{R_{\perp} I_b}{V_c} \frac{\omega \Delta y}{c(1 + \beta_{in})} \sin \phi \right)^2 \right\}. \quad (2.78)$$

2 Theoretical Background

The required generator power given in the above expression for a deflecting cavity is analogous to that of an accelerating cavity [35], which is the sum of the two terms. The first term in the expression is the active component, which represents the energy transfer between the beam and the cavity. The second term refers to the reactive component, where the net energy gain by the beam is zero but the beam acts to alter the phase of the fields within the cavity. This reactive part will be zero, if

$$(1 + \beta_{in}) \tan \psi = \frac{R_{\perp} I_b \omega \sin \phi}{V_c c}. \quad (2.79)$$

This corresponds to driving the cavity at off-resonance to achieve a proper detuning phase ψ , and the required change in the resonance frequency $\Delta\omega$ to achieve this detuning is given by equation (2.67).

2.7 Multipacting

Multipacting in a cavity is one of the undesirable surface phenomena that have a negative impact on its operation. The electrons emitted from a cavity surface encounter the electromagnetic field and gain energy before impacting the surface. If the impact energy is small, no electrons are ejected from the surface. In the case of high energy electrons, they penetrate deep inside the material, and ejected electrons cannot escape from the surface. Therefore, there is a range of impact energies where more than one electron is emitted to sustain the multipacting. In that case, a buildup of electrons occurs if the secondary electrons' motion is synchronized with the RF field and the secondary emission yield⁹ (SEY) is more than one. This phenomenon is known as multipacting. The two requirements for multipacting are that the electrons should have trajectories which repeat and that the impact energy of electrons is within a range where the SEY is greater than unity.

Multipacting is generally classified into two types: one-point and two-point multipacting. In one-point multipacting, the ejected electrons have trajectories that result in them returning to their original point, whereas in two-point multipacting, the

⁹The secondary emission yield is the ratio of the number of secondary electrons ejected to the number of primary electrons incident on the surface. The SEY varies with the electron's impact energy and depends on the surface material.

2 Theoretical Background

electrons have resonance trajectories between two surfaces. There is a possibility of two-point multipacting in the cavity being developed in this work; therefore, only two-point multipacting is discussed in this section.

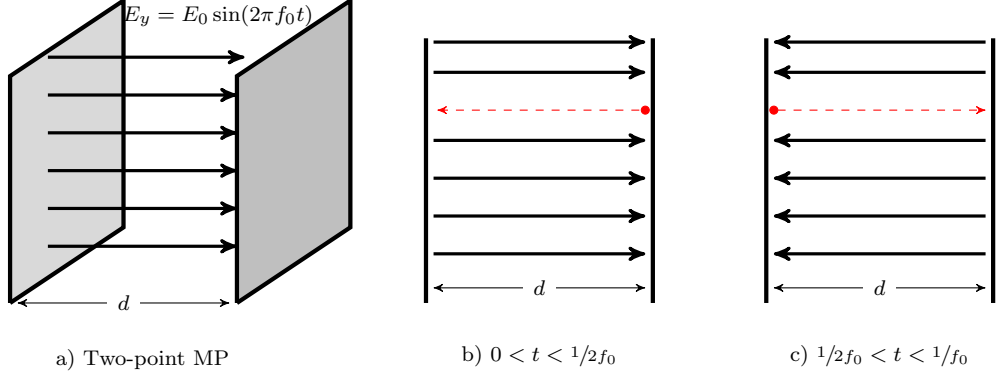


Figure 2.5: a) A sketch of two-point multipacting between parallel plates shown in 2D with an oscillating electric field (E_y) between the plates which are separated by a distance d . For the first half of the RF cycle (b), electrons travel from right to left plate, and in the second half cycle the electrons travel direction reverses (c).

Consider infinite parallel plates separated by a distance d , and assume that a uniform electric field E_y between the plates oscillates at the frequency f_0 (Figure 2.5). Then the electric field between the plates is expressed as

$$E_y = E_0 \sin(2\pi f_0 t), \quad (2.80)$$

where E_0 is the amplitude of the electric field. Due to the symmetry in the field and geometry, this 2D problem can be further simplified into a 1D problem as shown in Figure 2.5. Then, an electron emitted from the plate travels towards the opposite plate with an acceleration of

$$a(t) = \frac{eE_y}{m_e} = \frac{-eE_0}{m_e} \sin(2\pi f_0 t + \phi), \quad (2.81)$$

where ϕ is the RF phase at which the particle is emitted, and m_e and e are the mass and charge of an electron. The above expression is integrated w.r.t time to obtain the instantaneous velocity of a particle as

$$v(t) = \frac{-eE_0}{m_e \cdot (2\pi f_0)} \cdot (\cos(2\pi f_0 t + \phi) - \cos(\phi)) + v_0, \quad (2.82)$$

2 Theoretical Background

where v_0 is the initial velocity of an electron. In the current work, it is assumed that the ejected electrons are at rest ($v_0 = 0$). Integrating equation (2.82) over time gives the instantaneous position of the particle as

$$y(t) = \frac{eE_0}{m_e \cdot (2\pi f_0)^2} (\sin(2\pi f_0 t + \phi) - \sin(\phi) - (2\pi f_0)t \cos(\phi)). \quad (2.83)$$

In the case of a two-point multipacting, the electron has to travel a distance of d in half an RF period to achieve the necessary resonance condition required for multiplying to persist. This resonance time condition is given as

$$t = \frac{[2n - 1]\pi}{2\pi f_0}, \quad (2.84)$$

where n ($n = 1, 2, \dots$) is the order of multipacting. The resonance condition is satisfied when the distance between the plates is

$$d = \frac{-eE_{0,n}}{m_e \cdot (2\pi f_0)^2} (2 \cdot \sin(\phi) + [2n - 1]\pi \cos(\phi)), \quad (2.85)$$

or the electric field between the plates is

$$E_{0,n} = \frac{-d \cdot m_e \cdot (2\pi f_0)^2}{e(2 \cdot \sin(\phi) + [2n - 1]\pi \cos(\phi))}, \quad (2.86)$$

where $E_{0,n}$ is the electric field that supports the n^{th} order of multipacting.

Interestingly, there is a maximum electric field above which 2-point multipacting can not occur. Consider an electron is ejected at $\phi = 90^\circ$, and this electron accelerates towards the opposite plate for a quarter of the RF period and decelerates in the next quarter period. Therefore, the velocity of this electron is zero when it reaches the opposite plate and bombardment of this electron does not eject any secondary electrons out of the surface. The maximum electric field above which 2-point multipacting does not occur is when $\phi = 90^\circ$ and $n = 1$. By substituting these values in (2.86), the maximum electric field is obtained as

$$E_0|_{max} = \frac{m_e d (2\pi f_0)^2}{2e}. \quad (2.87)$$

However, there is no unique lower bound for the electric field below which multipacting cannot sustain. If the resonance condition given in equation (2.84) is satisfied for the n^{th} order, then the particle's velocity (v_n) and kinetic energy (K_n) at the time of collision with the opposite plate are expressed as

$$v_n = \frac{eE_0}{m_e \pi f_0} \cdot \cos(\phi_0) \quad \text{and} \quad K_n = \frac{1}{2} m_e v_n^2 = \frac{e}{2m_e} \left(\frac{E_0}{\pi f_0} \right)^2 \cdot \cos^2(\phi_0) [eV]. \quad (2.88)$$

2.8 Higher Order Mode

A beam passing through a cavity, may excite resonant modes which exist in the cavity. These modes may produce transverse and longitudinal instabilities in the beam and increase the power deposited on the cavity surface. These modes (HOM - higher order mode) are classified in accordance with their impact on the beam: accelerating, vertical deflecting, and horizontal deflecting. Accelerating modes are excited by the beam passing along the cavity axis, and the off-axis beam excites the deflecting modes. The shunt impedance of a mode defines how strongly the beam is coupled to the mode, and the shunt impedance of these modes is expressed as [33]

$$\begin{aligned} \left(\frac{R}{Q}\right)_{z,n} &= \frac{V_{z,n}^2}{\omega_n U} = \frac{\left| \int_0^{l_c} E_{z,n}(0,0,z) e^{-ik_n z} dz \right|^2}{\omega_n U}, \\ \left(\frac{R}{Q}\right)_{y,n} &= \frac{V_{y,n}^2}{\omega_n U} = \frac{\left| \int_0^{l_c} (E_{y,n}(0,0,z) - icB_{x,n}(0,0,z)) e^{-ik_n z} dz \right|^2}{\omega_n U}, \text{ and} \\ \left(\frac{R}{Q}\right)_{x,n} &= \frac{V_{x,n}^2}{\omega_n U} = \frac{\left| \int_0^{l_c} (E_{x,n}(0,0,z) + icB_{y,n}(0,0,z)) e^{-ik_n z} dz \right|^2}{\omega_n U}, \end{aligned} \quad (2.89)$$

where the subscript n signifies the mode number, $(R/Q)_{z,n}$ is the shunt impedance of an accelerating mode, and $(R/Q)_{y,n}$ and $(R/Q)_{x,n}$ are the shunt impedance of the vertical and horizontal deflecting mode, respectively.

The longitudinal electric field of the excited accelerating mode increases the longitudinal energy spread, whereas the transverse field components of the deflecting mode increase the beam emittance. Moreover, the decaying field of the HOM deposits power on the cavity surface. Therefore, the modes with a higher shunt impedance need to be reduced below a threshold using HOM couplers. In a normal conducting cavity, the field strength of a HOM gets damped fast due to the low quality factor of the cavity. Additionally, these cavities are operated at room temperature and the additional power deposited by the beam on a cavity surface does not significantly increase the thermal load.

3 Selection of the Deflecting Structure

Transverse kicking of a beam is a common phenomenon in the field of particle accelerators. A plethora of transverse deflecting structures has been proposed, designed, and operated to achieve particle separation, beam diagnostics, beam transport, beam separation, etc. Knowledge of the state-of-the-art deflecting structures will be beneficial for the selection of a suitable beam separator for the current work. The review emphasizes the structures which can be easily adapted to operate as a beam separator.

The first section discusses the classification of the deflecting structures based on the field components and mode of operation. Further, different deflecting structures and their applications are reviewed. Based on this review, a pulsed magnet, a stripline kicker, and an RF cavity were deemed suitable for the beam separation. These structures were adapted to the current requirements, and their comparison is discussed in the next section. As a result, the RF deflecting cavity was found to be appropriate. A detailed analysis for the identification of the cavity operating frequency is presented next. Subsequently, a few probable RF cavity designs suitable for the selected frequency are discussed at the end of this chapter.

3.1 Classification of Deflecting Structures

Deflecting structures that can be adapted as a beam separator fall into three categories: electric, magnetic, and electromagnetic (Figure 3.1). This classification is based on the field component that delivers the transverse force on a bunch. Deflecting structures are further subdivided based on their mode of operation: pulsed or CW. In the pulsed mode, the device is driven by a pulsed power source, and it has a steady field for the duration of the pulse. For this time period, they can be considered static deflectors. The field values, on the other hand, vary continuously

3 Selection of the Deflecting Structure

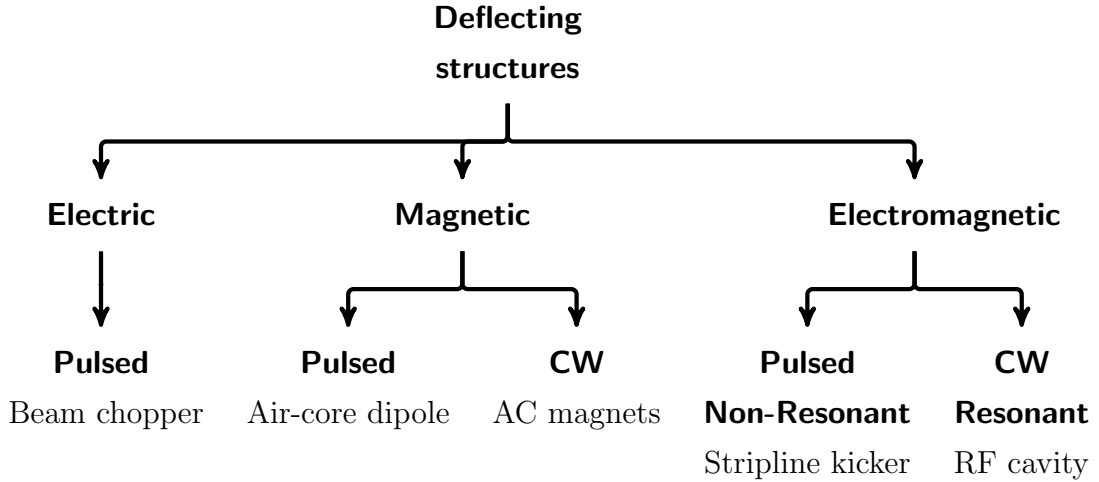


Figure 3.1: Classification of deflecting structures based on the field components and their mode of operation with an example.

with time when the deflecting structures are operated in a CW mode (or quasi-CW). The timing structure of the transverse force for the different operating modes is illustrated in Figure 3.2. As an example, the 2-way separation of a beam with a bunch repetition rate of f_b (1 MHz) is considered. In a pulsed mode operation with the pulse rate of f_p , beam separation can be achieved with the unipolar pulses at a rate of $f_b/2$ (Figure 3.2 (b)) or with the dual-polarity pulses at a rate of f_b (Figure 3.2 (c)). In the case of harmonic fields, the oscillating frequency of the transverse force, f_0 , should be an odd multiple of $f_b/2$, i.e. $(2n + 1) \cdot f_b/2$. The simplest scenario is when $n = 0$, where the transverse force oscillates at a subharmonic frequency of the bunch rate, $f_b/2$ (Figure 3.2 (d)). At $n \geq 1$, the oscillating transverse force is an ultraharmonic frequency ($3f_b/2, 5f_b/2, 7f_b/2, \dots$) of the bunch rate f_b (Figure 3.2 (e)). Usually, a quasi-CW mode operation is preferred at high ultraharmonic frequencies to reduce the power requirement (Figure 3.2 (f)). It is important to note that the timing scenarios discussed here are for on-crest deflection, and there exists infinite frequencies in the case of an off-crest deflection [38].

3 Selection of the Deflecting Structure

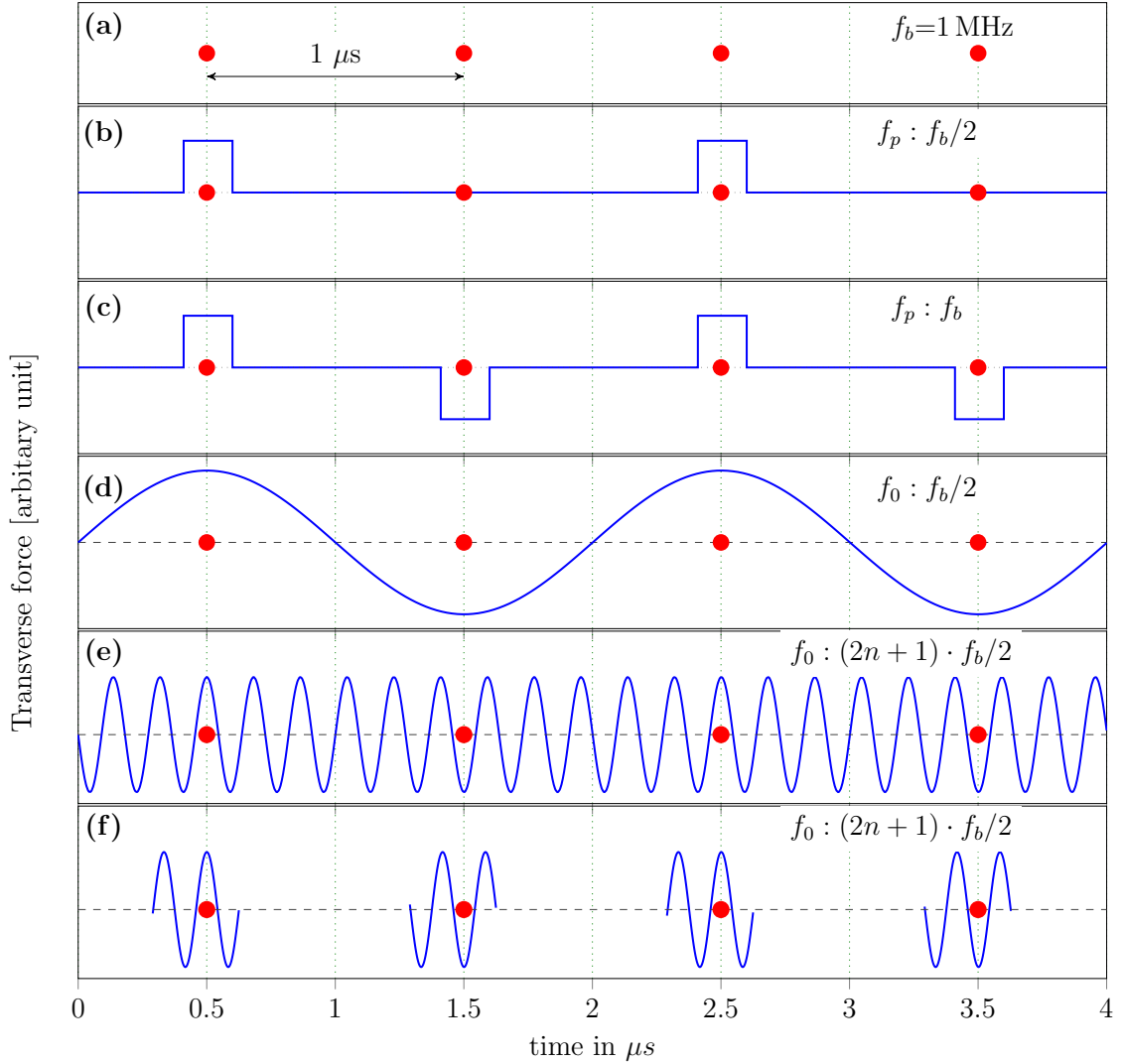


Figure 3.2: Illustration of the timing structure of a beam and the different operating modes of the deflecting structures: (a) beam structure with a bunch rate of f_b , (b) pulse structure with the uni-polarity pulses, (c) pulse structure with the alternate polarity pulses, (d) transverse force at the subharmonic frequency of the bunch rate in CW mode, (e) transverse force at the ultraharmonic frequency of the bunch rate in CW mode, and (f) transverse force at the ultraharmonic frequency of the bunch rate in quasi-CW mode.

3.1.1 Electric Deflecting Structures

The electric deflecting structure has a geometry similar to that of an electrostatic deflector that was discussed in Section 2.2.1. The opposite polarity pulses are applied to the electrodes where the beam enters. The pulses travel along the electrode,

3 Selection of the Deflecting Structure

creating a transverse electric field between the electrodes for the pulse's duration. This pulsating transverse field is used to kick a particular bunch in a beam. The other electrode end is terminated with a matching load to absorb the pulses, preventing them from being reflected. The reflected pulses may reduce the field strength required for kicking the bunches and also impart an unwanted kick to the succeeding bunches. A beam chopper is a perfect example of an electric deflecting structure, which is used in neutron facilities to deliver short temporal neutron pulses for neutron time-of-flight studies [39], and for altering the pulse structure of a beam [40–42].

Usually, the beam pulse structure obtained from an injector section has to be modified suitably to match the acceptance of the booster section¹, reduce the beam current, or match the user requirements. In this case, the required beam structure is achieved using a fast beam chopper that can selectively kick out the unwanted bunches. The beam chopping is performed before the acceleration of the particles to higher energy. Therefore, the pulses traveling at the speed of light must be matched to the velocity of low energy particles to ensure efficient kicking. Instead of a long electrode pair, a set of smaller parallel plates connected by a coaxial cable are used. In this setup, the pulse travel time is varied by modifying the coaxial cable length so that the pulses get synchronized with the bunches [43]. In the meander line chopper design, coaxial cables are avoided by embedding the parallel plates in a dielectric substrate, and they are also known as microstrip line beam choppers [41]. The pulses slow down in a dielectric substrate and synchronize with the slow-moving particles. Moreover, this configuration improves the mechanical stability of the structure. For an in-depth review of the beam choppers, the reader may refer to [39, 42, 44] and references therein.

A list of beam choppers and their properties are presented in Table 3.1. At the front end test stand project at Rutherford Appleton Laboratory, a beam chopping mechanism was demonstrated using two distinct beam choppers operating in tandem [43]. A microstrip line fast beam chopper with a fast rise/fall time (ns) was used upstream, and a lumped electrode type chopper downstream to achieve a longer pulse width (ms) [43]. At the Los Alamos National Laboratory (LANL) and CERN, beam chopping was achieved using a meander-line design structure [44, 45]. A slow

¹A set of accelerating cavities used after an injector to increase the beam energy.

3 Selection of the Deflecting Structure

Table 3.1: Important parameters of the beam chopper structures. The chopper length and vertical aperture are denoted by l_s and v_{ap} , the pulse voltage, rise/fall time, width and repetition rate are denoted by V_p , t_r/t_f , t_w , and f_p , the duty cycle of the macro pulse is represented by D, and the deflection angle by θ .

Accelerator/ laboratory	Beam	Structure		Pulse				Macro-pulse			Kick
	E_b	l_s	v_{ap}	V_p	t_r/t_f	t_w	f_p	width	D	rate	θ
	MeV	mm	mm	kV	ns	ns	MHz	ms	%	Hz	mrاد
RAL [43]	2.497	340	14	± 2.2	2	12	2.4	1.5	3.75	25	16
RAL [43]	2.497	360	11	± 6.0	12	240-10 ⁵	1.2	1.5	3.75	25	66
LANL-SNS [45]	2.5	350	18	± 2.35	10	945	1.06	1.0	32	60	18
SPIRAL-II [46, 47]	0.025	160	92	+10	15	180	0.001	-	0.01-CW	-	350
CERN SPL [44]	3.0	400	20	± 0.5	2	8-1700	44	0.8	40	1-50	0.31
PIP-2-IT [48]	2.1	500	16	± 0.25	-	-	81.25	0.01	1-2	20	7.4
FRANZ [49]	0.120	150	20-80	± 4.9	100/160	65	0.257	-	CW	-	175

chopper with a pair of electrodes was used at SPIRAL2² to achieve beam chopping, where the high voltage to the electrodes was switched off to allow the bunches to pass [46, 47]. At the PIP-2-IT (Proton Improvement Plan-II Injector Test Facility at Fermilab), a 50 Ω and 200 Ω impedance choppers were used to achieve a flexible bunch structure from a CW beam [48]. A unique Wien filter-type $\mathbf{E} \times \mathbf{B}$ beam chopper was designed and tested in the low-energy beam transport section of the “FRAnkfurt Neutron Source at the Stern-Gerlach-Zentrum” (FRANZ) [49]. In this chopper, a constant magnetic field with a pulsating electric field was used to chop off the unwanted part of a beam.

The beam choppers have a field rise/fall time in ns with the pulse width ranging from ns to ms. Moreover, the pulse repetition rate in the beam chopper ranges from kHz to MHz, and the flat-top pulse aids in uniformly kicking all the particles in a bunch. However, almost all the beam choppers are operated in a macro-pulse mode (burst mode) with a low duty factor. At the same time, these structures are suitable for deflecting only low energy beams. Thus, the beam chopper is not suitable for the current application as a beam separator.

²SPIRAL2 stands for Système de Production d’Ions Radioactifs en Ligne de 2e génération.

3.1.2 Magnetic Deflecting Structures

A magnet driven by a pulsed source generates a pulsating magnetic field, and an alternating power source produces a time-varying magnetic field. Beam separation is possible using either of the fields. However, this does not imply that any magnet can be transformed into a beam separator with a pulsed or alternating power source. It is only by designing the magnet, the pulsing circuit, and the auxiliary system in tandem that one can achieve the appropriate pulse field in the magnet. A short pulsed magnet offers the required pulsed fields necessary for fast extraction and injection of the bunches [50–53], whereas alternating field magnets are used in beam separation.

3.1.2.1 Pulsed Field Magnets

In circular accelerators/colliders, fast-acting pulsed magnets are used for the transfer of a beam between the different beamlines (injection/extraction), and these are also known as kicker magnets. Kicker magnets have been discussed in depth in [50–53] and references therein. The kicker magnets are broadly categorized into a traveling wave and a lumped inductance kicker.

A traveling wave or transmission line magnet consists of multiple cells, with each cell having an inductor and a capacitor, thus resembling a coaxial cable. The cell consists of two metallic plates, one connected to high voltage and the other to ground, forming a capacitor, and a C-shaped ferrite core sandwiched between the cells' high voltage plates [53]. The cell inductance and capacitance determine the characteristic impedance of the magnet, and a low inductance is required to achieve a short rise/fall time. In addition, a high impedance aids in lowering the flat-top ripple [53]. Most importantly, a proper termination of the kicker magnet avoids unwanted reflection of the pulses. At CERN, a 33-cell transmission line kicker was built for injection of the bunches into the LHC ring [54], and a pulse rise/fall time of $0.9\ \mu\text{s}$ was achieved with a pulse width of $8\ \mu\text{s}$. Further, the magnet was operated for only 18 s to achieve desired beam filling pattern [54]. A 30-cell traveling wave magnet was built to inject a beam into the KEK-Photon factory storage ring [55]. A pulse width of $1.25\ \mu\text{s}$ and rise/fall time of 600 ns was achieved. In [56], development of a fast pulsed magnet

3 Selection of the Deflecting Structure

system for beam switching at LCLS-II was discussed, with a pulse repetition rate of 100 kHz and rise time of 50 ns.

The lumped inductance kickers are conventional magnets with a coil wound around the core. Further, these magnets have a simple geometry compared to the transmission line kickers. However, the lumped magnet has a higher rise/fall time and also an additional mechanism is required in pulsed magnets to dampen the pulse reflections [57]. A lumped magnet was used for the injection and extraction of the two bunches between the damping ring and linac at KEKB [58]. A double half-sine-shaped pulse drove the magnet with a rise/fall time of 100 ns and a maximum pulse rate of 50 Hz. In an another beam injection application at KEKB, a ferrite core magnet was driven by a half-sine current pulse of 2.4 μ s width at a 12.5 Hz repetition rate [59]. In 1964, SLAC used a set of 5 pulsed magnets to split the main beam into two secondary beams [60]. The H-type magnet had a laminated iron core to reduce the losses and was driven by a sinusoidal signal of 1 kHz with a maximum repetition rate of 360 Hz. A similar pulsed magnet was proposed for time sharing the main beam of GANIL (Grand Accélérateur National d'Ions Lourds, Caen, France) with the different experimental stations [61], where the drive circuit generated rectangular pulses with a flat top of 8 seconds at a rate of 0.1 Hz. A conceptual design of beam switching using a pulsed magnet was proposed for J-PARC (Japan Proton Accelerator Research Complex) with a field rise time of 500 μ s, and with the pulse rate of 50 Hz [62].

The pulsed magnets were used to transfer a part of the proton beam out of the cyclotron at PSI [63], and at TRIUMF [64]. A window frame magnet with a ferrite core and an 18-turn coil was used at PSI, and the magnet was driven by a pulsed source with a pulse rise/fall time of 0.5 ms and a pulse width of 8 s with a duty factor of 1%. TRIUMF employed a ferrite core kicker magnet with a 12-turn coil to achieve a pulse rise/fall duration of 50 μ s with a pulse width of 1 ms and a pulse rate of 375 Hz [64].

Another interesting application for pulsed magnets is beam stoppers. In a radiation treatment facility, a series of pulsed magnets are used to allow or prevent the beam from entering the medical treatment room [65–67]. In these applications, pulsed magnets with multi-turn coils are used, and the complete magnet system is encased in an aluminum box to prevent the eddy currents induced by the magnet from

3 Selection of the Deflecting Structure

interfering with other equipment. The rise and fall time of the beam stoppers at CNAO (Centro Nazionale di Adroterapia Oncologica) and MedAustron was about 250 μs , whereas the maximum pulse rate were 10 Hz at former and 20 Hz at latter [65, 66]. In a similar kicker design at HUST-PTF (Huazhong University of Science and Technology-Proton Therapy Facility, Wuhan, China), a ferrite kicker was preferred to achieve a rise/fall time of less than 100 μs at a pulse rate of 500 Hz [67].

An advanced air-core pulsed magnet design was proposed in [68] to address the demand for a pulsed magnet with a small aperture. The magnet has a single coil with four rods spaced at 30° from the median plane and interconnected such that a dipole field is achieved. The coil is embedded in a ceramic tube of 5 mm thickness and a 30 mm radius to provide the necessary mechanical support. The magnet was operated at a lower pulse current with a 4 μs pulse width at a frequency of 1 Hz [69].

3.1.2.2 Alternating Field Magnets

The stringent pulse rise/fall period required for pulsed magnets is overcome by driving the magnets with an alternating current (AC) source, thus generating an alternating magnetic field necessary for beam separation. However, an alternating magnetic field generates eddy currents in the magnet components. This reduces the field strength and the field uniformity in the magnet aperture and increases the field rise/fall time and power loss in the magnet components. At the same time, eddy currents also affect the working of the surrounding equipment. Moreover, the influence of the eddy current increases in proportion to the frequency of the alternating magnetic field. As a result, AC magnets operate at a lower duty cycle (quasi-CW mode) in applications requiring a high-frequency magnetic field to limit the effects of eddy currents [70, 71].

At CERN, a beam transfer scheme with a longitudinal recombination of bunches using AC magnets was implemented [70]. The magnets were driven by an RF signal at 8.032 MHz in a quasi-CW mode for 2 μs with a duty factor of 0.1% and a rate of 1.2 Hz. In RHIC (Relativistic Heavy Ion Collider) at BNL, a fast-acting vertical and a horizontal deflecting AC dipole magnet were used to manipulate the non-linear beam dynamics of the beam [71], operated at the different frequencies of 64 kHz and 37 kHz, respectively. Moreover, to lessen the eddy current effect, the vertical and horizontal

3 Selection of the Deflecting Structure

correcting magnets were operated only for 2.4 s and 40-80 ms, respectively. At the Proton Engineering Frontier Project (PEFP), Pohang Accelerator Laboratory, Korea, splitting of a primary CW proton beam into five secondary beam was proposed using an H-shaped iron core AC magnet with a five-level staircase signal at a frequency of 2.5 Hz [72].

3.1.3 Electromagnetic Deflecting Structures

The structures discussed so far either used an electric or magnetic field for the kicking of a bunch. In electromagnetic structures, both fields exert a transverse force and they appear to be more efficient than the devices mentioned so far. These structures are classified into resonant and non-resonating structure. In the former, the fields oscillate harmonically based on the eigenmode of the structure, whereas in the non-resonating structure, both the fields are present only for the duration of the pulse.

3.1.3.1 Resonant Deflecting Structures

Generally, the monopole mode of an RF cavity is used to accelerate the particles in the longitudinal direction. In comparison, the dipole modes are used for the deflection of the bunches in the transverse direction, which is necessary for beam separation. Apart from beam separation, depending on the arrival time of the bunch, individual particles in a bunch can be set to experience different transverse kicks, and they are used for particle separation [10], crab crossing [73], beam diagnostics [74, 75], exchange of the bunch phase space [76], and for many other applications. In 1961, Schnell recommended a traveling-wave (TW) disc-loaded structure to separate K mesons and anti-protons for the bubble chamber experiment at CERN [10]. The cavity with an operating frequency of 2.856 MHz was designed and subsequently tested successfully [77]. This motivated the use of a similar type of cavity design for the particle separation at the Brookhaven AGS [11], SLAC [12], and ANL [13]. Advancements in superconducting technology inspired the superconducting deflector cavity design work at Karlsruhe Institute, Germany [78] and at BNL [79]. Another intriguing application utilizing transverse deflecting cavities is in the crab

3 Selection of the Deflecting Structure

crossing scheme, where the two opposite traveling beams collide at head-on to increase the luminosity of a collider [73]. In a transverse deflecting cavity (TCAV), the bunches arriving at the zero-crossing phase receive equal and opposite transverse kicks on the bunch head and tail, tilting the bunch required for crabbing. At KEKB, the crab crossing scheme was implemented using a squashed superconducting cavity operating in the TM_{110} mode at 508.89 MHz [80, 81], doubling the luminosity [82, 83]. The success at KEKB also inspired LHC to use the crab crossing scheme. However, the KEKB crab cavity design was abandoned due to very tight space constraints at LHC, and the feasibility of different crab cavity designs was investigated [84–86]. Subsequently, two cavity designs were selected, and currently, these cavities are being tested at SPS (Super Proton Synchrotron), CERN [87]. A crab crossing scheme using a TEM type cavity has been proposed for the future collider, eRHIC at BNL [88, 89]. Apart from bunch crabbing, the sinusoidal kick voltage of a TCAV is useful in beam diagnostics and phase space exchange. Similar to beam crabbing, the bunch center arriving at the zero-crossing phase receives zero kick, whereas the bunch head and tail receive opposite polarity kick. Moreover, the magnitude of the transverse kick varies along the bunch. After the cavity, each longitudinal bunch slice is transversely displaced with respect to the bunch center. Subsequently, the beam is projected onto a screen and measurement of the bunch spot size provides the information about the longitudinal phase space of the bunch [90]. Additionally, the transverse emittance of the bunch slices can be measured using multiple screens at appropriate phase advance locations [90]. For a more comprehensive description of the beam diagnostics see Refs. [91, 92]. In the beam diagnostic applications, a high frequency operation provides better resolution while at the same it reduces the RF power and space requirement [91–93]. This is why the disc-loaded cavities in the GHz range are preferred for beam diagnostics of high energy beams [18, 74, 93–98]. The same cavity developed for the particle separation [77] was used for measuring the longitudinal bunch phase at SLAC [90, 91]. A low energy beam at an injector requires low RF power for beam diagnostics. Therefore, instead of a longer multi-cell disc-loaded cavity, a compact single-cell TEM-type cavity operating in the TM_{110} like mode at 1.3 GHz was used for beam diagnostics at Cornell ERL (Energy Recovery Linac) [75, 99], ARIEL [100], and bERLinPro (Berlin ERL Prototype) [101].

3 Selection of the Deflecting Structure

A longer bunch makes it difficult to generate the short X-ray pulses required for the user experiments [102]. To overcome this limitation, the transverse-to-longitudinal phase space exchange of a bunch was achieved using deflecting cavities, which compresses the bunch in the longitudinal direction. These shortened bunches are routed through an undulator or bending magnet to generate X-ray pulses, which in turn are sent through an optical slit to achieve sub-ps X-ray pulses [102]. A detailed study of the bunch compression to generate short X-ray pulses in the Advanced Photon Source at ANL is discussed in [102]. A $1/2 - 1 - 1/2$ cell normal conducting 1.3 GHz TCAV was used to obtain short X-ray pulses at Argonne Wakefield Accelerator [103].

In addition to the crabbing, beam diagnostics, and phase space exchange, the TCAVs are also used for beam separation. In [14], the temporal and spatial separation of a stream of particles into four secondary beams using a set of four RF cavities operating in the TM_{110} mode was discussed. A 4-rod TCAV was proposed as a beam separator for CEBAF to distribute the beam to three experimental stations [32]. As a result, a TEM-mode cavity with an operating frequency of 499 MHz was designed [15, 104, 105], and a set of nine cavities was deployed to achieve 2-way and 3-way beam splitting. Upon the up-gradation of the CEBAF, four more cavities with an operating frequency of 750 MHz were used to achieve simultaneous beam transfer to four experimental halls [16]. A superconducting TCAV acting as a beam separator was proposed for the ARIEL electron linac to switch the beam to ERL and RIB (Radio Isotope Beam) facilities [106]. Subsequently, a novel cavity with an operating frequency of 650 MHz was designed, manufactured, and tested [107, 108].

Instead of a fast kicker magnet, TCAV can be used for bunch injection/extraction even at a MHz to GHz bunch rate, which is beyond the state-of-art of the pulsed magnets. However, TCAV imparts a time-varying sinusoidal kick voltage along the bunch, resulting in an inhomogeneous kicking of the particles in the bunch, and also adversely affect the adjacent bunches. Nevertheless, one can obtain a rectangular-shaped kick voltage by combining the sinusoidal kick voltages from a set of harmonic cavities, which would kick the bunch uniformly without affecting the neighboring bunches. An injection/extraction system based on the harmonic deflecting cavities was proposed for the Jefferson Lab Electron Ion Collider (JELIC) [109], which

3 Selection of the Deflecting Structure

will produce rectangular pulses at a rate of 47.63 MHz. Thereafter, a prototype quarter-wave resonator has been built to test the concept, and the cavity was driven simultaneously at five harmonic frequencies [110, 111]. At CTF3 (CLIC Test Facility 3), a TCAV was considered for the bunch train compression [112], and was demonstrated using a standing-wave disc-loaded cavity [113].

In heavy ion accelerators, a high beam current is achieved by interlacing the bunches of the two separately accelerated beams into a single beam known as funneling [114–116]. Because the working of a funneling system is the antithesis of beam switching, the devices intended for one application can be used in the other. An H-type multi-gap deflecting resonator design operating at MHz to GHz frequency was proposed for beam funneling at European Spallation Source (ESS) [117]. Subsequently, a novel prototype RF deflector operating at 1.2 GHz was designed and tested [118].

3.1.3.2 Non-Resonant Deflecting Structures

A stripline kicker is a non-resonant electromagnetic deflecting structure in which the pulses traveling on the stripline generate both the transverse electric and magnetic fields, and each field component exerts an equal transverse force in the same direction. The functioning of a stripline kicker was previously explained in section 2.2.3. The short pulsed transverse field generated by the stripline kicker at a high repetition rate makes it attractive for the injection and extraction of the bunches between the beamlines [27, 28, 119–121]. In addition, they are used in the transverse feedback systems to mitigate the multi-bunch instability caused in a storage ring [122], and beam separation application [123].

Table 3.2 lists the important features of selected stripline kickers. The following list of stripline kicker applications is not comprehensive, but it is intended to provide an insight to the pulse characteristics and kick voltage that stripline kickers can commonly achieve. Typically, the field rise time of ns with a pulse width ranging from tens of ns to μ s are achieved by the stripline kickers. However, the stripline kickers are usually operated in a macro-pulse mode with a repetition rate of less than 100 Hz to reduce the average power required.

3 Selection of the Deflecting Structure

Table 3.2: Important parameters of selected stripline kicker structures. The stripline length and vertical aperture are denoted by l_s and v_{ap} , the pulse voltage and width are denoted by V_p and t_w , the number of pulses in a pulse train is given by N_b , the repetition rate of the pulse train is given by f_p , V_{\perp} is the transverse kick voltage, P_{pk} and P_{av} are the peak and average power loss, and Ef_s is a constant that defines the efficiency of a stripline kicker ($Ef_s = V_{\perp}/(l_s \cdot V_p)$). Here, DR stands for Damping Ring, ATF for Accelerator Test Facility, and MBA for multi-bend achromat.

Accelerator/ laboratory	Stripline		Pulse				Voltage	Power loss		Effic.
	l_s [mm]	v_{ap} [mm]	V_p [kV]	t_w [ns]	N_b -	f_p [Hz]	V_{\perp} [MV]	P_{pk} [MW]	P_{av} [W]	Ef_s [$\frac{\text{kV}}{\text{cm} \cdot \text{kV}}$]
TESLA DR [27]	500	50	2.4	7	1130	10	0.1	0.23	18	0.83
DAFNE [119]	700	50	45	10	-	50	2.5	81	40.5	0.79
CTF3 [120, 124]	2000	40	14.5	200	-	5-50	2.4	8.38	83.7	0.83
KEK-ATF [28]	600	9	10	5.6	30	0.5	2.34	4	0.3	3.90
CLIC DR [121]	1700	20	12.5	1000	312	50	4.29	6.25	0.1	2.02
ELBE [123, 125]	700	30	0.5	25	-	200k	0.045	0.01	50	1.29
ALS-U [126, 127]	2000	6	5.3	50	11	1	7	1.1	0.62	6.60
APS-MBA [128]	720	9	15	17	324	-	4.48	9	49.6	4.15

3.2 Feasibility Study of the Possible Deflecting Structures for Beam Separation

The preceding section provided an overview of different deflecting structures and their applications. As the electric deflecting structures are only used for low-energy beams, they are not suitable for the current task. The magnetic and electromagnetic deflecting structures, on the other hand, can kick high energy beams in a MHz to GHz range, making them suitable for beam separator application. The feasibility of adapting the existing pulsed magnets, stripline kickers, and RF cavities to deliver a transverse voltage of 300 kV and to kick the bunches at a 13 MHz/1 MHz rate is discussed in this section. Furthermore, a preliminary design of the pulsed structures is carried out considering the approximate pulse parameters listed in Table 3.3.

3 Selection of the Deflecting Structure

Table 3.3: The approximate pulse characteristics expected from a deflecting pulsed structure of length 500 mm. Furthermore, the structure should deliver a transverse voltage V_{\perp} of 300 kV or an integrated transverse magnetic field of 1 mT m.

Pulse:	rate, f_p	rise/fall time, t_f/t_r	width, t_w
ELBE	13 MHz	25 ns	25 ns
DALI	1 MHz	200 ns	25 ns

3.2.1 Pulsed Magnet

The development of a pulsed magnet system necessitates the simultaneous design of the system's three main parts (magnet and coil, power supply, transmission line and pulse forming circuit) and all the auxiliary systems. The construction of an AC magnet operating at a MHz rate is beyond the current state of magnet technology; hence, only pulsed magnets are examined. The difficulties in selecting suitable magnet parts compatible with a high-frequency pulsed operation are discussed before the presentation of a pulsed magnet design that fulfills the current requirements.

The magnetic core, a material with high magnetic permeability, confines the magnetic field produced by a current-carrying coil and focuses it onto the magnet aperture. Compared to an air core, a magnetic core prevents flux leakage and multiplies the field strength in the aperture. As a result, the magnetic core lowers the coil current needed to produce a desired magnetic field. Usually, solid iron or ferrite-cores are used in DC magnets as the magnet's core [69]. In the case of AC or pulsed magnets, the eddy current induced by a varying magnetic field causes power loss in a solid core and demands active cooling of the core. However, developing a cooling system for the magnetic core is challenging. Instead of a solid core, thin laminated steel sheets are used to screen the eddy currents, but they are ineffective at smaller skin depths [129]. The use of an air-core eliminates the eddy currents and power losses in the core [68, 69]. The leaking magnetic flux, on the other hand, may potentially interfere with nearby devices and increase the coil current required to obtain a specified field strength. In fast pulsed magnets, ferrite-cores are preferred over other types of magnetic cores [19, 52, 64, 67]. Ferrite has a good frequency response up to the MHz range, lower hysteresis losses, and withstands a flux density of 0.3 T [50].

3 Selection of the Deflecting Structure

The field strength in the magnet aperture is determined by the number of coil turns, the coil current and voltage, and the coil shape. The number of turns in a coil dictates its inductance, which in turn affects the field rise/fall time and the required coil current and voltage. The coil voltage rises with an increase in coil turns, whereas the coil current falls off quadratically [64]. Furthermore, the field's rise/fall time is adversely affected by an increased coil inductance. As a result, a single-turn coil is recommended for a fast-acting kicker, as it lowers both the field rise/fall time and the required coil voltage [52]. A racetrack-shaped coil provides a better field homogeneity in the magnet aperture than a cylindrical coil [69].

Another important part of the magnet is the generation and transmission of fast pulses. High-frequency short pulses are generated using a pulse forming circuit, which consists of a DC source, a pulse forming line/network, and switches [52]. The pulse generating circuit is designed by considering the parameters of the magnet and pulse transmission cable to achieve the necessary rise/fall time. Advancements in the semiconductor switching technology have increased the switching devices' stability and reliability. At a MHz range switching, MOSFET is preferred [19], whereas IGBT is suitable at a kHz range [63, 64]. However, MOSFET and IGBT have voltage limitations of 1 kV and 3.3 kV, respectively. The high voltage and current required by the magnets are obtained by arranging the switches in parallel [19]. However, the switch triggering pulses have to be synchronized to achieve a flawless operation [130], and the design of the controls for a fast pulsing system is a complex task [53]. Although most of the components for the pulsing circuit are readily available, designing and assembling the components is challenging if the stated requirements are to be met.

The magnet and pulse forming circuits are usually positioned far apart and are connected by a long coaxial cable. As a result, the impedance of this cable has to be considered when designing the magnet system. In addition, the coil has to be terminated with a suitable load to prevent the pulse reflections, which alters the pulse rise/fall time and field strength. It is necessary to construct a metallic enclosure to confine the leaking magnetic field. Moreover, simulations have to be performed to ascertain the impact of the enclosure on the field's rise/fall time, strength and homogeneity.

3 Selection of the Deflecting Structure

A metallic beam pipe helps maintain an ultra-high vacuum (UHV) required to keep the beam from getting destroyed. Moreover, it acts as a path for the image current and prevents static charge build-up. The metallic beam pipe does not screen the time-invariant magnetic field generated by a DC magnet. However, it screens the alternating field generated by a pulsed and AC magnet. The metallic beam pipe can be avoided by placing a pulsed magnet inside a vacuum chamber. In this setup, it is necessary to ensure that all the magnet components are compatible with UHV. Furthermore, a reliable high voltage feedthrough and a large vacuum chamber are required. Another drawback is that the entire system has to be dismantled for any repair or maintenance. To avoid this, the magnet was placed outside the vacuum chamber, and the metallic beam pipe was replaced with a ceramic one [19, 54, 68]. However, to provide a conduction path for the image current and to avoid static charge build-up, a thin layer of metallic coating was provided on the ceramic surface [131]. In this case, the thickness of the coating affects the field rise/fall time, and a careful analysis of the beam-induced power in the coating has to be carried out.

A Basic Design of a Pulsed Magnet

As mentioned earlier, developing a pulsed magnet system necessitates the simultaneous design of the system's parts in unison. A complete design of the magnet is outside the scope of this work. To arrive at the basic design of a pulsed magnet, it was assumed that an appropriate pulse-forming circuit matching the pulse requirements listed in Table 3.3 exists. Moreover, the effect of the pulse transmission cable, the magnet enclosure, and the power losses in the coil and core were ignored for simplicity. The design methodology used here closely follows the works of [19, 52, 53, 55, 132]. The lumped inductance magnets have a simple geometry, but they have a slow response time [52]. The transmission line kicker magnets, on the other hand, have a fast response time and are used in applications where a high repetition rate pulsed-field with a smaller rise and fall time are required [19, 55]. As a result, a transmission line magnet with a C-shaped ferrite core and a single turn coil was preferred in this design. In addition, using a ceramic tube to house the magnet coil similar to that described in [68] helps retain the small magnet aperture and eliminates the metallic beam pipe.

3 Selection of the Deflecting Structure

The flux density B_y in the magnet aperture is given by (3.1) [52]:

$$B_y \approx \mu_0 \frac{N_c I_c}{v_{ap}} \quad (3.1)$$

where I_c denotes the coil current, N_c the number of coil turns and v_{ap} the vertical aperture of the magnet. For the vertical aperture of 30 mm, a coil current of 48 A is required to generate a 2 mT of magnetic field in the magnet's aperture.

In general, the characteristic impedance (Z) of the magnet is matched to the generator to minimize reflection and is given as $Z = \sqrt{L_c/C_c}$, where L_c and C_c are the inductance and capacitance of a magnet cell, respectively. A standard load of 50 Ω simplifies the design calculation. Note that the choice of the impedance value has an effect on the field rise/fall time and power loss. Furthermore, it was considered that the transmission line magnet consists of 10 cells. In this type of kicker, the inductance of a magnet cell is given by [55],

$$L_c = \mu_0 \frac{l_s}{N} \cdot \frac{h_{ap}}{v_{ap}}, \quad (3.2)$$

where l_s/N denotes the cell length, N the number of magnet cells, l_s the magnet length, and h_{ap} the horizontal size of the magnet aperture. Considering a square aperture, $h_{ap} = v_{ap}$, and l_s of 500 mm, the inductance of a single cell and the magnet was obtained as 6.3 nH and 63 nH, respectively. Additionally, to match the impedance Z , the cell capacitance C_c should be 2.5 pF. The field rise time in a magnet is the sum of the pulse rise time (t_r) and the magnet's field fill time (t_m). Because the field fill time of a magnet is given by $t_m = (L_c N)/Z$, a low cell inductance and a higher characteristic impedance result in a shorter fill time. The pulse rise/fall time of 25 ns specified in Table 3.3 is significantly higher than the field rise time of 1.25 ns computed for the magnet. Therefore, the pulse characteristics dictate the field rise time in this design.

The average power deposited on the load due to a trapezoidal pulse is given as

$$P_{av} = I_c^2 Z \cdot f_p \cdot \left(\frac{2 \cdot (t_r + t_m) + t_w}{2} \right), \quad (3.3)$$

where f_p is the pulse rate and t_w is the pulse width. Therefore, an average power of 28 kW and 6.5 kW occurs on the load for two-way separation of the 13 MHz and

3 Selection of the Deflecting Structure

Table 3.4: The properties of the preliminary design of the transmission line pulsed magnet of length 500 mm, and an integrated magnetic field of 1 mT m. Here, N , I_c , and V_c denote the number of coil turns, the current and voltage in a coil, respectively; t_r/t_f , t_w , and f_p the pulse’s rise/fall time, width, and repetition rate, and Z and P_{av} are the value of the load impedance and the average power loss at the load, respectively.

Bunch rate	Coil			Pulse			Load	
f_b [MHz]	N	I_c [A]	V_c [kV]	t_r/t_f [ns]	t_w [ns]	f_p [kW]	Z [Ω]	P_{av} [kW]
13/1	1	48	2.5	25	25	13/1	50	28/6.5

1 MHz bunches, respectively. The average power loss in the load can be reduced by decreasing the load impedance, but this will increase the cell capacitance and the field rise time. The important properties of this preliminary pulsed magnet design are summarized in Table 3.4.

3.2.2 Stripline Kicker

A stripline kicker is a pulsed deflecting structure, which can have a pulse rate in MHz range with a pulse rise/fall time in ns. The fast-acting pulse field of a stripline kicker is ideal for kicking out specific bunches from a beam without affecting the neighboring bunches in order to achieve beam separation. Moreover, a flat-top transverse voltage kicks all the particles in a bunch uniformly. After a discussion on the important criteria for designing a stripline kicker, a preliminary design of the stripline kicker that meets the current requirements is presented.

A pair of electrodes and pulsing circuit are the two primary components of a stripline kicker. The stripline kicker’s pulsing circuit faces challenges similar to those of pulsed magnets, which were previously discussed. Therefore, only the design of the electrodes is discussed. The geometry of the electrode pair has to be optimized in order to achieve the desired transverse shunt impedance and kick voltage uniformity. A stripline kicker has two basic TEM modes: the odd and the even mode [133, 134]. The electrodes are at different potentials in the odd mode, which is the kicker’s operating mode. At the even mode, electrodes are at the same potential, which is

3 Selection of the Deflecting Structure

the case when a beam passes through the structure. A characteristic impedance of 50Ω in the odd mode has to be achieved by optimizing the electrode's geometry, as this will help connect the structure to standard components and also reduces the reflection of the pulses. Additionally, the even mode characteristic impedance should be kept close to 50Ω in order to damp the field induced by the passing beam. However, it is not possible to match both modes' impedance simultaneously [135]. Refs.[136, 137] provide a detailed analysis of the different electrode cross-sectional shapes and their optimization. A half-moon electrode with tapered edges provides good field homogeneity, and it is compact enough to fit inside a small beam pipe [137]. A similar electrode shape design has been adapted in [134, 138, 139]. The electrodes are connected to the beam pipe by a non-metallic cylindrical structure, providing structural support and keeping the electrodes parallel [120]. In a smaller beam pipe, macro rings are preferred for electrode support [136]. Though the support structure isolates the electrode and beam pipe electrically, its influence on the kicker behavior can not be neglected. In addition, any mismatch in the characteristic impedance due to the power feedthrough must be addressed.

Typically, a stripline kicker's shunt impedance is increased by varying the electrode's length to reduce the power requirement. At lower frequencies, a longer electrode has a higher shunt impedance, while at higher frequencies, a shorter electrode has a larger shunt impedance [140]. However, the electrode's length also influences the pulse rise/fall time, where a shorter (longer) electrode has a smaller (larger) rise/fall time. Therefore, an array of shorter electrodes are used when the structure is pulsed at high frequencies [28]. In this case, the temporal synchronization of the pulses is a challenging task. Since the electrode acts as a transmission line, the power loss in the electrodes due to the pulses is negligible. The power deposited by the beam, however, must be considered. Since the stripline components are not water-cooled, any power loss at the connectors and electrode increases its temperature. This results in mechanical stress at support junctions, potentially resulting in a drift of the timing signal and damaging the feedthrough. Therefore, the shift in the timing signal needs to be corrected in real-time to achieve a stable kick voltage [28]. Moreover, a significant power will be deposited at the load when the kicker is pulsed at a high rate and duty cycle.

3 Selection of the Deflecting Structure

Table 3.5: The required pulse voltage, peak and average power loss at the $50\ \Omega$ load of the stripline kickers presented in Table 3.2 to deliver a V_{\perp} of 300 kV with the structure length (l_s) scaled to 50 cm and pulse width of 10 ns. Here, P_{av_1} and P_{av_2} are the average power loss at the load with the pulse rate at 13 MHz and 1 MHz, respectively.

Accelerator/ laboratory	Structure aperture	ef_s	Stripline [t_w : 10 ns, l_s : 50 cm; V_{\perp} : 300 kV]			
		$\frac{V_{\perp}[\text{kV}]}{l_s[\text{cm}] \cdot V_p[\text{kV}]}$	Pulse voltage	Peak power	Power loss	
	$v_{ap}[\text{mm}]$		V_p [kV]	P_{pk} [MW]	P_{av_1} [kW]	P_{av_2} [kW]
TESLA DR [27]	50	0.83	7.20	1.037	134.78	10.37
DAFNE [119]	50	0.79	7.56	1.143	148.60	11.43
CTF3 [120, 124]	40	0.83	7.25	1.051	136.66	10.51
KEK-ATF [28]	9	3.90	1.54	0.047	6.15	0.47
CLIC DR [121]	20	2.02	2.97	0.176	22.97	1.77
ELBE [125]	30	1.29	4.67	0.436	56.62	4.36
ALS-U [126, 127]	6	6.60	0.91	0.017	2.15	0.17
APS-MBA [128]	9	4.15	1.45	0.042	5.44	0.42

Prior to performing a preliminary design of the stripline kicker, the feasibility of adapting the stripline kickers presented in Table 3.2 was explored. For a fair comparison, it was considered that the kicker delivers a V_{\perp} of 300 kV with its length, l_s set to 500 mm. The required pulse voltage, the peak and average power loss at the load for different kicker structures adapted for the two-way separation of a beam with a bunch rate of 13 MHz and 1 MHz are presented in Table 3.5. Stripline kickers with a smaller aperture (v_{ap}) has lower power loss compared to larger aperture. Furthermore, the thermal management of the stripline kickers at these power levels is challenging.

A Basic Design of a Stripline Kicker

In this preliminary design study, it was assumed that a pulsing circuit capable of delivering pulses with a pulse width of 10 ns at a rate of 13 MHz and 1 MHz would be readily available, and only the aspects related to the kicker power were investigated. The electrode geometry has to be optimized to achieve a characteristic impedance

3 Selection of the Deflecting Structure

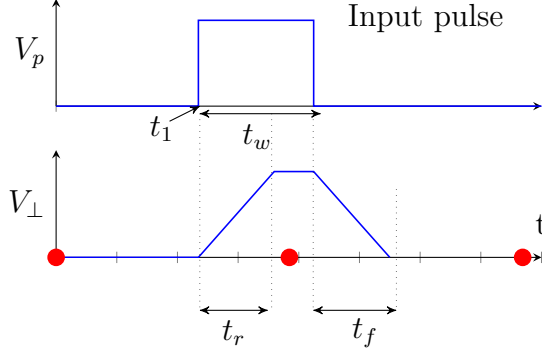


Figure 3.3: A sample pulse structure scheme of a stripline kicker, where the input pulse is applied on electrodes at time t_1 for a duration of t_w , and t_r is the field rise time.

of 50Ω . The transverse kick voltage V_{\perp} generated by a kicker is given by

$$V_{\perp} = 2g_{\perp} \cdot \frac{2V_p}{v_{ap}} \cdot l_s, \quad (3.4)$$

where V_p denotes the pulse voltage, v_{ap} the vertical gap between the electrodes, l_s the structure length, and g_{\perp} the geometry factor of the kicker. The factor, g_{\perp} , determines the concentration of transverse fields on the beam axis. By altering the electrode shape to focus the field onto the beam axis, it is possible to achieve a g_{\perp} value of unity, which denotes that the field is maxima. In the case of $g_{\perp} = 1$, it requires a pulse voltage V_p of 4.5 kV to achieve a V_{\perp} of 300 kV with v_{ap} of 30 mm. The next step of the design process involves considering the kicker's pulse time structure, which is shown in Figure 3.3. The rectangular voltage pulses of opposite polarity are applied on a pair of electrodes at time t_1 . The transverse field strength between the electrode starts increasing as the pulses move along the electrode, and they require time t_g to reach the opposite end of the electrode. The electrode length l_s determines the field rise time t_r and is given by $t_r = l_s/c$. Therefore, the field rise time has to be 1.5 ns for a 500 mm long electrode, which is significantly smaller than the pulse rise/fall time specified in Table 3.3. The pulse width (t_w) should be at least twice the field rise time so that the bunch experiences a constant transverse field throughout the structure. In this preliminary design, a conservative value of 10 ns was considered for the total pulse width, which includes both the pulse rise and fall time.

In general, the electrode is terminated with a characteristic line impedance to avoid the pulses' reflection. Thus, to be compatible with the commercial power sources, a characteristic impedance (Z) of 50Ω was selected. The peak pulse power (P_{pk})

3 Selection of the Deflecting Structure

Table 3.6: The properties of the stripline kicker's basic design discussed with the electrode length of 500 mm and are separated by 30 mm, and delivers a transverse kick voltage of 300 kV. Here, V_p , t_r/t_f , t_w and f_p denotes the voltage, rise and fall time, width and repetition rate of pulses, whereas, Z , P_{pk} , and P_{av} are the load impedance, peak and the average power loss at the load, respectively.

Bunch rate	Pulse characteristics				Load characteristics		
f_b [MHz]	V_p [kV]	t_r/t_f [ns]	t_w [ns]	f_p [MHz]	Z [Ω]	P_{pk} [kW]	P_{av} [kW]
13/1	± 4.5	5	5	13/1	50	405	39.5/3.1

required per strip is given by $P_{pk} = V_p^2/Z$, whereas the average power per strip for a pulse rate of f_p is given as $P_{av} = P_{pk} \cdot f_p \cdot t_w$. The above losses must be doubled to obtain the total power required by the kicker. The important properties of the preliminary stripline kicker design are summarized in Table 3.6. A peak power loss of 405 kW demands an effective cooling of the load. Furthermore, considering a trapezoidal pulse shape, the 2-way separation of 13 MHz and 1 MHz beam will result in the average power losses of 39.5 kW and 3.1 kW, respectively.

3.2.3 Transverse Deflecting Cavity

The resonant electromagnetic fields in a TCAV provide a larger kick voltage at a high repetition rate, which makes these cavities a potential candidate for the beam separation application. Furthermore, the strict rise/fall time required for the pulsed devices is irrelevant for an RF cavity. Unlike pulsed magnets, the cavity and the RF power source can be designed independently. Moreover, RF power sources are commercially available for a wide range of frequencies. The cavities can be operated at either room temperature or in a superconducting state; however, in this thesis primary focus is on normal conducting cavities due to their ease of manufacturing and operation. The difficulties encountered during the development of an RF cavity will be covered thoroughly in Chapters 4-8, and only a summary of this is presented here.

The cavity size and shape are determined mainly by its operating frequency, and

3 Selection of the Deflecting Structure

this ranges from MHz to GHz. Additionally, the frequency influences the surface power loss in the cavity. Normal conducting cavities are designed to achieve a high shunt impedance to reduce the power deposited on the cavity walls. Further considerations include a low peak electric field and surface power loss density. To avoid RF breakdown, the peak electric field should be lower than the Kilpatrick limit, and a low surface power loss density helps remove the heat from the cavity. Moreover, achieving a homogeneous field around the cavity axis is challenging. A careful study of the parasitic effects, i.e., multipacting, higher-order modes and wakefield, is required, and suitable countermeasures must be designed. Another significant challenge is manufacturing the cavity, where the cavity parts must be machined within tight tolerances. The cavity frequency must be pre-tuned before the final brazing/welding to compensate for fabrication errors.

As mentioned in Chapter 2, there is an infinite number of operating frequencies which can be used for the 2-way beam separation of a beam. Moreover, as the frequency determines the cavity shape and size, designing an RF cavity at all of these frequencies is time-consuming. As a result, only the viability of using an existing deflecting cavity for the beam separation is investigated. In addition, the beam separator development can be expedited if an off-the-shelf deflecting cavity meets the specified requirements.

Depending on the deflecting mode, TCAVs are categorized as either a TM mode cavity or a TEM mode cavity. The dipole TM mode of a pill-box cavity is suitable for transverse kicking of the bunches. At high frequencies, the overall size of the cylindrical cavities decreases. Therefore, an array of these structures are joined together to form a disc-loaded cavity. These cavities are further grouped as a traveling-wave (TW) or a standing-wave (SW) structure based on the wave pattern formed in the cavity. In an axis-symmetric cavity, the dipole mode has two degenerating modes at the same frequency, which are orthogonal to each other. To avoid the inadvertent excitation of the incorrect mode, the resonance frequency of the modes is separated. Mode separation is achieved by perturbing the mode field using a set of rods [11, 18, 74, 141, 142], or a pair of holes on the cell separation walls [12], or a squashed cell [10, 81].

An empirical relation between the cavity input power (P_c) and the transverse voltage

3 Selection of the Deflecting Structure

(V_{\perp}) generated by a TW disc-loaded cavity obtained from the calculation [11] and measurement [143] is given as

$$V_{\perp}[\text{MV}] \approx \zeta [\text{MV}/(\text{mMW}^{-2})] \cdot l_c[\text{m}] \cdot \sqrt{P_c[\text{MW}]}, \quad (3.5)$$

where ζ is the cavity efficiency factor, l_c is the cavity length, and units of a quantity are given within the brackets. The expression, $V_{\perp} = \sqrt{P_c \cdot R_{\perp}}$ is used to find the transverse voltage generated by a SW disc-loaded cavity.

The efficiency factor, ζ , and the shunt impedance, R_{\perp} , of the cavities can be obtained from the literature. Further, these values can be used in the equations (3.5) and (2.46) to calculate the required RF power by a cavity to obtain a specified V_{\perp} . Table 3.7 shows the important properties of selected TW and SW deflecting cavities and also the required RF power to achieve a V_{\perp} of 300 kV. The table also shows the required RF power with the cavity length scaled to 500 mm. The results clearly show that as the frequency increases, the required RF power for both disc-loaded configurations decreases, as does the cell size. As a result, disc-loaded cavities are preferred in high-frequency applications. However, at low frequencies, the overall size of the disc-loaded cavity and the required RF power increase, and a TEM type cavity is preferred due to its smaller transverse size.

A TEM type deflecting cavity has a smaller transverse size at a low frequency. Moreover, the inner conductor of a TEM type cavity can be shaped to concentrate the field along the cavity axis to achieve a higher shunt impedance and a better kick voltage homogeneity [156]. The main parameters of the selected normal conducting TEM type deflecting cavities are listed in Table 3.8, including the RF power required to achieve a V_{\perp} of 300 kV with the original cavity and the normalized power loss with respect to the reference cavity length of 500 mm. The RF power required by the TEM type cavities is significantly lower than that of the SW disc-loaded cavities (Table 3.7).

3.2.4 Comparative Analysis

A feasibility study was carried out for the adaptation of the existing deflecting structures (pulsed magnets, stripline kicker, and RF cavity) for the current work. Furthermore, a preliminary design of a pulsed magnet and a stripline kicker was

3 Selection of the Deflecting Structure

Table 3.7: Important properties of the selected TW and SW disc-loaded structures and the required RF power to achieve a V_{\perp} of 300 kV. Here, $P_{av,1}$ refers to the power required with the original cavity length, and $P_{av,2}$ is the normalized power loss with respect to the reference cavity length of 500 mm.

	Accelerator, Laboratory	Band	f_0	Cells	l_c	ζ^a	$P_{av_1}^*$	$P_{av_2}^*$
			[GHz]		[mm]	$\left[\frac{\text{MV}}{\text{m}\sqrt{\text{MW}}}\right]$	[kW]	[kW]
Travelling-wave cavities	PITZ, DESY [98]	S	2.997	14+2	533	1.5	140.8	157.7
	LCLS, SLAC [12, 91, 144]	S	2.856	69+2	2440	1.6	5.9	124.6
	CTF3 CR [145]	S	2.998	10+2	330	1.9	228.9	104.3
	FERMI@Elettra [18]	S	2.998	72+2	2400	2.4	2.7	81.6
	XFEL, PAL [95]	S	2.856	26+2	1200	2.7	8.6	49.4
	XFEL, SACLA [97]	C	5.712	77+2	1700	4.0	1.9	22.5
	LCLS, SLAC [146]	X	11.424	113+2	1000	5.4	3.1	12.5
	SXFEL, SINAP [147]	X	11.424	47+2	440	7.1	9.2	7.1
	ATF, BNL [148]	X	11.424	43+2	460	8.5	5.9	4.9
	Accelerator, Laboratory	Band	f_0	Cells	R_{\perp}^a	l_c	$P_{av_1}^*$	$P_{av_2}^*$
			[GHz]		[M Ω]	[mm]	[kW]	[kW]
Standing-wave cavities	AWA, ANL [149]	L	1.300	3	3.3	259.9	27.27	14.18
	CTF3 DL [113]	L	1.499	1	0.63	60	144	17.28
	Waseda Uni and KEKB [150]	S	2.855	2	1.34	89.4	67.16	12.01
	SPARC, INFN-LNF [74]	S	2.856	5	4.48	262.4	20.09	10.54
	TSE, Tsinghua Uni [151]	S	2.856	3	2.85	157.5	31.58	9.95
	REGA, DESY [152]	S	2.998	9	7.58	270	11.87	6.41
	LERFD, FERMI [153]	S	2.998	5	4.8	250	18.75	9.38
	Tsinghua University [154]	C	5.712	3	1.42	57.6	63.38	7.30
UCLA, Neptune lab [155]	X	9.596	9	6.12	140.6	14.71	4.14	

^a values are obtained from the literature

investigated. The properties of these possible structures were compared before selecting a suitable structure for the current work. The structures were assessed

3 Selection of the Deflecting Structure

Table 3.8: Important properties of selected TEM-class normal conducting deflecting cavities. The required RF power to achieve a V_{\perp} of 300 kV with the original cavity and the normalized power loss with respect to the reference cavity length of 500 mm are given as $P_{av,1}$ and $P_{av,2}$, respectively.

Cavity, accelerator	f_0 [MHz]	l_c [mm]	h_s [mm]	R_{\perp} [M Ω]	R_{\perp}/l_c [M Ω /m]	$P_{av,1}$ [W]	$P_{av,2}$ [W]
Multi-harmonic ¹ , JELIC [110]	47.63	628	1575	31.2	49.63	2884	9187
RF-Dipole ² [157]	139	500	340	358	716	251	251
RF-Dipole ² [38]	325	421	256	95	2256	947	798
NC 4-rod ² [38]	325	450	444	152	338	600	540
Old 4-rod, CEBAF [158]	499	300	292	104	346.7	865	519
New 4-rod, CEBAF [16, 159]	748.5	200	292	78.38	195.9	2297	919
Double-quarter-wave, JLAB [160]	499	179	-	6.4	35.8	14063	2514
Single-cell, Cornell ERL [99]	1300	109	210	10.54	96.7	8539	1861

¹ Proposed set of multi-harmonic cavities with a rectangular pulse with a width of 2 ns.

² Only a design study.

based on the following criteria: the ease with which the existing structure designs could be adapted to the current work, the availability of the necessary power source, the temporal and spatial uniformity of the kick voltage, the stability and reliability of the overall system, and development time for prototyping.

The adaptation of the existing pulsed magnet systems to the specified requirements is not possible as all the subsystems must be designed in tandem. Moreover, the eddy currents generated due to the pulsing of the magnet at a MHz poses a significant challenge in designing the core, coil, and enclosure of the magnet. In contrast, a slight modification in the structure of the existing stripline and cavities is required to meet the current needs. In particular, the structures should be altered to cater the high power loss. However, stripline kickers can only be operated in the burst mode (lower duty cycle) due to the unavailability of CW pulsed power sources in the MHz range.

The ability to generate CW pulses at a MHz rate is beyond the state-of-the-art pulsed power sources. As a result, the pulsed magnet and stripline kicker fail to

3 Selection of the Deflecting Structure

meet the current requirement of CW operation. In contrast, RF power sources for cavities can be sourced commercially, which can deliver up to MW of power over a wide frequency range.

In RF cavities, the kick voltage varies with time, and the particles within a bunch are deflected at a slightly different angle (discussed in the following sections). Additionally, the spatial variation of the transverse field must not be overlooked in the cavity design stage. In pulsed structures, on the other hand, the flat-top voltage pulse maintains a constant transverse field in the aperture throughout the transit of a bunch. This results in all the particles in the bunch experiencing the same kick voltage. Furthermore, the spatial field homogeneity of the magnet should be improved by modifying the geometry of the magnet core and coil. At the same time, the shape of the electrode should be altered in the stripline kicker to focus the field on the beam axis.

In a pulse-driven power source, each pulse is generated independently of the preceding pulses, which makes it hard to achieve pulse-to-pulse stability. Even though advancements in switching devices have increased the reliability of pulse power sources, achieving a flat-top pulse with a rise/fall time of ns is challenging. Moreover, the change in the structure's behavior during operation should be accurately measured to synchronize the timing of the pulses. Unlike pulsed devices, the cavity field exhibits a steady-state behavior, which makes it easy to measure and maintain a stable and repeatable kick voltage.

A key obstacle in designing a pulsed magnet is the mitigation of effects due to the eddy currents generated during high-frequency pulsing. The eddy currents increase the system's power loss and degrade the pulse rise/fall time and the field homogeneity. A ferrite core, a single-turn coil, a ceramic beam pipe, and a metallic enclosure for the magnet might reduce the eddy current effect, but not completely. To ensure that the system's performance as a whole is not affected, each component must be carefully designed. The placement of a pulsed magnet inside or outside the vacuum chamber poses unique challenges that must be adequately addressed. In contrast, a stripline kicker and a deflecting cavity have a simple geometry that eases their design and fabrication. The electrode supporting structure and pulse feedthrough of a stripline requires a close examination. To avoid electric breakdown and thermal

3 Selection of the Deflecting Structure

runaway, a cavity's peak surface electric field and surface power loss density should be maintained within safe limits.

After the review of the deflecting structures, the pulsed structures (magnet and stripline kicker) were viewed to be a suitable choice for the current work. However, the feasibility study concluded that the design, fabrication, and operation of these structures will be challenging to meet the specified requirements of a beam separator. Moreover, the operation of these structures at a MHz pulse rate in CW mode has not been reported in the literature. In contrast, there are several transverse deflecting cavities which have an operating frequency ranging from MHz to GHz and also satisfy the current requirements. Naturally, if an off-the-shelf TCAV fulfills all the prerequisites, the beam separator development work can be expedited. The results of this study clearly demonstrate that a TCAV is the right choice for the current work.

3.3 Choosing the Cavity Operating Frequency

The RF cavity emerged as a potential candidate for beam separation at ELBE among three types of deflecting structures. The cavity's physical shape, size, and RF properties vary based on its operating frequency. Therefore, the selection of an appropriate operating frequency is a preliminary step of the cavity design process. The main four criteria for the selection of the cavity frequency are as follows: a) kick voltage and deflection angle error, b) beam emittance growth, c) surface power losses, and d) kick field homogeneity. In the following sections, each criterion will be discussed in detail.

In addition to the above criteria, the selected frequency should address some of the technological constraints. Currently, at ELBE, there is a reliable low-level RF control system that controls the amplitude and phase of the field in the sub-harmonic buncher and the SRF cavities, which are driven at 260 MHz and 1.3 GHz, respectively. It was therefore decided that the operating frequency of the beam separator cavity should be close to one of the two frequencies to avoid any major modification to the control system [161]. Moreover, the RF power sources around these frequencies are commercially available. Additionally, the operating frequency should satisfy the

3 Selection of the Deflecting Structure

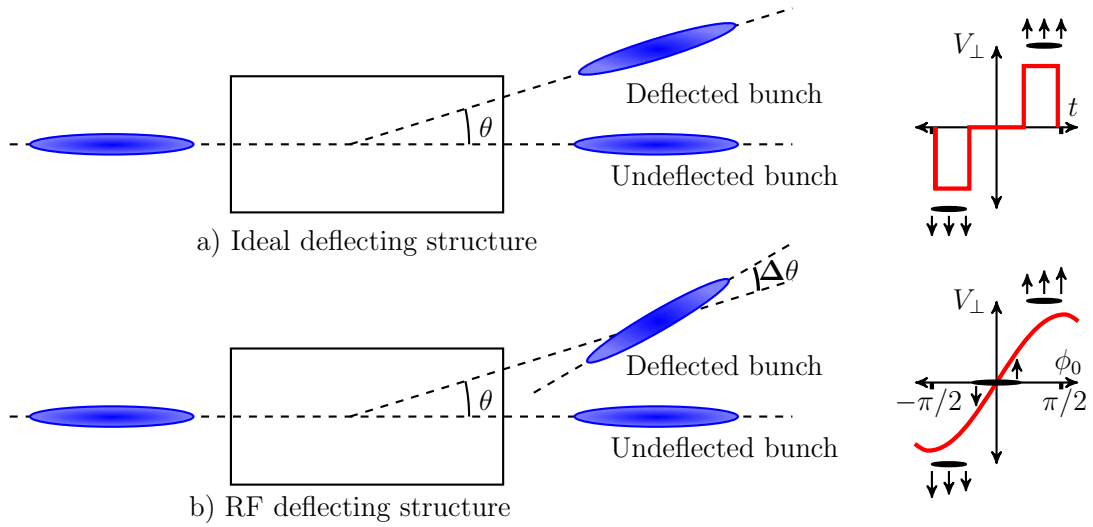


Figure 3.4: A sketch of the beam path of an ideal deflecting structure and an RF deflecting structure and the corresponding transverse kick voltage received by the bunches. The direction and length of an arrow corresponds to the polarity and magnitude of the transverse voltage.

different use case scenarios discussed at the end of this section. Above all, it should be possible to build a prototype cavity within the time frame of this thesis.

3.3.1 Kick Voltage and Deflection Angle Errors

In an ideal case, all the particles in a bunch should experience the same transverse kick in a deflecting structure (Figure 3.4 a). However, due to the harmonic fields in a cavity, the transverse voltage experienced by a particle depends on its longitudinal position in the bunch (Figure 3.4 b). The bunch arrival phase, ϕ_0 , refers to the phase of the electric field when the bunch is at the center of the cavity. Consider a zero-crossing phase ($\phi_0 = 0$), where the bunch center receives zero kick, and the head and tail of the bunch receive opposite polarity transverse voltages resulting in a yawing or pitching of the bunch (or crabbing). In the on-crest phase ($\phi_0 = \pi/2$), all the particles in the bunch receive the same polarity kick voltage, and the entire bunch gets deflected in a transverse direction. However, the magnitude of the kick voltage varies slightly along the bunch length resulting in the transverse voltage error (ΔV_{\perp}). This unavoidable kick voltage error in an RF cavity causes the bunch to chirp at an angle of $\Delta\theta$ around the bunch center.

3 Selection of the Deflecting Structure

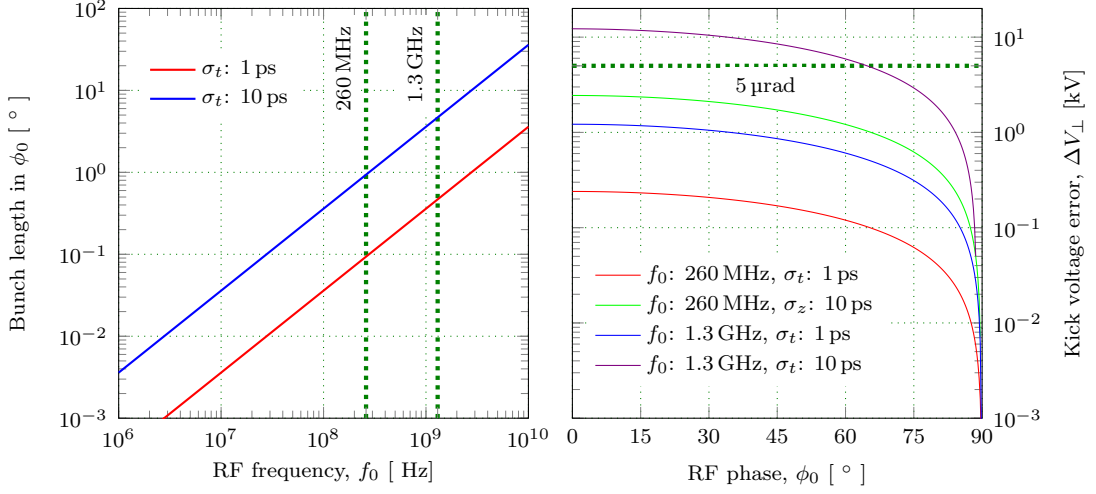


Figure 3.5: The bunch length expressed in terms of RF phase for different frequencies (left), and the transverse kick voltage error at different RF phases for the two frequencies of interest (right).

In a TCAV, the transverse voltages received by the particles at the head, tail and center of the bunch are given as

$$V_{\perp}|_{h,t} = V_{\perp} \sin \left(\phi_0 \pm \pi \frac{c\sigma_t}{\lambda_0} \right) \quad \text{and} \quad V_{\perp}|_c = V_{\perp} \sin(\phi_0), \quad (3.6)$$

where the subscripts h, t, and c denotes the particles at the head, tail, and center, and + refers to the bunch head, - to the bunch tail, σ_t the bunch length expressed in time, V_{\perp} to the peak deflecting voltage, and λ_0 to the wavelength of the resonance frequency. Thus, the transverse kick voltage error ΔV_{\perp} between the head (tail) and center of the bunch is given as

$$\Delta V_{\perp} = V_{\perp,h} - V_{\perp,c} = V_{\perp} \left(2 \cdot \cos \left(\phi_0 + \frac{\pi c\sigma_t}{2\lambda_0} \right) \cdot \sin \left(\frac{\pi c\sigma_t}{2\lambda_0} \right) \right). \quad (3.7)$$

The factor $c\sigma_t/\lambda_0$ expresses the bunch length in terms of the RF phase. Figure 3.5 shows the variation of ratio, $c\sigma_t/\lambda_0$, at different frequencies for two different σ_t . Additionally, the plot shows the kick voltage error ΔV_{\perp} at different RF phases for the frequencies of interest and the two different σ_t . A longer bunch covers a significant part of the RF phase, resulting in a higher kick voltage error than a smaller bunch at the same frequency. In addition to that, at higher frequencies, the kick voltage error is larger compared to the lower frequencies. At the zero-crossing phase, the kick

3 Selection of the Deflecting Structure

voltage error is at its maximum, and this error drops from maximum to minimum as the RF phase increases from the zero-crossing to the on-crest phase. The on-crest phase is preferable for the beam separation as it provides both the maximum kick voltage and the smallest kick voltage error.

If the bunch length is very small compared to λ_0 ($c\sigma_t/\lambda_0 \ll 1$), the sine term in (3.7) can be simplified, and the transverse voltage error reduces to

$$\Delta V_{\perp} = V_{\perp} \cos\left(\phi_0 + \frac{\pi c\sigma_t}{2\lambda_0}\right) \cdot \pi \frac{c\sigma_t}{\lambda_0}. \quad (3.8)$$

Thus, the kick angle error $\Delta\theta$ due to ΔV_{\perp} for a beam energy E_b is given as

$$\Delta\theta = \frac{\Delta V_{\perp}}{E_b} = \frac{V_{\perp}}{E_b} \cos\left(\phi_0 + \frac{\pi c\sigma_t}{2\lambda_0}\right) \frac{\pi c\sigma_t}{\lambda_0} = \theta \frac{\pi c\sigma_t}{\lambda_0} \cos\left(\phi_0 + \frac{\pi c\sigma_t}{2\lambda_0}\right). \quad (3.9)$$

The variation of kick angle errors for the different RF phases and frequencies considering a σ_t of 5 ps and a deflection angle of 3 mrad are plotted in Figure 3.6. For both the frequencies of interest, the kick angle error around the on-crest phase is lower than the maximum allowed value (5 μrad) [162]. However, at lower RF phases, the kick angle error at 1.3 GHz is larger than the maximum allowable value.

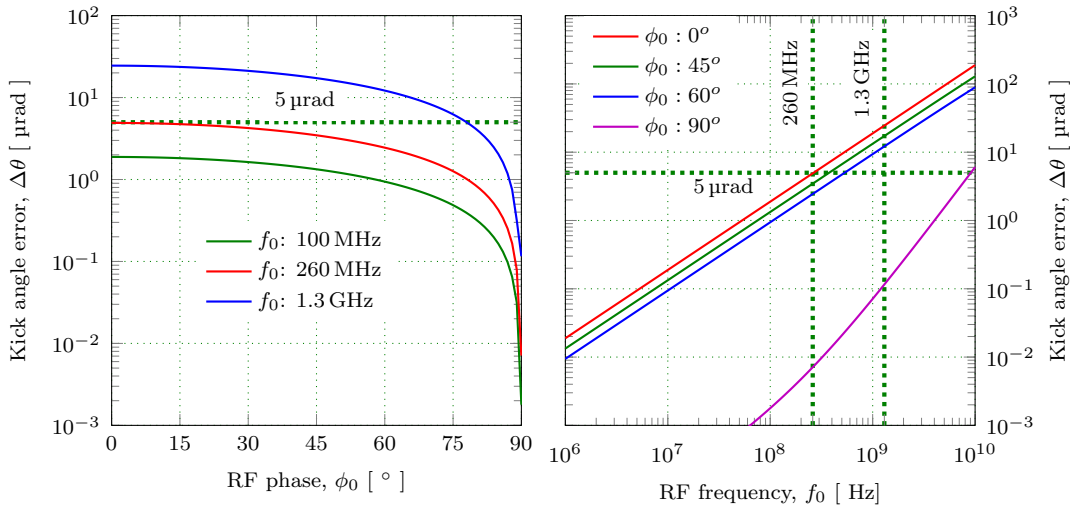


Figure 3.6: The kick angle error for different RF phases for the three frequencies (left), and variation of the kick angle error at four RF phases at different frequencies (right). A bunch length of 5 ps and the kick angle of 3 mrad is considered.

3.3.2 Projected Emittance Growth

The sinusoidal kick voltage from a TCAV delivers a non-uniform kick to the particles in a bunch, resulting in a spatial chirp. The spatial chirp of a bunch increases the projected emittance. In [163, 164], expressions for the projected emittance growth at the zero-crossing ($\phi_0 = 0$) and the on-crest ($\phi_0 = \pi/2$) phase are given as

$$\frac{\Delta\epsilon}{\epsilon_0} = \sqrt{1 + \left(\frac{2\pi\theta c\sigma_t}{\lambda}\right)^2 \frac{\beta_d\gamma}{\epsilon_N}} - 1 \quad (\phi_0 = 0) \quad (3.10)$$

$$\frac{\Delta\epsilon}{\epsilon_0} = \sqrt{1 + 32\pi^4\theta^2 \left(\frac{c\sigma_t}{\lambda}\right)^4 \frac{\beta_d\gamma}{\epsilon_N}} - 1 \quad (\phi_0 = \pi/2) \quad (3.11)$$

where $\Delta\epsilon/\epsilon_0$ is the relative emittance growth, β_d is the beta function at the deflector, γ is the Lorentz factor, and $\epsilon_N (= \gamma\epsilon_0)$ is the normalized emittance, and ϵ_0 is the geometric emittance. Interestingly, the variation of the kick voltage is linear at zero-crossing and quadratic at the on-crest phase. However, the relative emittance growth in the former is quadratic, whereas it is bi-quadratic for the latter.

An RF deflector was used to measure the bunch length [90, 91, 142], and the beam emittance growth in this case is given as

$$\frac{\Delta\epsilon}{\epsilon_0} = \sqrt{1 + \left(\frac{2\pi\theta\sigma_t}{\lambda} \sin(\Delta\psi) \cos(\phi_0)\right)^2 \frac{\beta\gamma}{\epsilon_N}} - 1 \quad , \quad (3.12)$$

where $\Delta\psi$ is the betatron phase advance from the deflector to the screen. A maximum resolution is achieved when the betatron phase advance and the RF phase are $\pi/2$ and 0, respectively. Thus, for the maximum resolution, equation (3.12) reduces to (3.10). The relative emittance growth at different RF frequencies when the bunch is deflected at the zero-crossing and on-crest is plotted in Figure 3.7, where σ_t is 2 ps, β_d is 2.5 m, beam energy is 100 MeV, θ is 3 mrad, and ϵ_N is 5 mm mrad [162]. The emittance growth is larger at the zero-crossing than the bunch kicked at on-crest, and the emittance growth at any other phase will lie between these two extremes. A maximum emittance growth of 0.1 % is allowed for on-crest kicking, and both the frequencies of interest meet this requirement.

3 Selection of the Deflecting Structure

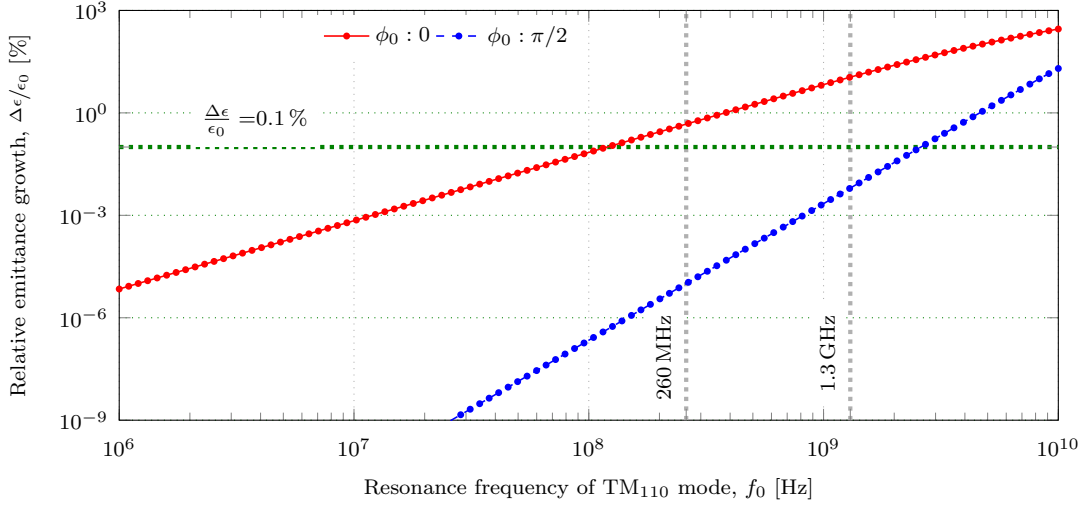


Figure 3.7: The relative projected emittance growth for different RF frequencies at the zero-crossing and the on-crest phase. Here, σ_t is 2 ps, β_d is 2.5 m, beam energy is 100 MeV, θ is 3 mrad, and ϵ_N is 5 mm mrad.

3.3.3 RF Power Loss

The particulars discussed concerning the kick angle error and emittance growth are valid for any TCAV, regardless of its shape, size, and cavity material. However, the RF power and the kick voltage homogeneity depend on the cavity geometry in addition to the resonance frequency. The numerical investigation of all the TCAV designs from the MHz to the GHz range for comparison is highly tedious and time consuming. Instead, the analytical solutions available for a pill-box cavity are used for computing the power loss and the kick voltage homogeneity at different frequencies. The first dipole mode TM_{110} of a pill-box cavity is considered as the deflecting mode. In addition, a copper cavity with a conductivity of $5.8 \times 10^7 \text{ S m}^{-1}$ is assumed. The resonance frequency of a TM_{110} mode, $f_0 = j_{1,1}c/r_c$, and the corresponding surface power loss is given as

$$P_c = \left(V_{\perp} \frac{j_{1,1} J_1'(j_{1,1})}{2\eta \sin\left(\frac{j_{1,1} l_c}{2r_c}\right)} \right)^2 \left(\frac{l_c + r_c}{r_c} \right) \left(\frac{1}{\sigma \delta} \right), \quad (3.13)$$

where $j_{1,1}$ is the first zero of the Bessel function of the first order $J_1(x)$, $J_1'(j_{1,1})$ is the value of the first derivative of the Bessel function of the first order at $j_{1,1}$, r_c and σ are the radius and the electrical conductivity of the cavity, V_{\perp} is the transverse voltage

3 Selection of the Deflecting Structure

delivered by the cavity or a cell, η is the wave impedance, and l_c is the length of the cavity or a cell. The length of the cavity and cells are set to $\lambda/2$ to maximize the achievable kick voltage. Another important factor is the average surface power loss density, S_{av} , which is the ratio of P_c to the total cavity surface area. This parameter determines the complexity of the thermal management system required to remove heat from the cavity.

The surface power loss at different frequencies are obtained for the two different type of cavities: a single-cell cavity of length $\lambda/2$ and a multi-cell cavity of length 1 m. The resonance frequency is modified in both cavities by changing the cavity (cell) radius. Figure 3.8 shows the power loss and the average power loss density at various resonance frequencies for a single-cell cavity to deliver a V_{\perp} of 300 kV. The RF power loss increases with increase in the cavity resonance frequency and

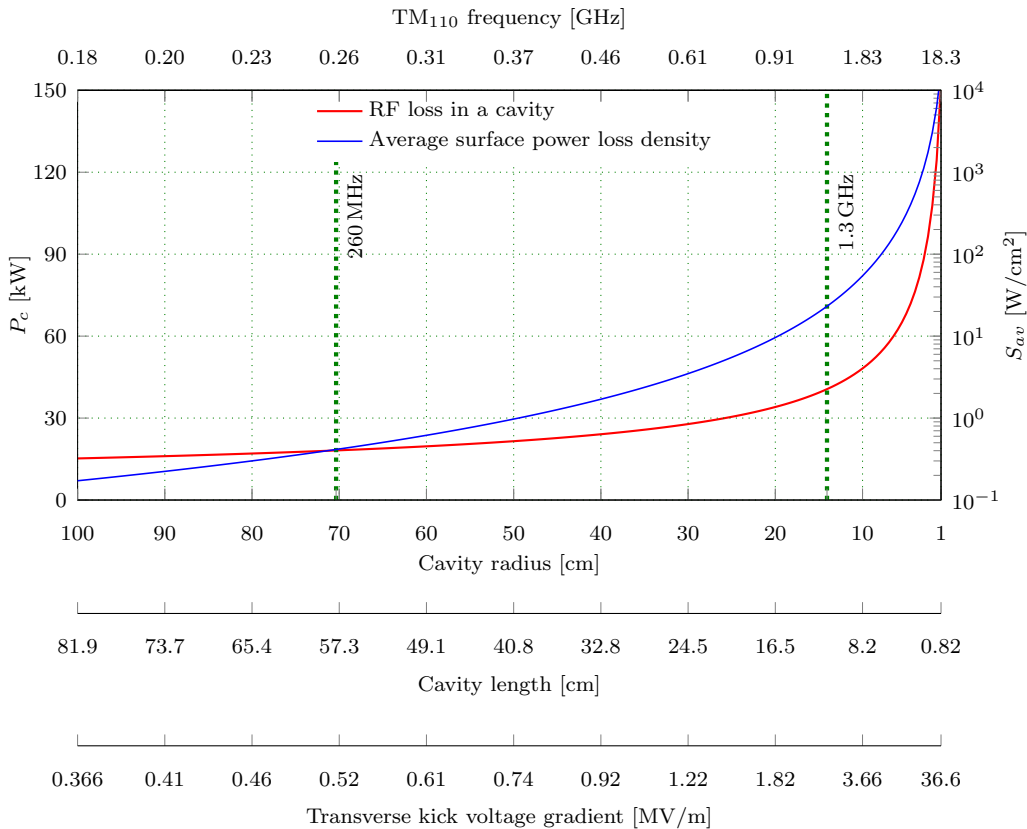


Figure 3.8: The surface power loss and average surface power loss density in the single-cell pill-box cavity which delivers a V_{\perp} of 300 kV.

3 Selection of the Deflecting Structure

the loss is proportional to the square root of the frequency. Furthermore, at higher frequencies, the average surface loss density increases due to the reduction in the cavity size. The kick voltage gradient is also larger due to the shorter cavity. A high gradient cavity, as one might expect, has a larger power loss. A fair assessment of power loss with regard to different frequencies can be performed using multi-cell cavities for a constant kick voltage gradient.

The RF power loss at various frequencies for the multi-cell cavity with a length of 1 m and a kick voltage gradient of 300 kV/m is plotted in Figure 3.9. Contrary to the single-cell cavity, both the cell losses and the total losses in a multi-cell cavity decrease with increasing frequency. The total power loss in a cavity is inversely proportional to the square root of the resonance frequency. However, the average power loss density in a multi-cell cavity behaves similarly to that of a single cell cavity due to a decrease in the cell size at higher frequencies.

From equation (2.50), it is evident that the power loss in a cavity is proportional

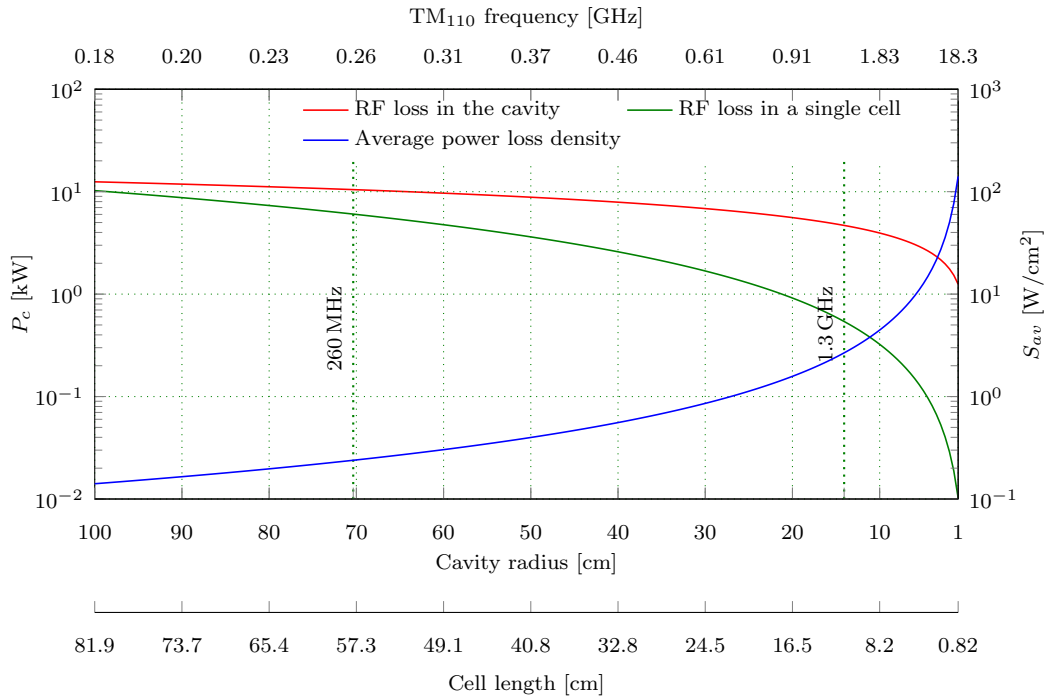


Figure 3.9: RF power loss per cell, total power loss in a multi-cell cavity, and the average surface loss density at various frequencies for the multi-cell pill-box cavity with a length of 1 m and a kick voltage gradient of 300 kV/m.

3 Selection of the Deflecting Structure

to the squared magnetic field strength, surface resistance, and cavity surface area. The surface resistance is directly proportional to the square root of the frequency. In a single-cell cavity, the field strength varies proportionally with the frequency to achieve a desired transverse voltage, whereas the surface area is inversely proportional to the square of the frequency. Consequently, the power loss in a single-cell cavity exhibits a square root relationship with the frequency. Conversely, in a multi-cell cavity, the field strength remains constant across all cells regardless of the frequency, and the surface area is inversely proportional to the frequency. As a result, the power loss in a single-cell cavity becomes inversely proportional to the square root of the frequency.

3.3.4 Kick Voltage Homogeneity

A uniform field along the cavity axis would provide the same transverse kick to both the on and off-axis beam. A circular region around the cavity axis is defined as a good field region, where the variation of the kick voltage error is within the limits. In the present case, a minimum good field region with a radius of 5 mm and a maximum error in the kick voltage of 0.15% is specified [162]. In the vertically polarized dipole mode, TM_{110} , the transverse kick is only due to the magnetic field H_x and the transverse magnetic field distribution in the xy -plane of the cavity is

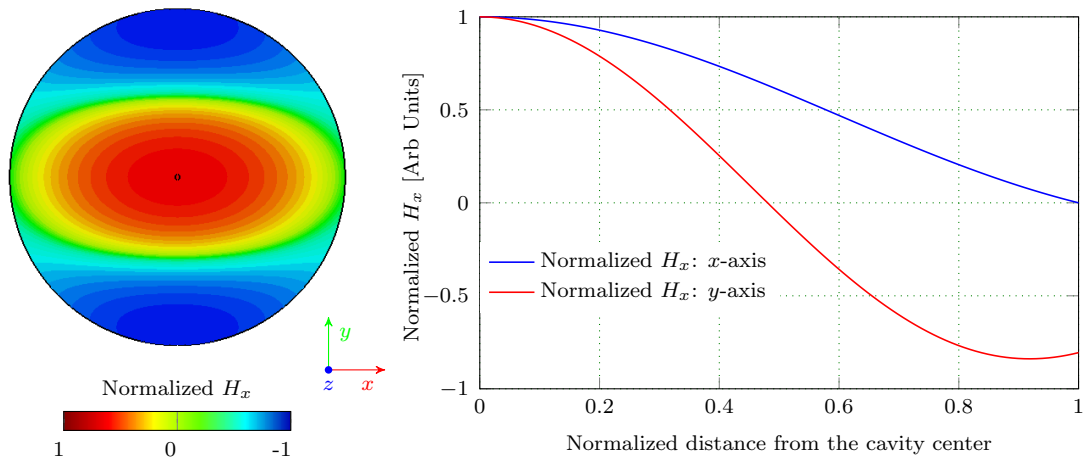


Figure 3.10: Distribution of the normalized magnetic field H_x in the xy -plane of the TM_{110} mode (left), and the normalized magnetic field H_x along the x and the y -axis (right).

3 Selection of the Deflecting Structure

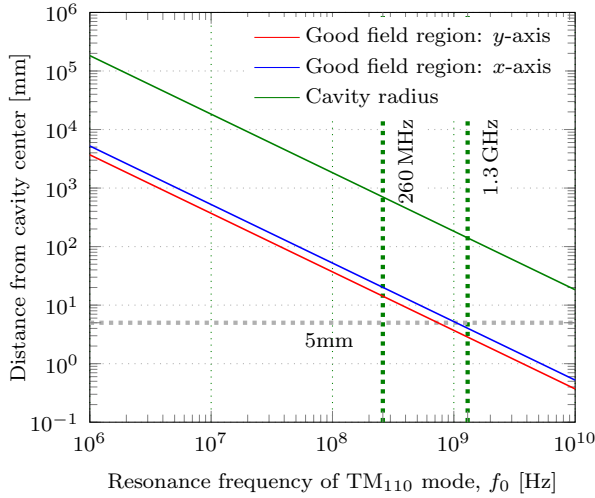


Figure 3.11: The radius of the good field region along the x and y -axis of a pill-box cavity for the various resonance frequencies when the cavity is operated in TM_{110} mode.

shown in Figure 3.10. Furthermore, the normalized magnetic field H_x along the x and y -axis are also plotted in Figure 3.10. The magnetic field is more uniform along the x -axis when compared to the y -axis. The radius of the good field region of a cavity at various frequencies is shown in Figure 3.11. As the frequency increases, the good field region shrinks proportionately with the cavity radius. The radius of the good field region at 260 MHz is larger than the required radius of 5 mm, whereas at 1.3 GHz, the radius is smaller than our requirement.

3.3.5 Discussion

A thorough investigation was conducted in order to determine the operating frequency of the RF cavity that will serve as a beam separator for the ELBE. Based on this study, the criteria for the selection of the cavity frequency and the corresponding values for the two frequencies of interest are listed in Table 3.9. A lower frequency helps to achieve a small kick angle error, a lower emittance growth, and a larger good field region. In addition to this, a single-cell cavity has relatively smaller surface losses at lower frequencies. A multi-cell cavity, on the other hand, requires less RF power at a high frequency than at a lower frequency. Nevertheless, the advantages of the low frequency operation outweigh the additional RF power required for a single-cell cavity. In particular, the power required for a single-cell cavity operating at a frequency of 260 MHz is just twice that of a multi-cell cavity operating at the

3 Selection of the Deflecting Structure

Table 3.9: A list of criteria for selecting the operating frequency of the TCAV and the corresponding values obtained in this section.

Parameter		Variation relative to f_0	Desired condition or value	RF frequency, f_0		Unit
				260 MHz	1.3 GHz	
Kick angle error	zero-crossing	$\propto f_0$	<5	4.9	24.5	μrad
	on-crest	$\propto f_0^2$		0.007	0.012	
Emittance growth	zero-crossing	$\propto f_0^2$	<0.1	0.45	10.9	%
	on-crest	$\propto f_0^4$		9.2μ	11.6 m	
RF power loss	single cell	$\propto \sqrt{f_0}$	low	20	45	kW
	multi-cell	$\propto \frac{1}{\sqrt{f_0}}$		9.5	4.2	
Radius of good field region	x-axis	$\propto \frac{1}{f_0}$	≥ 5	20	4	mm
	y-axis	$\propto \frac{1}{f_0}$		14	2.8	

same frequency, which is not the case for 1.3 GHz. Based on these reasons, it is clear that a low frequency cavity is suitable for the beam separation application. As a result, for the current work, the operating frequency of the RF cavity was decided to be closer to 260 MHz.

As mentioned earlier, a 2-way separation of a CW beam with a bunch rate of f_b is achievable if the frequency of the kick voltage is an odd multiple of half the bunch rate $((2n - 1)f_b/2)$. Therefore, the resonance frequency of 260 MHz is not suitable for splitting the ELBE beam as this frequency is an integer multiple of the beam rate (26 MHz). However, by shifting the frequency by ± 13 MHz, beam splitting can be easily achieved. Furthermore, the selected frequency should be compatible with different pulsing schemes specified in Table 3.10. It is evident from the table that a single frequency can not be used in all the scenarios. Nevertheless, if the cavity resonance frequency can shift by more than ± 0.5 MHz, then either 247 MHz or 273 MHz frequency can be used in most pulsing schemes. Eventually, the resonance frequency of the beam separator cavity was fixed to 273 MHz.

3 Selection of the Deflecting Structure

Table 3.10: The possible use case scenarios of the TCAV as a beam separator and dark current kicker for ELBE and DALI [162].

Use case	Pulse scheme	Possible kicker frequencies
nELBE and CBS parallel operation	100 kHz out of 200 kHz inter-spaced	..., 260.1 MHz, 260.3 MHz, ... 272.9 MHz, 273.1 MHz, ...
FEL/R111b parallel operation	13 MHz out of 26 MHz inter-spaced	..., 247 MHz, 273 MHz, ...
DALI	100 kHz out of 1 MHz	Not possible
DALI	1 MHz → 500 kHz 500 kHz	..., 260.5 MHz, 261.5 MHz, ... 272.5 MHz, 273.5 MHz, ...
Dark current kicker	100 kHz	260.1 MHz, ... , 273.1 MHz

3.4 Criteria for the Selection of a Beam Separator

Previously, the classification of the deflecting structures and their use in different applications have been discussed. Additionally, the feasibility of a pulsed magnet, a stripline kicker, and an RF cavity to be adapted as a beam separator was studied. The information acquired so far is summarized in Table 3.11, which outlines the essential criteria for the selection of a suitable deflecting structure as a beam separator. The main criteria on which the selection has to be made are: beam energy, bunch length and repetition rate, and kick voltage and its homogeneity. Another critical factor is the simplicity with which the structure can be developed and fabricated, as well as the ability to achieve a steady and reliable operation.

3.5 Identification of the Probable Cavity Designs

The next step in the beam separator design process is to short-list a few cavity designs based on the selected frequency. A pill-box cavity design was initially discussed before proceeding with the complex cavity designs presented in the literature. In a pill-box cavity, the magnetic field of TM_{110} mode oscillating at 273 MHz can be used for the

3 Selection of the Deflecting Structure

transverse kicking of the bunches. A cylindrical cavity with a radius of 670 mm and a length of 540 mm is required to obtain the dipole mode at 273 MHz. A huge cavity size will pose challenges in fabrication and installation. Moreover, the fundamental mode of this cavity is TM_{010} , which is an accelerating mode. Therefore, a lower order mode (LOM) coupler would be required to dampen the TM_{010} mode. Furthermore, due to the two orthogonal degenerative dipole modes, the unwanted mode must be separated in frequency to avoid inadvertently exciting it. All these drawbacks make a pill-box cavity unattractive for the beam separator. Furthermore, even the traveling-wave and standing-wave disc-loaded structures are not promising for the present application as the basic component of these structures, a cavity cell, is a pill-box cavity.

Table 3.11: Selection criteria for a beam separator based on the beam parameters, the kick voltage requirement, kick field homogeneity, and the ease of the design, fabrication, and CW operation of the device.

Criteria	Transverse deflecting structure				
	Beam chopper	Pulsed magnet	Stripline kicker	RF cavity	
Beam energy, E_b	$\beta < 1$	★★★★★	★★★★★	★★★☆☆	★★★☆☆
	$\beta \approx 1$	★★★☆☆	★★★★☆	★★★★★	★★★★★
Bunch rate, f_b	<kHz	★★★★★	★★★★★	★★★★★	★★★☆☆
	>kHz	★★★☆☆	★★★☆☆	★★★★☆	★★★★☆
	>MHz	★★★☆☆	★★★☆☆	★★★☆☆	★★★★★
Bunch length, σ_t	<ns	★★★☆☆	★★★☆☆	★★★☆☆	★★★★★
	>ns	★★★★★	★★★★★	★★★★★	★★★☆☆
Kick voltage, V_\perp	\leq kV	★★★★★	★★★★★	★★★★★	★★★☆☆
	>kV	★★★☆☆	★★★☆☆	★★★☆☆	★★★★★
Kick field homogeneity*		★★★★★	★★★☆☆	★★★★★	★★★★☆
Structure development†		★★★★★	★★★☆☆	★★★☆☆	★★★★★

* Temporal and spatial kick voltage homogeneity.

† Ease of design, fabrication, and stable and reliable operation of the structure.

3 Selection of the Deflecting Structure

A TEM cavity can partially circumvent the challenges posed by a pill-box cavity. The list of TEM-class deflecting cavities given in Table 3.8 can be considered for the present work. A multi-harmonic cavity system can be designed based on the system proposed for JELIC [110]. Further, the system will provide flat-top pulses for uniform kicking. However, frequency tuning of multiple harmonic modes of a cavity is very complex. In this case, even though the cavities are small, a set of cavities makes the beam separator system complex. Furthermore, the cavities are asymmetric, and the geometry needs to be optimized to cancel the longitudinal kick. Therefore, the multi-harmonic cavity design was not preferred for the present application.

The 4-rod TEM-class cavity is compact, and a set of cavities are used as a beam separator at CEBAF [158, 159]. Further, a similar cavity design was considered as a potential beam separator for a beam distribution scheme [38]. Therefore, this cavity design was considered one of the probable cavity designs.

In LHC, a set of crab cavities was proposed to increase the luminosity using a crabbing scheme given by Palmer. An in-depth study of the different TCAV designs was carried out, and three superconducting crab cavity designs were selected [165–167]. These cavity options include an optimized 4-rod cavity [165], an RF-dipole cavity [166], and a double-quarter-wave cavity [167]. The geometry of these superconducting cavities is compact, and they are optimized to achieve a high transverse voltage and low surface fields. Though these cavities are not designed for room temperature operation, the special features of these crab cavities make them a potential candidate for the beam separator.

The geometry of a superconducting cavity has more significant constraints due to the surface fields compared to a cavity operating at room temperature. Therefore, a novel normal conducting deflecting cavity design was proposed in [157] and it is based on the crab cavity design discussed in [166]. It was reported that the proposed cavity has a high transverse shunt impedance, low surface power loss, and good kick field homogeneity. Furthermore, the cavity has a compact shape even at a low frequency. Therefore, this optimistic cavity design has been included as the probable cavity design for a beam separator.

A comparison of the probable cavity designs and final cavity selection is discussed in the next chapter.

4 Scaling, Adaptation, and Comparison of the Probable Cavity Designs

Deflecting structures are common in particle accelerators, and they were examined in the preceding chapter. Based on this review, the RF cavity emerged as a strong contender for beam separation at ELBE due to its uniform kick voltage, good phase stability, and ease of operation in CW mode even at higher frequencies. In addition to the review, the selection of the cavity operating frequency as 273 MHz was described, and six cavity designs that are easily scalable to the target frequency were identified. This chapter discusses the scaling and adaptation of these possible cavity designs to the current requirements, and the figures of merit (FOM) are compared to choose a suitable cavity for the present work.

4.1 Cavity Requirements

The primary focus of the beam separator development is on the future accelerator project, DALI. However, to test and validate the efficacy of the structure, it should also be compatible with the existing accelerator, ELBE. The main requirements of the TCAV considered in this work are listed in Table 4.1. The TCAV should be compact, and its aperture must be confined to the range of equipment currently utilized in the ELBE. In the previous chapter, the transverse voltage, error in the deflection angle, kick field homogeneity, and operating frequency requirements of the cavity were discussed. The RF power loss in a cavity and the peak surface power loss density are the two other critical factors of the cavity, as these parameters decide on the cooling and RF power requirement for a normal conducting cavity. A conservative value of less than 5 kW and 2 W/cm² has been specified for the total RF power loss and peak surface power loss density [168]. Moreover, the peak surface

4 Scaling, Adaptation, and Comparison of the Probable Cavity Designs

Table 4.1: Main requirements of the TCAV being developed as a beam separator for the ELBE and the DALI.

Cavity parameters	Symbol	Value	Unit
Cavity size	$l_c \times w_c \times h_c$	$500 \times 300 \times 500$	mm
Aperture	v_{ap}	≈ 30	mm
RF frequency	f_0	273	MHz
Minimum frequency tuning range	$\pm \Delta f_{tr}$	± 0.75	MHz
Transverse kick voltage	V_{\perp}	300	kV
Field homogeneity	δV_{\perp}	< 0.15	%
Radius of the good field region	r_{gf}	5	mm
Required RF power	P_c	< 5	kW
Peak surface power loss density	S_{pk}	$\lesssim 2$	W/mm ²
Peak surface electric field	E_{pk}	$\lesssim 15$	MV/m

electric field should be well below the Killpatrick limit of 15 MV/m to avoid the RF breakdown at the maximum input power [37].

4.2 Cavity scaling and adaptation

The main purpose of any cavity design, whether a superconducting or normal conducting, is to reduce the RF surface losses. There are also a number of secondary goals and constraints that differ based on their operating temperature. The superconducting cavities are optimized to minimize the ratios ¹ E_{pk}/E_{\perp} and B_{pk}/E_{\perp} , in order to maximize the net deflection within the maximum electric and magnetic field achievable with the existing cryogenic technology [108]. In contrast, the constraints of the normal conducting cavity are the confinement of the peak surface electric field to below the Killpatrick limit and lowering the peak surface loss density to avoid thermal hotspots. Even though these limitations are related to lowering the surface

¹In the superconducting cavities, the design constraints are defined as E_{pk}/E_{acc} and B_{pk}/E_{acc} , where E_{pk} denotes the peak surface electric field, E_{acc} the cavity acceleration gradient, and B_{pk} the peak surface magnetic field.

4 *Scaling, Adaptation, and Comparison of the Probable Cavity Designs*

fields similar to the superconducting cavity, the room temperature cavity material does not have strict constraints. A larger electric field value than the Killpatrick limit can be achieved with better surface finishing and cavity cleaning, and an improved thermal management scheme can readily handle higher surface power loss density. On the other hand, the present cryogenic technology limits the maximum surface fields in the superconducting cavity, and the fields are already at its peak. Thus, these cavity shapes could be considered a baseline geometry for a normal conducting cavity design.

The probable TCAV designs have a different operating frequency than the targeted frequency of 273 MHz, and the resonance frequency can be shifted by suitably scaling all the dimensions of the cavity. The scaling factor is defined as the ratio of the original cavity frequency to the target frequency. Dimensions of a scaled cavity do not always satisfy all the design requirements specified in Table 4.1, and they must be altered to meet the requirements. The following sections discuss scaling and adaptation of the probable cavity designs.

4.2.1 **Adaptation of a 4-rod Cavity Design: Design I and II**

In the CEBAF accelerator, a set of 4-rod TCAV is being used to deliver the beam to the different experiment halls [105]. Moreover, this 4-rod cavity has inspired a crab cavity design required for the LHC [84]. As both these cavities have a similar field configuration in the deflecting mode, the adaptation of these cavity designs (Design I and II) are discussed together. A 4-rod cavity is a TEM coaxial resonator in which - as the name implies - two pairs of parallel rods are attached to both flat ends of a pill-box cavity (Figure 4.1). Each rod acts as a $\lambda/4$ resonator in this cavity, and there are four fundamental eigenmodes in addition to an infinite number of HOM. Mode 1 and mode 3 are the accelerating modes, whereas mode 2 and mode 4 are the deflecting modes. Furthermore, the electric and the magnetic fields are confined densely near the rods compared to the outer cavity regions (Figure 4.1).

Among the four fundamental modes, mode 2 is of interest for the bunches' transverse kicking. In mode 2, the transverse electric field gets concentrated in the gap between the parallel rods (Figure 4.2a), whereas the magnetic field clusters at the rod end attached to the cavity (Figure 4.2b), resulting in a higher surface loss in

4 Scaling, Adaptation, and Comparison of the Probable Cavity Designs

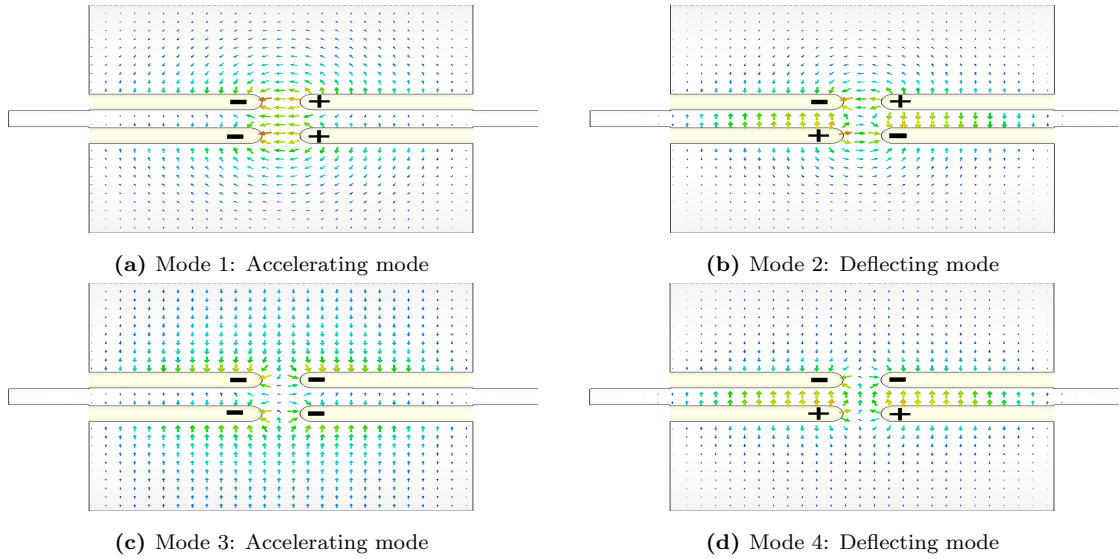


Figure 4.1: Illustration of the electric field distribution in the four fundamental modes of a 4-rod cavity.

this region (Figure 4.2c). Figure 4.3 shows the electric and magnetic field profile, and the corresponding instantaneous force experienced by an electron while moving along the cavity axis. In the deflecting mode, both the fields exert a transverse force along the same direction resulting in a net kick along the vertical plane.

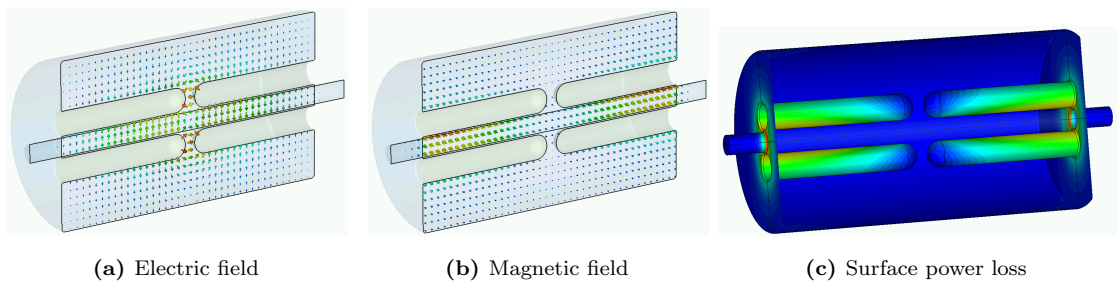


Figure 4.2: Distribution of the electric (a) and the magnetic field (b) in the deflecting mode (Mode 2) on the longitudinal cross section of the 4-rod cavity, and (c) shows the corresponding surface power loss distribution. The red and blue colors represent the maximum and minimum magnitude of a parameter.

4 Scaling, Adaptation, and Comparison of the Probable Cavity Designs

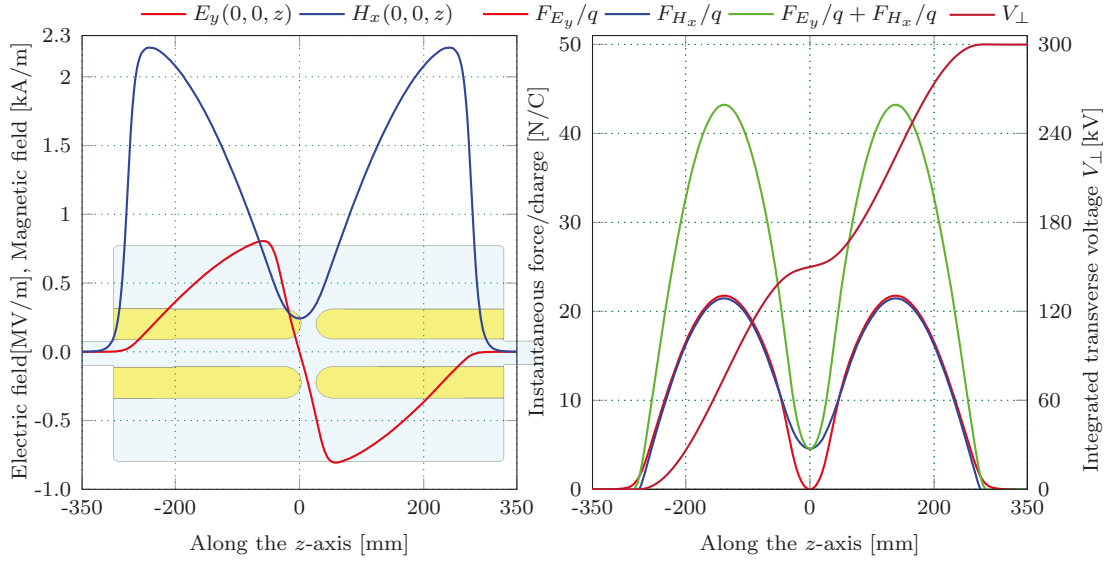


Figure 4.3: The transverse electric and magnetic fields along the beam axis of a 4-rod TCAV (left), and the instantaneous transverse force due to the electric field, magnetic field, and both the fields (right). Also shows the development of the transverse voltage along the cavity.

4.2.1.1 Design I: Adaptation of the CEBAF Cavity

A basic geometry of a 4-rod cavity is shown in Figure 4.4 with the main parameters labeled, and the corresponding values are listed in Table 4.2. The deflecting mode of the original cavity is at 499 MHz and its dimensions were scaled by a factor of 1.827 to

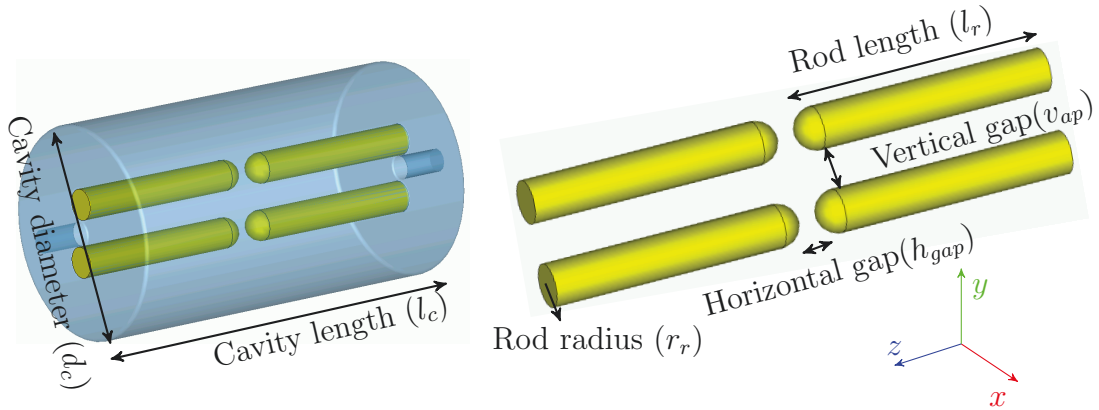


Figure 4.4: Geometry of a complete 4-rod cavity and the rods with the important geometry parameters labeled.

4 Scaling, Adaptation, and Comparison of the Probable Cavity Designs

Table 4.2: Important dimensions of the 4-rod CEBAF cavity [105, 158], the scaled cavity, and the final adapted cavity, i.e Design I. The parameters are labeled in Figure 4.4.

Cavity	Cavity dimensions				Rod properties			
	f_0	l_c	d_c	v_{ap}	r_r	v_{ap}	h_{gap}	l_r
	MHz	mm	mm	mm	mm	mm	mm	mm
Original cavity	499	300	292	15	10	35	18	142
Scaled cavity	273	548.1	533	27.4	18.25	64	32.9	259.4
Design I	273	500	270	30	20	35	20	240

shift the deflecting mode to 273 MHz. It is important to note that the scaled cavity length, diameter, and aperture fail to meet the dimensional constraints specified in Table 4.1. For this reason, the cavity geometry was adapted to meet the design requirements.

The rod geometry is crucial because the field components cluster around the rods, influencing the cavity resonance frequency and the FOM. The effect of the rod radius on the rod length and the FOM is plotted in Figure 4.5. Though the rod length determines the resonance frequency, an increase in the rod radius reduces the rod length for a fixed resonance frequency. Additionally, an increase in the rod radius

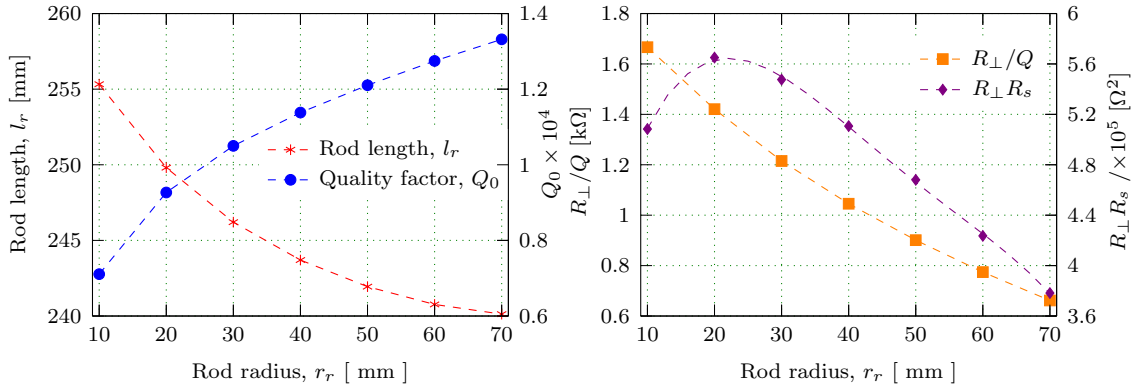


Figure 4.5: Variation of the rod length and the FOM for the different rod radii of Design I with the deflecting mode frequency fixed at 273 MHz.

4 Scaling, Adaptation, and Comparison of the Probable Cavity Designs

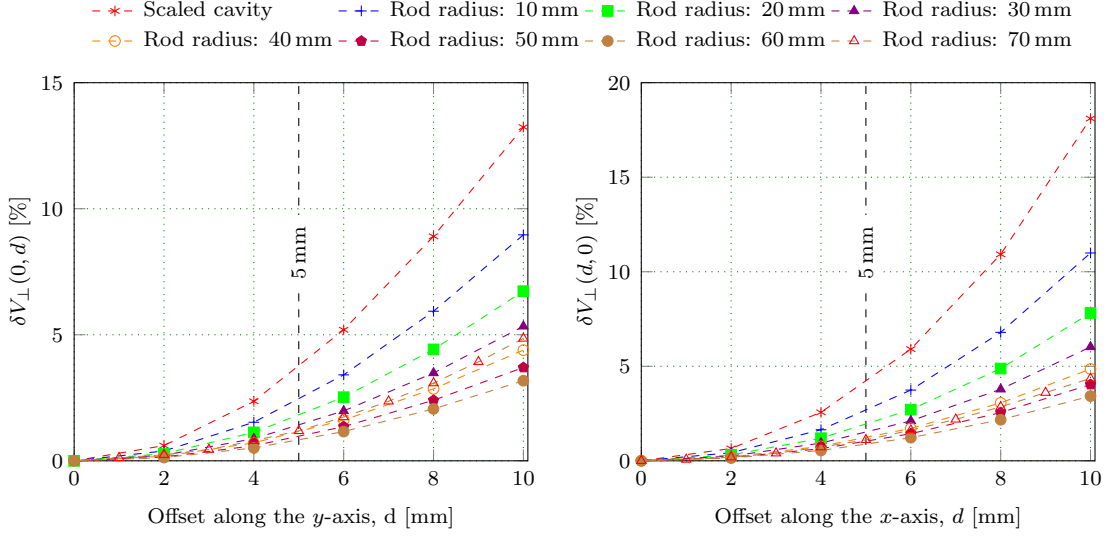


Figure 4.6: A comparison of the kick voltage homogeneity of the 4-rod scaled cavity and the Design I cavity of various rod radii. The relative kick voltage error variation along the x and y -axis are given by $\delta V_{\perp}(d, 0)$ and $\delta V_{\perp}(0, d)$, respectively.

also reduces the field strength in the cavity aperture, which in turn decreases R_{\perp}/Q . In contrast, spreading of the magnetic field on the larger rod surface increases the cavity quality factor. Altogether, $R_{\perp}R_s$ varies parabolically with the rod radius, and it is maximum when the rod radius is 20 mm. Therefore, the cavity with this rod size requires the least amount of RF power to generate a V_{\perp} of 300 kV.

In addition to the RF power loss, variation of the kick voltage homogeneity has to be analyzed. Figure 4.6 shows the variation of the kick voltage error along the x and y -axis. An increase in the rod radius distributes the electric field in the

Table 4.3: FOM of the scaled 4-rod CEBAF cavity and the adapted cavity, Design I, with the deflecting mode frequency fixed at 273 MHz. V_{\perp} is calculated for the total energy of 1 J in the cavity, and the P_c , S_{pk} , and E_{pk} are calculated for a V_{\perp} of 300 kV.

Parameter	V_{\perp} [MV]	R_{\perp}/Q [$10^3 \Omega$]	Q_0 -	G [Ω]	$R_{\perp}R_s$ [$10^3 \Omega^2$]	P_c [W]	E_{pk} [MV/m]	S_{pk} [W/cm ²]
Scaled cavity	2.86	4.78	11876	50.92	243.4	1589	2.65	4.82
Design I	4.75	13.16	8793	37.68	496.8	779	2.91	4.31

4 Scaling, Adaptation, and Comparison of the Probable Cavity Designs

cavity aperture, resulting in the lower kick voltage error. However, the kick voltage homogeneity falls far short of the required level. Therefore, an optimal rod radius of 20 mm was chosen for Design I. The influence of the cavity radius on the FOM was negligible, and the radius was set to 270 mm. The geometrical dimensions and the FOM of the adapted 4-rod cavity (Design I) are listed in Tables 4.2 and 4.3.

4.2.1.2 Design II: Adaptation of the 4-rod Crab Cavity

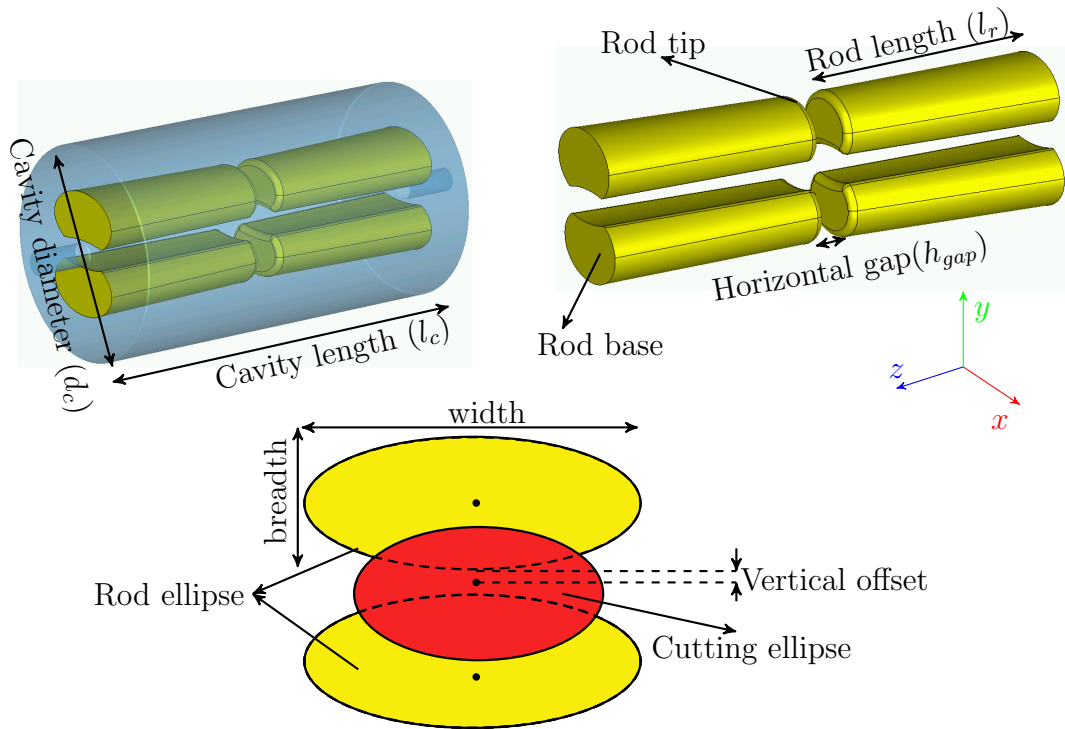


Figure 4.7: Geometry of a 4-rod crab cavity with the dimensions labeled. Also shows the construction of the kidney shaped rods with the construction ellipses (yellow) for the rods and the cutting ellipse (red) which subtracts the construction ellipse.

The crab cavity proposed in [84, 165] was one of the potential candidates for the LHC upgrade, which was inspired by the CEBAF 4-rod cavity. The main difference between these cavities is the rod geometry: instead of a rod with a circular cross-section, the crab cavity used a rod with a kidney-shaped cross-section to improve the kick voltage homogeneity. Moreover, the cross-section of the rod base and tip are different. A larger rod base area helps in spreading the magnetic field, reducing both

4 Scaling, Adaptation, and Comparison of the Probable Cavity Designs

Table 4.4: Important dimensions of the 4-rod crab cavity [165, p.10], the scaled cavity, and the final adapted cavity i.e Design II. Here, ellipse width and breadth are denoted by w and b , and the subscripts b , t and c refer to the ellipse of the rod base, rod tip, and the cutting ellipse, and the vertical offset between the construction and cutting ellipse is denoted by t_{of} . The parameters are labeled in Figure 4.7.

	Cavity				Rod base		Rod tip		Cut ellipse		offset	Gap
	f_0 MHz	l_c mm	d_c mm	v_{ap} mm	w_b mm	b_b mm	w_t mm	b_t mm	w_c mm	b_c mm	t_{of} mm	h_{gap} mm
Original	400	500.7	290	84	120	74	100	70	84	84	30	60
Scaled	273	732.2	424.1	123.1	175.5	108.2	146.3	102.4	122.9	122.9	43.9	87.8
Design II	273	500	270	30	108	67	90	63	150	35	0	20.5

the peak magnetic field and the RF losses. At the same time, a smaller cross-section of the rod tip concentrates the electric field in the gap region to achieve a higher kick voltage. Figure 4.7 shows the geometry of Design II with kidney-shaped rods and the corresponding values are presented in Table 4.4. Please refer to [165] for additional information on the construction of the rod geometry.

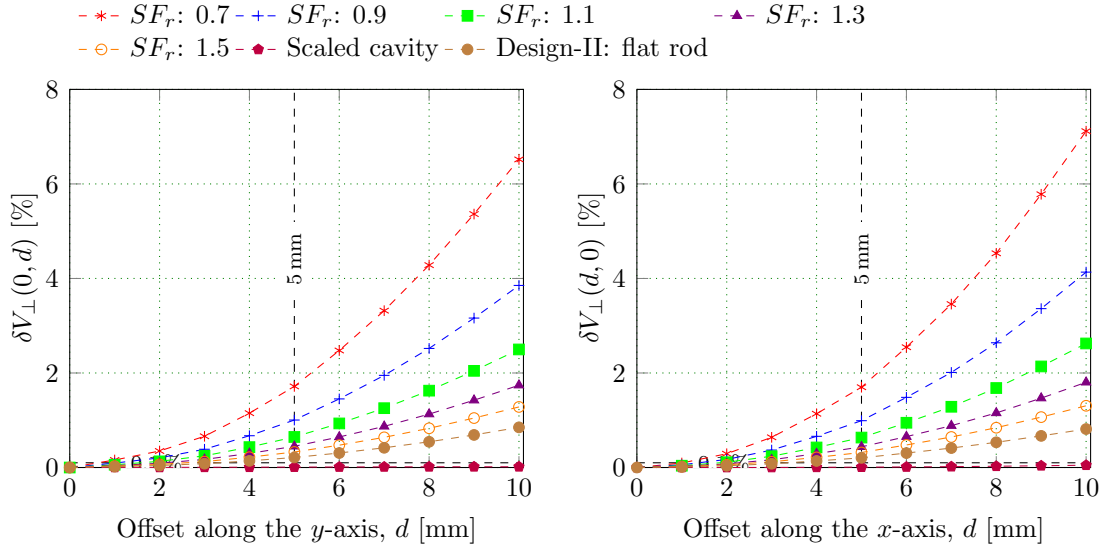


Figure 4.8: Comparison of the kick voltage homogeneity of the scaled kidney-shaped rods and the flat rods. The relative kick voltage error variation along the x and y -axis are given by $\delta V_{\perp,(x,0)}$ and $\delta V_{\perp}(0, d)$, respectively. The scaled cavity values are multiplied by a factor of 10 for better visual representation.

4 Scaling, Adaptation, and Comparison of the Probable Cavity Designs

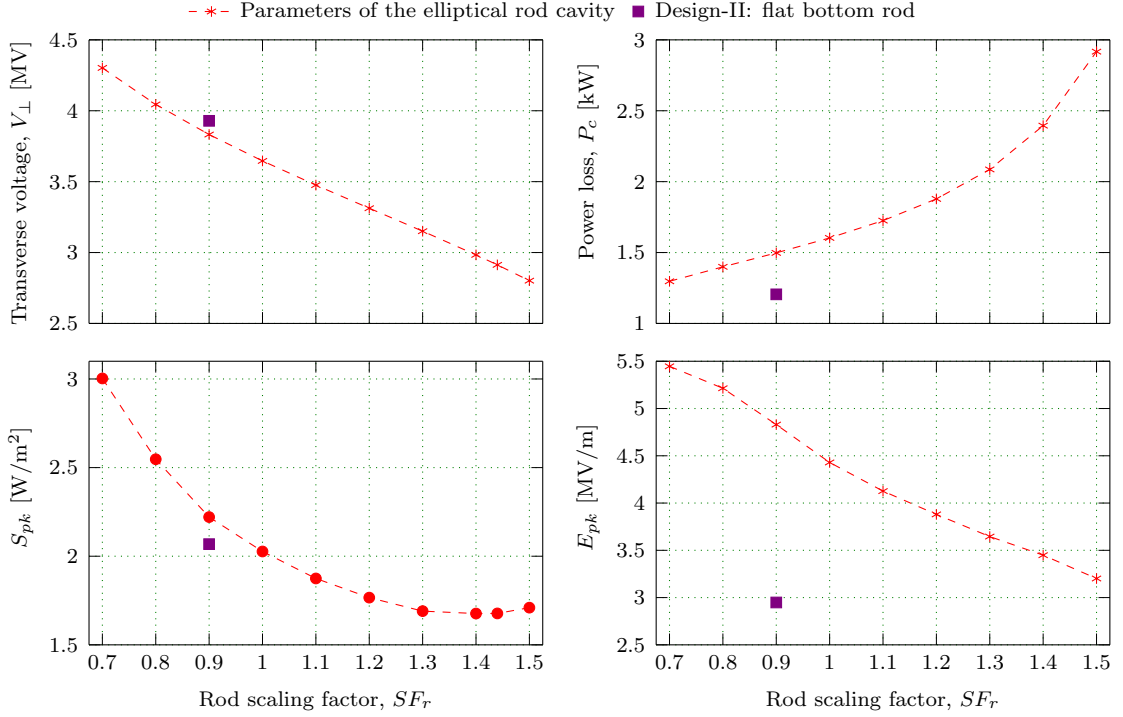


Figure 4.9: FOM for different sizes of kidney-shaped rods and flat rods. V_{\perp} is calculated for the total energy of 1 J in the cavity, and the P_c , S_{pk} , and E_{pk} are calculated for a V_{\perp} of 300 kV.

The operating frequency of the crab cavity is 400 MHz, and the cavity dimensions were scaled by 1.465 to shift the deflecting mode frequency to 273 MHz (Table 4.4). The kidney-shaped rods focus the electric field on the cavity axis, and its effectiveness in the scaled cavity can be seen in the kick voltage homogeneity (Figure 4.8). However, a larger aperture scaled cavity requires higher RF power. When adapting the scaled cavity to meet the requirements it became apparent that the rods would be humongous compared to the cavity size. Moreover, at a lower cavity aperture, a kidney-shaped rod worsens the kick voltage homogeneity. Therefore, only the rods were scaled by a scaling factor (SF_r) from 0.7 to 1.5 to determine the variation of the kick voltage homogeneity and the FOM (Figures 4.8 and 4.9).

An increase in the rod size improves the kick voltage homogeneity but increases the RF power loss. Nevertheless, the kick voltage homogeneity obtained by scaling the rod is poorer than that obtained by the scaling of the crab cavity. Therefore, a flatter rod was preferred for a smaller cavity aperture, and this was achieved by increasing the width of the cutting ellipse of the rod (w_c). The FOM and the kick

4 Scaling, Adaptation, and Comparison of the Probable Cavity Designs

Table 4.5: FOM of the scaled 4-rod crab cavity and its adapted cavity, Design II, with the deflecting mode frequency at 273 MHz. V_{\perp} is calculated for the total energy of 1 J in the cavity, and the P_c , S_{pk} , and E_{pk} are calculated for a V_{\perp} of 300 kV.

Parameter	V_{\perp} [MV]	R_{\perp}/Q [$10^3 \Omega$]	Q_0 -	G [Ω]	$R_{\perp}R_s$ [$10^3 \Omega^2$]	P_c [W]	E_{pk} [MV/m]	S_{pk} [W/cm ²]
Scaled cavity	1.34	1.05	15457	66.06	69.37	5574	2.18	3.11
Design II	3.93	8.99	8309	35.69	320.94	1205	2.07	2.95

voltage homogeneity for a flat rod cavity, Design II, are presented in Table 4.5 and Figure 4.8.

4.2.2 Design III and IV: Adaptation of the RF-dipole Crab Cavity

A compact TCAV based on two parallel rods was proposed in [169]. Here, the parallel rods were positioned perpendicular to the cavity axis and each rod acts as a $\lambda/2$ resonator. The established TEM mode is used for deflecting the particles. This cavity geometry was further optimized to match the requirements of the LHC crab cavity [166] (Figure 4.10), and a set of these crab cavities are being currently tested at the LHC [170]. In the deflecting mode of this optimized cavity, both the electric and magnetic fields contribute to the transverse kick in the same plane but in the opposite directions (Figure 4.11). However, the Lorentz force due to the electric field is greater than the magnetic field, resulting in a net transverse kick opposite to the electric field vector (Figure 4.11).

Two RF-dipole crab cavity designs that have an angled trapezoidal stem and an outer conductor with either a circular or a rectangular cross section were proposed in [33, p. 99], and are shown in Figure 4.10 with the dimensions of the original cavity listed in Table 4.6. An in-depth analysis and optimization of the cavity geometry have been discussed in [33]. Thus, only the adaptation of the cavity geometry to fulfill the current requirements is discussed.

The cavity length and aperture are set to 500 mm and 30 mm, respectively. A wider loading element generates a uniform magnetic field in the cavity aperture, resulting

4 Scaling, Adaptation, and Comparison of the Probable Cavity Designs

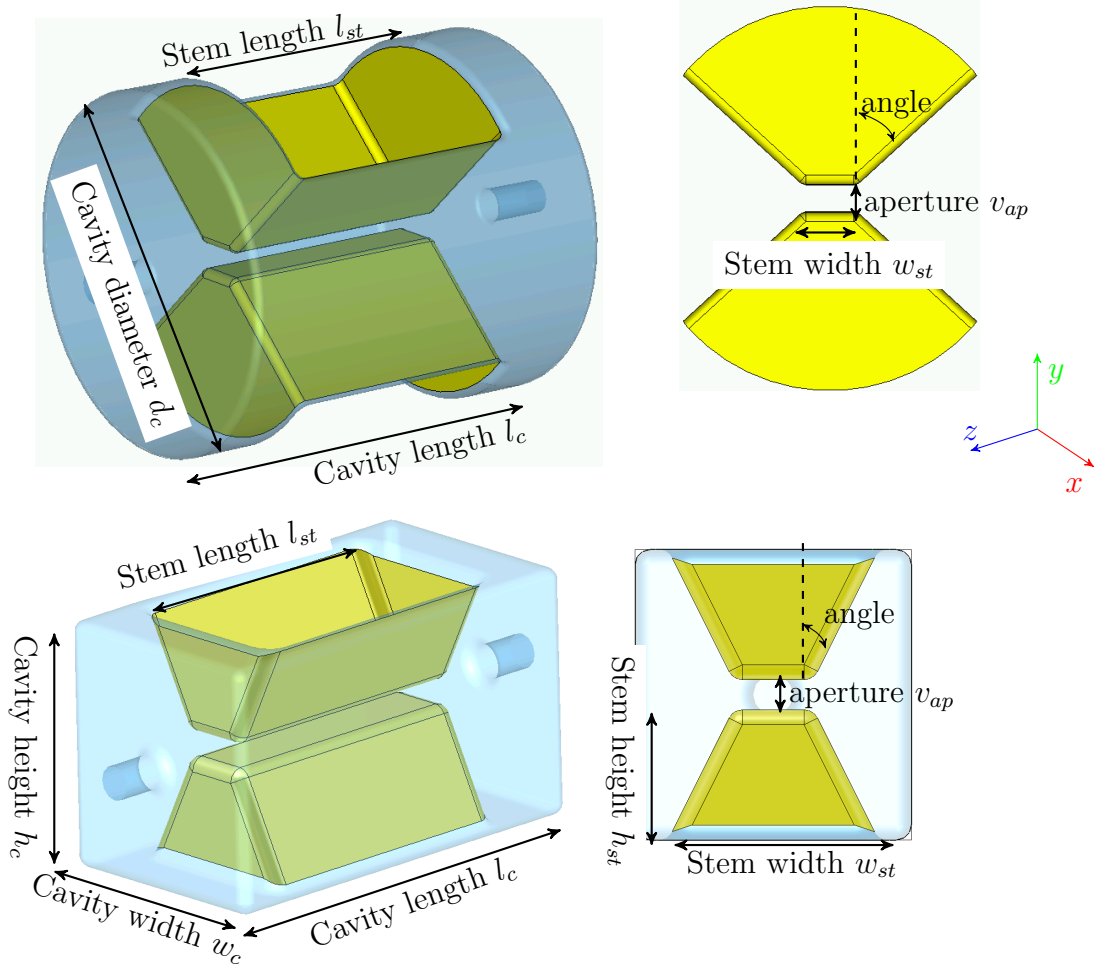


Figure 4.10: Geometries of the RF-dipole crab cavity with the circular and rectangular outer cross section discussed in [33, p.99].

in a better kick voltage homogeneity. However, this decreases the value of $R_{\perp}R_s$ and increases the RF power loss. As a compromise, the stem width of 80 mm was selected to achieve a good kick voltage homogeneity and a lower surface power loss. Moreover, the cavity's deflecting mode frequency was tuned by changing the cavity radius for the circular outer conductor and the cavity height for the rectangular outer conductor. The FOM and the kick voltage homogeneity of the scaled cavities, and the Design III and IV, are shown in Table 4.7 and Figure 4.12, respectively.

4 Scaling, Adaptation, and Comparison of the Probable Cavity Designs

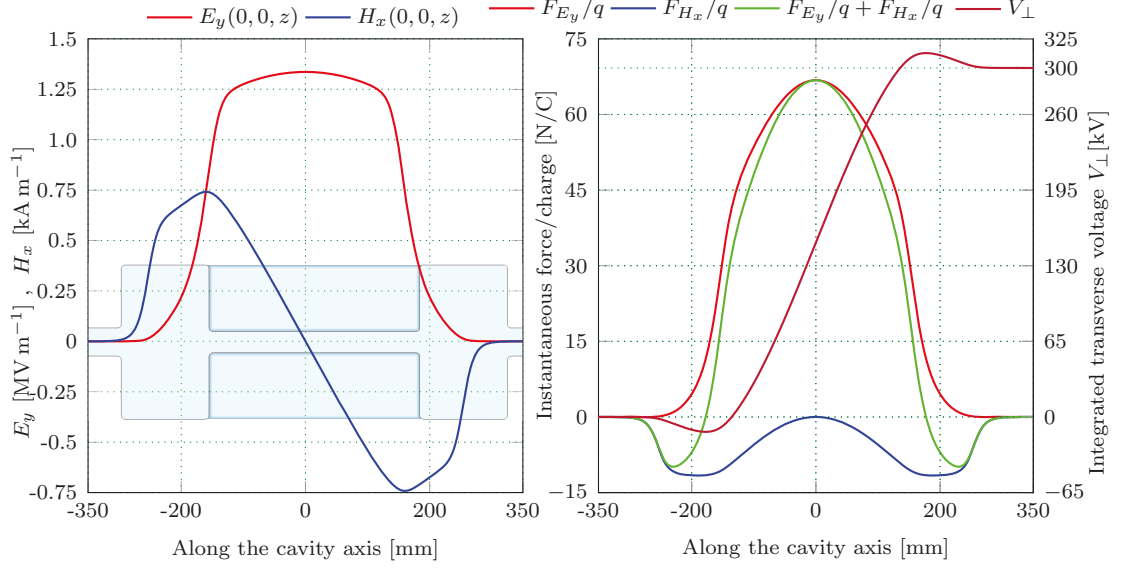


Figure 4.11: The transverse electric and magnetic fields along the beam axis of an RF-dipole TCAV (left), and the instantaneous transverse force due to the electric field, magnetic field, and both the fields (right). Also shows the development of the transverse voltage along the cavity.

Table 4.6: Important dimensions of the RF-dipole cavity having a trapezoidal stem and an outer conductor with a circular and a rectangular cross section [33], and the corresponding scaled and the adapted cavity designs (Design III and IV). The parameters are labeled in Figure 4.10.

Parameters	Circular outer cross section			Rectangular outer cross section			Unit
	Original	Scaled	Design III	Original	Scaled	Design IV	
f_0	400	273	273	400	273	273	MHz
length	527	773	500	527	773	500	mm
diameter	340	498	376	-	-	-	mm
height	-	-	-	295	437	290	mm
width	-	-	-	295	437	275	mm
aperture	84.0	123	30	84	123	30	mm
length	350	513	332	350	513	332	mm
width	80	117	80	85	124	80	mm
angle	50	50	50	30	30	30	°

4 Scaling, Adaptation, and Comparison of the Probable Cavity Designs

Table 4.7: FOM of the scaled RF-dipole cavities with a trapezoidal stem and an outer conductor of a circular and a rectangular cross section, and the corresponding adapted cavity designs, Design III and IV. V_{\perp} is calculated for the total energy of 1 J in the cavity, and the P_c , S_{pk} , and E_{pk} are calculated for a V_{\perp} of 300 kV.

Cross section	Parameters	V_{\perp}	R_{\perp}/Q	Q_0	G	$R_{\perp}R_s$	P_c	E_{pk}	S_{pk}
		[MV]	[$10^3 \Omega$]	-	[Ω]	[$10^3 \Omega^2$]	[W]	[MV/m]	[W/cm ²]
Circular	Scaled	0.77	0.35	27053	116.23	40.80	9469	2.37	2.99
	Design III	2.95	5.08	16787	72.06	365.89	1056	1.66	0.69
Rectangular	Scaled	0.88	0.45	24392	104.89	47.10	8203	2.61	1.74
	Design IV	3.14	5.74	14759	63.35	363.71	1063	1.69	0.59

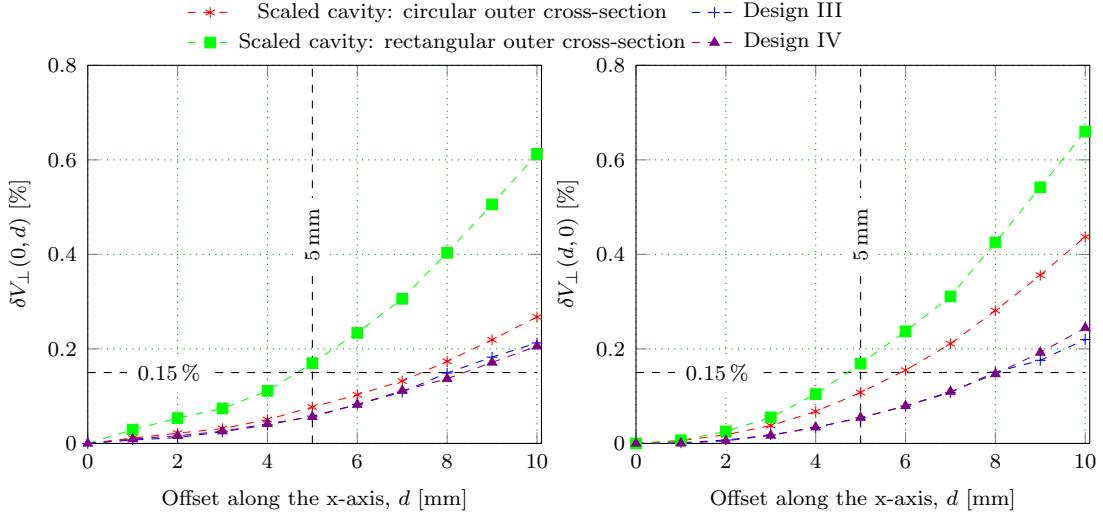


Figure 4.12: The kick voltage homogeneity of RF-dipole cavities with a circular and rectangular outside conductor, as well as the respective adapted designs, Design III and IV. The relative kick voltage error variation along the x and y -axis are given by $\delta V_{\perp}(d, 0)$ and $\delta V_{\perp}(0, d)$, respectively.

4.2.3 Design V: Adaptation of the Double-quarter-wave Crab Cavity

In addition to the 4-rod and RF-dipole crab cavity discussed above, a double-quarter wave TCAV was proposed as a crab cavity for the LHC [87, 167, 171]. The deflecting mode field configuration of this double-quarter wave cavity resembles to that of the RF-dipole crab cavity discussed before, where elliptical cross section loading elements

4 Scaling, Adaptation, and Comparison of the Probable Cavity Designs

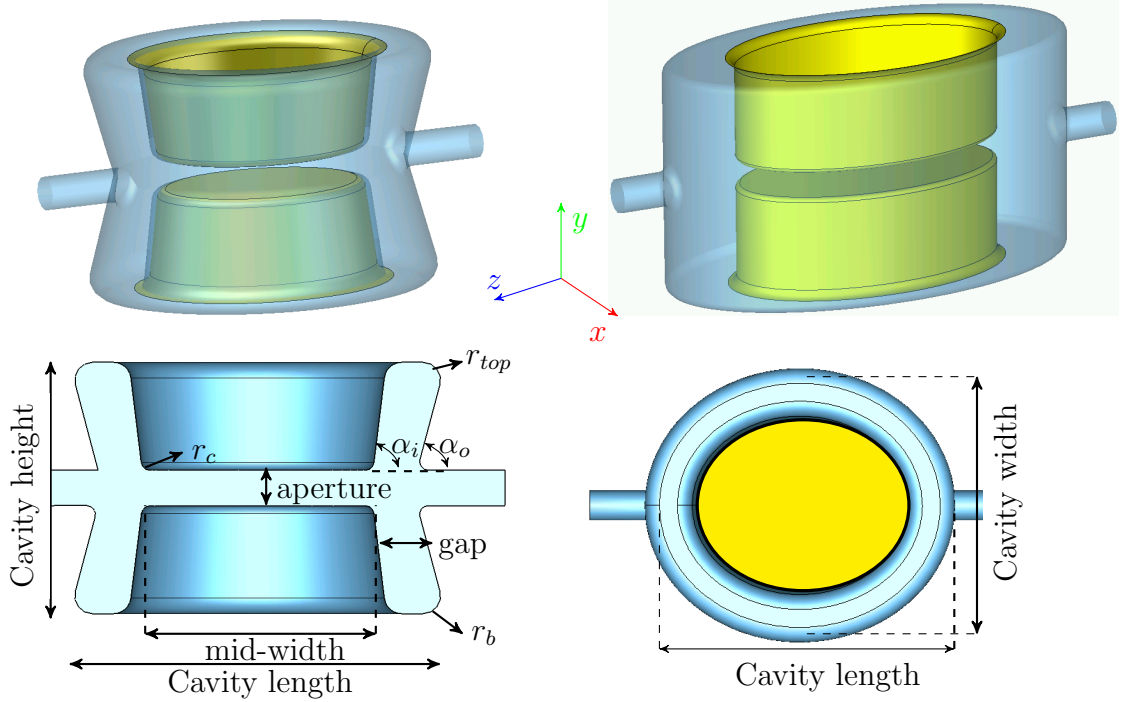


Figure 4.13: Geometrical model of a double-quarter-wave crab cavity [171], with important dimensions labeled.

are used (Figure 4.13). Space constraints at the LHC resulted in a smaller transverse size at the cavity center. Due to the lack of such constraints in the current application, a straighter outer conductor and loading elements are considered ($\alpha_i = \alpha_o = 0^\circ$). The geometry of the original and the adapted double-quarter wave cavity are shown in Figure 4.13, and the corresponding dimensions are listed in Table 4.8.

In the original double-quarter wave cavity, the ratio of the length to the width of the cavity (aspect ratio) was fixed to 1.16. A scaled cavity with the same ratio would result in a larger transverse size. The variation of the FOM and the kick voltage homogeneity for the different aspect ratios were calculated and the results are shown in Figures 4.14 and 4.15. A better kick voltage homogeneity is obtained with a lower aspect ratio due to the uniform distribution of the electric field in the cavity aperture. However, this results in a longer path for the surface currents, resulting in an increase of the surface power losses. As a compromise, an optimum aspect ratio of 1.43 was chosen, which provides a reasonable power loss, a good kick voltage homogeneity and a compact cavity. The FOM of the scaled and the adapted cavity

4 Scaling, Adaptation, and Comparison of the Probable Cavity Designs

Table 4.8: Important dimensions of the double-quarter wave crab cavity [172], the scaled cavity, and the final adapted cavity i.e. Design V. The parameters are labeled in Figure 4.13, and aspect ratio is the ratio of the cavity length to the cavity width.

Parameter	Original cavity	Scaled cavity	Design V	Unit	
f_0	400	273	273	MHz	
length	362	530.4	500	mm	
Cavity	height	394	577.3	190	mm
	width	337	493.8	350	mm
	mid-width	291	426.4	350	mm
	α_i, α_o	82,75	82,75	90,90	deg
	aperture	84	123.1	30	mm
Gap distance	60	87.9	88	mm	
Aspect ratio*	1.16	1.16	1.43	mm	
Blend r_{top}, r_b, r_c	20, 15, 20	29.3, 22, 29.3	20, 20, 20	mm	

(Design V) are given in Table 4.9.

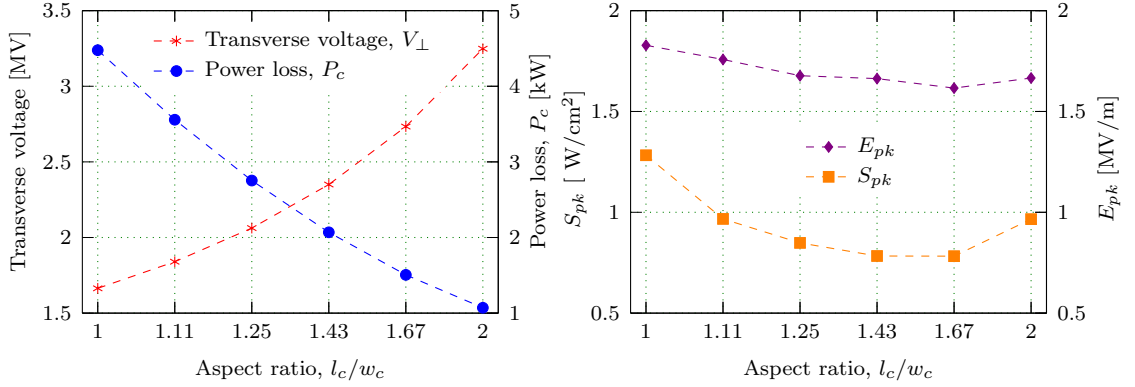


Figure 4.14: FOM for the different cavity aspect ratios (l_c/w_c) with the deflecting mode fixed at 273 MHz. The power loss, S_{pk} , and E_{pk} are calculated for the V_\perp of 300 kV. V_\perp is calculated for the total energy of 1 J in the cavity, and the P_c , S_{pk} , and E_{pk} are calculated for a V_\perp of 300 kV.

4 Scaling, Adaptation, and Comparison of the Probable Cavity Designs

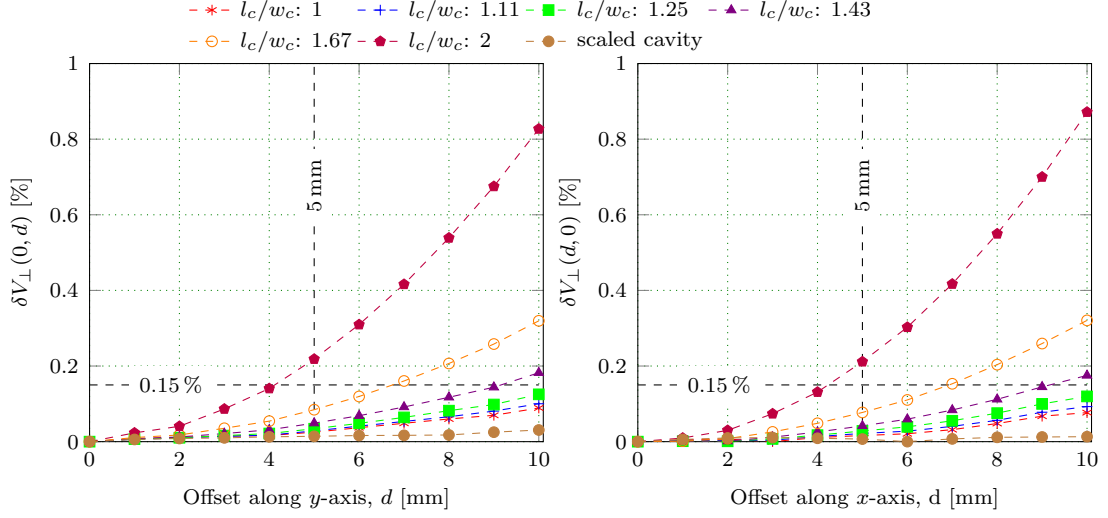


Figure 4.15: The kick voltage homogeneity of the scaled cavity, and also for the different aspect ratios (l_c/w_c) of the cavity. The relative kick voltage error along the x and y -axis are given by $\delta V_{\perp}(d, 0)$ and $\delta V_{\perp}(0, d)$, respectively.

Table 4.9: FOM of the scaled double-quarter wave crab cavity and its adapted cavity, Design V, with the deflecting mode fixed at 273 MHz. V_{\perp} is calculated for the total energy of 1 J in the cavity, and the P_c , S_{pk} , and E_{pk} are calculated for a V_{\perp} of 300 kV.

Parameter	V_{\perp} [MV]	R_{\perp}/Q [Ω]	Q_0 -	G [Ω]	$R_{\perp}R_s$ [Ω^2]	P_c [W]	E_{pk} [MV/m]	S_{pk} [W/cm ²]
Scaled	0.74	322	16413	68.34	22690	17031	2.22	2.42
Design V	2.35	3220	13519	58.03	186860	2069	1.66	0.78

4.2.4 Evolution of Design VI

In [157], a novel TCAV design operating at room temperature was proposed, and the potential use of this cavity as a beam separator has been discussed in [38]. The TCAV combines the feature of the two crab cavity designs: the outer cavity resembles the RF-dipole crab cavity and the curved stem corresponds to the double-quarter wave crab cavity. Most importantly, the free end of the loading element (stem) is extended horizontally to increase the transverse kick voltage. This modification also improves the kick voltage homogeneity and reduces the cavity height. The field distribution

4 Scaling, Adaptation, and Comparison of the Probable Cavity Designs

in this cavity is similar to that of the designs III-V, where both the electric and magnetic fields kick the beam. In contrast to other designs, the transverse force resulting from both fields is in the same direction. The proposed cavity design looks promising for an adaptation to the current work. However, at the beginning of this study the geometric data of the cavity was not available to remodel it. Moreover, in [157], results of the detailed cavity optimization steps were missing. Thus, the cavity was designed from the base design.

Version A

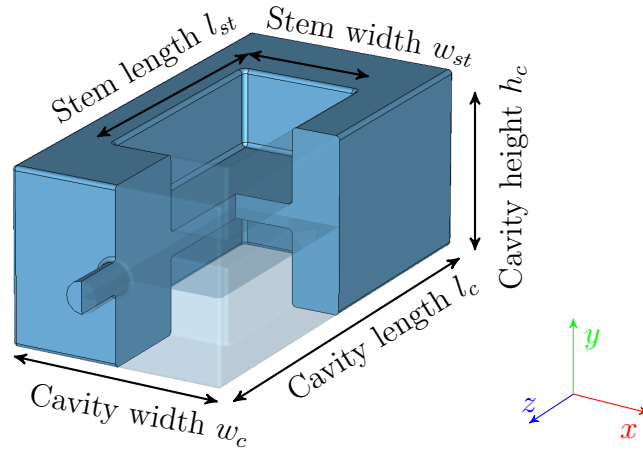


Figure 4.16: The base geometry of the TCAV with a rectangular cross-section stem and outer conductor.

The cavity with a stem and outer conductor of a rectangular cross-section was considered as a base design for this study (Figure 4.16). The stem acts as a $\lambda/4$ resonator and its geometry is a critical component of the cavity. Thus, the preliminary step of this analysis involves a study of the effect of the stem size on the FOM and the kick voltage homogeneity. The cavity height is a free parameter, which is varied to tune the resonance frequency of the cavity to 273 MHz. Other dimensions of the cavity are fixed based on the requirements specified in Table 4.1. It is indeed worth noting that, because the cavity aperture is fixed, adjusting the cavity height also impacts the stem height. Moreover, identical stems are considered to achieve a symmetric transverse field distribution in the deflecting mode and also to avoid any

4 Scaling, Adaptation, and Comparison of the Probable Cavity Designs

longitudinal voltage along the cavity axis.

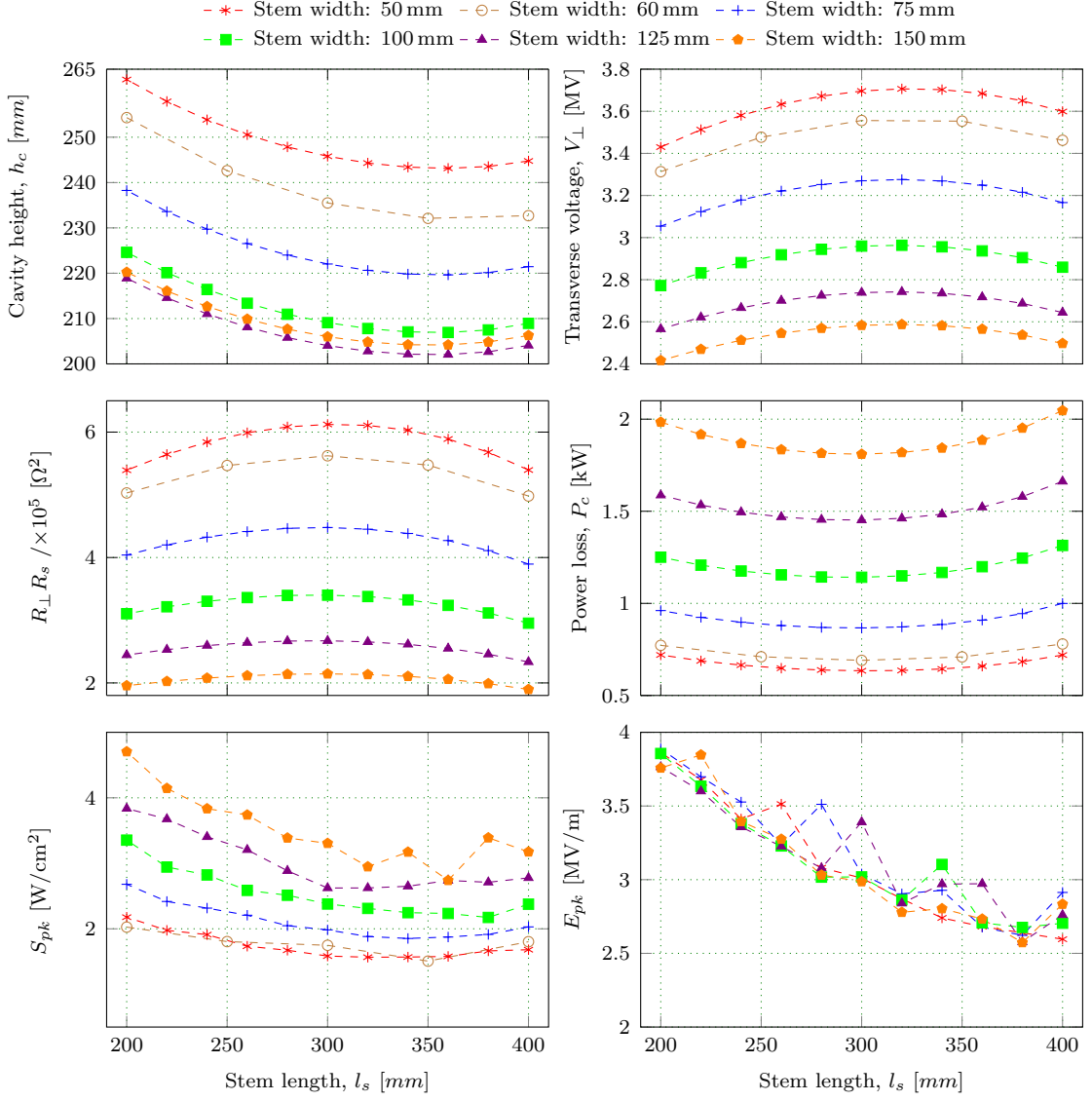


Figure 4.17: Variation of cavity height and FOM for different stem width and stem length for the deflecting mode frequency at 273 MHz. The V_{\perp} is calculated for the total energy of 1 J in the cavity, whereas the surface power loss, S_{pk} , and E_{pk} are calculated for the V_{\perp} of 300 kV.

The variation of the cavity height and the FOM for the different combinations of the stem width and length with the resonance frequency fixed at 273 MHz are shown in Figure 4.17. The stem height dictates the frequency of a $\lambda/4$ cavity. Nevertheless, the transverse size of a stem also profoundly affects the resonance frequency. Therefore, to keep the resonance frequency fixed, the stem height needs to be reduced when

4 Scaling, Adaptation, and Comparison of the Probable Cavity Designs

the stem's transverse size increases.

For a fixed energy in the cavity, increasing the stem width spreads the electric field over a larger stem area, resulting in a weaker on-axis electric field and lower V_{\perp} . In contrary, an increase in the stem length spreads the electric field along the cavity axis which increases the V_{\perp} gradually before reaching a maximum. A further increase in the stem length lowers the electric field strength and decreases the V_{\perp} . Thus, the RF surface loss varies parabolically with the stem length. Irrespective of the stem width, the power loss is minimal when the stem length is around 300 mm. In essence, the results suggest that 300 mm is the optimal stem length.

The transverse size of the stem has a profound effect on the kick voltage homogeneity. Figure 4.18 shows the kick voltage homogeneity for the different stem widths for an optimal stem length of 300 mm. A wider stem has a better kick voltage homogeneity than a narrow stem due to uniform electric field distribution in the cavity aperture. In the good field region, the maximum allowed percentage variation of δV_{\perp} is 0.15%, and the stem width larger than 60 mm satisfies the requirement. Altogether, considering both the goals - power loss and kick voltage homogeneity, the stem width and length were fixed to 60 mm and 300 mm, respectively.

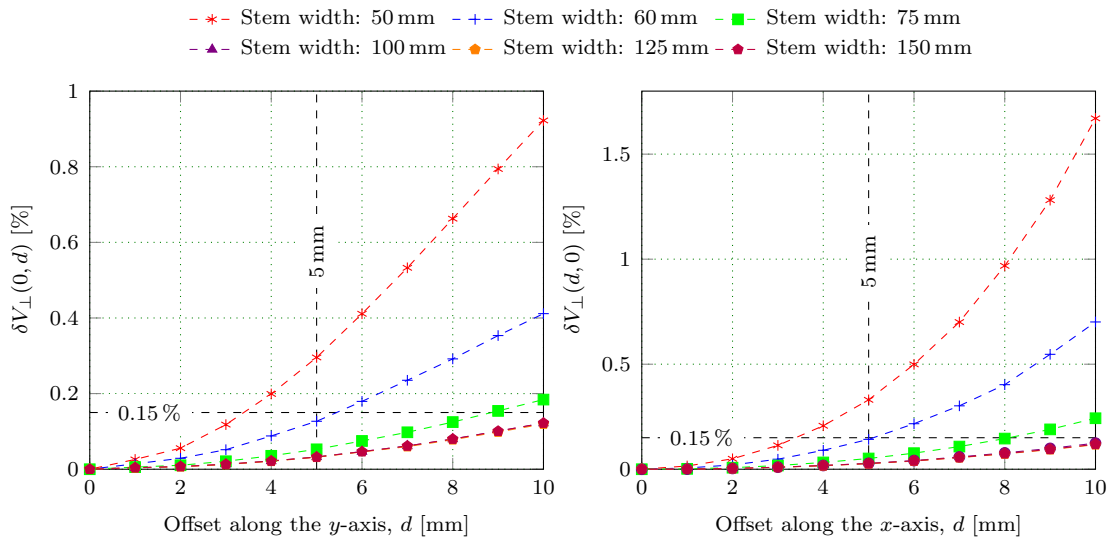


Figure 4.18: Comparison of the kick voltage homogeneity for the different stem widths with the stem length fixed at 300 mm. The relative kick voltage error along the x and y -axis are given by $\delta V_{\perp}(d, 0)$ and $\delta V_{\perp}(0, d)$, respectively.

4 Scaling, Adaptation, and Comparison of the Probable Cavity Designs

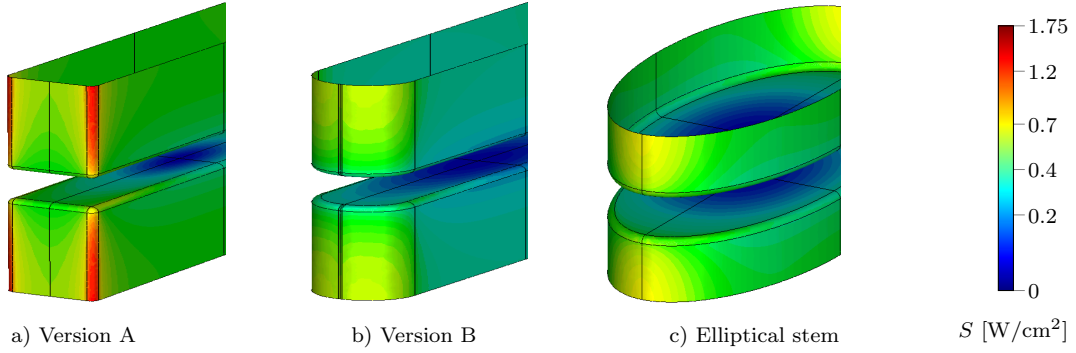


Figure 4.19: Distribution of the surface power loss density on the surface of the different cross-sectional stems.

Version B

In the version A of the cavity, the magnetic field gets concentrated on the stem's shorter edge, resulting in a higher surface power loss density (Figure 4.19 a), which in turn increases the total power loss in the cavity. Naturally, a larger blend radius at the stem's corner would redistribute the surface magnetic field on a larger stem area, resulting in a lower S_{pk} and power loss (Figure 4.19 b). To verify this, a parametric study of the stem blend radius was carried out, and the critical cavity FOM are plotted in Figure 4.20. The blending of the stem's corner has a negligible effect on the cavity height, V_{\perp} , and Q_0 . Nevertheless, the power loss decreases by 5 %

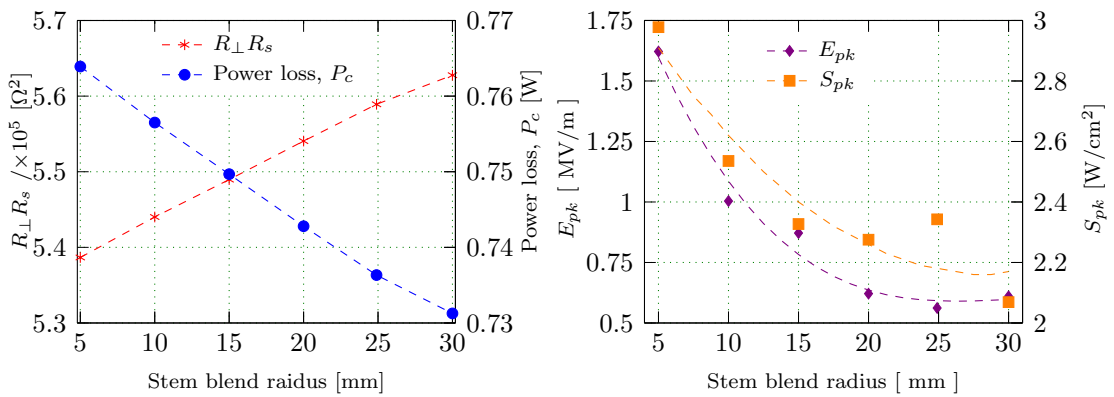


Figure 4.20: FOM of the cavity for different stem blend radii with the stem length and frequency fixed at 300 mm and 273 MHz, respectively. The power loss, S_{pk} , and E_{pk} are calculated for the V_{\perp} of 300 kV.

4 Scaling, Adaptation, and Comparison of the Probable Cavity Designs

when comparing the minimum and the maximum blending radius. At the same time, the E_{pk} is halved and S_{pk} is reduced by a 20%. As predicted, the surface current redistributes on the stem corner and the power loss density decreases (Figure 4.19 b). Thus, a stem with an oblong cross-section was selected.

As the smooth stem corner reduces the surface power loss density, this raises a question: would a stem with an elliptical cross-section (Figure 4.19 c) distribute the surface magnetic fields better and reduce the S_{pk} ? To check this, the FOM of an elliptical cross-section stem with different aspect ratios² were obtained and the results are shown in Figure 4.21. The stem length was fixed at 300 mm, and only the stem width was varied to obtain different aspect ratios. An increase in the aspect ratio increases the cavity height but decreases the surface power loss. However, this increases the strength of the surface fields due to the reduction in the stem area, increasing both the E_{pk} and S_{pk} .

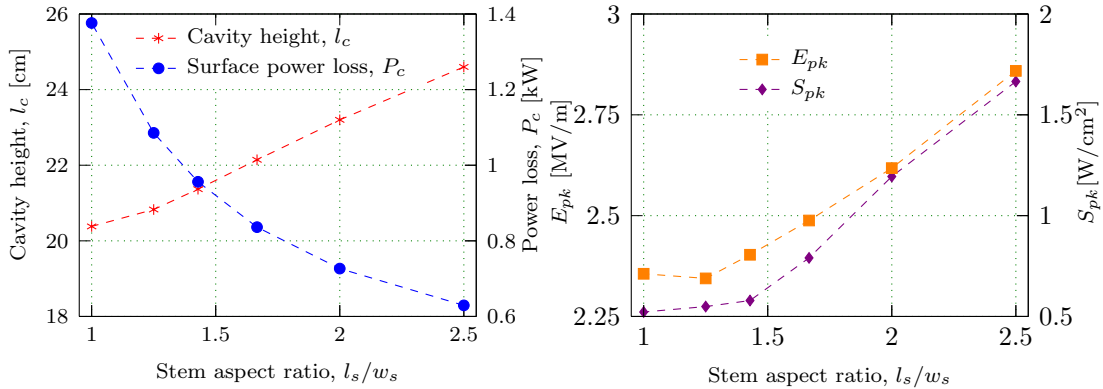


Figure 4.21: FOM of the cavity for the different stem aspect ratios with the deflecting mode frequency fixed at 273 MHz. The power loss, S_{pk} , and E_{pk} are calculated for the V_{\perp} of 300 kV.

In addition to the FOM, the kick voltage homogeneity of the cavity with different stem aspect ratios and stem blend radii were computed and the results are compared in the Figure 4.22. The stem with a smaller blend radius or with a smaller aspect ratio (circular stem) provides a better kick voltage homogeneity. However, the former has higher peak surface fields and the latter has a higher surface power loss. Even though an oblong-shaped stem has a lower kick voltage homogeneity than a circular

²Ratio of the elliptical stem's length to its width.

4 Scaling, Adaptation, and Comparison of the Probable Cavity Designs

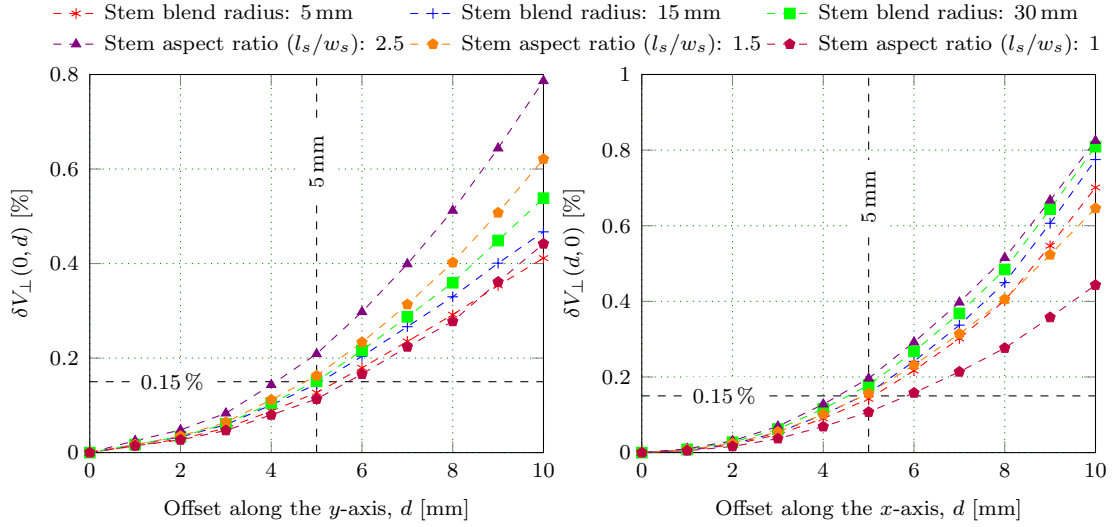


Figure 4.22: Comparison of the kick voltage homogeneity of the cavity for different stem blended radii and stem aspect ratios with the relative kick voltage error along the x and y -axis are given by $\delta V_{\perp}(d, 0)$ and $\delta V_{\perp}(0, d)$, respectively.

stem, it was selected because of a lower E_{pk} , S_{pk} , and surface power loss, as well as it meets the requirements specified for the kick voltage homogeneity.

Version C

As already mentioned, the transverse kick in this cavity is predominantly due to the strong electric field between the stems, whereas the small transverse kick due to the magnetic field opposes that to the electric field (Figure 4.11). Thus, the effective transverse kick can be enhanced by either increasing the electric field or suppressing the magnetic field, and this can be achieved by extending the stem base as shown in Figure 4.23.

The protrusion not only increases the on-axis electric field (Figure 4.24 a) but also

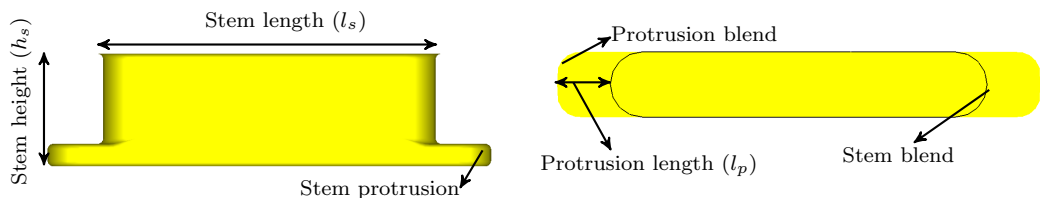


Figure 4.23: The side and top view of a stem highlighting the protrusion of the stem base.

4 Scaling, Adaptation, and Comparison of the Probable Cavity Designs

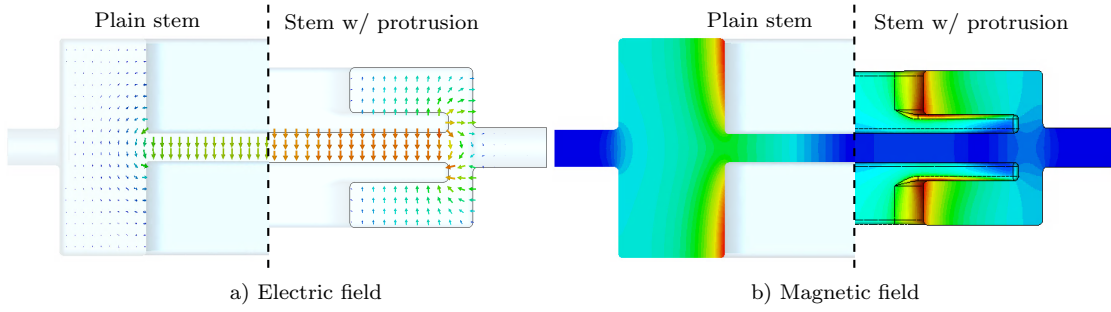


Figure 4.24: The electric and magnetic field distribution in the cavity with a plain stem and a protrusion in the stem's base. The field values refers to the total energy of 1 J in the cavity.

blocks the magnetic field from reaching the cavity axis (Figure 4.24 b). A parametric study was carried out to analyze the effect of the stem protrusion for the various stem lengths with the protrusion thickness kept at 20 mm, and the results are plotted in Figure 4.25. An increase in the protrusion length decreases the stem height required to retain the resonance frequency at 273 MHz, as the effective length of the $\lambda/2$ resonator is the combination of the stem height and the protrusion length. Moreover, the magnetic field gets concentrated due to the reduction in the stem height, resulting in a reduction of the intrinsic quality factor of the cavity and increases the S_{pk} . As expected, an increase in the protrusion length results in an increase of V_{\perp} and R_{\perp}/Q , whereas the electric field gets distributed on the larger stem area resulting in a lower E_{pk} . However, as the protrusion length increases, the gap between the outer conductor and the stem protrusion decreases and a higher electric field is observed in this region compared to the cavity aperture (Figure 4.24 a). This results in an increase of E_{pk} for a higher protrusion length. Even though the R_{\perp}/Q is higher for a longer protruded stem, the value of $R_{\perp}R_s$ and power loss vary parabolically with the protrusion length (Figure 4.25).

In addition to the FOM, the kick voltage homogeneity of the cavity with a stem length set to 300 mm and with different protrusion lengths is plotted in Figure 4.29. As predicted, the stem protrusion improves the electric field uniformity in the cavity aperture and also avoids the magnetic field, resulting in better kick voltage homogeneity. However, for a longer stem protrusion, the improvement in kick voltage homogeneity is not very significant. Further, the protrusion length above 80 mm not only increases the power loss but also increases the E_{pk} and S_{pk} (Figure 4.25).

4 Scaling, Adaptation, and Comparison of the Probable Cavity Designs

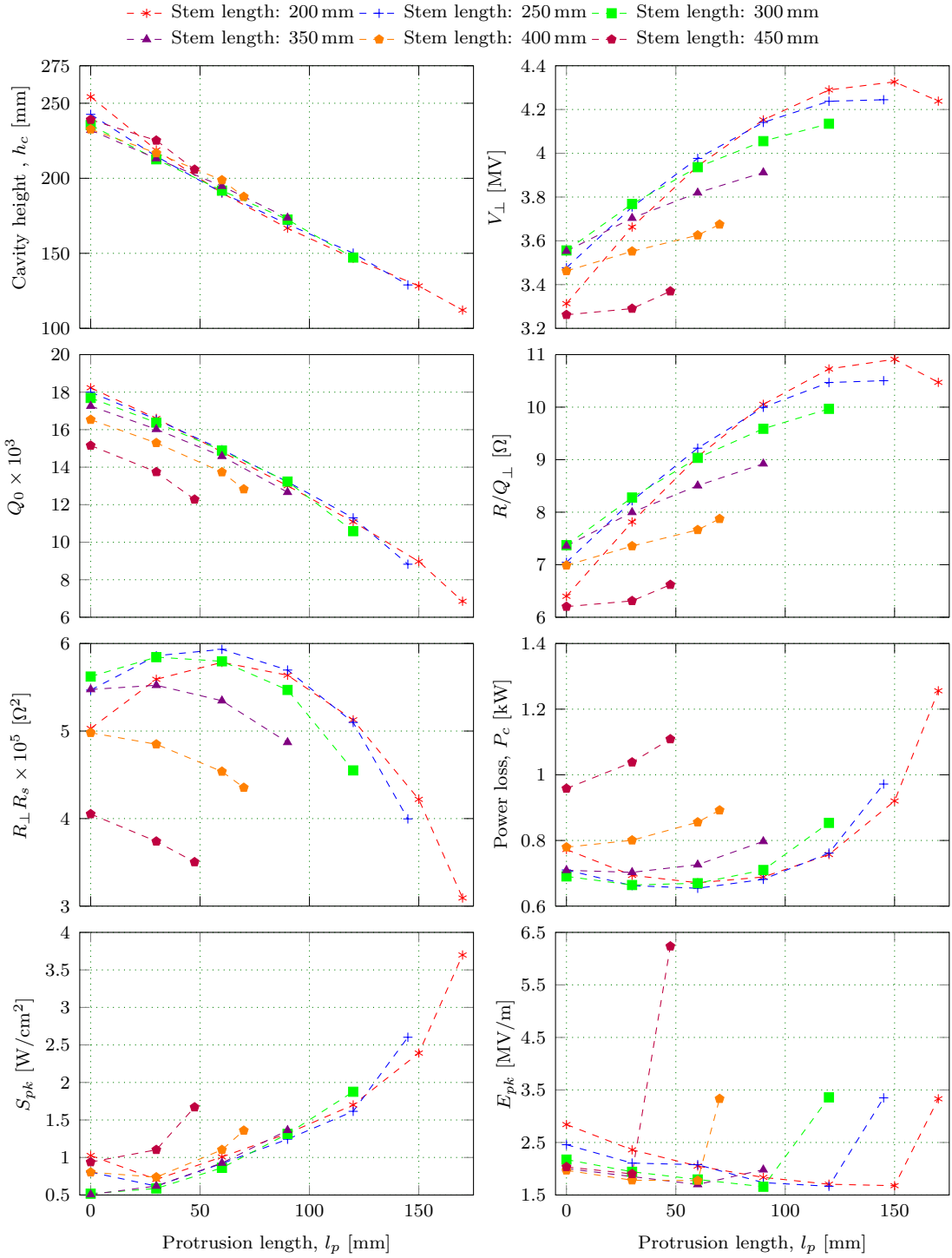


Figure 4.25: Variation of the cavity height and FOM for different stem and protrusion lengths with the deflecting mode frequency fixed at 273 MHz. The V_{\perp} is calculated for an 1 J of energy in the cavity, whereas P_c , S_{pk} and E_{pk} are calculated for a V_{\perp} of 300 kV.

4 Scaling, Adaptation, and Comparison of the Probable Cavity Designs

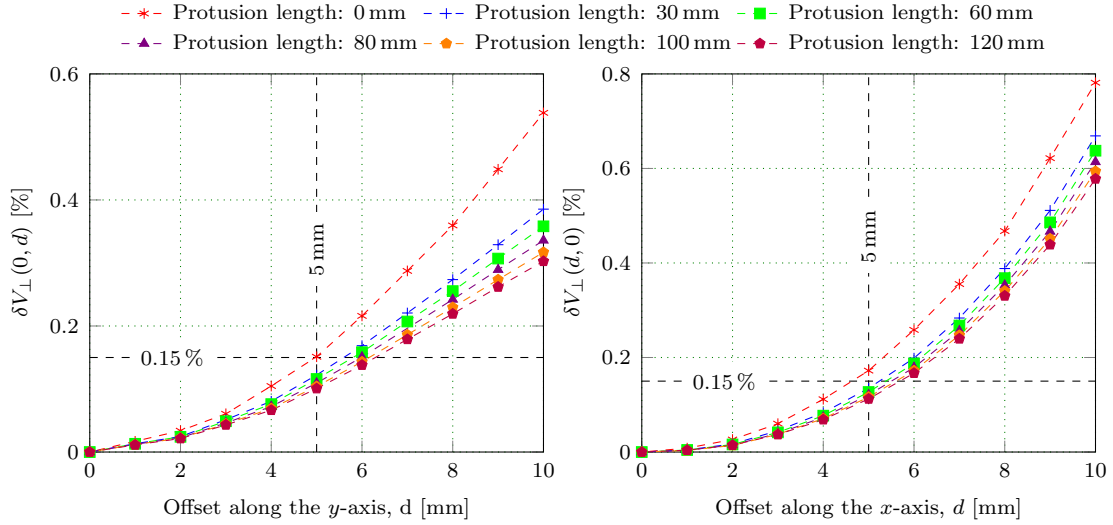


Figure 4.26: The kick voltage homogeneity for different protrusion lengths with the stem length and protrusion thickness fixed to 300 mm and 20 mm, respectively. The relative kick voltage error along the x and y -axis are given by $\delta V_{\perp}(d, 0)$ and $\delta V_{\perp}(0, d)$, respectively.

Therefore, the protrusion length of 80 mm was selected for the 300 mm stem length.

Cavity Length

The length of a cavity is usually fixed to $\approx \beta\lambda/2$ to maximize the transverse kick. However, at low frequencies, the cavity length would be significant, making cavity fabrication difficult and taking up the valuable space of an accelerator. In the present case, the cavity length is varied by scaling the geometry along the z -axis, and the FOM for different cavity lengths is plotted in Figure 4.27. The parameters, V_{\perp} and $R_{\perp}Rs$, vary parabolically with respect to the cavity length. For a cavity length of 549 mm ($\approx \lambda/2$), the required RF power to achieve a V_{\perp} of 300 kV is minimal. To meet the requirements indicated in Table 4.1, shortening the cavity length to 490 mm resulted in a marginal increase in the surface power loss of less than 3%.

Cavity Aperture

In the deflecting mode, the beam's transverse kicking is purely due to the transverse electric field present between the stems. This field strength can be varied by either varying the RF power fed into the cavity or altering the distance between the stems

4 Scaling, Adaptation, and Comparison of the Probable Cavity Designs

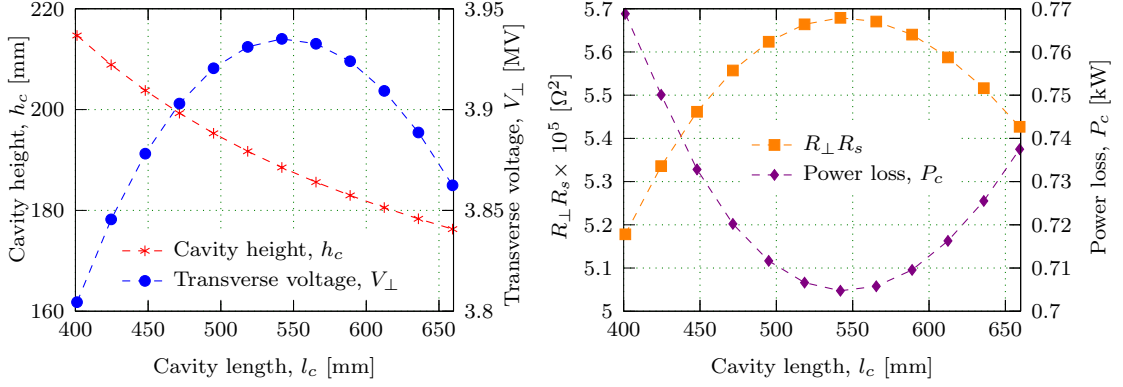


Figure 4.27: Variation of cavity height and FOM for different cavity length for the deflecting mode frequency at 273 MHz. The V_{\perp} is calculated for total energy of 1 J in a cavity and power loss is calculated for V_{\perp} of 300 kV.

(cavity aperture, v_{ap}). In the later case, the field intensity varies inversely with the distance between the stems. Therefore, a narrow cavity aperture leads to a stronger electric field, leading to a higher kick voltage for a constant RF power. Moreover, a closer spacing between the plates enhances the kick voltage homogeneity.

A parametric study was carried out to ascertain the impact of the cavity aperture on the FOM and the kick voltage homogeneity, and the results are shown in Figures 4.28 and 4.29. As expected, a decrease in the cavity aperture increases V_{\perp} ,

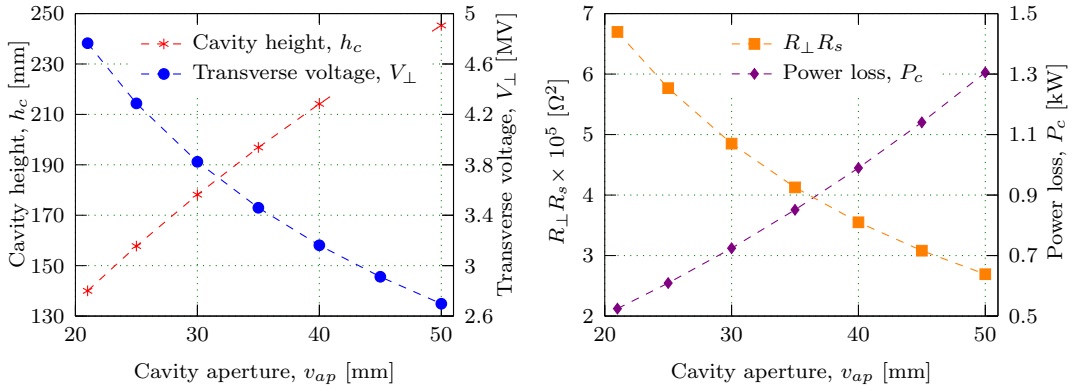


Figure 4.28: Variation of cavity height and important FOM for Design VI for various cavity apertures with the deflecting mode frequency at 273 MHz. The V_{\perp} is calculated for total energy of 1 J in a cavity and power loss is calculated for V_{\perp} of 300 kV.

4 Scaling, Adaptation, and Comparison of the Probable Cavity Designs

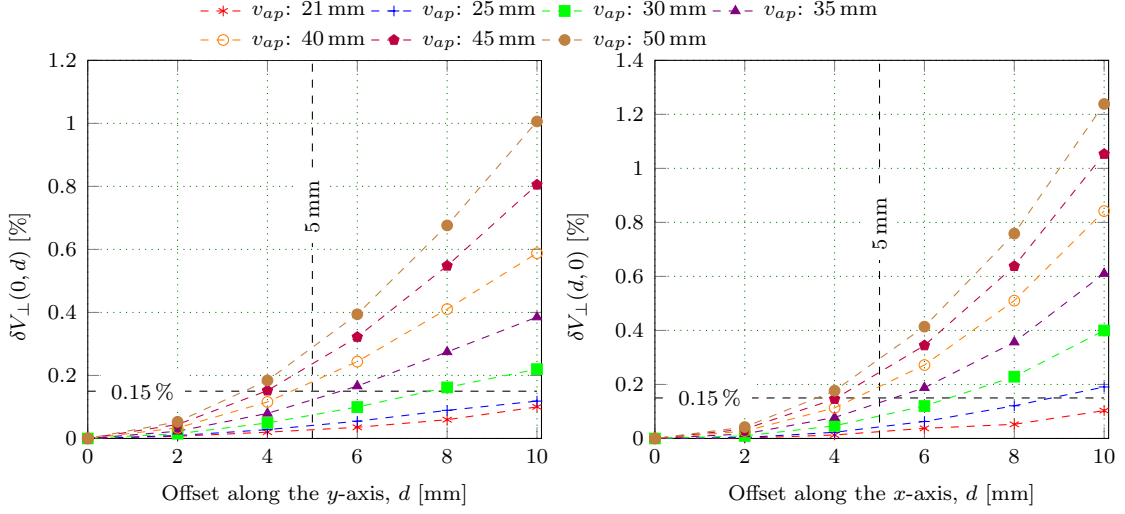


Figure 4.29: Comparison of the kick voltage homogeneity of Design VI for different cavity apertures. The relative kick voltage error along the x and y -axis are given by $\delta V_{\perp}(d, 0)$ and $\delta V_{\perp}(0, d)$, respectively.

and the power loss varies quadratically with the cavity aperture. Additionally, a smaller cavity aperture has a better kick voltage homogeneity than a larger aperture. Even though a cavity with a smaller aperture reduces the required RF power, factors like a minimum beam clearance distance, multipacting and the power loss due to HOM need to be considered when selecting the cavity aperture. The cavity aperture was set to 30 mm in accordance with the cavity requirements specified in Table 4.1, and the other effects are discussed in the next chapter. The important FOM of the Design VI are listed in Table 4.10.

Table 4.10: Important FOM of Design VI. V_{\perp} is calculated for the total energy of 1 J in the cavity, and the P_c , S_{pk} , and E_{pk} are calculated for a V_{\perp} of 300 kV.

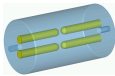
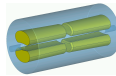

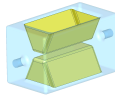

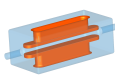
Parameter	V_{\perp} [MV]	R_{\perp}/Q [Ω]	Q_0 -	G [Ω]	$R_{\perp}R_s$ [$\text{k}\Omega^2$]	P_c [W]	E_{pk} [MV/m]	S_{pk} [W/cm ²]
Design VI	3.99	9.27	13309	57.03	529.8	729	2.49	1.21

4.3 Comparison of the Cavity Designs

The scaling and adaption of the six likely TCAV designs that meet the current requirements were discussed, and the cavity dimensions and the FOM are listed in Table 4.11. The Designs I, II and VI are slightly more compact than the other designs. In design I and II, the deflecting mode is not the fundamental mode. Because of the presence of a lower order mode (LOM), an additional coupler might be required to damp this mode. In the other designs, however, the fundamental mode is the deflecting mode, and no additional coupler is required to damp the LOM. In addition to the fundamental mode and LOM, an infinite number of eigenmodes exist in a cavity at higher frequencies. The frequency of the first higher-order mode in Designs I and II is closer to the fundamental mode than in the other designs. A larger frequency separation between these modes facilitates the design of efficient dampers (mode couplers) without affecting the deflecting mode fields.

The main FOM for comparing the normal conducting cavity designs are $R_{\perp}R_s$, surface power loss (P_c), the peak surface electric field (E_{pk}) and the peak surface power loss density (S_{pk}). A cavity with a higher value of $R_{\perp}R_s$ requires a lower RF power to deliver a given transverse voltage. The Designs I and VI have a higher value of $R_{\perp}R_s$ than the other designs, and the same is reflected in the RF power required to achieve a V_{\perp} of 300 kV. In the case of the peak electric field, all the designs have a value lower than 3 MV/m which is way below the Killpatrick voltage limit of 15 MV/m. In Design I, the concentration of the magnetic field around the rods results in a higher S_{pk} , and requires a complex cooling mechanism to avoid thermal runaway. A lower S_{pk} in Designs III - V is not surprising as these superconducting cavity designs were optimized for the lower surface magnetic fields. Though the S_{pk} achieved in Design VI is higher than Designs III to V, the value is within the given requirements.

Table 4.11: Comparison of the cavity dimensions and FOM of the six TCAV designs with the deflecting mode frequency at 273 MHz. V_{\perp} is calculated for the total energy of 1 J in the cavity, and the P_c , S_{pk} , and E_{pk} are calculated for a V_{\perp} of 300 kV.

Parameter	Unit						
		Design I	Design II	Design III	Design IV	Design V	Design VI
Cavity height (h_c)	mm	270	270	376	290	190	181
Cavity width (w_c)	mm				275	350	275
Cavity length (l_c)	mm	500	500	500	500	500	500
Frequency of LOM	MHz	223.7	207.2	-	-	-	-
Frequency of 1 st HOM	MHz	302.7	309.6	505.4	509.9	565.7	410.5
Transverse voltage (V_{\perp})	MV	4.75	3.93	2.95	3.14	2.35	3.99
Transverse R/Q (R_{\perp}/Q)	k Ω	13.16	8.99	5.08	5.74	3.22	9.27
Quality factor (Q)	-	8793	8309	16787	14759	13519	13309
Transverse impedance (R_{\perp})	M Ω	115.71	74.69	85.28	84.72	43.53	123.37
Geometry factor (G)	Ω	37.68	35.69	72.06	63.35	58.03	57.03
$R_{\perp}R_s$	$\times 10^3 \Omega^2$	496.8	320.9	365.9	363.7	186.9	529.8
Power loss (P_c)	W	779	1205	1056	1063	2069	729
Peak electric field (E_{pk})	MV/m	2.91	2.07	1.66	1.69	1.66	2.49
Peak loss density (S_{pk})	W/cm ²	4.31	2.95	0.69	0.59	0.78	1.21

4 Scaling, Adaptation, and Comparison of the Probable Cavity Designs

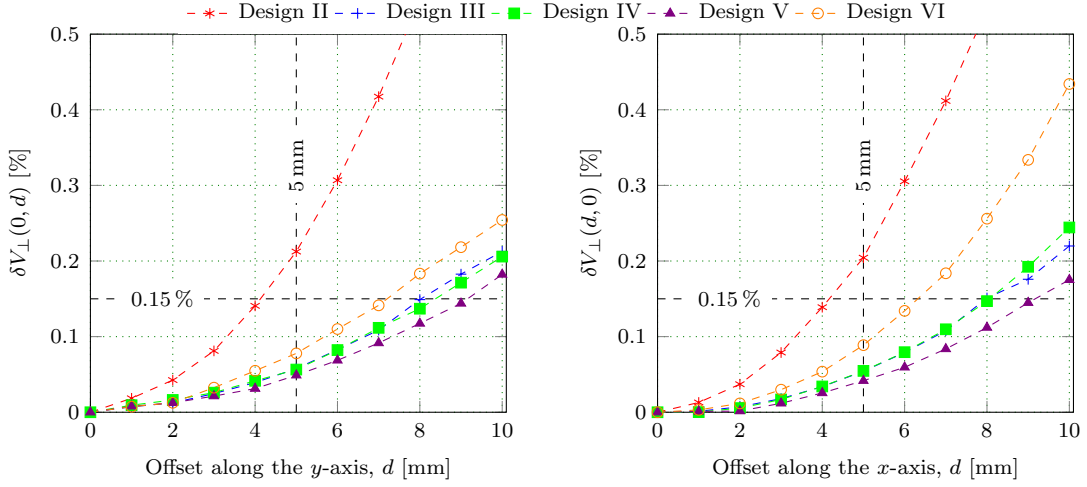


Figure 4.30: Comparison of the kick voltage homogeneity of the probable TCAV designs. V_{\perp} is calculated for the total energy of 1 J in the cavity, and the P_c , S_{pk} , and E_{pk} are calculated for a V_{\perp} of 300 kV.

In addition to the FOM, a comparison of the kick voltage homogeneity of the designs is made in Figure 4.30. Since Design I has a poor kick voltage homogeneity (Figure 4.6), the curve is excluded from the graph. The designs III to VI have a good kick voltage homogeneity that satisfies the given requirement specified in Table 4.1. Though Design VI has a lower kick voltage homogeneity than the other three designs, the low power loss of this design outweighs this drawback. Overall, the comparison study suggests that Design VI is ideal as a beam separator for the current work. The next chapter discusses the design of the additional cavity components.

5 Development of the Cavity Components and Further Analysis

The previous chapter discussed the numerical analysis of the probable cavity designs. The FOM and kick voltage homogeneity of the six cavity designs were examined, and the design VI emerged as a suitable deflecting cavity for the ELBE. The next step of the design process involves the development of the cavity components. New cavity components require considerable time to design, manufacture and validate. A long development time can be avoided by modifying an existing component design to fit the current requirements. To that purpose, the ELBE's pre-buncher cavity components are a good choice. The first section contains a brief introduction of the pre-buncher cavity components. In the subsequent sections, an adaptation of the cavity components to current requirements are discussed. Following the design of the cavity components, the beam loading in the cavity is examined. In the next section, the phenomena of multipacting in the cavity is analysed. The impact of HOMs on the cavity is discussed in the last section.

5.1 Pre-buncher Cavity

In ELBE, the beam from a thermionic gun has a long bunch length which needs to be compressed longitudinally before the beam is passed to the TESLA cavities. This is achieved using a sub-harmonic pre-buncher cavity operating at 260 MHz. The cavity decelerates the particles present at the bunch head, whereas the particles at the tail get accelerated, and thereby reducing the bunch length. The pre-buncher cavity operates at room temperature and requires a maximum RF power of 600 W at 260 MHz. Until now, the performance of the cavity and its components have been satisfactory. As the pre-buncher operating frequency and power requirement lie near

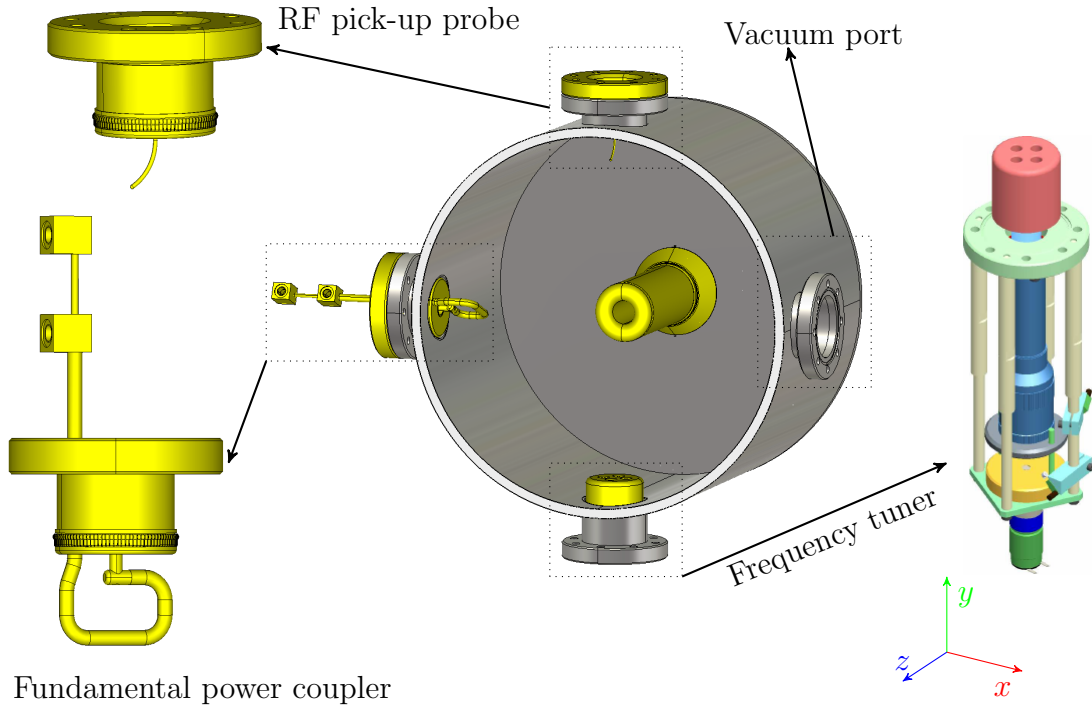


Figure 5.1: A cross-sectional view of the ELBE pre-buncher and the cavity components: fundamental power coupler, frequency tuner and pick-up probe.

to the beam separator requirements, it was decided to adapt the pre-buncher cavity components for the present cavity. Figure 5.1 shows the important components of the pre-buncher cavity [161].

5.2 Fundamental Power Coupler

The transfer of RF energy from a power source to a cavity is achieved through a power coupler. A power coupler can be a waveguide that transfers the power through a slot on a cavity or a coaxial coupler with a loop/antenna. Furthermore, the couplers are classified based on the field component of a cavity mode through which the power transfer occurs, and the strength of coupling defines how strongly the cavity fields interact with the coupler. In the pre-buncher, a loop type coaxial fundamental power coupler (FPC) is used to couple the power through a magnetic field. The coupling factor of a loop coupler depends on the integral magnetic field enclosed by the loop,

5 Development of the Cavity Components and Further Analysis

which depends on the loop area and its orientation with respect to the magnetic field in the cavity. The rotation of the coupler changes the magnetic field enclosed by the loop and thereby changes the coupling factor. Furthermore, the coupler loop is water cooled to eliminate thermal issues at high RF power levels.

A maximum RF power is transferred to a cavity when the input coupling factor, β_{in} , equals one. However, to compensate for any manufacturing errors and beam loading effects, the coupling factor should be variable, which is achieved by rotating the coupler. The loop must be designed such that β_{in} of 1 is achieved when the loop area is at an angle of 45° to the deflecting mode magnetic field. In this way, rotation of the coupler can produce both $\beta_{in} > 1$ and $\beta_{in} < 1$. The coupler loop has a concentric pipe to carry coolant, and a sharp bend would hinder the flow, which may result in poor heat transfer. Therefore, sharp bends in the loop have to be avoided by keeping the loop bending radius greater than the outer pipe diameter.

In light of the aforementioned constraints, three coupler loop designs were examined (Figure 5.2), with all the three couplers when placed at the cavity center have $\beta_{in} \approx 1$ when the loop is oriented at 45° . The first design was the scaled down version of the pre-buncher loop. In the second design, to avoid sharp bends, a center rod of the coaxial antenna was extended to achieve a rectangular loop. A semi-circular loop area was obtained in the third design with no sharp bends. There are infinite locations where the coupler can be placed in the cavity. However, for the sake of simplicity, the placement of the coupler was confined to the center and corner of the cavity.

Three coupler designs placed at the center and corner of the cavity with different orientations of the loop were simulated to obtain β_{in} , and the results are presented in Figure 5.2. The couplers at the cavity center have β_{in} curve symmetric about the 0° to 180° plane. However, the couplers at the cavity corner have β_{in} curve symmetric about the 135° to 315° plane. Furthermore, due to the presence of a stronger magnetic field near the stem, both couplers have a higher β_{in} when the coupler loop points at the stem than when it points towards the outer cavity enclosure. The couplers at the corner, on the other hand, have a smaller β_{in} than the ones in the center, since the loop at the former site does not enclose the stronger magnetic field.

The results from the simulation suggest that all the loop designs satisfy our require-

5 Development of the Cavity Components and Further Analysis

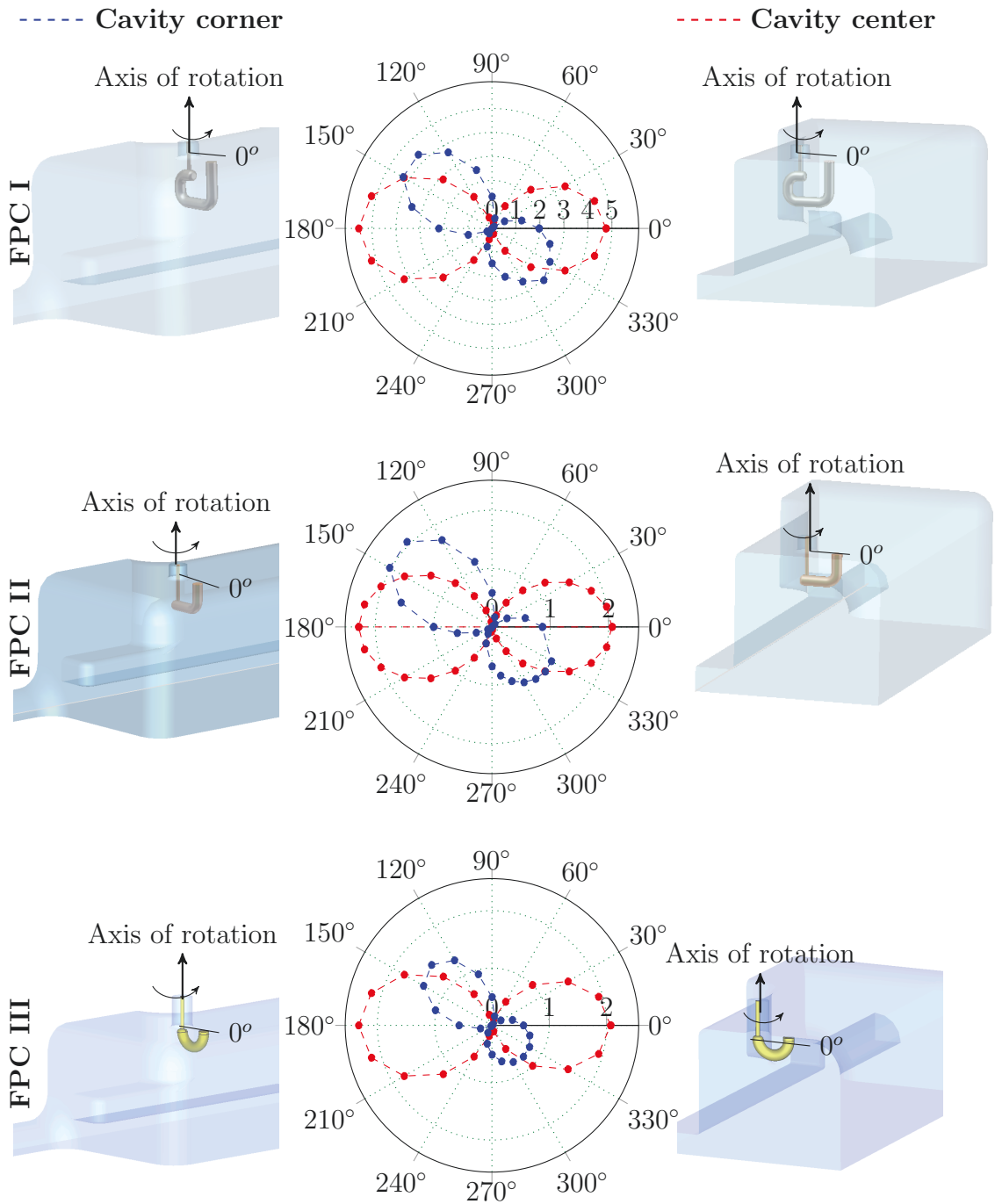


Figure 5.2: The coupling strength, β_{in} , of the three coupling loop designs with the FPC placed at the corner and center of the cavity with different orientations of the loop.

ments. However, a better resolution of β_{in} can be achieved by rotating the coupler placed at the cavity center. Although all three loop designs at the cavity center match our requirements, manufacturing feasibility and thermal behavior of the loop must be investigated. The FPC I design has three bends with a tight bending radius, which is difficult to fabricate. The FPC II design has only a single bend, but the long center conductor is not water cooled. It is possible that this will raise the temperature of the center conductor, causing damage to the feedthrough. In the FPC III design, the loop has a larger bending radius that is relatively easy to fabricate. In the end, the FPC III design was selected for the above reasons.

5.3 Pick-up Probe

Ideally, the forward and reflected power measured before the main coupler will be sufficient to estimate the RF power loss in a cavity. In addition to that, a loosely coupled antenna (pick-up probe) is used to sample the field for a reliable measurement. The pick-up probe should be loosely coupled ($\beta_{pu} \ll 1$) so as not to disturb the cavity field. The power measured at the pick-up port will correspond to the actual field strength inside a cavity.

In the pre-buncher cavity, a curved inner conductor extended from the coaxial coupler acts as an antenna and couples to the cavity electric field for the field measurement (Figure 5.1). The antenna position in the cavity and its length determine the field coupling strength. To keep the cavity field symmetric, the pick-up can be placed directly opposite to the FPC (option I) or adjacent to the stem (option II), as shown in Figure 5.3. In option I, both couplers are in close proximity, and there may be cross-coupling of the field for certain orientations of the fundamental power coupler and antenna lengths. Therefore, option II was selected to avoid any cross-coupling of the field. The external quality factor Q_{pu} was computed for various antenna lengths and the results are presented in Figure 5.3. A longer antenna penetrates deep into the cavity and samples a stronger electric field, resulting in a higher β_{pu} (or lower Q_{pu}). For the initial RF testing of the deflecting cavity, the antenna length used in the pre-buncher was retained. However, the antenna can be trimmed as necessary to fulfill any future requirements.

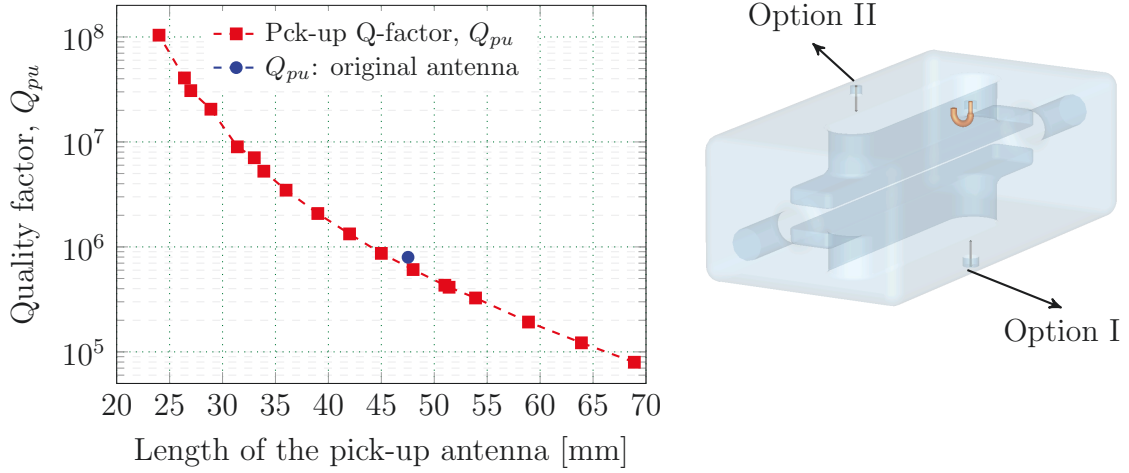


Figure 5.3: A sketch showing the two options for the pick-up probe location in the cavity (right). The graph shows the variation of the pick-up quality factor, Q_{pu} , for the different antenna lengths for option II (left).

5.4 Frequency Tuners

Usually, the resonance frequency of a superconducting cavity is tuned by physically deforming the cavity geometry. However, a similar technique cannot be emulated for a normal conducting cavity due to the thick cavity walls. Therefore, the cavity resonance frequency is tuned by driving a solid plunger/plate in or out of a cavity. The frequency tuning system of the pre-buncher cavity consists of a cylindrical copper head connected to a micrometer, and the micrometer is driven by a geared DC motor to precisely move the tuner head in and out of the cavity (Figure 5.1). This tuning scheme permits for the remote active tuning of the cavity, and a tuner movement of ± 25 mm produces a frequency shift of ± 100 kHz in the pre-buncher cavity.

The location of the beam separator in the ELBE beamline is still unclear at this moment. Therefore, it was decided that the cavity tuning range should be ± 750 kHz so that the cavity can be used for different use scenarios discussed in Table 3.10. Moreover, a higher frequency tuning range can compensate for the frequency drift due to fabrication errors and thermal expansion of the cavity. Therefore, an active tuning mechanism similar to the pre-buncher cavity was proposed for the beam separator cavity.

5 Development of the Cavity Components and Further Analysis

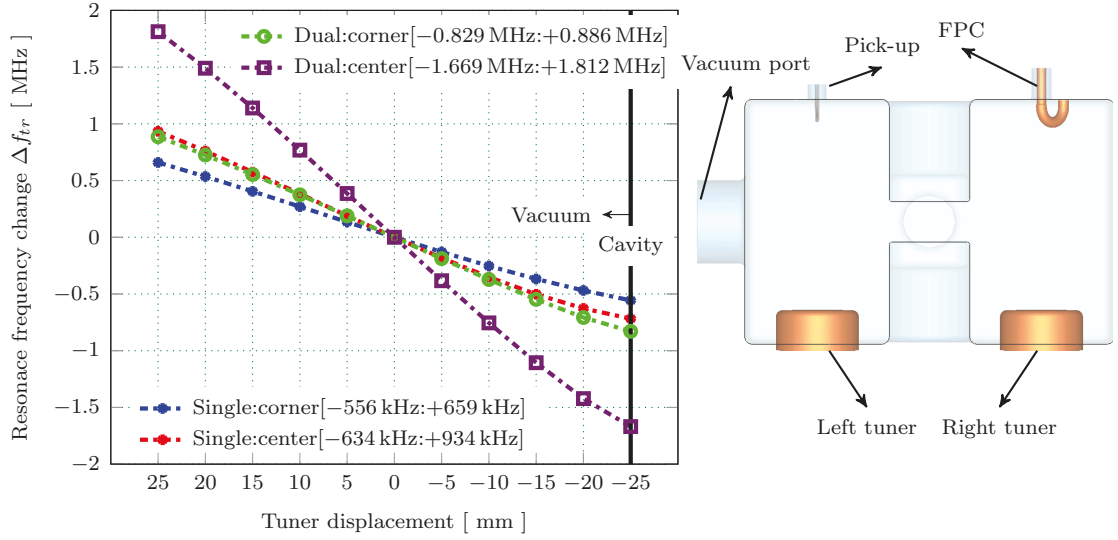


Figure 5.4: Graph shows the frequency shift (Δf_{tr}) due to single and dual tuners placed at the center and corner of the cavity and the cross-sectional view of the cavity showing different cavity components is also presented (right).

The frequency tuner can be positioned at the cavity center or corner, and single or dual tuners can be used. The frequency shift due to the single and dual tuners placed in the centre and corner of the cavity at various tuner positions are plotted in Figure 5.4. A single tuner at the cavity center provides a frequency shift of -634 kHz to $+934$ kHz, which is higher than the shift generated by the tuner placed at the corner. In any case, using a single tuner does not deliver the requisite frequency shift while simultaneously introducing field asymmetry. The dual tuners at center, on the other hand, provide a frequency tuning range of -1.669 MHz to $+1.812$ MHz, which satisfies our requirement. Furthermore, dual tuners at the cavity center provide a superior field symmetry.

5.5 Multipacting Analysis

The resonant multiplication of electrons in a cavity, also known as multipacting, is an important phenomenon that needs to be taken into consideration when designing a cavity. This unwanted resonant acceleration of electrons inside a cavity would extract the RF power fed to the cavity and reduce the actual cavity field strength.

5 Development of the Cavity Components and Further Analysis

Moreover, a repeated collision of the electrons on a cavity surface would increase the temperature locally. Subsequently, this may lead to vacuum breakdown due to degassing of the cavity surface. The different types of multipacting have been discussed in Section 2.7.

In the present deflecting cavity, a strong uniform electric field is present between the stems, whereas the magnetic field is absent (Figure 5.5). Therefore, there is a high possibility that the 2-point multipacting may sustain in this region. The graph in Figure 5.5 shows the magnitude of the sinusoidally oscillating electric field between the stems for different cavity aperture and RF power levels with the deflecting mode frequency fixed at 273 MHz. An upper limit exists for the electric field above which 2-point multipacting does not occur for a given frequency and distance between the plates (or stems)(Equation 2.87), and this is represented by a dot in Figure 5.5. In the present case with the stems separated by 30 mm, a 2-point multipacting can be ruled out in the cavity aperture for an RF power above 55 W.

Based on the analytical equations, it was predicted that the 2-point multipacting in the cavity aperture region will be absent for the RF power above 55 W. Nevertheless, the 2-point multipacting might sustain in the stem region at lower power levels. The electric field between the stems for the first six orders of multipacting at different

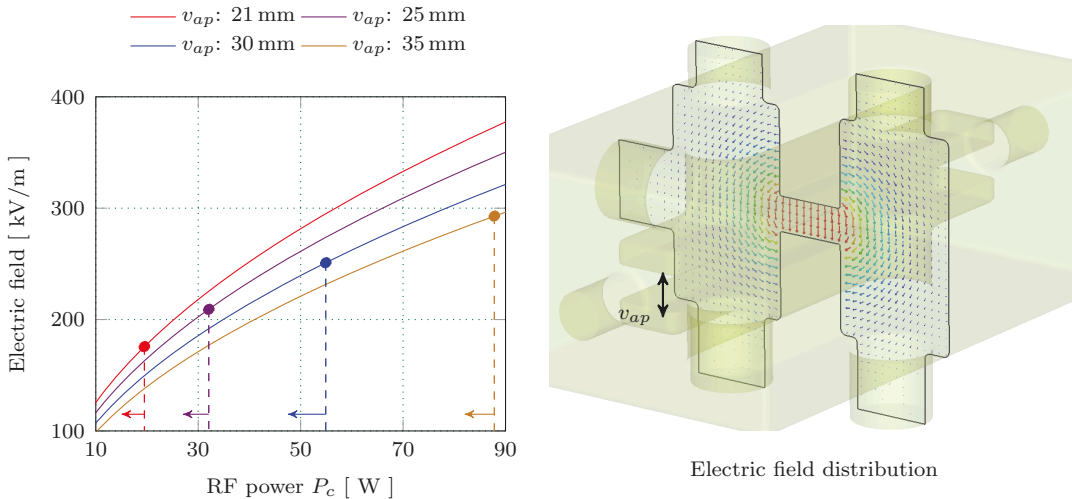


Figure 5.5: The magnitude of the electric field between the stems for different RF power levels and cavity apertures, and the dot refers to the maximum electric field above which 2-point multipacting can not sustain (left). A strong uniform electric field distribution between the stems is shown in the right picture.

5 Development of the Cavity Components and Further Analysis

RF phases at which the ejected electrons can match the resonance condition of multipacting is given in Figure 5.6. Further, the figure shows the impact energy of the electrons for these six orders of multipacting. The shaded region in the graph shows the region where the secondary emission yield of copper is greater than one. For an order of multipacting above six, the impact energy of an electron is low to eject a secondary electron, and multipacting can be ruled out. However, the electrons which have impact energy in the shaded region (Figure 5.6) can produce secondary electrons to sustain multipacting, and the corresponding RF power ranges from 0.5 W to 50 W. Overall, 2-point multipacting in the cavity can be ruled out at the nominal operating power levels. However, it has a higher probability during the vacuum conditioning ¹ of the cavity. Thus, multipacting may sustain at lower power levels and result in a longer conditioning time at these power levels.

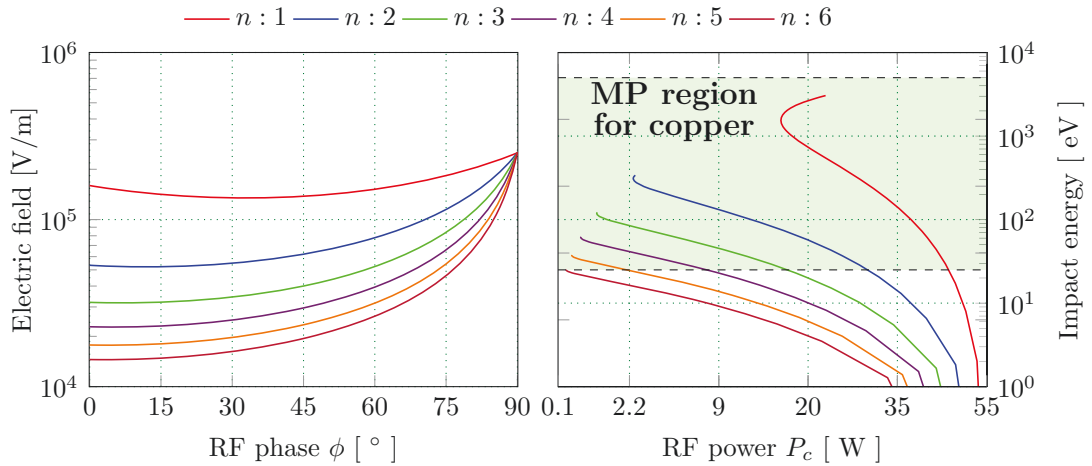


Figure 5.6: The electric field at different RF phases and order of multipacting for which the resonance condition for multipacting is satisfied (left). The variation of impact energy of the electrons for various RF power levels and orders of multipacting in a cavity (right). The shaded region represents the multipacting region for copper. The cavity aperture under consideration is 30 mm.

¹In this process, the input power to the cavity is increased gradually until the vacuum conditions to a level where the maximum input power is sustainable.

5.6 Required RF Power and Beam Loading

In Section 2.6.2, an expression for the deflecting voltage and required generator power due to the beam loading and cavity detuning was derived as

$$V_c e^{i\phi} = V_{g,r} \cos \psi e^{i\psi} + V_{b,r} \cos \psi e^{i\psi}, \quad (5.1)$$

$$P_g = \frac{V_c^2 (1 + \beta_{in})^2}{R_{\perp} 4\beta_{in}} \left\{ \left(1 + \frac{R_{\perp} I_b}{V_c} \frac{\omega \Delta y}{c(1 + \beta_{in})} \cos \phi \right)^2 + \left(\tan \psi - \frac{R_{\perp} I_b}{V_c} \frac{\omega \Delta y}{c(1 + \beta_{in})} \sin \phi \right)^2 \right\}. \quad (5.2)$$

The above expressions can be understood by considering an off-axis beam at different RF phases (ϕ). At the zero-crossing phase ($\phi = 0$), the off-axis longitudinal electric field is in phase with the bunches, whereas the on-axis transverse electric field is out of phase. Therefore, the integral of the longitudinal electric field is non-zero, but that of the transverse electric field is zero. Consequently, the voltage induced in the cavity by an off-axis beam might add to or subtract from the generator voltage. The cosine term present in the equation (5.2) refers to the beam-induced voltage, and the sign of Δy decides whether the induced voltage adds or subtracts the generator voltage (Figure 5.7 a). The amplitude of the induced voltage is proportional to the beam current and the magnitude of beam displacement, and it is inversely proportional to the cavity coupling factor. The field induced by the beam would get coupled out of the cavity by a coupler with a high β_{in} .

If the bunches arrive at on-crest ($\phi = \pi/2$), the integral of the off-axis longitudinal electric field would be zero, whereas that of the transverse electric field will be non-zero. Therefore, the particles' energy in a bunch changes barely, but the bunch receives a net transverse kick. Nevertheless, the voltage induced by the beam would alter the phase of the generator voltage (Figure 5.7 b). Thus the required generator power at on-crest reduces to

$$P_g = \frac{V_c^2 (1 + \beta_{in})^2}{R_{\perp} 4\beta_{in}} \left\{ 1 + \left(\tan \psi - \frac{R_{\perp} I_b}{V_c} \frac{\omega \Delta y}{c(1 + \beta_{in})} \right)^2 \right\}. \quad (5.3)$$

5 Development of the Cavity Components and Further Analysis

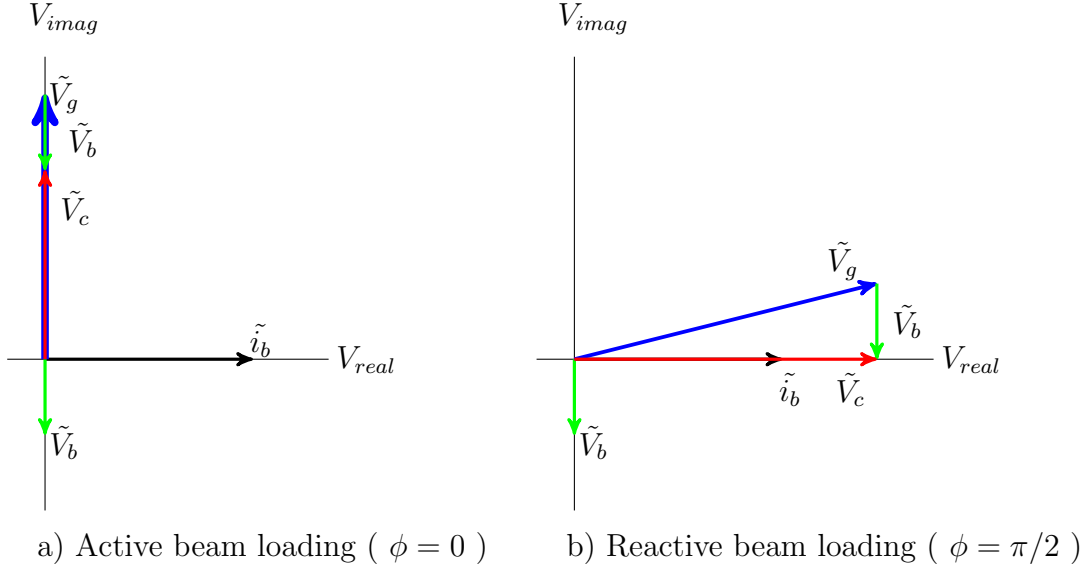


Figure 5.7: Vector diagram for the deflecting cavity when the beam loading is purely active (a) and reactive (b). The beam current is aligned with the real part of the voltage, and \tilde{V}_b , \tilde{V}_g , \tilde{V}_c refers to the beam induced voltage, the generator voltage and the cavity voltage in phasor notation, respectively.

The reactive part of the generator power has an additional term due to the cavity detuning. Therefore, the voltage induced by the beam can be compensated by detuning the cavity by

$$\tan \psi = \frac{R_{\perp} I_b}{2V_c} \frac{\omega \Delta y}{c(1 + \beta_{in})} \sin \phi. \quad (5.4)$$

Substituting the expression for $\tan \psi$ from equation (2.67) into the above expression and rearranging the terms renders the required frequency detuning as

$$\Delta\omega = -\frac{R_{\perp}/Q I_b \omega^2 \Delta y}{2V_c c} \sin \phi. \quad (5.5)$$

The reactive part of the voltage induced by the beam at on-crest can be compensated by detuning the cavity by frequency $\Delta\omega$.

The maximum power induced by an offset beam in a cavity is given as

$$P_b = \frac{R_{\perp} I_b^2}{4\beta_{in}} \left(\frac{\omega \Delta y}{c} \right)^2. \quad (5.6)$$

In a deflecting cavity, the power by the beam in the deflecting mode is smaller than that of an accelerating cavity by a factor of $(\omega \Delta y/c)^2$. Therefore, a 1 mA beam at an

offset of 10 mm will induce around 90 mW of power into the deflecting mode of the cavity. The beam-induced power is four orders lower than the cavity's RF power loss. Furthermore, β_{in} slightly > 1 would be sufficient to correct any beam loading effect, facilitating the transfer of maximum power from the generator to the cavity.

5.7 HOM Analysis

A beam traveling along the cavity may excite HOMs in the cavity. In the current cavity design, as the deflecting mode is the cavity's fundamental mode, this eliminates the requirement for a specific coupler to dampen the LOM. A brief analysis of HOMs in the cavity is discussed in this section.

The beam tube and vacuum port are circular waveguides that act as a high-pass filter for the HOMs of a cavity. These modes which have frequencies above the cut-off frequency of the ports are coupled out of the cavity. Therefore, only the modes with frequencies below the tube cutoff frequency are of interest. The cutoff frequency of the TM_{01} and TE_{11} mode of a circular waveguide [30] with radius r_c are

$$f_{c,TM} = \frac{c j_{0,1}}{2\pi r} \text{ and } f_{c,TE} = \frac{c j'_{1,1}}{2\pi r}, \quad (5.7)$$

where $j_{0,1} = 2.405$ and $j'_{1,1} = 1.841$ are the first zero of the Bessel function (J_0) and J'_1 , respectively. Subsequently, the cut-off frequency of the beam-pipe and vacuum tube are listed in Table 5.1. Therefore, the HOM with the resonance frequency higher than 2.791 GHz can be neglected from the analysis.

The shunt impedance of the first 100 modes of the deflecting cavity computed using equation (2.89) is plotted in Figure 5.8. The transverse shunt impedance calculated with the direct method agrees well with that computed using the Panofsky-Wenzel Theorem. The first four modes correspond to the two stems and have a higher shunt

Table 5.1: Cutoff frequency of the beampipe and the vacuum connection port.

Circular waveguide	Radius [mm]	f_{cutoff} TM_{01} [GHz]	f_{cutoff} TE_{11} [GHz]
Beampipe	18.0	6.379	4.884
Vacuum port	31.5	3.645	2.791

5 Development of the Cavity Components and Further Analysis

impedance than other HOM. The first and second mode are the deflecting modes, and the third and fourth modes are the longitudinal modes that are very close in frequency. The HOMs have a lower shunt impedance and a lower Q-factor than the fundamental mode. Moreover, the intrinsic Q-factor of the cavity operating at room temperature is way lower than that of a cavity at superconducting state. Therefore, the HOMs excited by the beam gets damped very fast in a normal conducting cavity compared to a superconducting cavity. Furthermore, the power induced by the HOMs in the cavity is far lower than the surface losses from the operating mode. In overall, the effect of HOMs induced by the beam can be neglected for the present cavity. Since the specific beam parameters for the beam separation application are not fixed, only a quick investigation of the HOM effect on the cavity was performed. In the future, an in-depth analysis will be required depending on the cavity's location in the beamline.

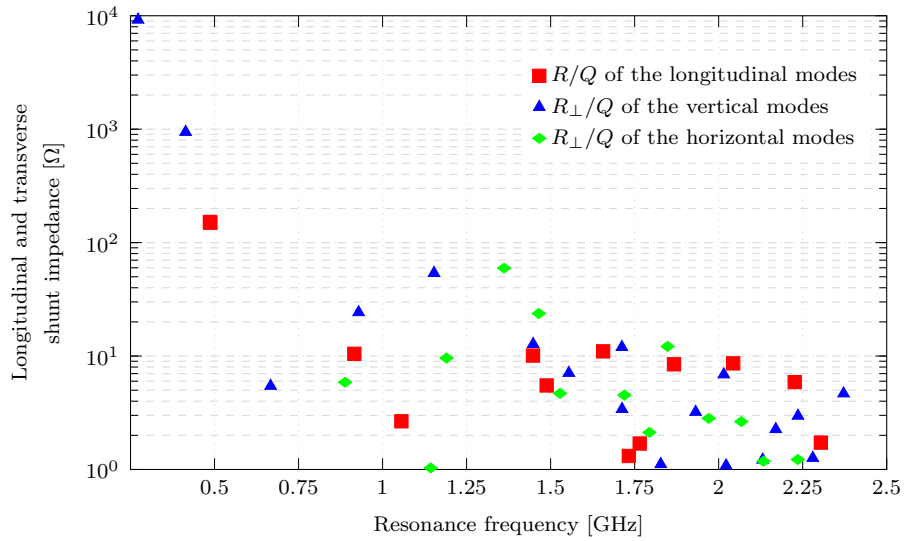


Figure 5.8: The shunt impedance of the longitudinal, horizontal, and vertical deflecting modes of the deflecting cavity.

6 Multiphysics Analysis of the Cavity

The previous chapters discussed the electromagnetic analysis of the cavity. A multiphysics analysis of the cavity is the next phase in the cavity development process and is discussed in this chapter. The first section discusses a brief introduction to the multiphysics simulation setup. Calculation of the frequency sensitivity of the cavity surfaces is discussed in the next section. The following section covers the selection of the cavity material and the cavity wall thickness. The penultimate section outlines the variation of the ambient temperature, the RF power loss and the coolant temperature on the cavity's resonance frequency. The last section of this chapter presents a list of guidelines for manufacturing the cavity.

6.1 Simulation Setup for Multiphysics

The electromagnetic study resulted in a vacuum part of the cavity geometry, and only a strong metallic structure can keep this geometry from being deformed by external forces. However, the cavity deforms due to the atmospheric pressure, the Lorentz force from the RF field, and the thermal expansion due to the surface power losses and the change in the coolant temperature. Any deformation of the cavity geometry shifts the resonance frequency, and the drift in the resonance frequency increases the input RF power to maintain a given kick voltage at a fixed frequency. For this reason, the resonance frequency shift must be compensated actively to keep the required power at a minimum. Unquestionably, the behavior of the cavity structure needs to be analyzed in different inter-coupled physics domains for a solid and stable cavity geometry.

Multiphysics problems can be classified into strongly and weakly coupled problems [173] based on the coupling strength between the domains (Figure 6.1). In this context, a two-way coupling is considered as strong, where the interacting domains

6 Multiphysics Analysis of the Cavity

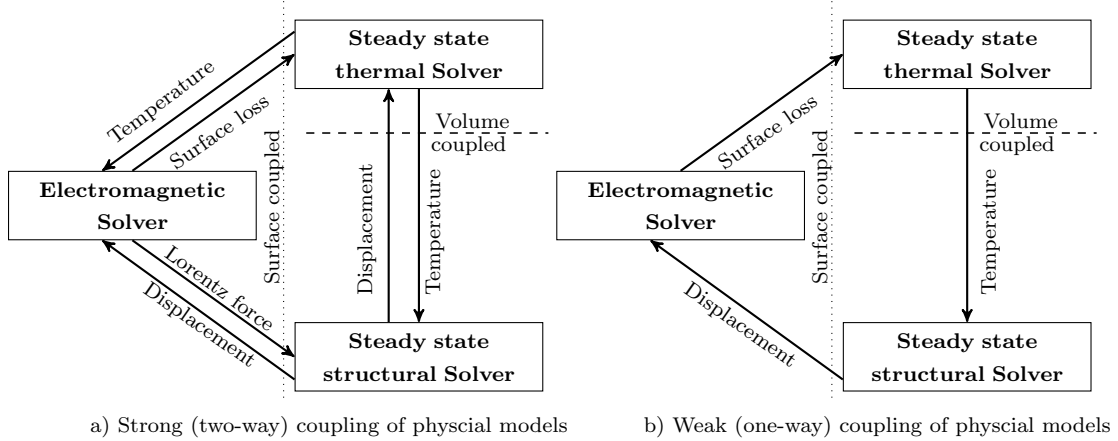


Figure 6.1: Illustration of the two types of multiphysics coupling analysis: a) Strong (two-way) coupling between the physics process and b) Weak (one-way) coupling between the physics process. The connection or coupling between the sub-domain is between the boundaries in the surface-coupled case, whereas the interaction is in the same spatial domain in the volume-coupled case.

need to be simultaneously updated as the material properties and the constitutive parameters are interlinked and nonlinear. In contrast, a one-way coupling is considered as weak and an iterative approach can be used to solve this type of problems [173].

In the case of an RF cavity, the surface power loss is determined by the cavity material's resistivity, which is influenced by its temperature. Additionally, variations in cavity temperature modify the cavity shape. This is an example of a strongly coupled problem, where the surface loss affects not just the temperature but also the cavity's resistivity, which influences the power loss. The temperature difference can be minimal if the heat deposited on the cavity surface is efficiently removed with a good cooling mechanism. Then the change in the material's resistivity will be small and can be neglected. Moreover, a slight temperature change has no significant effect on the cavity's geometry and the cavity surface fields. The problem can be classified as a weakly linked problem in this scenario. Since a good cooling mechanism will be designed for the present deflecting cavity, the current multiphysics analysis of the cavity is regarded as a weakly coupled problem, and the process flow for this analysis is shown in Figure 6.2. Furthermore, for the purpose of simplicity, the analysis is carried out by ignoring all of the cavity components.

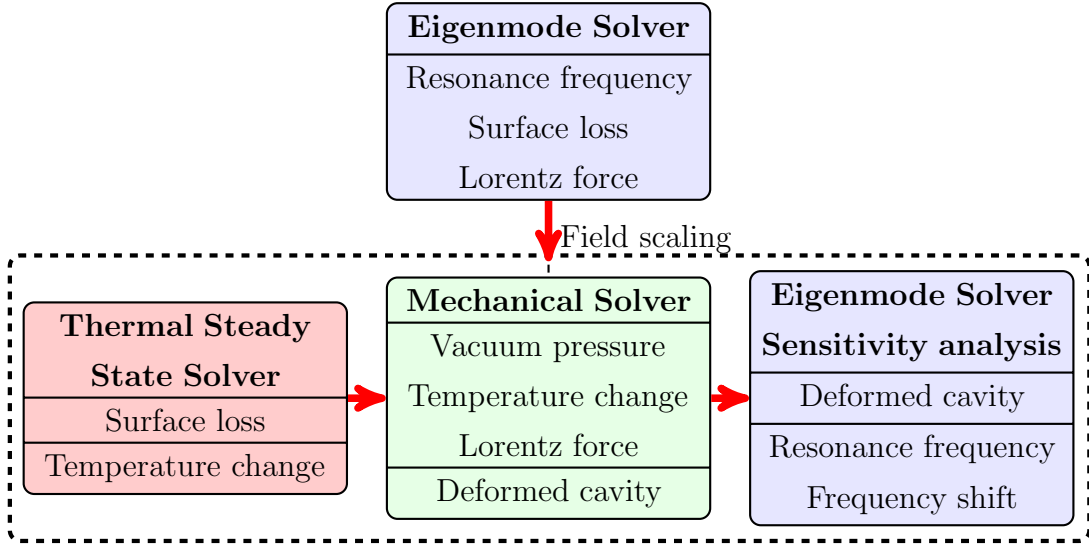


Figure 6.2: The process flow of the cavity multiphysics analysis carried out with CST Studio Suite[®] [36] considering a weakly coupled problem. The solvers included in the black dotted line were sequentially executed in the parametric analysis.

6.1.1 Eigenmode Analysis

The multiphysics process started with the electromagnetic analysis of the cavity geometry to obtain the deflecting mode’s resonance frequency and related field distribution. Subsequently, the transverse kick voltage, the surface power loss, and the Lorentz force were computed using the field values. Note that the default field values obtained from CST Microwave Studio[®] [36] correspond to 1 J of total energy in the cavity. To obtain the field values that correspond to the real conditions, the default field values were scaled by a factor: the ratio of the required transverse voltage to the default transverse kick voltage. The surface loss calculated using the scaled field values gives the actual power loss in the cavity, and this is a heat source for the thermal analysis. The Lorentz force obtained from the scaled fields is a source for the mechanical solver.

6.1.2 Thermal Analysis

The RF power deposited on the cavity’s inner surface must be removed continuously to keep the cavity temperature stable. The heat conducts from the inner surface

6 Multiphysics Analysis of the Cavity

towards the outer cavity surface and the coolant channels, which are at a lower temperature. Thereafter, the heat is removed from the cavity surface through natural convection, whereas the coolant flowing in the channels removes heat through forced convection. At lower temperatures, the radiation heat transfer can be neglected. Eventually, the temperature across the cavity reaches a steady state for a constant RF power and coolant temperature. Due to this reason, a steady-state thermal analysis was carried out to obtain the temperature distribution across the cavity. In the thermal analysis, only the metallic component was considered because the vacuum inside a cavity does not affect heat transport. The surface power loss density is higher at the curved part of the stem, which is why coolant channels were provided in this area (will be discussed in Section 6.5). Furthermore, an adequate coolant flow rate and pressure will be maintained to remove the heat efficiently. As a result, the temperature difference between the inlet and outlet coolant is expected to be very low. Consequently, the coolant channel acts as a heat sink, and the temperature of this entire area is set to a fixed coolant temperature. Furthermore, the exterior cavity surfaces are assigned a natural convective boundary condition. The scaled RF surface power loss obtained from the eigenmode analysis acted as a thermal source in this solver. The symmetric boundary conditions are applied along all three symmetric planes.

Finally, the temperature distribution in the cavity was obtained by solving the steady-state thermal equations. Due to the uneven power loss distribution and the coolant channels, the temperature in the cavity was distributed non-uniformly. This resulted in the thermal expansion of the cavity, which is obtained from the mechanical solver.

6.1.3 Structural Analysis

A cavity deforms due to changes in ambient and coolant temperature, the Lorentz force from the RF field, the atmospheric pressure exerted on the evacuated cavity's walls, and its weight. The effect of all these factors on the cavity geometry can be obtained from the structural analysis. Like in the thermal analysis, only the metallic part of the cavity is considered. Due to symmetry of the cavity, the analysis is confined to $1/8^{th}$ of the cavity geometry (Figure 6.3 a).

A fixed boundary condition is required in all the 3 axes to confine the movement

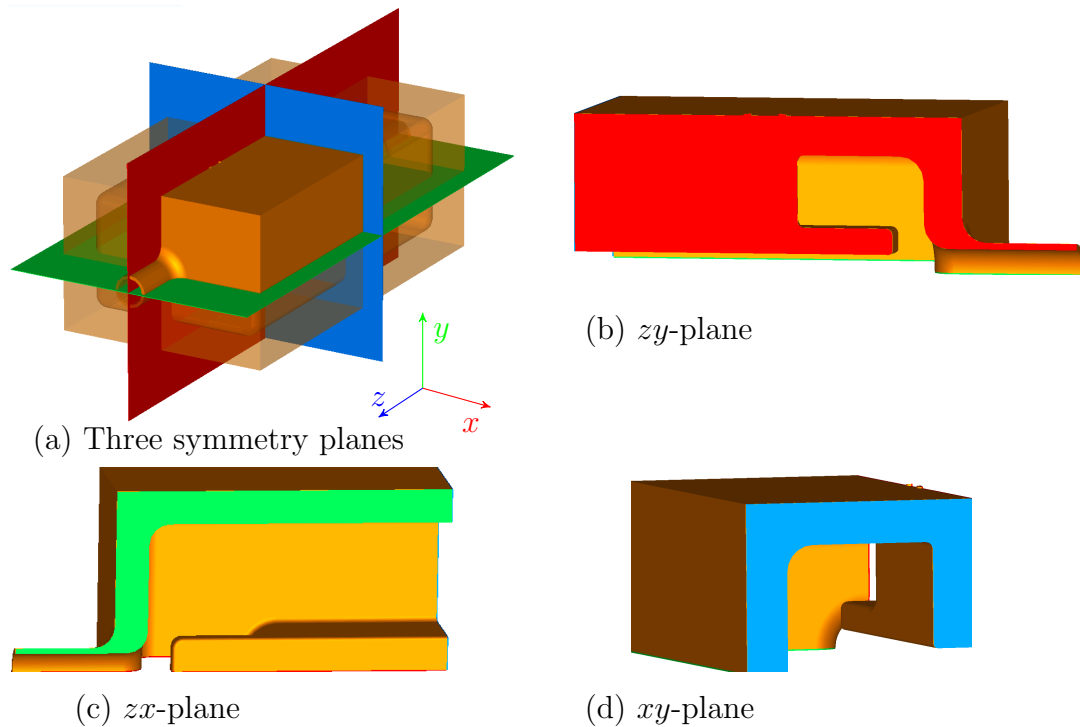


Figure 6.3: The cavity is symmetric in all three planes and the cavity surfaces split by the symmetric planes are assigned a fixed boundary condition normal to its surface. Also shows the $1/8^{th}$ of the cavity model considered in the structural analysis.

of a cavity. The cavity surfaces split by the symmetric planes are assigned a fixed boundary condition normal to its surface (Figure 6.3 b, c and d). The Lorentz force and temperature distribution are imported from the eigenmode and thermal solver, respectively. The atmospheric pressure on the outer cavity surface is assigned as a traction boundary condition, and the gravity effect is assigned directly in the solver. The governing equations are then solved to obtain the deformed cavity. The frequency shift caused by this deformation is determined by the eigenmode sensitivity analysis.

6.1.4 Eigenmode Sensitivity Analysis

Generally, the resonance frequency of the deformed cavity can be determined in two ways. In the first method, a new vacuum model of the cavity is re-constructed from the deformed metallic cavity, and then the eigenmode analysis of the new

model is carried out once again to obtain the resonance frequency. In the second method, perturbative method, the knowledge of the surface deformation and the cavity surface electromagnetic fields are used to compute the frequency shift. For example using the adjoint approach mentioned in [174], or generalization of Slater's theorem discussed in [175]. A suitable method to find the resonance frequency for a given problem depends on the extent of the deformation.

If the deformation of a cavity is small, then re-meshing of the new vacuum model introduces mesh noise, affecting the accuracy of the results obtained from the first method. However, the second method uses the original geometry, avoiding the mesh noise error. The first method, on the other hand, is preferable when the deformation is large, whereas the second method is for smaller deformation. A built-in routine in CST Microwave Studio[®] employs the second approach to compute the frequency sensitivity of a deformed cavity [174] and the same was used in this study.

6.2 Frequency Sensitivity of the Cavity Surfaces

The strength and distribution of the electromagnetic field on all the surfaces of a cavity are not uniform. Therefore, each cavity surface influences the resonance frequency differently. The cavity parts with high-frequency sensitivity surfaces should have a higher fabrication tolerance than other parts. In addition, the sensitive cavity parts must be rigid enough to withstand any deformation due to external factors. A qualitative way to identify the frequency sensitivity of a cavity surface is via its surface fields. A stronger surface field corresponds to a higher frequency sensitivity, whereas a weaker field results in a lower sensitivity. This method is suitable only when either an electric or magnetic field is present on a surface. If both fields are prominent on a surface, the quantitative approach using Slater's theorem should be followed [176]. Consider a small perturbation of a cavity surface which changes the cavity volume by ΔV_{pr} , then the resulting resonance frequency shift Δf_{pr} is given as

$$\frac{\Delta f_{pr}}{f_0} = \frac{1}{4U} \iiint_{\Delta V_{pr}} (\mu_0 \mathbf{H} \cdot \mathbf{H} - \epsilon_0 \mathbf{E} \cdot \mathbf{E}) dV, \quad (6.1)$$

where U is the stored energy in the cavity, ΔV_{pr} is the volume of the perturbation in the cavity, $\Delta f_{pr} (= f_{pr} - f_0)$ is the frequency difference, f_0 and f_{pr} are the resonance

6 Multiphysics Analysis of the Cavity

frequency of the unperturbed and perturbed cavity, respectively, and \mathbf{H} and \mathbf{E} are the unperturbed magnetic and the electric field at the perturbed location. Slater's theorem states that if a stronger magnetic field region is removed from a cavity results in increase in frequency ($\Delta f_{pr} \uparrow$), and frequency decreases ($\Delta f_{pr} \downarrow$) if a stronger electric field is removed.

In addition to the Slater's theorem, the frequency sensitivity of a cavity surface can be determined by performing a parametric sweep of a dimension linked with the surface. This method is straightforward to be employed for a few cavity surfaces. However, it will be computationally expensive when the frequency sensitivity of many surfaces are required. In contrast, the field values obtained from a single solver run can be used to compute the frequency sensitivity values from the equation (6.1). But, extracting, exporting, and processing the field values requires additional effort. Alternatively, an in-built routine of CST MWS[®] based on the adjoint approach method can be used to find the frequency sensitivity of a surface [174].

In general, the resonance frequency of a cavity is substantially influenced by the cavity surfaces with a larger area or stronger surface fields. Figure 6.4 shows the six critical faces of the deflecting cavity. The frequency sensitivity is expressed as Hz/mm, which specifies the resonance frequency shift due to the displacement of a surface along its normal by a mm. The frequency sensitivity of the critical surfaces specified in Figure 6.4 is listed in Table 6.1. Additionally, the table compares the sensitivity values obtained directly from the in-built function of CST MWS[®] with the values computed from the Slater's theorem. The sensitivity values computed using the two methods were in a good agreement. Since the cavity faces A to E have

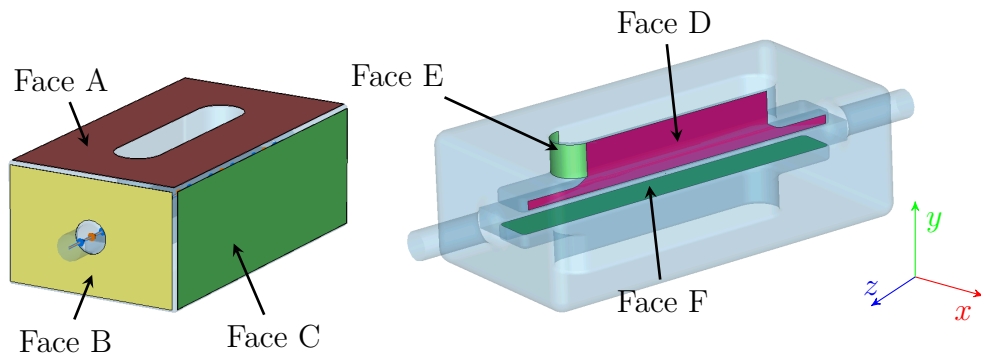


Figure 6.4: The important cavity faces considered for the frequency sensitivity analysis.

6 Multiphysics Analysis of the Cavity

Table 6.1: Comparison of the frequency sensitivity values obtained from CST MWS[®] and the Slater’s theorem for the critical cavity faces highlighted in Figure 6.4.

Cavity surface	Shift direction	Volume change	Frequency sensitivity [kHz/mm]		
			CST MWS [®]	Slater’s Theorem	Error [%]
Face A	$-y$	$-\Delta v$	804.9	780.6	3.0
Face B	$-z$	$-\Delta v$	48.5	45.8	5.6
Face C	$-x$	$-\Delta v$	358.2	350.2	2.2
Face D	$-x$	$-\Delta v$	134.9	129.3	4.2
Face E	$+r$	$-\Delta v$	253.2	241.1	4.7
Face F	$+y$	$-\Delta v$	-2771.6	-2656.5	4.2

only a surface magnetic field, their displacement increases the resonance frequency. A stronger surface electric field on Face F significantly reduces the cavity frequency. The frequency sensitivity of the critical cavity faces suggests that the stem and cavity aperture dimensions are the critical parts of the cavity. Moreover, these cavity parts strongly influence the cavity resonance frequency. As a result, smaller machining tolerances were specified for these parts of the cavity. Also, a solid stem was preferred to avoid the deformation of the stem due to external factors.

6.3 Cavity Material and Wall Thickness

The cavities operating at room temperature are usually machined from copper, stainless steel, or aluminum. In an aluminum cavity, a strong multipacting is expected due to a high SEY [177]. For this reason aluminum is not the preferred cavity material. Typically, copper and steel are the most suitable choice due to their high mechanical strength, machinability, and lower SEY. However, steel has a lower electrical conductivity than copper, resulting in a higher surface loss. A thin copper/silver coating on a steel cavity, on the other hand, can decrease the power loss. The thin coated layer can be neglected in the thermo-mechanical simulation and is considered only for calculating the surface power loss. The properties of the material considered in the simulation are given in Table 6.2.

6 Multiphysics Analysis of the Cavity

Table 6.2: The electrical, thermal, and mechanical properties of the materials used in the multiphysics analysis.

Material	Electrical conductivity	Density	Thermal conductivity	Specific heat capacity	Expansion co-efficient	Young's modulus	Poisson's ratio
	S/m	kg/m ³	W m ⁻¹ K ⁻¹	J kg ⁻¹ K ⁻¹	10 ⁻⁶ K ⁻¹	kN/mm ²	
OFHC copper ⁺	5.9×10^7	8930	401	0.39	17	120	0.33
Stainless steel *	1.33×10^6	8000	15	500	16	205	0.29
Silver coating	6.3×10^7	-	-	-	-	-	-

⁺ Oxygen-Free High-Conductivity copper.

* A special type of stainless steel known as AISI 316LN (1.4429).

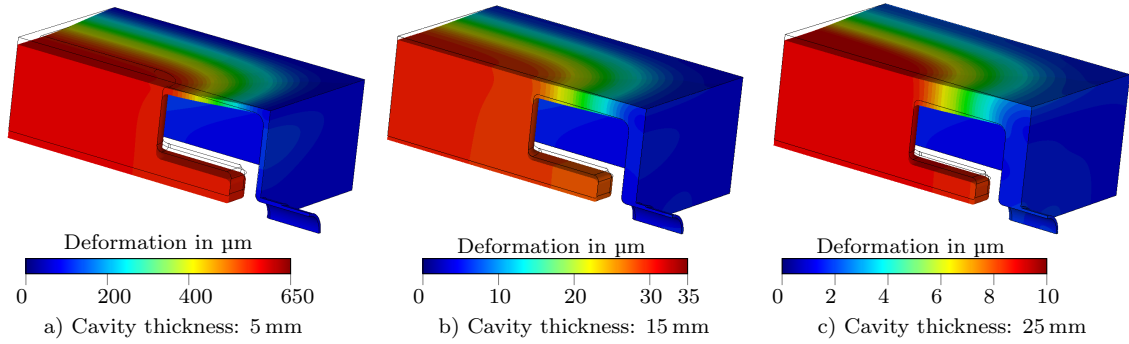


Figure 6.5: Copper cavity deformation due to the atmospheric pressure for three different wall thicknesses with the outline of the original cavity marked by a solid black line. For better visualization, the deformation in the model is scaled by a factor of 10, 100, and 500 times for the wall thickness of 5 mm, 15 mm, and 25 mm, respectively. The effect due to cavity is neglected.

Once the cavity is evacuated, the outer cavity walls experience an atmospheric pressure of 1 bar. Therefore, the cavity wall should be thick enough to withstand this pressure. Though a thick wall and a high-strength material is rigid enough to resist the atmospheric pressure, this cavity will be expensive and also difficult to machine, transport, and install. As a result, an optimum wall thickness must be identified that is inexpensive and simple to fabricate while keeping the frequency shift within the maximum allowable value. For the case at hand, a maximal frequency shift of 50 kHz has been specified.

The structural analysis of the copper and stainless steel cavity was carried out to obtain the cavity deformation due to the atmospheric pressure for different wall

6 Multiphysics Analysis of the Cavity

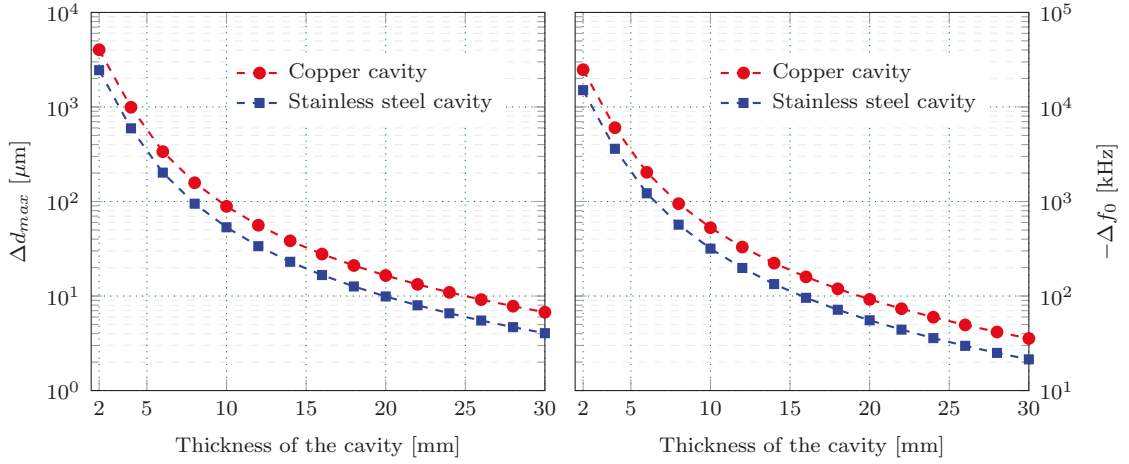


Figure 6.6: Maximum deformation and frequency shift for various wall thicknesses of copper and stainless steel cavities with a pressure of 1 bar on the outer cavity surface.

thicknesses. In the case of a copper cavity with a thin wall, the outer wall withstands the atmospheric pressure better than the top and bottom surfaces (Figure 6.5). Moreover, the solid stems connected to the top and bottom surface move inwards into the cavity, which reduced the cavity aperture and decreased the resonance frequency. However, a thick cavity wall arrests the stem movement, reducing the frequency shift. The maximum deformation (Δd_{max}) and frequency shift (Δf_0)¹ of the copper and steel cavity for the different wall thicknesses are plotted in Figure 6.6. A steel cavity defies the atmospheric pressure better than a copper cavity due to its higher material strength, resulting in a lower frequency shift (Figure 6.6). As expected, an increase in the cavity wall thickness reduces the deformation for both the copper and stainless steel cavities. A copper cavity requires a wall thickness of 25 mm to keep the resonance frequency shift below 50 kHz, whereas a steel cavity requires only 20 mm. Even though steel was superior to copper in avoiding deformation for a given thickness, the surface power loss is higher. Since the surface loss is inversely proportional to the square root of the cavity material's conductivity, the loss in a steel cavity is almost ≈ 2.9 times that of a copper cavity. Nevertheless, a thin layer of copper coating on a steel can reduce the power loss to that of a copper cavity.

¹Here, Δd_{max} refers to the maximum deformation in the cavity obtained from simulation and Δf_0 is the frequency difference between the deformed and original cavity.

6 Multiphysics Analysis of the Cavity

However, the copper coating would pose additional technological challenges that would be difficult to address within the time frame of this thesis.

The von Mises stress distribution on a 25 mm thick copper cavity due to an atmospheric pressure of 1 bar is shown in Figure 6.7. The maximum von Mises stress of 6.5 MPa was obtained on the cavity surface which is much lower than the yield strength of copper (60 MPa). Finally, a copper cavity with a wall thickness of 25 mm was selected.

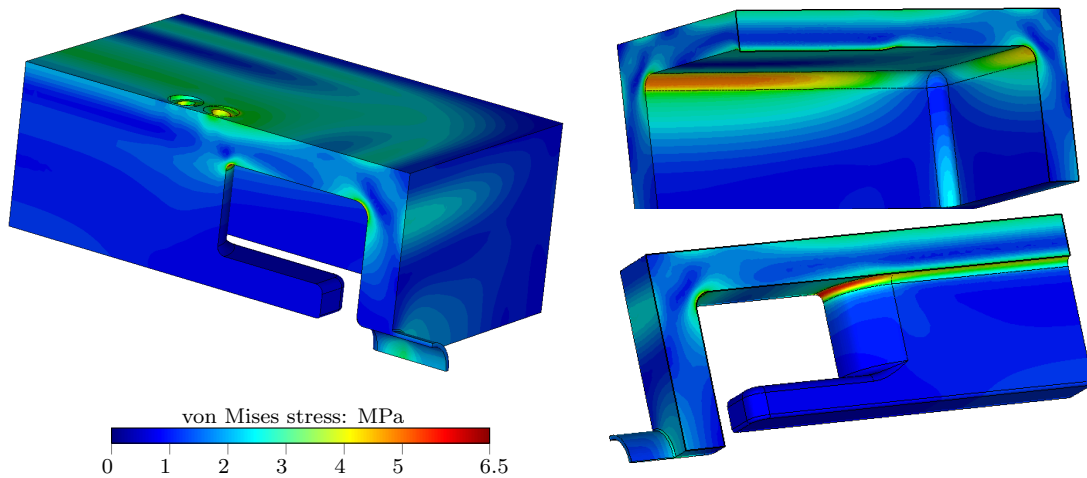


Figure 6.7: Distribution of the von Mises stress on a 25 mm thick copper cavity in an evacuated state.

6.4 Effect of Ambient Temperature

The thermal environment around the cavity is influenced by diurnal and seasonal temperature changes. During the cavity design, the ambient temperature was fixed to 20 °C, and the cavity dimensions were specified for fabrication on that basis. However, a variation in the ambient temperature expands or contracts the cavity, which impacts the cavity resonance frequency. Multiphysics simulations were performed to understand the cavity behavior at different ambient temperatures, and the maximum displacement and the frequency shift are plotted in Figure 6.8. At temperatures lower than 20 °C the resonance frequency decreases, with the opposite applying for temperatures above 20 °C. The cavity has a frequency sensitivity of 4.5 kHz/°C to

the ambient temperature.

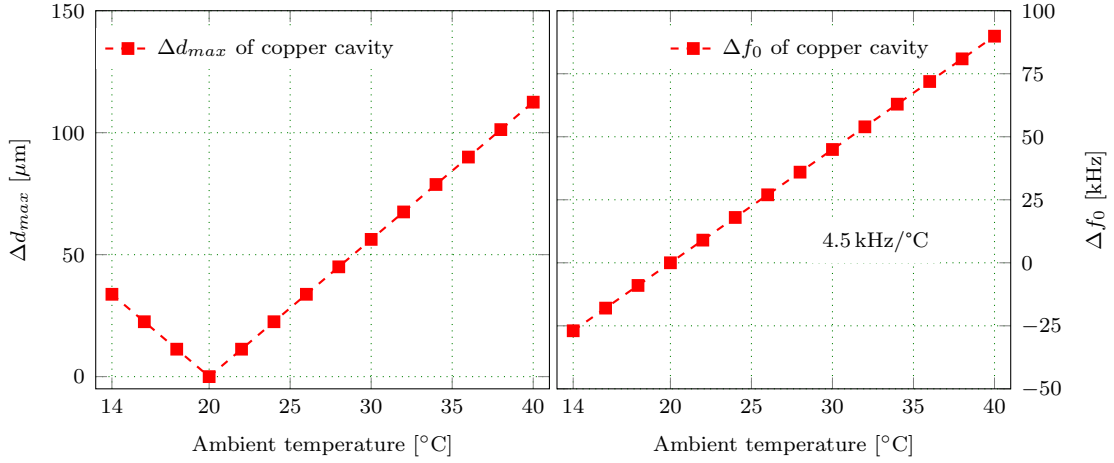


Figure 6.8: Maximum deformation in the cavity and resonance frequency shift of the copper cavity at different ambient temperatures.

6.5 Effect of RF Power and Coolant Temperature

In addition to the ambient temperature, the RF power and coolant temperature contribute to the thermal deformation of the cavity. The power deposited on the cavity has to be removed continuously to keep the cavity temperature stable. In the cavity, the curved part of the stem has a high surface power loss density (Figure 6.9), and therefore a set of cooling channels were provided in this area for active cooling. The heat transfer through natural convection was sufficient to remove the RF losses from the outer cavity walls.

The cavity temperature changes gradually when the RF power and coolant flow were applied. The temperature distribution across the cavity was not uniform because both the power loss and the cooling were not evenly distributed across the cavity. Figure 6.10 shows the steady-state temperature distribution across the cavity for an RF power of 800 W with coolant and ambient temperature at 30 °C and 20 °C, respectively. The area next to the cooling channels has a temperature equivalent to the coolant temperature (30 °C). The temperature of the outer cavity wall was a little higher than that of the stem because of lower heat transfer in this area due

6 Multiphysics Analysis of the Cavity

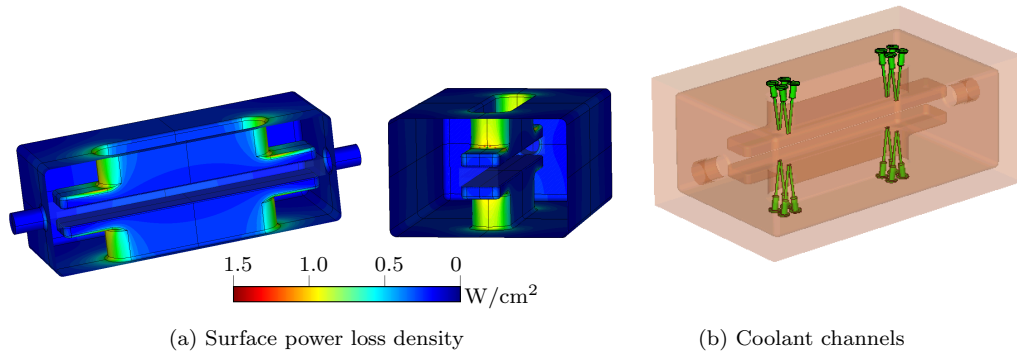


Figure 6.9: Surface power loss density distribution across the inner cavity surface for an RF power loss of 800 W (a) and location of the coolant channels are highlighted in green (b).

to the natural convection. The part of the stem which is protruded has a maximum temperature in the cavity (33°C) because of a very low heat-flow density in this region. In the case of the nominal operating power of 800 W, a maximum temperature rise of 3°C with respect to the coolant temperature was observed.

In addition to the thermal expansion, the atmospheric pressure on the cavity walls deforms the cavity. The deformation of the cavity due to atmospheric pressure is shown in Figure 6.11 (a). Figure 6.11 (c) shows the thermal expansion of the cavity due to the coolant and power loss. Comparing the Figures 6.11 (b) and (c) where the deformation is normalized, shows that the deformation due to the vacuum is smaller compared to that of the thermal expansion. Therefore, the thermal expansion of the cavity is resisted partially by the atmospheric pressure (Figure 6.11 (d)). Most importantly, the cavity aperture, which has higher frequency sensitivity, experiences

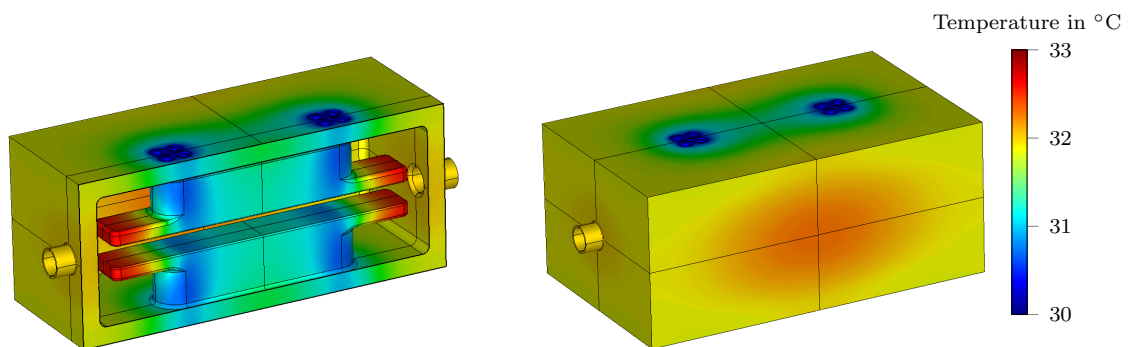


Figure 6.10: Temperature distribution across the copper cavity for an RF power loss of 800 W, with a coolant and ambient temperature of 30°C and 20°C , respectively.

6 Multiphysics Analysis of the Cavity

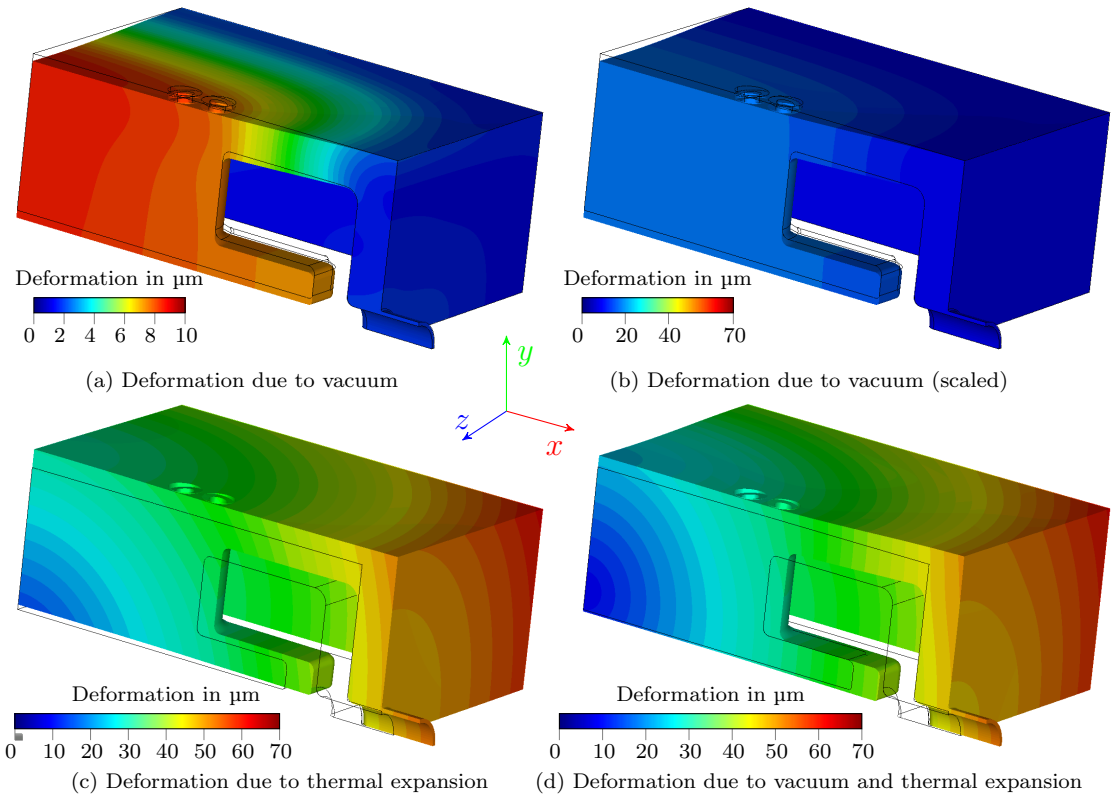


Figure 6.11: Deformation of the copper cavity with a wall thickness of 25 mm: a) due to the atmospheric pressure, (b) due to atmospheric pressure with the maximum deformation of the scale set to 10 μm , (c) due to P_c of 800 W with the coolant and ambient temperature of 30 $^\circ\text{C}$ and 20 $^\circ\text{C}$, respectively, and (d) due to atmospheric pressure, P_c of 800 W with the coolant and ambient temperature of 30 $^\circ\text{C}$ and 20 $^\circ\text{C}$, respectively. Outline of the original cavity is marked by a black line and the deformation of the model is scaled by 100 times.

a lower displacement than the outer cavity. Thus, the frequency change due to the vacuum and the thermal load is minimal. Additionally, the cavity detuning due to power ramp up needs to be compensated by the frequency tuners.

A set of simulations was carried out to find the resonance frequency shift for different RF power levels and coolant temperatures, and the results are plotted in Figure 6.12. The cavity resonance frequency decreases as the surface power loss increases and has a frequency sensitivity of -14 Hz/W . However, a rise in the coolant temperature decreases the resonance frequency by $4.3 \text{ kHz}/^\circ\text{C}$, matching the results obtained from

6 Multiphysics Analysis of the Cavity

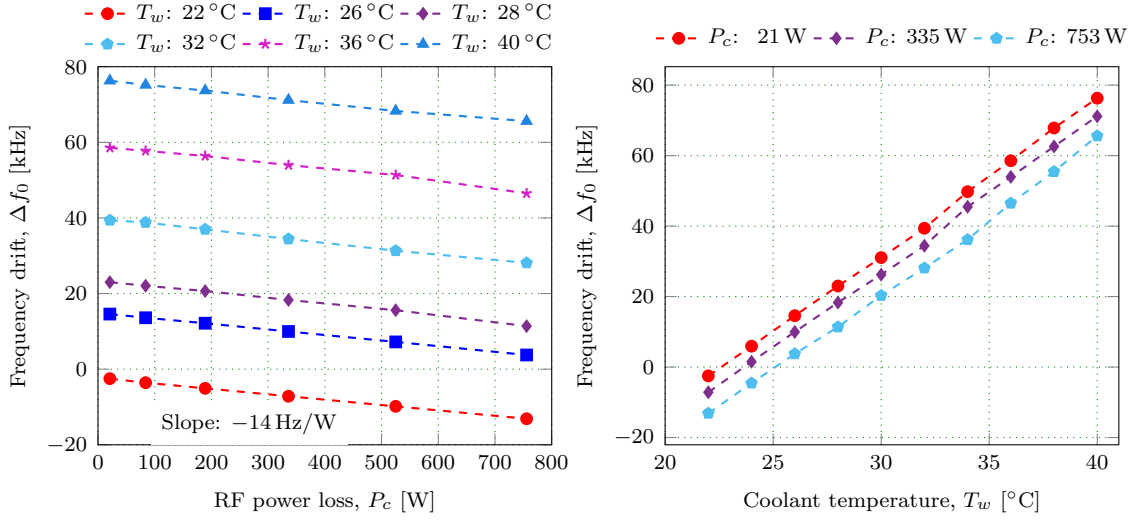


Figure 6.12: Resonance frequency shift of the copper cavity for different RF power levels and coolant temperatures.

the previous section.

6.6 Conclusion

The results obtained from the frequency sensitivity and multiphysics analysis were invaluable, and represent a necessary basis for the planning of the cavity fabrication. Moreover, the multiphysics analysis provided a basic understanding of the cavity behavior with regard to the thermal and mechanical aspects. The following inferences were made from the results of this study:

- The stem should be solid to prevent a significant shift in the cavity resonance frequency.
- The cavity should be fabricated from copper to avoid a high power loss.
- A cavity wall thickness of 25 mm would be sufficient to keep the resonance frequency change due to the atmospheric pressure below ± 50 kHz.
- Dimensional tolerances of 0.1 mm and 0.05 mm were specified for the outer cavity and stem regions, respectively. With these tolerances, the resonance

6 Multiphysics Analysis of the Cavity

frequency shift due to machining could be kept below ± 500 kHz (0.2% of the resonance frequency).

- Two cooling channels in each curved part of the stem should be sufficient to keep the maximum temperature change in the cavity less than $+3^\circ\text{C}$.

7 Cavity Fabrication

The main objectives of the cavity design were to obtain a better FOM, an effective RF power transfer, a broader frequency tuning range, and a good mechanical and thermal stability. The steps taken to achieve these goals have been thoroughly explored in the previous chapters. The next step in the cavity development process is to fabricate the cavity, which is discussed in this chapter. It is technically challenging to fabricate the cavity out of a single copper block, which drives up the manufacturing cost. To make the machining process easier, the cavity has to be separated into smaller parts, and then all of the machined parts are to be brazed together. The first section discusses the two different ways to divide the cavity for fabrication. The following part goes over the fabrication process in detail, highlighting the difficulties that were encountered. The dimensions of the machined parts do not match the 3D model used in simulation. As a result, the resonance frequency of the assembled cavity deviates from the target frequency, which needs to be corrected before final brazing. The pre-tuning of the cavity frequency is discussed in the third section. The following section provides a brief introduction to the vacuum brazing of the cavity. A visual inspection of the brazed cavity revealed the spillage of a brazing filler material on the inner cavity surfaces. The effect of spillage on the cavity operation is discussed at the end of this chapter.

7.1 Cavity Fabrication Methods

A cavity machined from a single block of copper will avoid brazing joints, thereby reducing any negative impact on the cavity FOM. However, this increases the technical difficulty in machining and raises the fabrication cost. As a consequence, the cavity must be divided into smaller portions, allowing for greater accuracy during the machining of these parts. Nevertheless, there is a downside to this approach. It is

7 Cavity Fabrication

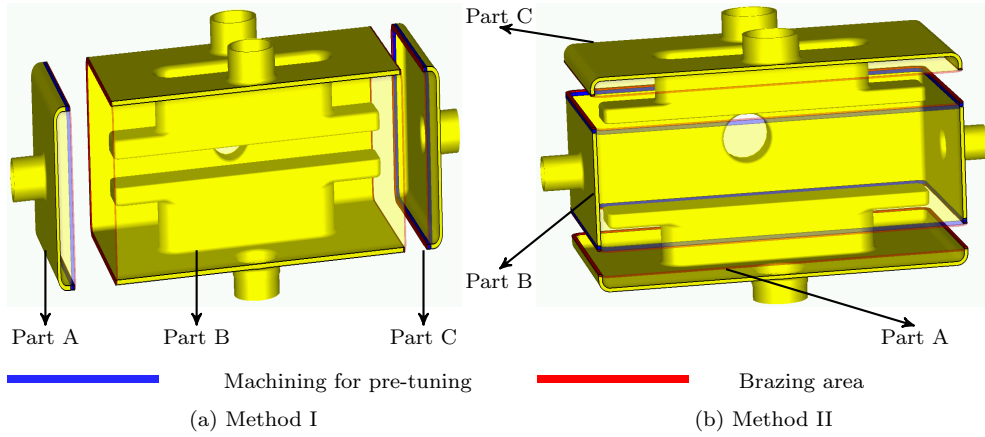


Figure 7.1: Cavity divided into three parts considering two different fabrication methods.

generally difficult to predict the effect of the brazing joints on the overall dimensions of a structure. Since the number of brazing joints increases with the number of cavity parts, the tolerances obtained during machining may suffer due to brazing. As a compromise, the cavity should be divided into fewer parts to limit the number of brazing joints and still match the specified tolerances. The cavity was divided into three sections considering these limitations. Primarily, the cavity can be divided in two ways for fabrication (Figure 7.1), and the merits and demerits of the two fabrication methods are discussed below.

7.1.1 Fabrication Method I

In the first method, both the stems are machined from a single block to form Part B, and the other two parts are machined separately (Figure 7.1 (a)). This method is similar to the fabrication methodology followed in the machining of an SRF cavity discussed in [107]. In this method, the Part B would be machined to the exact dimension, and the Part A and C would have excess length where they join with Part B. The excess material can be trimmed for the frequency pre-tuning of the cavity before performing the final vacuum brazing. In the present cavity, this excess length has a frequency sensitivity of -93.51 kHz/mm. A lower sensitivity value of the trimming region has two benefits - the frequency tuning can be very precise and any anomaly due to the brazing will only have a minimal effect on the resonance

frequency.

7.1.2 Fabrication Method II

In the second method, Part A and Part C are machined separately from a different copper blocks with a higher precision (Figure 7.1 (b)). Part B, on the other hand, may have an extra length where it meets Parts A and B. The excess material is removed simultaneously from the two sides of Part B to retain the field symmetry in the cavity during the frequency pre-tuning. In the present deflecting cavity, the trimming of additional length has a frequency sensitivity of -2.76 MHz/mm. The higher frequency sensitivity demands precise trimming of the excess material and a superior brazing quality.

7.1.3 Comparison of the Fabrication Methods

At first glance, Method I seems to be the better of the two methods for fabricating the cavity. Moreover, an SRF cavity with a similar shape of the present cavity has been manufactured using Method I [107]. However, the size of the SRF cavity is close to $1/3$ of the present cavity. It was therefore possible to machine Part B of the SRF cavity from a single block of niobium. In the present case, the machining of the bulky Part B out of a single copper block demands for advanced machines and workmanship, significantly increasing the manufacturing cost and time. This limitation outweighs the advantage of the lower frequency sensitivity offered by Method I. Method II has a significant advantage over Method I with regard to machining, as both the stems which are the most frequency sensitive parts can be machined separately. However, a high frequency sensitivity of the trim length in Method II demands for a more precise trimming and brazing. Method II was eventually chosen, with an accuracy of $50\ \mu\text{m}$ defined for trimming of the excess length from Part B.

7.2 Fabrication of the Cavity

The cavity was fabricated by an external vendor, Reuter Technologie GmbH, an expert in high precision machining and vacuum brazing of copper structures. The

7 Cavity Fabrication

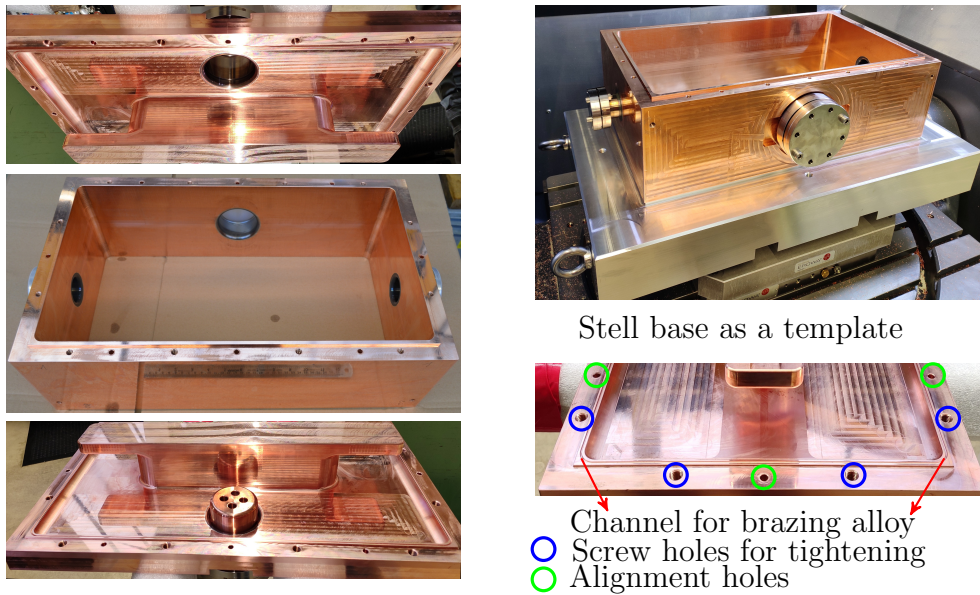


Figure 7.2: Three parts of the copper cavity were machined separately and the stainless steel base was used as a template for machining the parts.

additional cavity components were manufactured in-house. Part B of the cavity was machined using an OFHC copper block ($560 \times 340 \times 175$ mm). A separate block ($60 \times 340 \times 120$ mm) was cut in to two parts to machine Part A and C. An additional stainless steel fixture (Figure 7.2) was fabricated to meet the specified dimensional tolerances. This fixture functioned as a template for aligning the cavity parts during machining. And also, screw holes were provided to fix the copper parts on the steel base. Moreover, these holes were used to seal the cavity tight during the frequency pre-tuning process. The alignment of the cavity parts during the assembly and brazing was ensured by having an array of keyholes in the mating area of the parts (Figure 7.2). The dimensions of the machined parts were measured and verified against the design values. In addition, the Root Mean Square (RMS) surface roughness (R_z) was measured on different parts of the cavity inner surface. The measured values ranged from $0.3 \mu\text{m}$ to $2 \mu\text{m}$, which was significantly lower than the specified value of $3 \mu\text{m}$. Since the surface roughness measurement could not be carried out all over the cavity, the RMS surface roughness of the entire cavity was approximated to be $1.25 \mu\text{m}$.

7.3 Frequency Pre-tuning of the Cavity

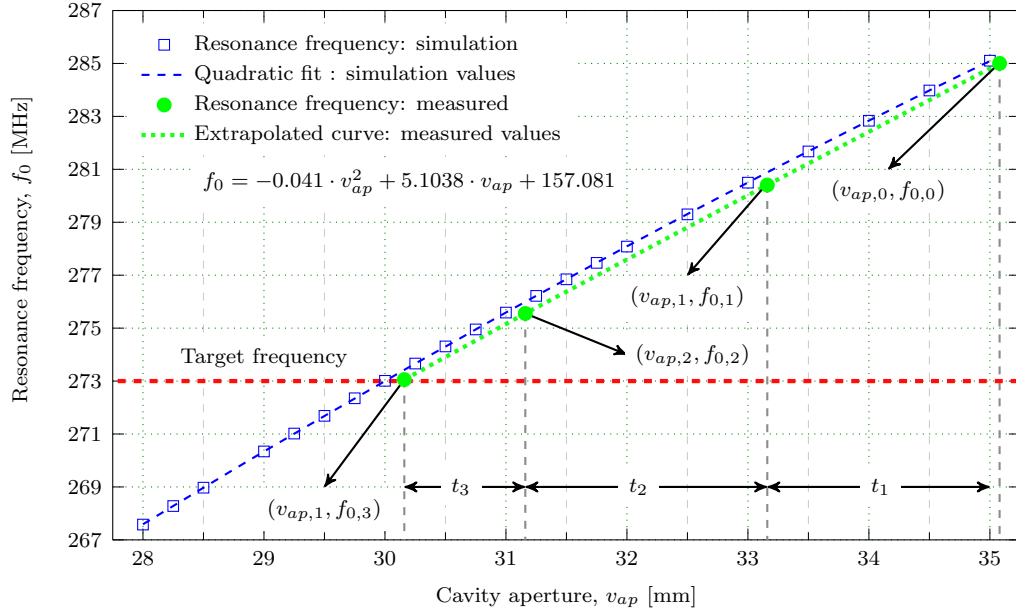


Figure 7.3: The cavity resonance frequency for different apertures and a quadratic fitted curve. The resonance frequency measured during the pre-tuning process and the corresponding extrapolated curve are plotted (in green). The values obtained during pre-tuning process are listed in Table 7.2.

Despite the fact that the cavity parts were machined with great accuracy, fabrication errors cannot be eliminated totally. Machining errors intrinsically change the cavity geometry and affect the resonance frequency of the cavity. This shift in frequency should be measured and corrected before final brazing of the cavity parts. Thus, Part B of the cavity had an excess length of 2.5 mm on its either side. The excess material of Part B increased the cavity aperture from the design value of 30 mm to 35 mm and this resulted in a frequency shift of +12 MHz. The variation of the cavity resonance frequency f_0 due to different cavity apertures that was obtained through simulations is shown in Figure 7.3, and the frequency points are fitted to a quadratic function.

The trimming of the excess length of Part C decreases both the cavity aperture, v_{ap} , and the resonance frequency, f_0 . The step-by-step trimming of the excess length and then measuring the cavity aperture and the resonance frequency renders data points that would on extrapolation provide the trim length required to achieve the target

7 Cavity Fabrication

Table 7.1: Procedure followed during the frequency pre-tuning of the cavity.

The three cavity parts are stacked vertically, aligned and tightened. Then the cavity components are installed.

Initial step

- Measure the cavity aperture ($v_{ap,0}$) and the resonance frequency ($f_{0,0}$)

1st machining step

- Trim each end of Part B by 1 mm ($t_1/2$)
- Measure the cavity aperture ($v_{ap,1}$) and resonance frequency ($f_{0,1}$)

2nd machining step

- Trim each end of Part B by 1 mm ($t_2/2$)
- Measure the cavity aperture ($v_{ap,2}$) and the resonance frequency ($f_{0,2}$)

Three measurements are plotted (Figure.7.3) and the curve is extrapolated. The final trim length t_3 is obtained from the cavity aperture of the plot at 273 MHz.

3rd machining step

- Trim each end of Part B by t_3

Final measurement

- Measure the cavity aperture ($v_{ap,3}$) and the resonance frequency ($f_{0,3}$)
-

frequency. If a higher number of machining steps is allowed, it would be possible to reach the target frequency without extrapolating the frequency values. However, this raises both the cost and the time required to construct the cavity. As a result, three data points were considered sufficient for extrapolating a quadratic curve, and three machining steps were chosen.

A systematic procedure was laid out to pre-tune the cavity frequency (Table 7.1). Before every machining step, the cavity sections were stacked, lined up with aid of the alignment holes and bolted to achieve leak-tight joints. Then the distance between the stems and the cavity's resonance frequency was measured. Importantly, all the cavity components were installed to ensure that the pre-tuning process would also compensate for errors arising from these components. A trim length of 2 mm

7 Cavity Fabrication

Table 7.2: Measurement values obtained during the frequency pre-tuning of the cavity. The values need to be considered in combination with the contents of Table 7.1 and Figure 7.3

Pre-tuning steps	Trim length	Cavity aperture v_{ap} [mm]			Resonance frequency f_0 [MHz]		
	t [mm]	Expected	Measured	Error	Expected	Measured	Error
Initial step	-	35.08	35.08($v_{ap,0}$)	0	285.237	285.002($f_{0,0}$)	0.235
1 st machining	2.00 (t_1)	33.08	33.16($v_{ap,1}$)	0.08	280.830	280.407($f_{0,1}$)	0.422
2 nd machining	2.00 (t_2)	31.16	31.16($v_{ap,2}$)	0	275.966	275.554($f_{0,2}$)	0.412
3 rd machining	0.98 (t_3)	30.18	30.16($v_{ap,3}$)	0.02	273.000	273.056($f_{0,3}$)	0.056

was fixed for the first two machining steps to ensure that there was sufficient excess length left for the final machining step. The result of the frequency pre-tuning is shown in Table 7.2 and Figure 7.3. After three machining steps, the cavity resonance frequency was offset only by +56 kHz, which can be compensated easily with the available frequency tuners.

7.4 Vacuum Brazing

Vacuum brazing is the preferred method for joining the copper parts to achieve high dimensional tolerances. In this process, a precise amount of brazing alloy (filler) is placed in the specifically designed channels at the joints. Additional fixtures are provided to restrain the parts from shifting at higher temperatures. The complete structure is placed in a vacuum chamber, and the chamber is evacuated before slowly increasing the temperature. The chamber temperature is then raised to the melting temperature of the filler material. The chamber is maintained at this temperature for a defined time so that the filler melts and diffuses into the copper. The strength of a brazed joint depends predominantly on the dwell time and temperature of the chamber. After the dwell time, the vacuum chamber is allowed to cool down slowly to room temperature. In this brazing process, differential expansion of the cavity parts is avoided, as the entire cavity is heated and cooled gradually. This achieves a better brazed joint quality than torch brazing.

In the current work, the silver-based brazing alloy, L-Ag72 (Ag-72% and Cu-28%),

7 Cavity Fabrication

was used, and Figure 7.2 shows the channels where the brazing alloy was placed. No additional fixtures were required as the weight of the cavity parts alone was heavy enough to keep the parts in a fixed position. After the vacuum brazing, a Helium-leak test of the cavity was carried out successfully and this very well confirms the leak tightness of the brazed joint.

7.5 Inspection of the Brazed Cavity

A visual examination of the inside of the cavity revealed some foreign matter on its bottom surface. Upon closer inspection of the cavity interior, it was found that the filler material had spilled from the channels and deposited at the cavity corners (Figure 7.4). Endoscopic and telescopic cameras were used to further investigate the extent of this spillage, and a collage of photos taken during this investigation is shown in Figure 7.4.

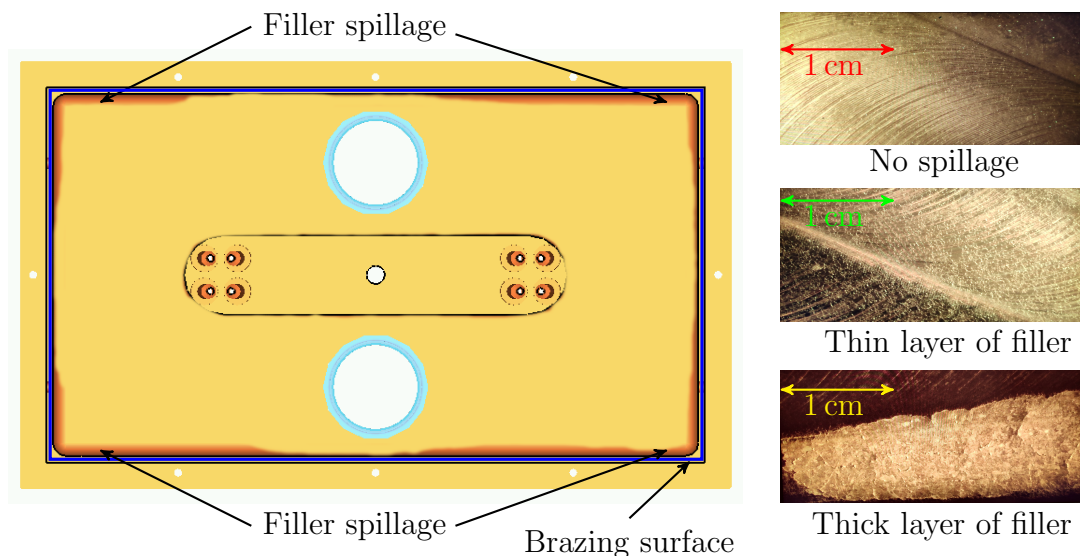


Figure 7.4: A sketch of the cavity bottom surface highlighting the filler overflow region and the filler channel (left), and the photos of different regions captured with a telescopic camera. The distances mentioned are the approximate values.

The main observations made using the visual inspections are:

- The filler material spillage was observed only at the bottom corners of the

7 Cavity Fabrication

cavity.

- There was no trace of the filler material flow from the top brazed area.
- The thickness of the spillage was not uniform across the area. A thickness measurement was not possible as the spillage region was not physically accessible from the outside. However, the visuals suggest that the thickness is less than 1 mm.
- The thin layer of the spillage area has a grainy/patchy surface, whereas the thick layer of the spillage area appears crystalline.

The most likely reason for the spillage may be a slightly higher amount of filler material in the bottom channel than in the top channel. Initially, it was anticipated that the leakage of the filler material might have weakened the brazed joints. The successful Helium leak test, on the other hand, demonstrates that the cavity can endure a high vacuum. The spillage is of a lower thickness and is confined to the cavity corners. As both electric and magnetic field intensity are low in this region, the effect of spillage on the cavity resonance frequency and the intrinsic quality factor may not be significant. However, the surface phenomena like field emissions, electric breakdowns, and multipacting in the area can not be ruled out. The ultrasonic cleaning of the cavity may result in a smoother spillage region, minimizing the likelihood of these surface phenomena.

8 RF Testing of the Cavity

The next phase of the cavity development process is to test the cavity at the nominal RF power. Additionally, the field profile in the cavity must be measured. All these aspects are discussed in this chapter. In the first section, the cold RF testing results obtained before brazing the cavity are compared against the brazed cavity. The following section discusses the investigative steps carried out to identify the reason behind the cavity's low intrinsic quality factor. The third section describes the bead pull measurement setup, and the results of the field profile measurements are presented. The penultimate section describes the warm RF test setup and the vacuum conditioning of the cavity. The last section outlines the issues with the developed deflecting cavity and also possible solutions to improve the cavity design.

8.1 Initial RF Measurements

The scattering characteristics measured across a frequency range reveal the cavity's resonance frequency as well as the coupling factors of the fundamental power coupler and pick-up probe [30]. The two-port S-parameter measurements were carried out using a vector network analyzer (N5230A) from Agilent Technologies. Prior to the measurements, the coaxial measuring cables were calibrated. The main parameters, the transmission coefficient S_{21} and reflection coefficient S_{11} are shown in Figure 8.1. The frequency at which S_{21} (S_{11}) is maximum (minimum) corresponds to the resonance frequency f_0 of the cavity, where the maximum power is transferred to the cavity. At other frequencies, the RF power fed into the cavity decreases, and half the maximum RF power is fed into the cavity at the frequencies -3 dB below the maximum value of S_{21} . The difference between these frequencies is known as bandwidth (Δf_{bw}). The loaded quality factor, Q_L , is the ratio of the resonance frequency to its bandwidth ($f_0/\Delta f_{bw}$). The representation of S_{11} on a Smith chart indicates

8 RF Testing of the Cavity

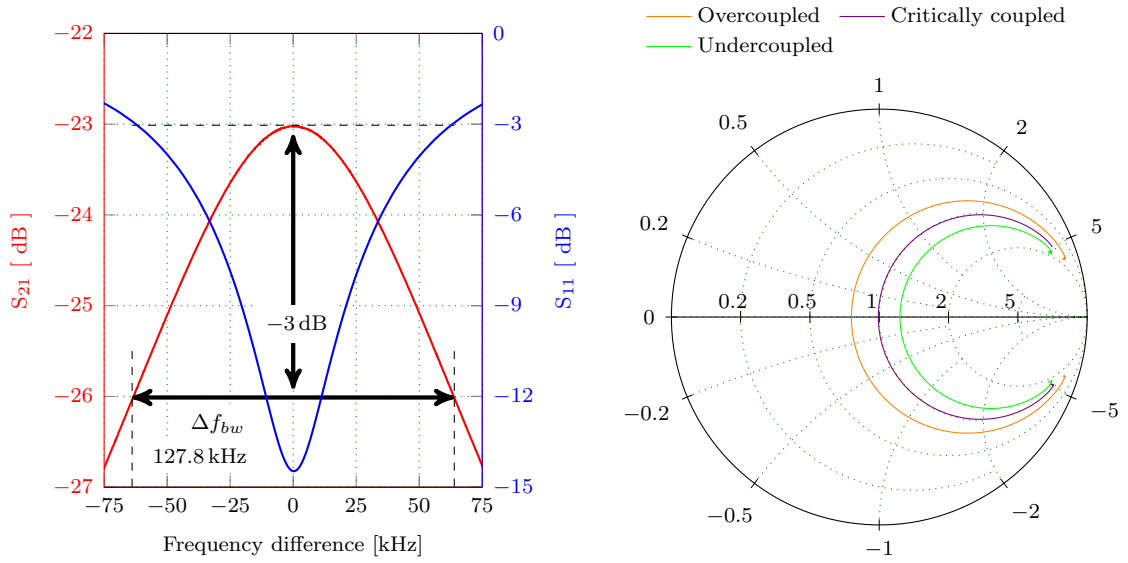


Figure 8.1: Calculating loaded quality factor of a cavity Q_L from the measured S_{21} parameter (left) and representation of S_{11} on a Smith chart for three different coupling factors (right).

whether the coupler is undercoupled, overcoupled, or critically coupled (Figure 8.1), which helps to orient the coupler to achieve a desired coupling factor [29].

The physical and RF properties of the cavity measured during pre- and post-brazing are compared with the design values in Table 8.1. After the frequency pre-tuning of the cavity, the aperture of the cavity was measured as 30.16 mm, whereas the aperture increased to 30.2 mm post-brazing. The stem was not accessible to measure its parallelism, pitch and tilt from the outside. Furthermore, the resonance frequency of the brazed cavity increased by +66 kHz, but this increase can easily be compensated by the available frequency tuners. The intrinsic quality factor of the cavity before brazing was measured to be 5800, which was almost half the design value. This can be attributed to the electrical disjoint between the cavity parts, which increased the surface resistance and lowered the Q_0 . It was expected that the brazing would provide a good electrical path for the currents to flow, improving the Q_0 . Though the measurement after brazing showed a slight improvement in the quality factor, it only amounted to half of the design value.

Table 8.1: Cavity properties measured during pre- and post-brazing, and the design values.

Parameter		Design	Pre-brazing	Post-brazing	Unit
Cavity aperture	v_{ap}	30	30.16	30.2	mm
RF frequency	f_0	273	273.056	273.122	MHz
Coupler orientation*		45	90	80	°
Q-loaded	Q_L	5094	2700	3250	-
Q-unloaded	Q_0	10188	5800	6500	-
Tuning range	$+\Delta f_{tr}$	+1.81	+1.846	+1.859	MHz
	$-\Delta f_{tr}$	-1.67	-1.679	-1.674	MHz

* Orientation of the main power coupler to obtain $\beta_{in} \approx 1$

8.2 Investigation of the Low Quality Factor

The resonance frequency of the deflecting mode measured pre- and post-brazing was close to the design value, whereas the measured intrinsic quality factor was half the design value. The power losses in the cavity determine the intrinsic quality factor. A lower quality factor increases the power losses in the cavity, and a decrease in the quality factor by half doubles the RF power required to achieve a specified kick voltage. Therefore, it was important to investigate the degradation of the quality factor in the present case. The loaded quality factor of a cavity Q_L is given as

$$\frac{1}{Q_L} = \frac{1}{Q_0} + \frac{1}{Q_{in}} + \frac{1}{Q_{pu}}, \quad (8.1)$$

where Q_0 is the intrinsic quality factor of the cavity, Q_{in} and Q_{pu} are the external quality factors of the fundamental power coupler and pick-up probe, respectively. Q_{in} and Q_{pu} refer to the power coupled out of the cavity, and Q_0 refers to all the other power losses, i.e. the power loss on the frequency tuners, the power coupler, the pick-up probe, the RF filter at the vacuum port, and the power loss on the actual cavity surface. Thus, each of these losses must be assessed independently to determine the element that lowers the cavity's quality factor. In addition to these losses, the cavity surface roughness influences the power loss, and its effect is

discussed separately.

8.2.1 Effect of the Cavity Surface Roughness

At high frequencies, the current induced by the RF field is mostly confined to the conductor's surface. Thus, the surface roughness of a cavity influences the flow of the current, affecting the cavity's quality factor. An increase in the surface roughness results in a longer path for the surface currents, which can be quantified as a decrease in the material conductivity [179]. In [180], Hammerstand and Bekkadal presented an expression for the conductivity of a material with a surface roughness defined as

$$\frac{\sigma_{R_z}}{\sigma} = \left[1 + \frac{2}{\pi} \tan^{-1} \left(1.4 \cdot \left(\frac{R_z}{\delta} \right)^2 \right) \right]^{-2}, \quad (8.2)$$

where δ denotes the skin depth, σ the DC conductivity of a material, and σ_{R_z} the conductivity of the material due to the RMS surface roughness of R_z .

The expression for computing the quality factor of a cavity, Q_0 , and the surface resistance of a cavity, R_s , given in equations (2.48) and (2.51) can be combined to express Q_o in terms of the electrical conductivity σ as

$$Q_0 = \frac{\omega U}{P_c} = \sqrt{4f_0\mu_o} \sqrt{\sigma} \frac{\iiint_{\Omega} \mathbf{H} \cdot \mathbf{H}^* dV}{\oint_S |\mathbf{H}_t|^2 dS} \quad (8.3)$$

As a result, the new quality factor of a cavity is expressed as

$$\frac{Q_{R_z}}{Q_0} = \sqrt{\frac{\sigma_{R_z}}{\sigma}}. \quad (8.4)$$

The ratios expressed in equations (8.2) and (8.4) for the different values of R_z/δ are plotted in Figure 8.2. In case $R_z \ll \delta$, the decrease in the quality factor is small, but the quality factor decreases rapidly as R_z increases. Moreover, for $R_z/\delta > 2$, the quality factor gets saturated at half the original value.

The deflecting cavity's quality factor depends predominantly on the cavity surface, as the power loss is more significant in this area than on the cavity components. Undoubtedly, the surface roughness of this area has a more significant influence on the cavity's quality factor. In simulation, the electrical conductivity of the copper was set to 5.9×10^7 S/m, and the intrinsic quality factor of the plain cavity was

8 RF Testing of the Cavity

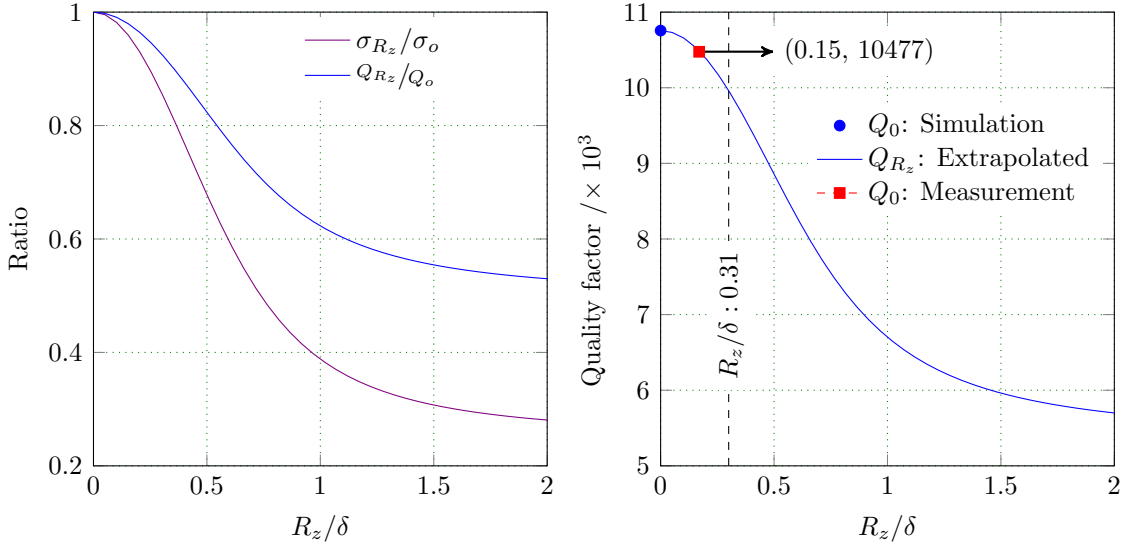


Figure 8.2: The variation of σ_{R_z}/σ and Q_{R_z}/Q for different ratios of the surface roughness to skin depth (R_z/δ) as predicted through the Hammerstand and Bekkadal model [179] (left). Extrapolation of the cavity quality factor obtained from the simulation using the model, including the measured quality factor and the RMS surface roughness (right).

obtained as 10756. Using this value in equation (8.4), the expected quality factor at different ratios of R_z/δ is plotted in Figure 8.2. During fabrication, the RMS surface roughness of the cavity was approximated as $1.25\ \mu\text{m}$, which corresponds to R_z/δ of 0.31. For this ratio, the estimated quality factor from the Hammerstand and Bekkadal model is ≈ 10000 (Figure 8.2). However, the intrinsic quality factor of the plain cavity was measured as 10476 (discussed in the next section), which is higher than the value estimated through the model. This suggests that the approximated R_z of $1.25\ \mu\text{m}$ was a very conservative estimation. Furthermore, the detrimental impact of the filler leakage on the copper’s electrical conductivity can be ruled out. Most significantly, the main cavity can be crossed off the list of probable factors that degrade the cavity’s quality factor.

8.2.2 Influence of the Cavity Components

The initial S-parameter measurements were carried out with all the cavity components installed. Thus, the calculated intrinsic quality factor includes the effect of the plain cavity and its components. It is impossible to obtain the influence of each component

8 RF Testing of the Cavity

on the quality factor from this measurement setup. Moreover, if the existing power coupler and the pick-up probe are used as the measurement ports, the effect of these components on Q_0 can not be isolated. Therefore, two loosely coupled antennas with an external quality factor greater than 10^7 were placed at the beam pipe for S-parameter measurements. Figure 8.3 shows a sketch of the measurement setup with the cavity, the labeled cavity ports, the cavity components, and the antennas.

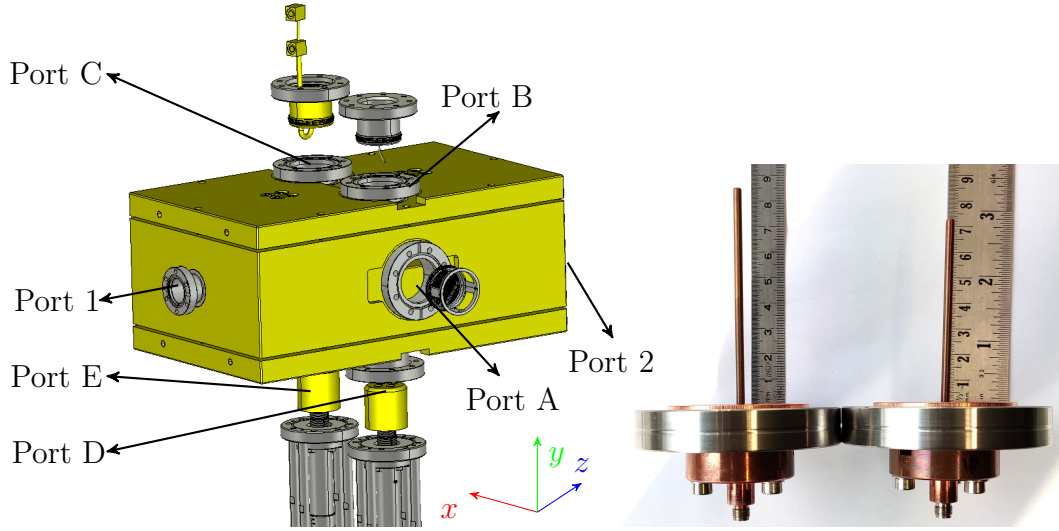


Figure 8.3: A sketch of the cavity showing all the cavity ports and the components associated with the ports (left), and the two over-coupled antennas are used at the Port 1 and Port 2 (right) for measuring the S-parameters.

Since the quality factors of the measuring antennas are three orders of magnitude larger than of the cavity, the quality factor obtained from the measured S_{21} parameter can be regarded as the measured quality factor of the cavity (cavity and the installed components) and is denoted by Q_m . Therefore, the quality factor Q_m obtained with all the cavity components installed can be rendered as

$$\frac{1}{Q_m} = \frac{1}{Q_{pc}} + \frac{1}{Q_1} + \frac{1}{Q_2} + \frac{1}{Q_A} + \frac{1}{Q_B} + \frac{1}{Q_C} + \frac{1}{Q_D} + \frac{1}{Q_E}, \quad (8.5)$$

where Q_{pc} refers to the intrinsic quality factor of the plain cavity, Q_1 and Q_2 are the external quality factor of the measurement antennas placed at Port 1 and Port 2, respectively, Q_A , Q_B , Q_C , Q_D , and Q_E are the quality factors due to the power loss on the components installed at Port A to E, respectively.

8 RF Testing of the Cavity

Table 8.2: Measurement and simulation values of the cavity resonance frequency and the quality factor. The measurements are carried out with the ports kept open and/or close using a stainless steel flange.

Parameter	Ports							Simu- lation
Open ports	A to E	B to E	A, C, D, E	A, B, D, E	A, B, C, E	A, B, C, D	None	
Closed ports	None	A	B	C	D	E	A to E	
f_0 [MHz]	270.250	270.253	270.255	270.251	270.251	270.254	270.256	270.326
Q_{pc} [-]	10477	10435	10496	10457	10477	10458	10476	10741

8.2.2.1 Plain cavity

The external quality factors Q_1 and Q_2 of the measurement antenna can be neglected from equation (8.5) as they have a quality factor in the range of 10^7 . If no other cavity components are installed, the measured quality factor Q_m then would directly correspond to the intrinsic quality factor of the plain cavity Q_{pc} . The quality factors measured with the cavity ports kept open or closed by a metallic flange are presented in Table 8.2. The results suggest that the ports are long enough to dampen the deflecting mode fields; therefore, the status of the port (open or closed) has a negligible influence on the cavity's resonant frequency and the quality factor. However, the intrinsic quality factor obtained from the simulation differs slightly from the measured value. This discrepancy in value can be attributed to the surface roughness of the cavity. Hereafter, the intrinsic quality factor Q_{pc} of the plain cavity is set to 10477, and the measurement of the external quality factor of the components is discussed next.

8.2.2.2 RF Filter at Port A

The ultra-high vacuum required inside for the cavity operation is achieved using a vacuum pump, which connects the cavity through Port A. A leak of the cavity field via Port A might damage the pump. In the pre-buncher cavity of the ELBE, an RF filter was used to avoid the leakage of the cavity field (Figure 8.4 (a)). It was therefore decided to use a similar RF filter at the vacuum port in the present work. The filter has a rectangular steel mesh firmly fixed on a steel cup by a curved steel

8 RF Testing of the Cavity

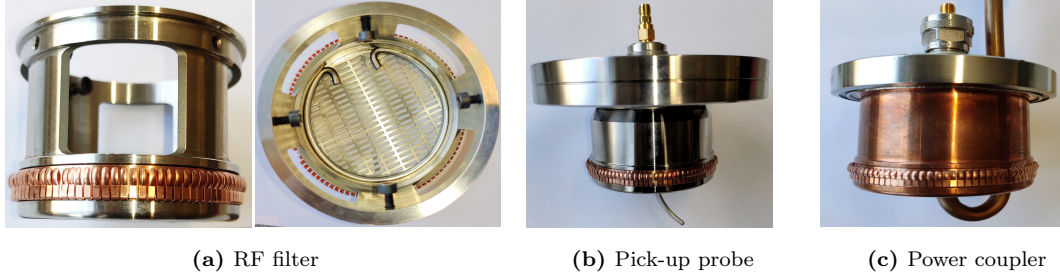


Figure 8.4: A snapshot of the actual RF filter (a), pick-up probe (b), and main power coupler (c) of the cavity which are placed at Port A, Port B and Port C, respectively.

rod. The mesh gap is small enough to block the field but large enough to pump the particles out of the cavity.

In the simulation, the RF filter shape was defined as a flat steel surface. The results of the simulation are given in Table 8.3, with the closing of Port A increased the cavity resonance frequency by 213 kHz, and the external quality factor of the steel surface was computed to be 6.27×10^5 . The results of the measurement with the RF filter at Port A are listed in Table 8.3, and the frequency shift from the measurement was almost identical to that obtained from the simulation. The measured Q_m , on the other hand, was less than half of the simulation's value. Usually, a corrugated copper strip (RF fingerstock) surrounds the cavity component to avoid RF leakage through the gap between the component and the cavity. The measurement with

Table 8.3: The cavity resonance frequency and the quality factor were measured with the RF filter and the pick-up probe placed at Port A, and the simulation results.

Port A		f_0 [MHz]	Q_m	Q_A
Simu- lation	Plain cavity	270.326	10741	-
	RF filter (flat surface)	270.539	10572	6.27×10^5
Measurement	Plain cavity	270.252	10465	-
	RF filter	270.489	4796	8852
	RF filter & RF fingerstock	270.449	6816	19506
	Pick-up probe	270.480	9820	156597
	Pick-up probe & RF fingerstock	270.448	9983	211276

this ring improved the Q-factor, but it was still lower than the designed value. The pick-up probe was inserted at Port A to confirm that the decrease in the quality factor is only attributable to the RF filter and not the position of the port in the cavity. The measured Q_m in this arrangement differed by less than 4.6% of that of the plain cavity, implying that mainly the RF-filter lowers the quality factor. The RF filter has a higher surface resistance compared to that of the flat surface of the pick-up probe. Moreover, the low conductivity steel mesh provides a small area for the surface currents to flow, and also the poor electrical contact between the mesh and the cup further increases the surface resistance. This results in the degradation of the Q_0 . It was also necessary to determine whether any other cavity component contributes to the decline of the quality factor.

8.2.2.3 The Pick-up Probe at Port B

The cavity's field is sampled for measurement by the pick-up probe, and the complete component is constructed of stainless steel (Figure 8.4 (b)). If the pick-up antenna is terminated with a matched load, the field coupled out of the cavity would be dissipated at the load, influencing the quality factor measurement. Therefore, the measurements were carried out with the pick-up probe terminated with an open circuit. The simulation and measurement results with the pick-up probe placed at Port B are listed in Table 8.4. The resonance frequency shift due to the pick-up probe at Port B matches the simulation result. Moreover, the Q_B obtained from the simulation correlates well with the measurement values. The high Q_B of the pick-up probe suggests that it has less influence on the degradation of the cavity quality factor.

8.2.2.4 Fundamental Power Coupler at Port C

The power coupler handles a higher RF power than the pick-up probe; therefore, it is constructed of copper with an active water cooling mechanism (Figure 8.4 (c)). The loop couples to the cavity magnetic field, and its orientation determines the coupling strength. The FPC can be terminated with a matched load (50Ω) or an

8 RF Testing of the Cavity

Table 8.4: Results of the RF measurement carried out with the pick-up probe placed at Port B of the cavity, and the simulation results are presented for a comparison.

		Port B	f_0 [MHz]	Q_m	Q_B
Simulation		plain cavity	270.326	10741	-
		Pick-up probe	270.532	10572	6.93×10^5
Measurement		plain cavity	270.252	10465	-
		Pick-up probe	270.453	10006	2.28×10^5
		Pick-up probe+RF fingerstock	270.486	10285	5.98×10^5

open circuit. If the termination is open, equation (8.5) reduces to

$$\frac{1}{Q_m} = \frac{1}{Q_{pc}} + \frac{1}{Q_C}. \quad (8.6)$$

However, if the FPC is terminated with a matched load, the coupled field is absorbed at the load. Then the equation (8.5) modifies to

$$\frac{1}{Q_m} = \frac{1}{Q_{pc}} + \frac{1}{Q_C} + \frac{1}{Q_{in}}. \quad (8.7)$$

The cavity resonance frequency and the quality factor measured with the main coupler placed at Port C in different orientations are presented in Figure 8.5. The loop orientation is considered to be 0, when the loop is directed towards the stem,

Table 8.5: Results of the RF measurement carried out with the power coupler placed at Port C of the cavity with open and matched terminations.

Port C Main coupler	Coupler orientation [°]	RF frequency [MHz]	Measurement Q_m	Calculated	
				Q_C	Q_{in}
Open	0	270.481	10189	3.86×10^5	-
50 Ω	0	270.514	3710	3.86×10^5	5834
Open	45	270.478	10155	3.43×10^5	-
50 Ω	45	270.515	5175	3.43×10^5	10552
Open	90	270.504	10282	5.88×10^5	-
50 Ω	90	270.506	9943	5.88×10^5	301575

8 RF Testing of the Cavity

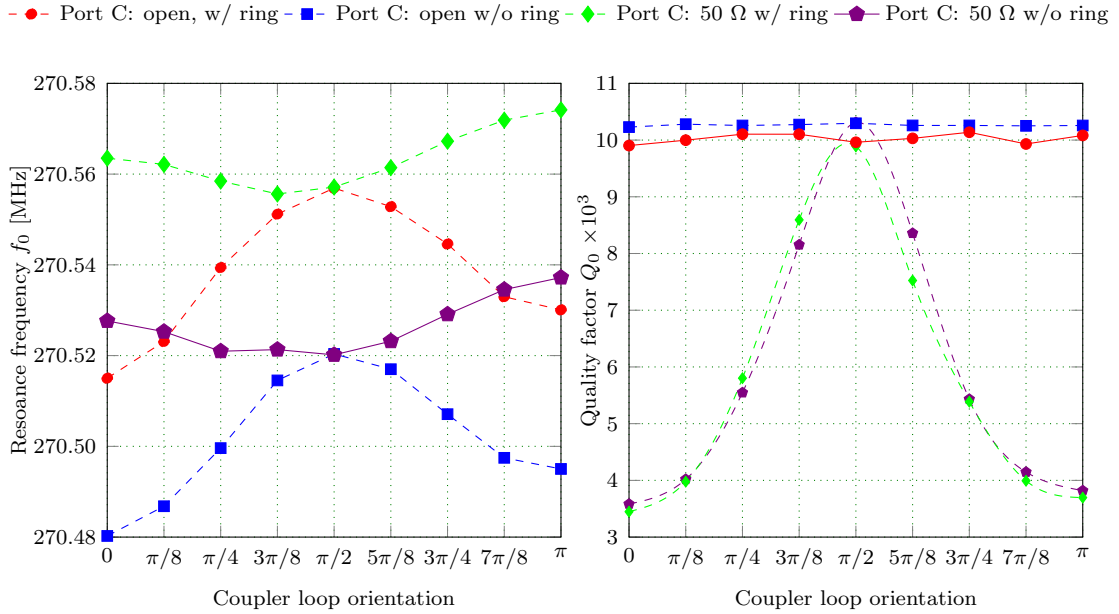


Figure 8.5: The cavity resonance frequency and the quality factor measured for different orientations of the coupler loop with and without the RF fingerstock. Here, at 0 the loop is directed towards the stem, at $\pi/2$ it is parallel to the stem, and at π it is oriented away from the stem.

and π it is oriented away from the stem. The resonance frequency varies sinusoidally based on the loop orientation. This corresponds to the field perturbed by the loop. Similarly, the quality factor measured with the power coupler terminated in a matched load varied sinusoidally. Table 8.5 shows the Q_C and Q_{in} computed for different orientations of the main coupler using the equations (8.6) and (8.7). The quality factor values computed from the measurements are consistent for different orientations and match the simulation values (Figure 5.2). Since the power coupler at Port C has a higher Q_C , it does not contribute to the deterioration of the cavity's quality factor.

8.2.2.5 Frequency Tuners at Port D and Port E

The deflecting mode frequency is tuned by driving the two plunger-type tuners in and out of the cavity. Therefore, the effect of a tuner on the cavity quality factor depends on the position of the tuner head. The initial set of measurements were taken by separately moving the tuner one at a time at three different positions. Subsequently,

8 RF Testing of the Cavity

Table 8.6: Results of the RF measurement carried out with the tuners placed separately at their respective ports and in three different positions. Here, ‘-1’, ‘0’, and ‘+1’ refers to the tuner head completely moved out of the cavity (at -25 mm), nominal position (at 0 mm), and completely inside the cavity (at 25 mm), respectively.

Tuner position		f_0 [MHz]		Q_m		Computed Q_D/Q_E	
Port D	Port E	RF fingerstock	w/o fingerstock	RF fingerstock	w/o fingerstock	RF fingerstock	w/o fingerstock
-	-	270.250	270.250	-	10477	-	-
-	-1	270.484	270.453	9799	10458	1.51×10^5	5.77×10^6
-1	-	270.452	270.435	9979	10437	2.09×10^5	2.73×10^6
-	0	271.313	271.261	8687	9761	5.09×10^4	1.42×10^5
0	-	271.247	271.200	8499	9767	4.50×10^4	1.44×10^5
-	+1	272.214	272.194	6447	4536	1.68×10^4	7.99×10^3
+1	-	272.073	272.046	6414	3559	1.65×10^4	5.39×10^3

the quality factor of an individual tuner (Q_D or Q_E) was obtained at these positions independent of the other tuner (Table 8.6). The tuner position at ‘-1’, ‘0’, and ‘+1’ refers to the tuner completely moved out of the cavity (at -25 mm), nominal position (at 0 mm), and completely inside the cavity (at $+25$ mm), respectively. As the tuner advances into the cavity, it perturbs the stronger magnetic field, and the cavity’s quality factor decreases sharply with the inward movement of the tuner. The quality factor of a tuner drops by an order of magnitude when it is entirely outside the cavity (position ‘-1’) compared to when it is completely inside (position ‘+1’). In the case of a tuner without an RF fingerstock, the corresponding decrease is of three orders of magnitude.

In the second set of measurements, the collective effect of both tuners on the Q_m was measured. The tuners were placed simultaneously at their respective ports, and the measurements were carried out with the tuners in three different positions (Table 8.7). The Q_D and Q_E values computed in Table 8.6, and the measured Q_{pc} of the plain cavity were used to predict the Q_m (Table 8.7). The error between the measured and the predicted values for the frequency and the quality factor is low for the tuner positioned at ‘-1’ and ‘0’. The error increases when the tuner is completely inside the cavity (position ‘+1’). At the nominal operating position of the tuner (position ‘0’), the combined quality factor of the tuners Q_{DE} was measured as 3.12×10^5 . A high quality factor of the tuners in the nominal position suggests that these tuners

8 RF Testing of the Cavity

do not contribute strongly towards the cavity quality factor degradation.

Table 8.7: Results of the RF measurement carried out with both tuners and RF fingerstock placed simultaneously at their respective ports at three different positions, and also the quality factor predicted from the values given in Table 8.6.

Tuner position		f_0 [MHz]			Q_m			Q_{DE}
Port D	Port E	Meas	Predi	Err[kHz]	Meas	Predi	Err[%]	Meas
-1	-1	270.681	270.686	5	9127	9359	2.54	7.08×10^5
-1	0	271.476	271.515	39	8195	8342	1.79	3.76×10^5
0	-1	271.474	271.481	7	8221	8046	2.13	3.82×10^5
0	0	272.296	272.310	14	7842	7282	7.14	3.12×10^5
+1	0	273.121	273.136	15	6181	5692	7.91	1.51×10^4
0	+1	273.128	273.211	83	6544	5644	13.75	1.74×10^4
-1	+1	272.306	272.416	110	6758	6260	7.34	1.90×10^4
+1	-1	272.305	272.307	2	6678	6147	7.95	1.84×10^4
+1	+1	274.006	274.037	31	5532	4639	16.14	1.17×10^4

8.2.3 Conclusion

The quality factor of the cavity components obtained previously is listed in Table 8.8. Substituting these values in equation (8.5) one can obtain the intrinsic quality factor of the cavity with the parts installed (Table 8.9). In the case of a cavity with all the components installed, the quality factor Q_m calculated with the individual measured values (Table 8.8) agrees with that of the directly measured value (Table 8.9). In addition, the relevant simulation results are nearly identical. On the other hand, the measured quality factor is significantly lower than the value obtained from the simulation. The discrepancy between the simulation and measurement values can likely be attributed to several factors, including variations in the conductivity of copper and steel, non-uniform current flow resulting from brazing joints, and surface roughness of the cavity. In the measurement setup, almost 33% of the total power loss occurs on the RF filter, resulting in a lower quality factor. The RF filter contributes strongly to the degradation of the quality factor compared to other cavity

8 RF Testing of the Cavity

Table 8.8: The quality factor of the individual cavity components obtained from the measurements and simulation.

Port	Component	Symbol	Measurement		Simulation	
			Q-factor	% of $1/Q_m$	Q-factor	% of $1/Q_m$
-	Plain cavity	Q_{pc}	10465	61.8	10741	94.0
Port A	RF filter	Q_A	19506	33.2	6.27×10^5	1.6
Port B	Pick-up probe	Q_B	5.98×10^5	1.1	6.93×10^5	1.5
Port C	Main coupler	Q_C	5.88×10^5	1.9	2.26×10^6	0.4
Port D	Tuner 1	Q_D	6.24×10^5	1.0	8.25×10^5	1.2
Port E	Tuner 2	Q_E	6.24×10^5	1.0	7.96×10^5	1.3

components. After removing the RF filter from Port A, a considerable increase in the quality factor was measured (Table 8.9). However, this might lead to leaking of the cavity field to the vacuum pump. Because the operating mode is one order lower than the cut-off frequency of the Port A (Table 5.1), the field will decay substantially before reaching the opposite end of the port. As a result, it was decided not to use the RF filter at Port A, which increased the measured quality factor by almost 50%.

Table 8.9: The quality factor of the cavity calculated using equation 8.5 with the quality factor of the individual components listed in Table 8.8.

	Q_m of a cavity with all the components	Q_m of a cavity without RF filter
Calculated from the measured values	6468	9791
Directly Measured	6500	9551
Calculated from the simulation values	10096	10188
Obtained from simulation	10261	10718

8.3 Bead-pull Measurement

The RF measurements have confirmed the presence of a mode at 273 MHz. Moreover, the characteristics of the frequency tuners and main coupler obtained from the simulation correlate with the results of the S-parameters measurement. These findings, on the other hand, fall short of establishing the field profile and its strength along the cavity axis. A direct field measurement technique with an antenna might disturb the cavity field profile. This necessitates the use of an indirect field measuring method - bead-pull measurement technique - a bead disturbs a tiny amount of the cavity field and the corresponding shift in the resonance frequency shift is measured which correlates with the disturbed field [176]. Recalling the equation (6.1), the relative change of the cavity resonance frequency is given as

$$\frac{\Delta f_{pr}}{f_0} = \frac{1}{4U} \iiint_{\Delta V_{pr}} (\mu_0 \mathbf{H} \cdot \mathbf{H} - \varepsilon_0 \mathbf{E} \cdot \mathbf{E}) dV, \quad (8.8)$$

where U is the stored energy in the cavity, ΔV_{pr} is the volume of the perturbation in the cavity, $\Delta f_{pr}(= f_{pr} - f_0)$ is the frequency difference, f_0 and f_{pr} are the resonance frequency of the unperturbed and perturbed cavity, respectively, and \mathbf{H} and \mathbf{E} are the unperturbed magnetic and the electric field at the perturbed location. If the perturbing volume is very small, then the aforesaid expression can be represented as follows [181]:

$$\frac{\Delta f_{pr}}{f_0} = \underbrace{\alpha_{\mathbf{E}_\perp} \varepsilon_0 \frac{|\mathbf{E}_\perp|^2}{U} + \alpha_{\mathbf{E}_\parallel} \varepsilon_0 \frac{|\mathbf{E}_\parallel|^2}{U}}_{\text{electric field}} + \underbrace{\alpha_{\mathbf{H}_\perp} \mu_0 \frac{|\mathbf{H}_\perp|^2}{U} + \alpha_{\mathbf{H}_\parallel} \mu_0 \frac{|\mathbf{H}_\parallel|^2}{U}}_{\text{magnetic field}}, \quad (8.9)$$

where ε_0 and μ_0 are the permittivity and the permeability in the vacuum, and \mathbf{E}_\perp , \mathbf{E}_\parallel , \mathbf{H}_\perp , and \mathbf{H}_\parallel are the electric and the magnetic fields perpendicular and parallel to the perturbing object. The coefficients $\alpha_{\mathbf{E}_\perp}$, $\alpha_{\mathbf{E}_\parallel}$, $\alpha_{\mathbf{H}_\perp}$, and $\alpha_{\mathbf{H}_\parallel}$ are the form factors of the perturbing object associated with \mathbf{E}_\perp , \mathbf{E}_\parallel , \mathbf{H}_\perp , and \mathbf{H}_\parallel , respectively. These form factors depend on the perturbing object's geometry and material [74]. The analytical formulas to calculate these form factors of a simple beads are discussed in [165, 182]. Otherwise, a pill-box cavity is used to calibrate the beads [74, 181]. The perturbing objects that affect a specific field component can be obtained by carefully selecting the perturbing material's shape, size, permittivity and permeability. For instance,

a needle-shaped ceramic object will majorly perturb \mathbf{E}_{\parallel} field without affecting the magnetic field, whereas a metallic sphere will perturb all the field components evenly.

8.3.1 Measurement Setup

A bead-pull measurement setup was built to measure the field profile along the axis of the deflecting cavity (Figure 8.6). A thin thread (fishing line) runs along the length of the cavity axis, and a small perturbing object (bead) was threaded on to this string. The one end of the string was attached to a DC motor and the other to a counterweight. The DC motor maintains a consistent rotation speed at a set voltage, causing the bead to move at a constant rate. As the bead travels along the cavity axis it perturbs the field and the shift in cavity resonance frequency was continually monitored. The measurement of the frequency shift is preferred when the bead moves in steps and the frequency changes are significant. In the case of a continuously moving bead and at smaller frequency changes, measuring the phase shift of the resonance frequency is more reliable. The measured phase shift, $\Delta\phi$ was converted back to the relative frequency change using

$$\frac{\Delta f_{pr}}{f_0} = \frac{1}{2Q_L} \tan \Delta\phi, \quad (8.10)$$

where $\Delta\phi$ is the phase shift of the S_{21} parameter measured at f_0 .

The initial field measurements were carried out with different fishing wires attached to a metallic spherical bead. A string with a diameter of 0.08 mm provided a smoother

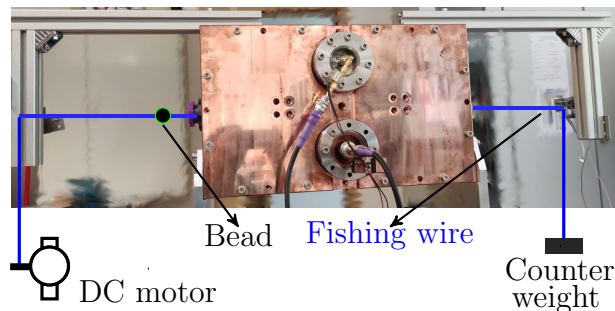


Figure 8.6: The actual bead-pull measurement setup built to measure the field profile along the cavity axis of a deflecting cavity. A small perturbing object (bead) tethered by a thin string (fishing wire) is moved along the cavity axis using a DC motor.

field profile than the other strings. A constant 10 V applied to the DC motor provided a linear speed of 19 mm s^{-1} , which eventually allowed to measure the RF phase at every 0.1 mm along the cavity axis.

8.3.2 Field Profile From the Simulation

The deflecting mode has a strong transverse electric field between the plates, whereas the magnetic field is present only near the ends of the cavity. The electric and magnetic field profiles along the longitudinal direction at on-axis and at an off-set of 11 mm are shown in Figure 8.7. The strong transverse electric field between the stems does not vary significantly between on- and off-axis. Similarly, the on-axis transverse magnetic field is unaltered compared to the off-axis. In contrast, a strong longitudinal electric field E_z occurs off the cavity axis, but it is essentially non-existent on the cavity axis. The magnetic field is scaled by η so that the kick strength due to the field components is comparable. Moreover, the field components are normalized to the square root of the cavity's energy \sqrt{U} .

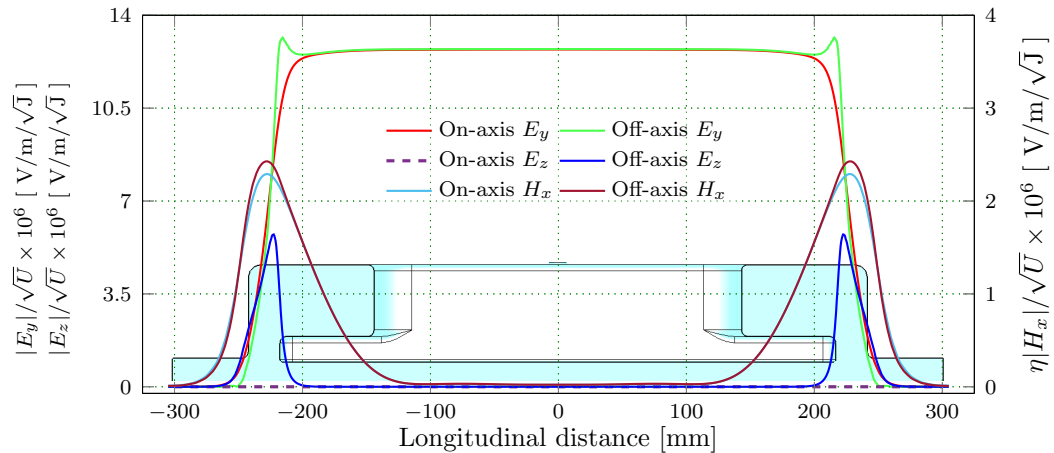






Figure 8.7: The on- and off-axis electric and magnetic field components of the deflecting mode along the longitudinal direction obtained through simulation. In this case, an offset distance Δy of 11 mm is considered.

Table 8.10: Geometrical dimensions of the needle and sphere made of dielectric and metal used in the bead-pull measurement experiment.

Type (notation)	Diameter [mm]	Length [mm]	
Dielectric needle (dn)	1	9.07	
Metallic needle (mn)	0.94	9.03	
Dielectric sphere (ds)	5.8	-	
Metallic sphere (ms)	5	-	

8.3.3 Field Profile From the Measurements

To obtain the transverse mode field profile along the beam axis, the transverse fields $E_y(0, 0, z)$ and $H_x(0, 0, z)$, as well as the longitudinal field $E_z(0, 0, z)$ must be measured¹. It is impossible to measure all these field components using a single bead. The on- and off-axis transverse fields are measured using a spherical bead due to its non-directional geometry. The cylindrical bead (needle) couples strongly to the field parallel to its length, and it is preferred for measuring the longitudinal fields. Furthermore, a ceramic bead perturbs only the electric field, whereas a metallic bead disturbs both the electric and the magnetic fields. The dimensions of the ceramic and metallic beads used in this measurements are given in Table 8.10.

8.3.3.1 Transverse On-axis Field Components

Spheres have a non-directional geometry, and a spherical bead's perturbation of the cavity field is also non-directional. Therefore, the transverse fields were measured using the spherical beads (Table 8.10). In the deflecting mode, the cavity only has the transverse fields along the cavity axis, and the relative frequency change for a dielectric and metallic sphere is given as

$$\frac{\Delta f_{pr}}{f_0} = \alpha_{\mathbf{E}_{\perp}, ds} \varepsilon_0 \frac{|\mathbf{E}_{\perp}|^2}{U}, \quad (8.11)$$

$$\frac{\Delta f_{pr}}{f_0} = \alpha_{\mathbf{E}_{\perp}, ms} \varepsilon_0 \frac{|\mathbf{E}_{\perp}|^2}{U} + \alpha_{\mathbf{H}_{\perp}, ms} \mu_0 \frac{|\mathbf{H}_{\perp}|^2}{U}, \quad (8.12)$$

¹These terms are simply represented as E_y , H_x , and E_z .

8 RF Testing of the Cavity

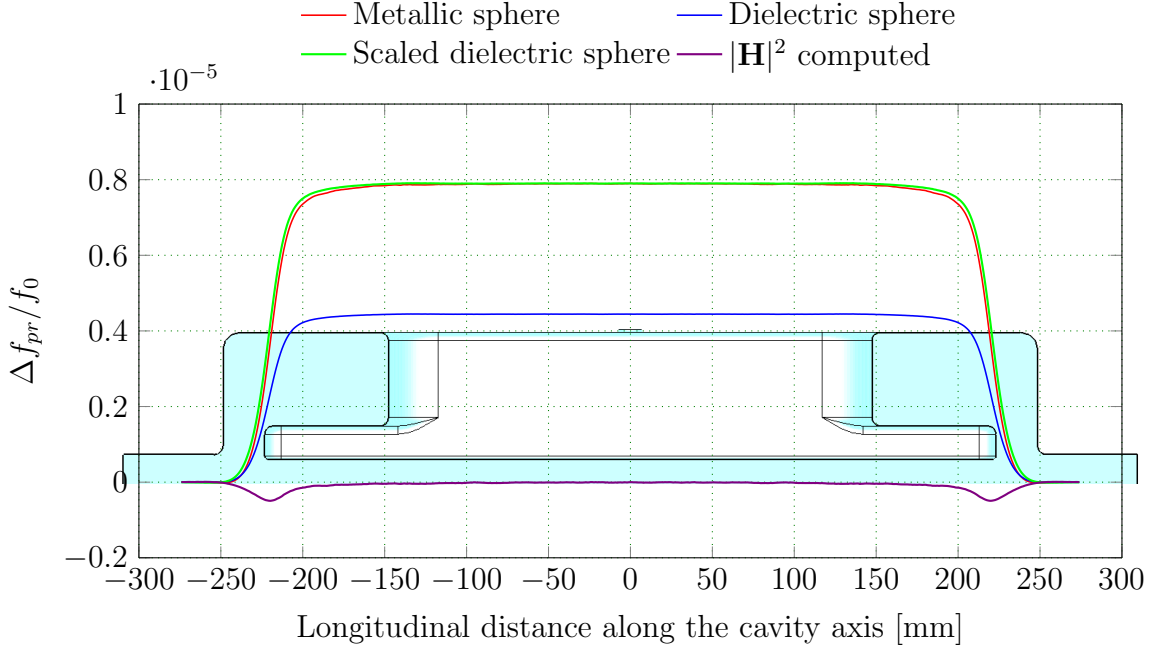


Figure 8.8: The relative frequency change along the cavity axis measured with the metallic and the dielectric spherical bead. The graph represents the mean of 40 measurements, and the difference between the values of the scaled dielectric and those of the metallic sphere render $|\mathbf{H}|^2$.

where subscripts ds and ms refer to the dielectric and the metallic sphere, $\alpha_{\mathbf{E}_{\perp,ds}}$ is the tangential electric form factor of the dielectric sphere, and $\alpha_{\mathbf{E}_{\perp,ms}}$ and $\alpha_{\mathbf{H}_{\perp,ms}}$ are the tangential electric and magnetic form factors of the metallic sphere, respectively. The phase shift due to the metallic and dielectric spherical bead moving along the cavity axis was converted back to the relative frequency change using equation (8.10). More than 40 measurements were performed for each bead to rule out any systematic errors, and the mean of these measurements is presented in Figure 8.8. The frequency change obtained with the dielectric sphere directly corresponds to E_y , whereas the influence of H_x has to be extracted from the values measured with the metallic bead. The mode field profile determined from the simulation (Figure 8.7) indicates that only E_y exists at the cavity center. Therefore, the measured frequency change due to both the metallic and dielectric bead at the cavity center should only correspond to E_y . Thus, taking the difference of the metallic and dielectric sphere values would aid in isolating H_x . However, the form factors, $\alpha_{\mathbf{E}_{\perp,ds}}$ and $\alpha_{\mathbf{E}_{\perp,ms}}$ are not the same, and as a

result, the values measured at the cavity center differ in both the cases. Nevertheless, the dielectric field values were scaled such that the values obtained at the cavity center were identical to those of the metallic sphere. Subsequently, the difference between the metallic and scaled dielectric values renders $|\mathbf{H}|^2$. Qualitatively, the field profiles obtained from the bead pull measurement (Figure 8.8) fit the simulation results (Figure 8.7).

8.3.3.2 Longitudinal Off-axis Field Components

The on-axis field components obtained in the previous measurement were sufficient to compute the R_{\perp}/Q of the cavity. In addition to this, the longitudinal electric field values can also be used to calculate R_{\perp}/Q on the basis of the Panofsky-Wenzel theorem. The longitudinal electric fields were measured using a thin cylindrical bead (needle). The off-axis longitudinal field can be determined using either a metallic or a dielectric needle. First, the field measurement was carried out using a dielectric needle. The relative frequency change due to a dielectric needle at the cavity on- and off-axis is given as

$$\frac{\Delta f_0}{f_0} = \alpha_{\mathbf{E}_{\perp},dn} \varepsilon_0 \frac{|\mathbf{E}_{\perp}|^2}{U}, \quad (8.13)$$

$$\frac{\Delta f_0}{f_0} = \alpha_{\mathbf{E}_{\parallel},dn} \varepsilon_0 \frac{|\mathbf{E}_{\parallel}|^2}{U} + \alpha_{\mathbf{E}_{\perp},dn} \varepsilon_0 \frac{|\mathbf{E}_{\perp}|^2}{U}, \quad (8.14)$$

where the subscript dn refers to the dielectric needle, $\alpha_{\mathbf{E}_{\parallel},dn}$ and $\alpha_{\mathbf{E}_{\perp},dn}$ are the longitudinal and the transverse electric field form factors of the dielectric needle. As the transverse field is uniform in the cavity aperture (Figure 8.7), the difference between (8.14) and (8.13) will be proportional to the longitudinal electric field at the off-axis (Figure 8.9).

The field measurement using a metallic needle follows the same technique as that performed with a dielectric needle, with the minor exception that the metallic needle perturbs both the electric and the magnetic fields. Thus, the expression for the relative frequency change due to a metallic needle at the cavity on- and off-axis is

8 RF Testing of the Cavity

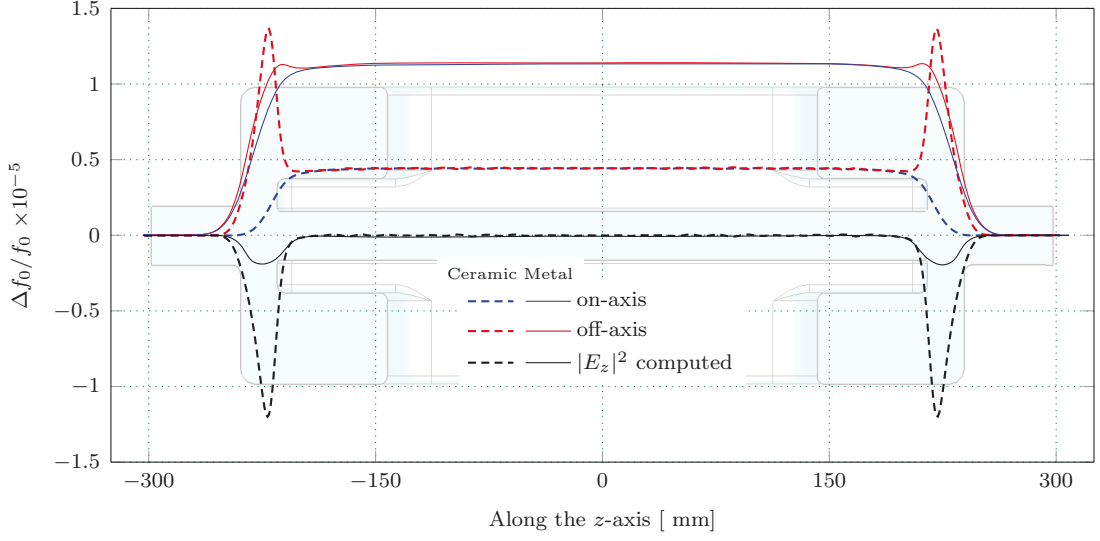


Figure 8.9: The relative frequency shift measured on- and off-axis along the z -axis using a ceramic and a metallic cylinder with an offset along the y -axis (Δy of 11 mm). The longitudinal electric field at the off-axis is obtained by taking the difference between the on- and the off-axis measurement values (black).

rendered as

$$\frac{\Delta f_0}{f_0} = \alpha_{\mathbf{E}_{\parallel},mn} \varepsilon_0 \frac{|\mathbf{E}_{\parallel}|^2}{U} + \alpha_{\mathbf{H}_{\perp},mn} \mu_0 \frac{|\mathbf{H}_{\perp}|^2}{U}, \quad (8.15)$$

$$\frac{\Delta f_0}{f_0} = \alpha_{\mathbf{E}_{\perp},mn} \varepsilon_0 \frac{|\mathbf{E}_{\perp}|^2}{U} + \alpha_{\mathbf{E}_{\parallel},mn} \varepsilon_0 \frac{|\mathbf{E}_{\parallel}|^2}{U} + \alpha_{\mathbf{H}_{\perp},mn} \mu_0 \frac{|\mathbf{H}_{\perp}|^2}{U}, \quad (8.16)$$

where the subscript mn refers to the metallic needle, $\alpha_{\mathbf{H}_{\perp},mn}$ the transverse magnetic field form factor of the metallic needle, and $\alpha_{\mathbf{E}_{\parallel},ms}$ and $\alpha_{\mathbf{E}_{\perp},ms}$ are the longitudinal and transverse electric field form factors of the metallic needle. Interestingly, both the transverse electric and the magnetic fields are very similar in this region (Figure 8.7). Thus, subtracting the on- and off-axis measurement values yields the longitudinal electric field along the off-axis (Figure 8.9). The measured relative frequency change observed with a metallic cylinder, when compared to a ceramic cylinder, shows a smaller value. This difference arises because the stronger perturbation of the electric field caused by the metal is countered by the presence of the magnetic field. Additionally, shape of the computed square electric field differs between the metallic and ceramic cylinders, potentially due to misalignment of the fishing wire.

8.4 Warm RF Test of the Cavity

Following the measurement of the deflecting mode field profile, the cavity was cleaned to ISO 5 cleanroom standards. In addition, the cavity components were cleaned using an ultrasonic bath. After the cleaning process, the spillage region inside the cavity was found to be smooth upon visual inspection. Any close-up examination would have contaminated the cavity. Subsequently, all the components were installed in a cleanroom. The main power coupler was oriented to achieve $\beta_{in} \approx 1$, whereas the pick-up probe was adjusted to obtain a stronger signal for the field measurement. Finally, the tuner positions were adjusted to achieve the target frequency of 273 MHz. The air inside the cavity was pumped out using the two sets of vacuum pumps (rotary and ion getter pumps). During the evacuation, a leak was noticed at the brazing joint of the main coupler. Epoxy resin was used to stop the leakage, which did not affect the performance of the main coupler. Subsequently, a base level vacuum of 6×10^{-9} mbar was reached. The variation in the resonance frequency of a cavity due to its evacuation is given as

$$\Delta f_0 = f_0 (\sqrt{\varepsilon_r} - 1), \quad (8.17)$$

where ε_r is the relative permittivity of the air, which has a value of 1.00059 at an ambient room temperature. Therefore, the frequency shift in the present case on evacuating the cavity should be 80.5 kHz. Additionally, the atmospheric force exerted on the cavity wall deforms the cavity resulting in a frequency change, and this was estimated to be -48 kHz from the simulations. As a result, the net frequency change due to the evacuation of the cavity should be $+32.5$ kHz. The measured shift in the cavity resonance frequency after the evacuation was only $+25.3$ kHz.

8.4.1 RF Test Setup

An experimental setup was built to conduct the warm RF testing of the deflecting cavity (Figure 8.10). A signal generator drives the power amplifier to obtain the desired frequency and power level. A semiconductor-based RF power amplifier which can deliver a maximum power of 1 kW in the frequency range of 272–274 MHz was procured. The low loss coaxial cables were used to transfer the RF power from

8 RF Testing of the Cavity

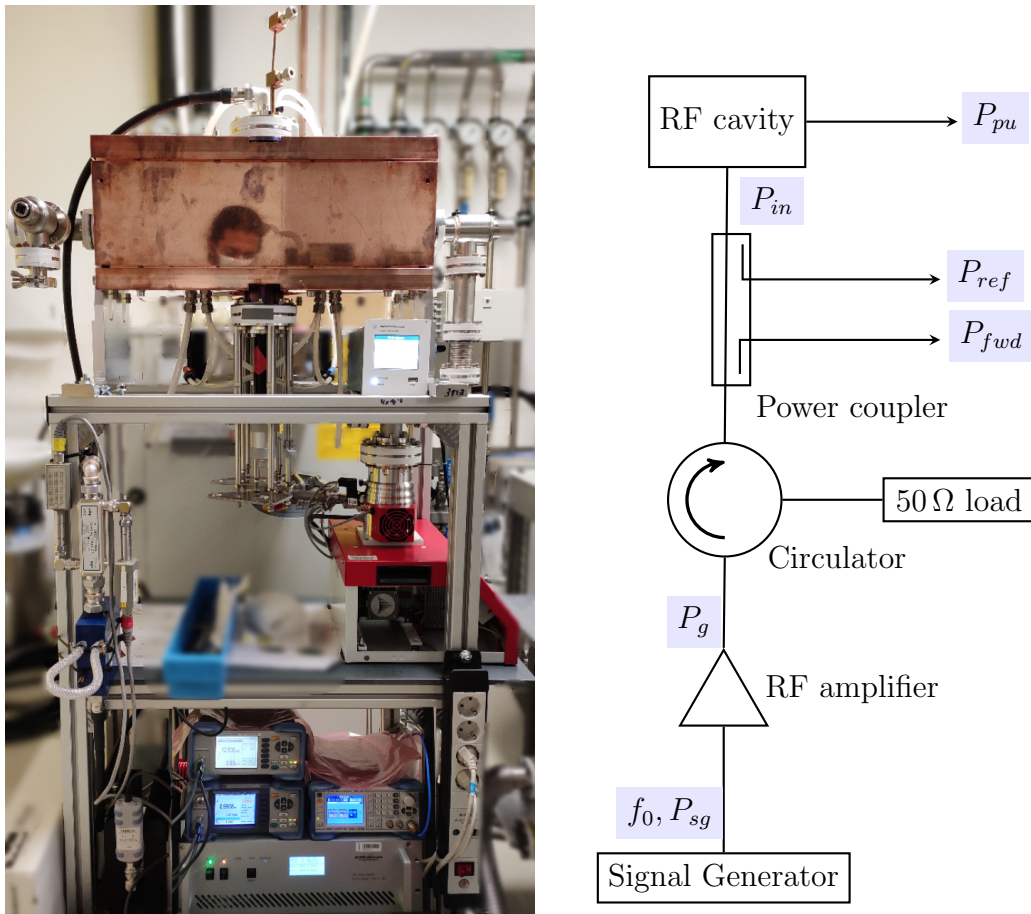


Figure 8.10: The cavity and the associated components arranged for the warm RF test (left); the sketch shows the RF devices and the power measurement points.

the amplifier to the cavity. Furthermore, a water-cooled circulator protects the amplifier from the reflected power. A bi-directional power coupler, attenuators and power meters were used to sample and measure the RF power at different points. The transmission losses of the coaxial cables and the attenuator were measured to calibrate the power meters. A temperature-controlled chiller provides cooling water required for the cavity, the main coupler, the amplifier, and the circulator. Additionally, rotary and ion getter pumps were used to evacuate the cavity. Safety interlocks were provided to trip the amplifier during bad vacuum and low coolant flow rate incidents.

The RF power flow and the power measurement points of the warm RF test setup are shown in Figure 8.10. The signal generator produces a low-level RF signal with

a frequency of f_0 and a power of P_{sg} , which drives the power amplifier. To avoid overdriving of the amplifier, a soft interlock was implemented on the signal generator to restrict the maximum P_{sg} . The low-level signal gets amplified to an RF power of P_g . Subsequently, the RF power was transferred to the cavity through a circulator and a bi-directional power coupler. The circulator safeguards the amplifier by routing the reflected power from the cavity towards a $50\ \Omega$ load. The bi-directional power coupler samples both the forward and the reflected power to and from the cavity. The sampled forward power, P_{fwd} , and the reflected power, P_{ref} , were connected to the power meter for measurement. The difference between P_{fwd} and P_{ref} gives the power fed into the cavity, P_{in} . A pick-up antenna samples the cavity field, and this RF power, P_{pu} , was measured with a power meter. Therefore, the total power dissipated in the cavity, P_c , is the difference between the power fed into the cavity P_{in} and sampled power P_{pu} .

8.4.2 Frequency Shift due to the Temperature Variation

A cavity deforms as a result of changes in the ambient and coolant temperature, resulting in a shift in the cavity's resonance frequency that can be measured using the existing test setup. The cavity reaches a thermal steady state at a set coolant temperature, and the frequency sensitivity of the cavity can be determined by measuring the frequency at different temperatures. However, the chiller failed to maintain a fixed temperature, leading to inconsistent results. As an alternative, the frequency measurements were performed with the cavity cooled down from an elevated temperature. Once the chiller was set to $45\ ^\circ\text{C}$, all the temperature measurement points showed $43\ ^\circ\text{C}$. Subsequently, the chiller was switched off and the cavity was allowed to cool down naturally. During the cooling process, the S-parameters were measured at regular intervals in addition to the cavity temperature at different locations (Figure 8.11). The contraction of the coupling loop of the main coupler at lower temperatures increased the input coupling factor Q_{in} (Figure 8.12). The cavity's resonance frequency decreased in proportion to the cavity temperature, and the measurement values corroborate the simulation results. Moreover, the cavity's frequency sensitivity to the temperature obtained through measurement agrees with the simulation.

8 RF Testing of the Cavity

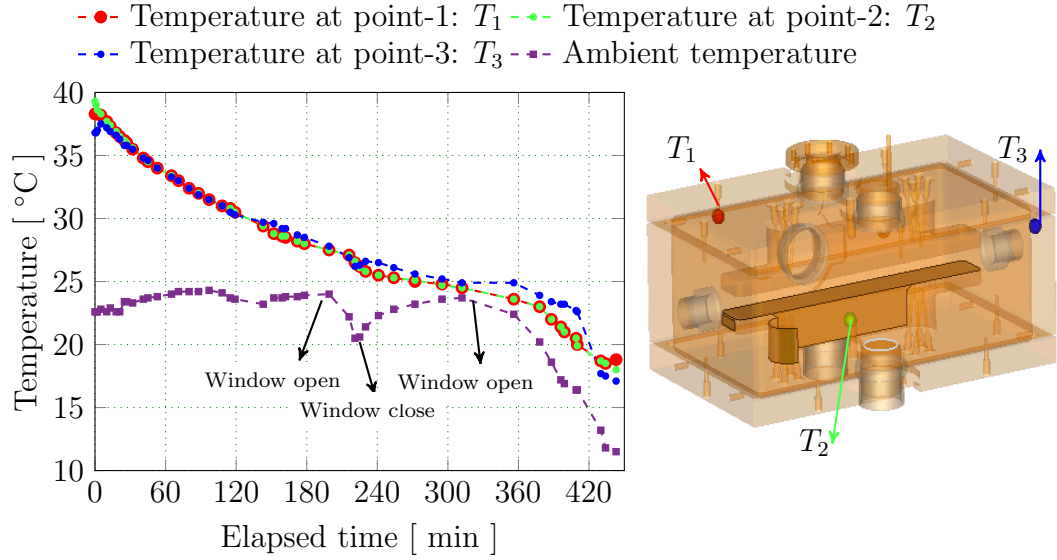


Figure 8.11: Temperature readings during the cavity cooling down process and the location of the thermocouples in the cavity.

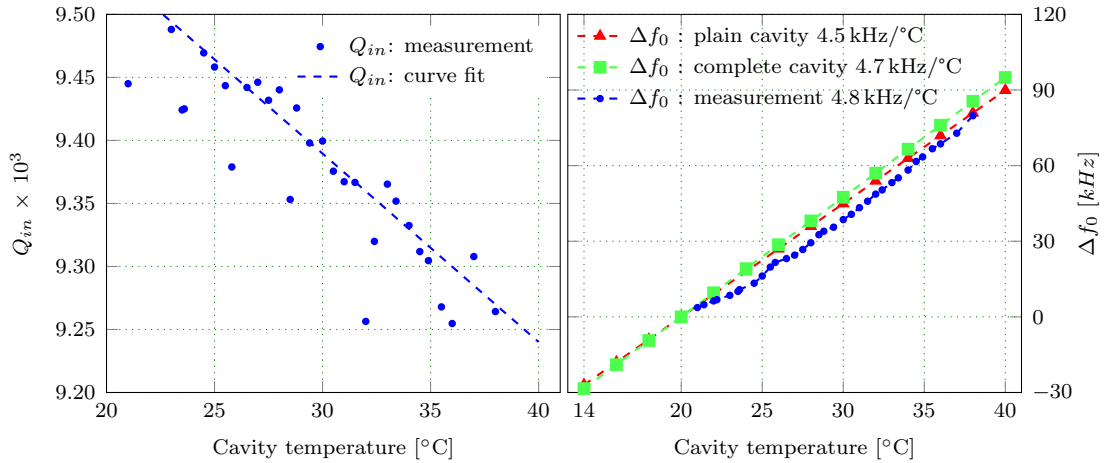


Figure 8.12: Variation of the input coupling factor of the main coupler and the resonance frequency shift at different cavity temperatures.

8.4.3 Vacuum Conditioning

The cavity was evacuated and a base pressure of 6×10^{-9} mbar was reached before feeding the RF power into the cavity. First, the cavity was fed with a low RF power (<1 W) to avoid vacuum surge, and later it was increased gradually. A sudden spike of pressure at around 1.8 W tripped the power amplifier. Initial speculation attributed

8 RF Testing of the Cavity

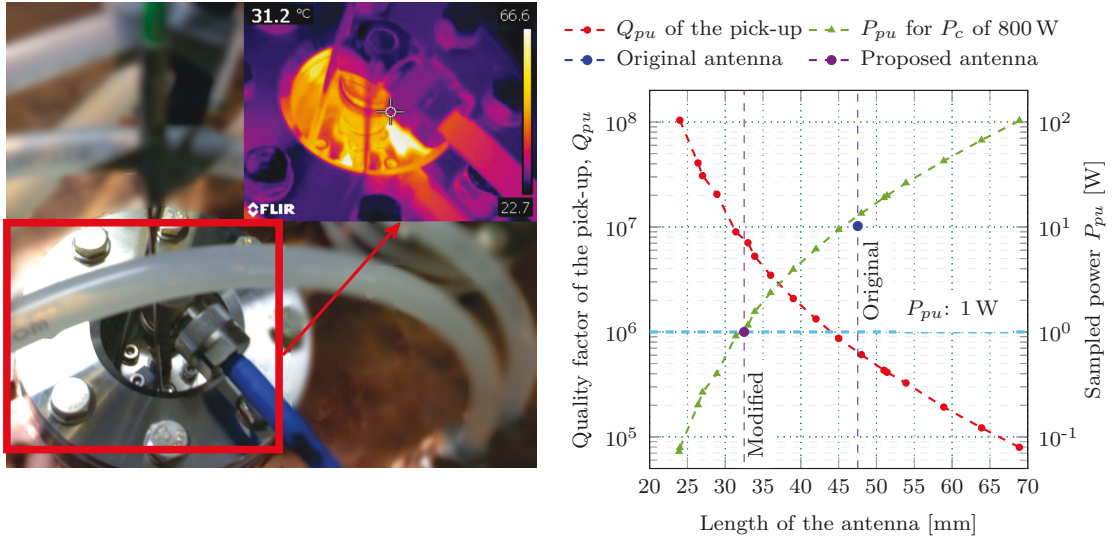


Figure 8.13: Snapshot of the pick-up probe surface captured through an infrared camera when 400 W of power was fed to the cavity. Variation of the power coupled out of the cavity through the pick-up probe for different antenna lengths with the input power to the cavity fixed at 800 W.

this to the cavity surface’s degassing due to increase in its temperature. Therefore, the input power to the cavity was pulsed. However, at this power setting, there was no significant improvement in the vacuum even after conditioning the cavity for a day. This suggested that the activity in the vacuum is due to the multipacting in the stem area, as anticipated by the analytical calculations (Figure 5.6). Nevertheless, it was possible to increase the power without compromising the cavity vacuum. This shows the presence of a soft multipacting barrier at around 1.8 W of the input RF power.

Gradually, the input power was increased to 400 W in steps. At this power level, the temperature readings from the thermocouple placed on the pick-up port surface showed 65 °C, and were verified by the image taken from an infrared camera (Figure 8.13). All the other components and surfaces of the cavity, on the other hand, were at room temperature. Since the pick-up probe was not water-cooled, the power loss on the pick-up cup and antenna increased its temperature significantly. Moreover, the inner surface of the pick-up and antenna will be at a much higher temperature than their outer surface. Even though the pick-up probe is robust enough to operate at 150 °C, a high temperature might lead to degassing, or might damage the ceramic

part of the feedthrough. To avoid this, the input power was not raised any further, and a set of corrective measures were implemented.

The pick-up probe consists of a stainless steel cup and the antenna. The lower conductivity of steel and a longer pick-up antenna increases the surface power loss on these components. Because this area is not actively cooled, the poor heat conduction increased its surface temperature. This can be overcome by either decreasing the power loss on the pick-up probe or by making a provision for an active cooling in this area. The power loss on the pick-up probe can be reduced by replacing or coating the steel parts of the pick-up with a metal of higher electrical conductivity. The temperature distribution on the pick-up and antenna obtained from simulation is shown in Figure 8.14. The tip of the antenna is at a higher temperature than the surface of the pick-up cup. The maximum temperature on the pick-up of different materials at various input power is shown in Figure 8.14. In the multiphysics simulation carried out in CST Multiphysics Studio[®], the thermal contact resistance between the pick-up cup and the cavity was neglected, which is not the case in reality. Thus the estimated maximum temperature for different power levels from the simulation is lower than the measured value. The surface power losses on the pick-up cup and antenna of different materials obtained from the simulation are listed in Table 8.11. Compared to a steel pick-up, a copper pick-up has a smaller power loss and a lower temperature due to its higher thermal and electrical conductivity. A cooling channel on the pick-up probe may have served as an alternative to the above modifications and prevented the overheating issue. However, this proposal

Table 8.11: The surface power losses on the pick-up cup and antenna of different material for the cavity input power of 800 W obtained from the simulation.

Material	Conductivity	Power loss on the pick-up cup [W]	Power loss on the antenna [W]	
	S/m		old length	new length
Steel	6.9×10^6	14.32	2.37	0.66
Copper	5.7×10^7	5.28	0.82	0.24
Silver	6.2×10^7	5.12	0.75	0.23

8 RF Testing of the Cavity

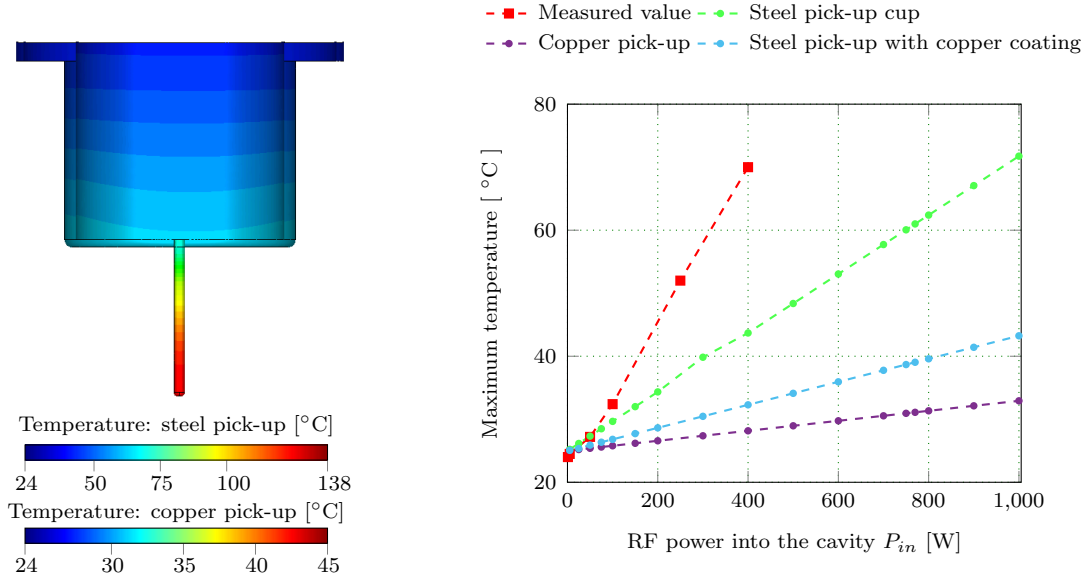


Figure 8.14: Temperature distribution on the pick-up and antenna for the input power of 800 W for a steel and copper pick-up. The graph shows the variation of maximum temperature on the pick-up cup and antenna for different power level.

was ruled out due to a shortage of human resources at the time. As a result, it was decided to shorten the antenna to 32.5 mm and coat the pick-up cup and antenna. Because the cost of coating with either copper or silver was the same, a 20 μm silver coating was applied on the pick-up cup and antenna. However, after the antenna's coating failed twice, it was decided to retain the steel antenna and merely shorten its length. Figure 8.15 shows the silver-coated pick-up cup, the old and the new antenna.

The cavity's warm testing resumed after installing the silver-coated pick-up cup and a shortened antenna. The S-parameter measurements showed that the pick-up couples 0.125% of the input power, which was further verified from the power measurement readings. A maximum temperature of 38°C was measured on the pick-up surface when the input power to the cavity was increased to 800 W. The cavity pressure of 6×10^{-8} mbar was recorded after the fifth day of continuous operation of the cavity at this power level. Moreover, no significant temperature change in the cavity components was observed. The vacuum conditioning of the cavity was successfully completed and is now ready for installation in the beam line.

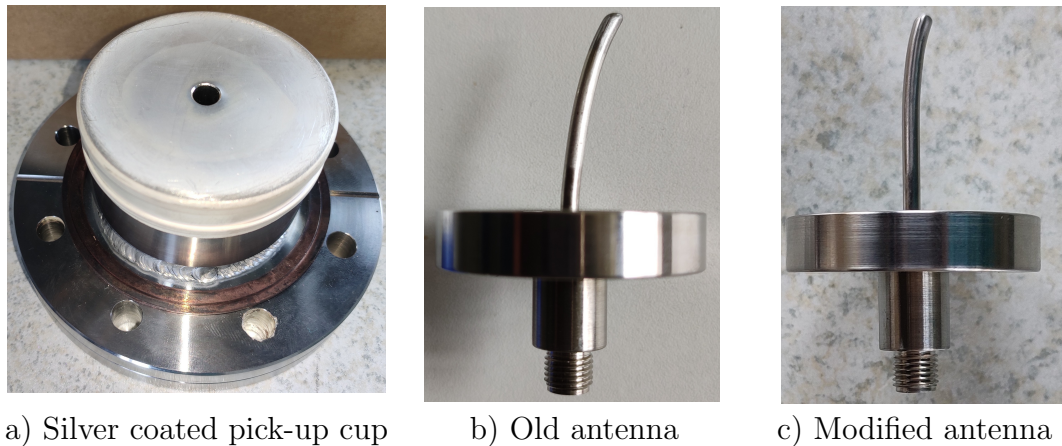


Figure 8.15: Silver coated pick-up cup, the old and the modified antenna of the cavity.

8.5 Steps to Improve the Cavity Performance

The deflecting cavity developed in the framework of this thesis has met the design requirements specified for the beam separator of the ELBE and DALI accelerators. Moreover, the cavity has performed satisfactorily during the high-power RF testing, and a reasonable vacuum level was achieved. A differential vacuum pumping can be employed if a stringent vacuum level is required. During the cavity design, fabrication, and testing process, certain shortcomings of the present design were observed and are discussed in this section. Additionally, the possible modifications in the design for an improvement are discussed. To speed up the cavity development process, the cavity components (frequency tuners, pick-up probe and main power coupler) were directly adapted from the existing designs without any major modification. In addition to the cavity, the modifications in the adapted cavity components are also discussed.

8.5.1 Quality Factor of the Cavity

The surface power loss on a cavity predominantly depends on the quality factor of the cavity which in turn depends on the conductivity of the material used to fabricate the cavity and its components. The possible steps to improve the quality factor of a cavity are discussed below.

- The stainless steel beam pipes and port tubes used in the deflecting cavity

8 RF Testing of the Cavity

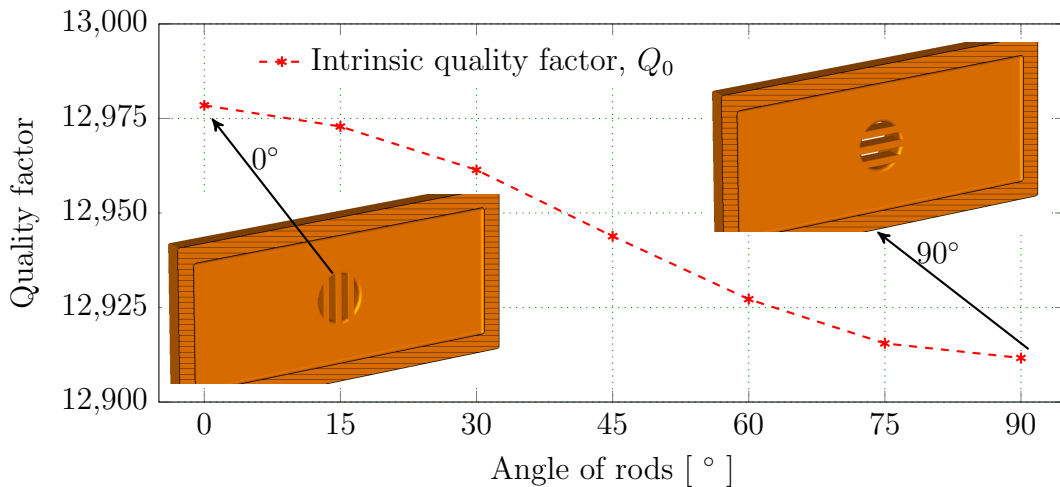


Figure 8.16: Variation of the intrinsic quality factor of a plain copper cavity with the vacuum port partially closed with a set of rods at different orientations.

almost caused a 8 % reduction in the cavity's quality factor. In order to improve the quality factor, all the ports should be made of copper.

- In the pre-buncher cavity at ELBE, an RF filter is used to stop the leakage of the cavity field through the vacuum port. A similar concept was used in the deflecting cavity, which resulted in the degradation of the cavity quality factor. Subsequently, the RF filter was removed, and improvement in the quality factor was noticed. Even though the cut-off frequency of the vacuum port is much higher than the operating frequency, a larger opening of the port results in a lower quality factor. Modifying the opening of the vacuum port, as shown in Figure 8.16 will increase the quality factor. Moreover, orienting the rods parallel to the current generated in the deflecting mode improves the quality factor.
- Another element that degraded the cavity quality factor was the stainless steel pick-up cup and antenna. The silver-coated pick-up cup decreased the surface temperature and improved the quality factor. Using a copper pick-up and antenna would improve the quality factor.
- The RF fingerstock encases the cavity components to prevent the cavity field from leaking out (Figure 8.4). These RF fingerstock are positioned nearer the

surface of the inner cavity, where they are exposed to a stronger RF field. As a result, a higher quality factor was measured without these RF fingers during the low power measurements. At high RF power levels, on the other hand, RF fingerstock cannot be ruled out. In order to minimize the field leakage while maintaining a higher quality factor, the best position for the RF finger should be identified.

- At present, the use of the deflecting cavity in the ELBE is not yet decided. In consequence, a tuning range of ± 750 kHz was specified for the cavity to permit a variety of applications. This tuning range was achieved by moving the twin plunger type frequency tuners by ± 25 mm. However, in future applications with the fixed resonance frequency, tuners with a smaller movement range will be beneficial, as this would increase the quality factor.

8.5.2 Mechanical Design and Fabrication

The following discussion focuses on the potential ways to enhance the mechanical design and fabrication of the cavity and its components.

- As copper has good electrical and thermal conductivity than steel, a copper pick-up and antenna will reduce power loss on its surfaces and transfer heat efficiently. The integration of the cooling channels on the pick-up cup must be explored to avoid excessive surface temperatures at a high input power.
- Currently, no active cooling mechanism is provided to remove the heat deposited on the frequency tuner's head. Therefore, this might raise its temperature significantly at high input power, resulting in de-gassing and damage to the tuner drive mechanism. If the cavity is operated at a higher RF power than the current design level, active cooling of the tuners must be considered.
- An offset distance of 2.5 mm was set for each brazing joint to compensate for the frequency shift due to the manufacturing error of the cavity parts. Furthermore, three machining steps were specified in the frequency pre-tuning process. Meticulous planning and manufacturing techniques helped in achieving the target frequency. As a result, the number of pre-tuning processes can be

8 RF Testing of the Cavity

reduced further by employing the fabrication techniques and pre-tuning process outlined in this work.

- In the present work, the spillage of the brazing alloy during the vacuum brazing was a cause of concern. To avoid this in future, the brazing alloy channel must be resized, and the quantity of brazing alloy must be selected carefully. In order to get rid of the spillage, micro blasting and etching techniques might also be investigated.

9 Summary and Outlook

The linear electron accelerator, ELBE, can deliver 1 mA beam current at a 13 MHz bunch repetition rate in continuous-wave mode with a maximum beam energy of 40 MeV. The accelerator drives six distinct secondary particle and radiation sources used in a wide range of experiments. It is currently not possible to run more than one ELBE secondary source at the same time. Therefore, a beam separator structure was proposed, which can separate the bunches spatially, enabling the delivery of a beam to different user stations to perform many experiments simultaneously. Furthermore, this maximizes facility usage. In the framework of this thesis, an RF deflecting cavity was designed, fabricated, and tested, which can be used to obtain multiple spatially separated beams from the existing single beam so that multiple secondary sources can be operated simultaneously. Moreover, the cavity developed in this work provides sufficient confidence to have a multiple beamline concept in the planned future accelerator, DALI, at HZDR, Dresden, Germany.

The thesis starts with an introduction to the electron accelerator ELBE and lists the beam parameters required for the different user experiments. This was followed by a discussion of the motivation and objectives of the thesis. Chapter 2 presents a brief introduction to electromagnetics and RF cavities, which represents the theoretical foundation of this thesis. After this, the existing transverse structures were reviewed to provide an insight into the state-of-the-art deflecting structures. A particular focus of this section was placed on the structures suitable for generating a pulsed or an alternate kick voltage. Based on this review, a pulsed magnet, a stripline kicker and an RF cavity were considered potential structures for the beam separation, and the adaptation of these three structures to the current work was studied. A pulsed power source drives the magnet and the stripline kicker to generate a pulsating transverse kick. In contrast, the kick amplitude of an RF cavity varies sinusoidally. The generation of high repetition rate pulses in the continuous wave mode to deflect

9 Summary and Outlook

the bunches at MHz rate is well above the ability of the existing pulsed power supplies. Moreover, achieving pulse-to-pulse stability is difficult as the pulses are generated in each cycle. The operating frequency of RF cavities, on the other hand, ranges from MHz to GHz. Furthermore, the low-level RF system detects the continuously decaying RF field in the cavity and adjusts the cavity's input power to maintain a consistent kick voltage over time. As a result, the RF cavity was selected for the current beam separator application.

The selection of the cavity operating frequency based on the kick voltage error, beam emittance growth, power loss, and kick voltage homogeneity is discussed in Section 3.3. The harmonic oscillating fields of an RF cavity impart a kick voltage gradient along the bunch, which results in a different kick angle for the particles in a bunch. Furthermore, the kick angle error leads to the projected emittance growth of a beam. A kick voltage with a low frequency is beneficial in reducing the kick voltage error and emittance growth (Figures 3.6 and 3.7). Additionally, cavity with a low frequency has a better kick voltage homogeneity than a cavity with a high frequency. In contrast, a cavity with a higher frequency has a lower power loss. Overall, the benefits of the lower frequency outweigh the additional RF power requirement. Following that, the cavity operating frequency of the cavity was decided as 273 MHz. The findings of this research are summarized in Table 3.11, which can be referred to choose an appropriate deflecting structure for a beam separator application based on the different criteria.

At the chosen frequency, 273 MHz, a conventional TM_{110} mode deflecting cavity is huge compared to the $\lambda/4$ cavities that operate in a TE-like mode. A review of the most recent cavity designs reveals six prospective cavity designs that might be appropriate for the current study. The currently operational 4-rod deflecting cavity at CEBAF, JLAB was the first design choice, and the subsequent four designs were the crab cavity designs proposed for the LHC upgrade. A novel normal conducting TCAV design discussed in [157] was the final design choice. The geometry of the first five cavity designs (I to V) were remodeled on the basis of the data available in the literature. The cavity geometries were scaled and adapted to match the requirements specified in Table 4.1. The last cavity choice, on the other hand, was re-designed from the base design due to the unavailability of its geometrical information in

9 Summary and Outlook

[157]. As a next step, the figure of merits of the six cavity designs were obtained through simulation and are listed in Table 4.11. All chosen designs are compact in size, and have a peak electric field lower than the Killpatric limit of 15 MV m^{-1} . Design I and VI have a higher value of the product of shunt impedance and surface resistance ($R_{\perp} R_s$) than the other designs resulting in a power loss of 729 W and 779 W, respectively. However, the circular rods in Design I lead to an in-homogeneous field along the cavity axis, impairing the kick voltage homogeneity. Furthermore, a separate coupler might be required to suppress the lower order mode of Design I. At the end, Design VI was selected over other designs due to its lower power loss and peak surface power loss density, as well as better kick voltage homogeneity.

The additional cavity components required for the deflecting cavity were adapted from those of the pre-buncher cavity of the ELBE. The loop size of the fundamental power coupler was modified to achieve a coupling factor greater or less than 1 based on the loop's orientation. Whereas, the antenna length of the pick-up probe was retained. Additionally, two plunger-type frequency tuners provide a tuning range of $\pm 1.7 \text{ MHz}$. A 2-point multipacting might persist in the cavity aperture, and this was estimated at a lower, easily conditionable power level ($P_c < 50 \text{ W}$). Only the off-axis beam can excite the deflecting mode in a deflecting cavity. Thus, the off-axis beam with the bunches arriving at on-crest affects the cavity field phase, which can be compensated by detuning the cavity frequency as given in equation 5.5. In this case, a 1 mA beam moving at a 10 mm offset to the cavity axis induces a 90 mW of power on the cavity, which is four orders lower than the cavity's surface power loss. The higher order modes excited by a beam persist longer in a superconducting cavity due to its high-quality factor. The cavities functioning at room temperature, on the other hand, have a lower quality factor, which quickly dampens the field strength of these modes. Moreover, the power deposited by these higher order modes in the present cavity is insignificant compared to the actual RF loss.

The mechanical design of the cavity is discussed in Chapter 6. The frequency sensitivity analysis of the cavity surfaces suggests that the stem influences the frequency more strongly than the outer cavity. Furthermore, the region between the stem dictates the kick voltage and its homogeneity. Therefore, a solid stem was preferred, and dimensional tolerance of 0.05 mm was specified for the stem. The effect of the

9 Summary and Outlook

atmospheric pressure on different wall thicknesses indicates that a 25 mm thick copper wall is necessary to keep the frequency shift below 50 kHz. A multiphysics analysis was carried out to identify the frequency shift caused by variations in the ambient and coolant temperature and the power level. The frequency drift due to these factors is low enough (4.5 kHz/°C and -14 Hz/W) and can easily be compensated by the frequency tuners.

The cavity was divided into three parts to ease machining and to minimize the risks due to a higher number of brazing joints. Two different cavity fabrication methods are compared in Section 7.1. In the selected method, the two stem parts are machined separately, achieving a higher precision than the other method. The cavity parts were machined from the oxygen free high conductivity copper blocks. The surface roughness measurements were performed on the different parts of the cavity, and a Root Means Square roughness of $1.25\ \mu\text{m}$ was recorded. The frequency pre-tuning of the cavity was carried out by removing the excess material from the cavity part. After three machining steps, the measured resonance frequency is offset from the target frequency by +56 kHz. The cavity parts were assembled, and vacuum brazing was performed. It was noticed that the brazing alloy has split over the cavity surface during the vacuum brazing. However, the field strength in this area is weak, and its influence on the cavity performance is negligible.

The measured intrinsic quality factor of the cavity was slightly greater than half of the value obtained through simulation. The surface roughness of the cavity does not contribute significantly to the degradation of the quality factor. The influence of each cavity component on the quality factor was measured separately. The RF filter at the vacuum port degrades the quality factor more strongly than the other components. The intrinsic quality factor of the cavity without the RF filter was measured to be 9450. A bead-pull measurement setup was built to obtain the deflecting mode field profile along the cavity axis. Dielectric and metallic spherical beads were used to measure the on-axis transverse electric and magnetic field profile. A dielectric and a metallic needle were also used to measure the longitudinal electric field at an offset to the cavity axis. The field profiles from the bead-pull measurement and simulation are identical. In the course of this work, specific challenges and shortcomings of the present cavity design were observed, and steps to improve the design are discussed

9 Summary and Outlook

in Section 8.5.

The cavity and its components were cleaned in an ultrasonic bath to fulfill the requirements of an ultra-high vacuum operation. After that, the cavity parts were assembled in a cleanroom. A warm RF testing setup was built to vacuum condition the cavity. Initially, a low RF power was fed into the cavity, and the power level was increased after ensuring a stable vacuum at each step. At 400 W, the temperature on the pick-up surface increased to 66 °C. To avoid damaging the pick-up probe, the pick-up cup was silver coated and the antenna was shortened. After this, the cavity was tested up to 800 W and a temperature of 36 °C was measured on the pick-up surface. Furthermore, the experiment was run for five consecutive days with no adverse effect on the vacuum or temperature, and eventually, the cavity was vacuum conditioned successfully.

In closing, the thesis has discussed in detail the development of a RF deflecting cavity as a beam separator for the ELBE. The next stage of this work involves deploying the vacuum-conditioned cavity in the beamline.

Outlook

In this work, a deflecting cavity was designed, fabricated and tested. The next step is to install the cavity in a beamline and test the structure with the actual beam. However, beam dynamics simulation studies must be carried out to identify the suitable location for the cavity in the existing ELBE beamline. Apart from this, beam diagnostics and monitoring devices have to be installed. Since the spatial separation of the bunches due to the cavity's transverse kick voltage is small, a more extended drift space is required to observe the bunch separation. Alternatively, a septum or quadrupole magnet has to be employed at a suitable location to amplify the spatial separation of the bunches. The results from the continuation of the present work will aid in designing a suitable beamline for the planned future accelerator, DALI.

Appendices

A Numerical Techniques and Convergence Study

This appendix gives a brief overview of the numerical techniques employed in the thesis and is followed by a mesh convergence study.

A.1 Numerical Techniques

Physical phenomena can be defined using partial differential equations, and an analytical solution to these equations exists only for some simple geometries. Usually, it requires numerical techniques to solve these equations for a complex shape, and some of the techniques are the Finite Difference Method (FDM), Boundary Element Method (BEM), Finite Element Method (FEM), Finite Volume Method (FVM), and Finite Integration Technique (FIT). The thermal steady state solver and the mechanical solver of CST Multiphysics Studio[®] are based on FEM, whereas the eigenmode solver of CST Microwave Studio[®] supports both the FIT and FEM. The basics of FEM and FIT are given here, and for a more detailed description, please refer to [183, 184].

In FEM, the solution region is divided into finite elements, and the basis functions are defined to interpolate the unknown values within these elements. In the next step, the weak form of the governing equation is obtained. Subsequently, the global equations system for the whole domain is assembled using the local element equations with the imposition of the boundary conditions. The obtained global matrix system, which is typically sparse, is solved to obtain the unknown values. The eigenvalue problem is written as

$$\mathbf{K}\mathbf{x} = \lambda_e\mathbf{M}\mathbf{x}, \tag{A.1}$$

A Numerical Techniques and Convergence Study

where λ_e is the eigenvalue of the matrix pair (\mathbf{K}, \mathbf{M}) , \mathbf{x} is the non-zero eigenvector which corresponds to the unknown values, and the matrices \mathbf{K} and \mathbf{M} are referred as the stiffness and mass matrix, respectively. In case of the RF cavity, on solving the equation (A.1) one obtains the resonating frequency of the eigenmode from λ_e ($= \omega^2 \mu \epsilon$) and the electric field distribution in the cavity from \mathbf{x} . In the case of the static mechanical and thermal steady state problem, a set of simultaneous algebraic equations are obtained and they are written as

$$[\mathbf{K}] \{\mathbf{u}\} = \{\mathbf{F}\}, \quad (\text{A.2})$$

where $[\mathbf{K}]$ is the stiffness (conductivity) matrix, $\{\mathbf{F}\}$ is the force (heat source) vector, and $\{\mathbf{u}\}$ is the displacement (temperature) vector for the mechanical (thermal) solver. The inverse of the $[\mathbf{K}]$ is calculated and the product of $[\mathbf{K}]^{-1}$ with $\{\mathbf{F}\}$ gives the unknown vector $\{\mathbf{u}\}$. Similar to FEM, the computation volume is discretized in FIT. This method uses two computational grids, primary grid and dual grid. Every edge of the primary grid intersect with a facet of the dual grid, and vice versa. The integral-state variables are defined on the geometrical entries of both the primary and dual grid. Using these variables in the integral form of Maxwell's equation one can obtain the integral-state representation of Maxwell's grid equations, which is nothing but a set of matrix equations. In a source-free and lossless medium, these matrix equations can be combined to obtain the eigenvalue problem as

$$\mathbf{M}_\epsilon^{-1} \tilde{\mathbf{C}} \mathbf{M}_{\mu^{-1}} \mathbf{C} \hat{\mathbf{e}} = \omega^2 \hat{\mathbf{e}}, \quad (\text{A.3})$$

where \mathbf{M}_ϵ and $\mathbf{M}_{\mu^{-1}}$ are the material matrices which correspond to permittivity and permeability, \mathbf{C} and $\tilde{\mathbf{C}}$ are the discrete curl operator of the primary and dual grid, and the eigenvalue and eigenvector are denoted by ω^2 and $\hat{\mathbf{e}}$, respectively. The above set of equations are solved to obtain the resonance frequency and field profile of an eigenmode in an RF cavity.

A.2 Convergence Study

In a numerical approach, the computational domain is discretized into elements (or mesh cells), and a geometry modeling error results from an inaccurate fit of the

A Numerical Techniques and Convergence Study

geometry with the mesh cells. This error can be reduced by dividing the geometry into more refined mesh sizes, but this increases the number of mesh cells, increasing the computation time required to solve the problem. Therefore, a compromise must be made between the required numerical accuracy and the available computational time. The area contributing to higher error is refined at every solution step, and the process is repeated until the relative error is below the specified limit or the error does not depend on the mesh. A relative error of a quantity is defined as

$$\delta_{\text{step}} = \left| \frac{\text{value of the quantity in the current solution step}}{\text{value of the quantity in the previous solution step}} - 1 \right|.$$

In the convergence test, the relative error is plotted w.r.t. number of mesh cells. A decrease in the relative error with an increase in mesh cells indicates that the solution converges. The cavity geometry (Design VI) and the deflecting mode field are symmetric on all three planes. The relative error of the deflecting mode frequency and required computational time as a function of mesh cells is shown in Figure A.1. Increased mesh cells decrease (increase) the relative error (computational time) for both the conditions, with and without symmetry planes, indicating convergence of the solution. However, a smaller number of mesh cells and less computation time is required to achieve a specified relative error when the symmetry plane condition is used in comparison to without the symmetry plane. All the computations discussed in this thesis were carried out in version 2017 on two servers with Intel[®]Xeon[®]E5-2687W v2 processor with 16 cores and 256 GB of RAM at 3.40 GHz.

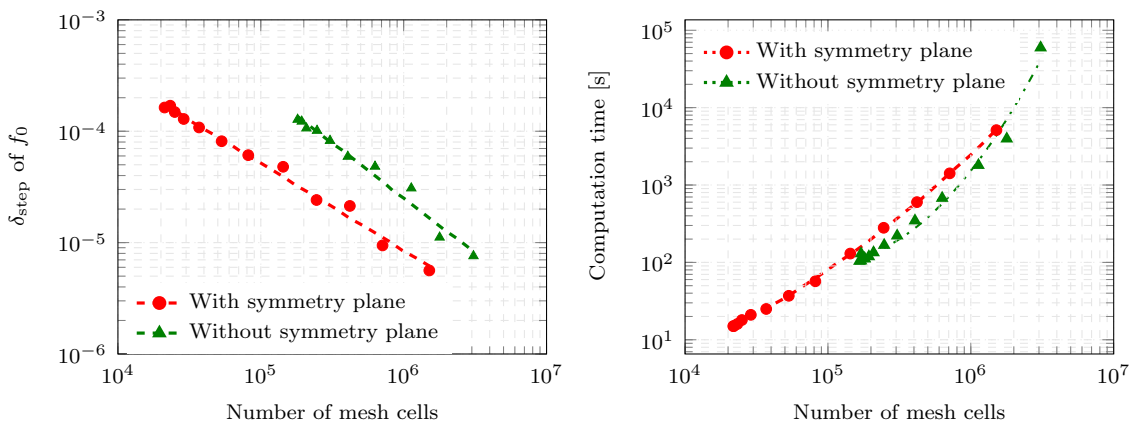


Figure A.1: Mesh convergence study of the eigenmode simulation with and without symmetry plane using the tetrahedral mesh carried out in CST MWS[®].

Bibliography

- [1] P. Michel, “ELBE Center for High-Power Radiation Sources,” *JLSRF*, vol. 2, p. A39, 2016. doi: 10.17815/JLSRF-2-58
- [2] HZDR, “The superconducting electron linear accelerator ELBE,” <https://www.hzdr.de/db/Cms?pNid=584>, 2022, [Online; accessed 28.11.2022].
- [3] U. Lehnert, P. Evtushenko *et al.*, “First operation of the ELBE linear accelerator,” in *LINAC*, 2002, pp. 379–381.
- [4] A. Arnold, H. Büttig *et al.*, “Development of a superconducting radio frequency photoelectron injector,” *Nucl Instrum Methods Phys Res A*, vol. 577, no. 3, pp. 440–454, jul 2007. doi: 10.1016/j.nima.2007.04.171
- [5] B. Aune, R. Bandelmann *et al.*, “Superconducting TESLA cavities,” *Phys. Rev. Spec. Top. - Accel. Beams*, vol. 3, no. 9, p. 092001, sep 2000. doi: 10.1103/PhysRevSTAB.3.092001
- [6] HZDR, “ELBE Center for High-Power Radiation Sources,” <https://www.hzdr.de/db/Cms?pOid=45082>, 2022, [Online; accessed 28.11.2022].
- [7] B. Green, S. Kovalev *et al.*, “High-field high-repetition-rate sources for the coherent THz control of matter,” *Sci. Rep.*, vol. 6, no. 22256, 2016. doi: 10.1038/srep22256
- [8] J. M. Klopff, M. Helm *et al.*, “FELBE-Upgrades and Status of the IR/THz FEL User Facility at HZDR,” in *IRMMW-THz*. IEEE Computer Society, 2018, pp. 1–2. doi: 10.1109/IRMMW-THz.2018.8510402
- [9] P. Michel, “Personal correspondence,” 2021.
- [10] W. Schnell, “Discussion of a radio-frequency particle separator for the CERN Proton Synchrotron,” Tech. Rep., 1961. [Online]. Available: <http://cds.cern.ch/record/278086>
- [11] H. Hahn and H. J. Halama, “Design of the Deflector for the rf Beam Separator at the Brookhaven AGS,” *Rev. Sci. Instrum.*, vol. 36, no. 12, pp. 1788–1796, 1965. doi: 10.1063/1.1719466

Bibliography

- [12] T. H. Fieguth and R. A. Gear-Hart, “RF separator and separated beam at SLAC,” Tech. Rep., 1975. [Online]. Available: <http://www.slac.stanford.edu/pubs/slacpubs/1500/slac-pub-1552.pdf>
- [13] A. Moretti and P. F. Schultz, “Operation of Argonne National Laboratory’s RF Particle Separator in the Travelling Wave Mode,” *IEEE Trans. Nucl. Sci.*, vol. 22, no. 3, pp. 1113–1115, jun 1975. doi: 10.1109/TNS.1975.4327823
- [14] V. Neil and V.K., “Four-way rf beam separator,” Tech. Rep., aug 1982. [Online]. Available: <http://www.osti.gov/servlets/purl/6154516-WDeNCu/>
- [15] R. Kazimi, J. Fugitt *et al.*, “CEBAF’s new RF separator structure test results,” in *Proc. Int. Conf. Part. Accel.* IEEE, 1993, pp. 1109–1111. doi: 10.1109/PAC.1993.308668
- [16] H. Wang, G. Cheng *et al.*, “Cavity design, fabrication and test performance of 750MHz, 4-rod separators for CEBAF 4-hall beam delivery system,” in *IPAC*, 2015, p. WEPWI029. doi: 10.18429/JACoW-IPAC2015-WEPWI029
- [17] V. Balandin, W. Decking, and N. Golubeva, “Optics for the beam switchyard at the european XFEL,” in *IPAC*, 2011, p. WEPC008.
- [18] M. Dal Forno, P. Craievich *et al.*, “High energy RF deflectors for the FERMI@ELETTRA project,” in *IPAC*, Shanghai, China, 2013, p. THPFI010.
- [19] T. Beukers, J. Amann, and Y. Nosochkov, “A Beam Spreader System for LCLS-II*,” in *NAPAC*, 2019, p. MOPLO01.
- [20] T. Hara, K. Fukami *et al.*, “Pulse-by-pulse multi-beam-line operation for x-ray free-electron lasers,” *Phys. Rev. Accel. Beams*, vol. 19, no. 2, pp. 1–7, 2016. doi: 10.1103/PhysRevAccelBeams.19.020703
- [21] K. Tono, T. Hara *et al.*, “Multiple-beamline operation of SACLA 1,” *J. Synchrotron Rad.*, vol. 26, pp. 595–602, 2019. doi: 10.1107/S1600577519001607
- [22] M. Paraliiev, C. Gough *et al.*, “High stability resonant kicker development for the SwissFEL switch yard,” *FEL*, pp. 103–106, 2014.
- [23] M. Placidi, J.-Y. Jung *et al.*, “Compact spreader schemes,” *Nucl. Inst. Methods Phys. Res. A*, vol. 768, pp. 14–19, dec 2014. doi: 10.1016/j.nima.2014.09.017
- [24] D. W. Storey, Y.-C. Chao, and L. Merminga, “Beam dynamics driven requirements on the ARIEL e-linac SRF separator cavity,” in *PAC*, 2013, p. THPBA01.

Bibliography

- [25] J. C. Maxwell, *A Treatise on Electricity and Magnetism*, ser. Cambridge Library Collection - Physical Sciences. Cambridge University Press, 2010, vol. 1.
- [26] J. D. Jackson, *Classical electrodynamics; 2nd ed.* New York, NY: Wiley, 1975.
- [27] B. I. Grishanov, F. V. Podgornya *et al.*, “Very fast kicker with high repetition rate for accelerator applications,” *Nucl. Instruments Methods Phys. Res. Sect. A Accel. Spectrometers, Detect. Assoc. Equip.*, vol. 396, no. 1-2, pp. 28–34, sep 1997. doi: 10.1016/S0168-9002(97)00739-0
- [28] T. Naito, S. Araki *et al.*, “Multibunch beam extraction using the strip-line kicker at the KEK Accelerator Test Facility,” *Phys. Rev. Spec. Top. - Accel. Beams*, vol. 14, no. 5, pp. 051002–9, 2011. doi: 10.1103/PhysRevSTAB.14.051002
- [29] T. P. Wangler, *RF Linear Accelerators*. New York, USA: John Wiley & Sons, Ltd, 1998.
- [30] D. M. Pozar, *Microwave Engineering, 4th Edition*. Wiley, 2011. ISBN 9781118213636
- [31] T. Moreno, *Microwave transmission design data*. McGraw-Hill, 1948.
- [32] C. Leemann, G. Yao, and C. G. Yao, “A highly effective deflecting structure,” in *Linear Accel. Conf.*, vol. 232, Albuquerque, New Mexico, USA, oct 1990, pp. 232–234.
- [33] S. U. D. Silva, “Investigation and Optimization of a New Compact Superconducting Cavity,” Ph.D. dissertation, Old Dominion University, 2013.
- [34] W. K. H. Panofsky and W. A. Wenzel, “Some Considerations Concerning the Transverse Deflection of Charged Particles in Radio-Frequency Fields,” *Rev. Sci. Instrum.*, vol. 27, no. 11, p. 967, nov 1956. doi: 10.1063/1.1715427
- [35] H. Padamsee, J. Knobloch *et al.*, *RF superconductivity for accelerators*, 2nd ed. Wiley Online Library, 2008, vol. 2011.
- [36] “CST Studio Suite®,” 2017. [Online]. Available: <https://www.3ds.com/products-services/simulia/products/cst-studio-suite/>
- [37] W. D. Kilpatrick, “A Criterion for Vacuum Sparking Designed to Include Both RF and DC,” *Rev. Sci. Instrum.*, vol. 28, no. 10, pp. 824–826, oct 1957. doi: 10.1063/1.1715731
- [38] L. Doolittle, M. Placidi *et al.*, “Cascading RF deflectors in compact beam spreader schemes,” *Nucl. Instruments Methods Phys. Res. Sect. A Accel. Spectrometers, Detect. Assoc. Equip.*, vol. 899, no. May, pp. 32–42, aug 2018. doi: 10.1016/j.nima.2018.04.039

Bibliography

- [39] A. Shor, B. Kaizer *et al.*, “Fast chopper for single radio-frequency quadrupole bunch selection for neutron time-of-flight capabilities,” *Phys. Rev. Accel. Beams*, vol. 22, no. 2, pp. 020403–13, 2019. doi: 10.1103/PhysRevAccelBeams.22.020403
- [40] R. Bentley, J. S. Lunsford, and G. P. Lawrence, “Pulsed beam chopper for LAMPF,” *IEEE Trans. Nucl. Sci.*, vol. 22, no. 03, pp. 1526–1528, 1975.
- [41] F. Caspers, “Review of Fast Beam Chopping,” in *LINAC*, 2004.
- [42] L. G and D. G. M, “High frequency chopper of the heavy-ion accelerator,” Tech. Rep., 2007. [Online]. Available: <http://cds.cern.ch/record/1355188>
- [43] M. A. Clarke-Gayther, “A two stage fast beam chopper for next generation high power proton drivers,” in *IPAC 2011 - 2nd Int. Part. Accel. Conf.*, 2011, pp. 1786–1788.
- [44] T. Kroyer, F. Caspers, and E. Mahner, “The CERN SPL Chopper Structure: A Status Report,” Tech. Rep., 2007. [Online]. Available: <https://cds.cern.ch/record/1015712>
- [45] R. Hardekopf, S. S. Kurennoy *et al.*, “Design, construction, and initial operation of the SNS MEBT chopper system,” in *EPAC*, 2004, pp. 150–152.
- [46] A. Caruso, F. Consoli *et al.*, “The LEBT chopper for the SPIRAL2 project,” in *IPAC*, 2011, p. TUPS082.
- [47] A. Shor, D. Vartsky *et al.*, “Fast beam chopper at SARAF accelerator via RF deflector before RFQ,” *J. Instrum.*, vol. 7, no. 6, 2012. doi: 10.1088/1748-0221/7/06/C06003
- [48] A. Shemyakin, C. Baffes *et al.*, “Design of 162-MHz CW bunch-by-bunch chopper and prototype testing results,” in *Work. High-Intensity High-Brightness Hadron Beams*, Daejeon, Korea, 2018, pp. 428–433. doi: 10.18429/JACoW-HB2018-THP1WC03
- [49] C. Wiesner, M. Droba *et al.*, “Experimental performance of an $E \times B$ chopper system,” *Phys. Rev. Accel. Beams*, vol. 20, no. 2, p. 020101, feb 2017. doi: 10.1103/PhysRevAccelBeams.20.020101
- [50] E. B. Forsyth and M. Fruitman, “Fast Kickers,” in *Part. Accel.*, vol. 1, 1970, pp. 27–39.
- [51] L. Ducimetière and G. Switzerland, “Advances of transmission line kicker magnets,” in *Part. Accel. Conf.*, Knoxville, Tennessee, 2005, pp. 235–240.
- [52] M. J. Barnes, L. Ducimetière *et al.*, “Injection and extraction magnets: kicker magnets,” CERN Accelerator School CAS 2009: Specialised Course on Magnets, Tech. Rep., mar 2011. [Online]. Available: <https://arxiv.org/pdf/1103.1583.pdf>

Bibliography

- [53] M. J. Barnes, J. Borburgh, and V. Mertens, “Injection and Extraction Related Hardware: Kickers and Septa,” in *Accel. Colliders*. Springer, 2013, pp. 305–319. [Online]. Available: http://materials.springer.com/lb/docs/sm_lbs_978-3-642-23053-0_31
- [54] L. Ducimetière, N. Garrel *et al.*, “The LHC injection kicker magnet,” in *Proc. IEEE Part. Accel. Conf.*, vol. 2, 2003, pp. 1162–1164. doi: 10.1109/pac.2003.1289639
- [55] A. Ueda, T. Ushiku, and T. Mitsuhashi, “Construction of travelling wave kicker magnet and pulse power supply for the KEK-Photon factory storage ring,” in *Proc. IEEE Part. Accel. Conf.*, vol. 5, 2001, pp. 4050–4052. doi: 10.1109/pac.2001.988341
- [56] M. Placidi, P. J. Emma *et al.*, “Design concepts of a beam spreader for a next generation free electron laser,” in *IPAC*, 2012, p. TUPPP071.
- [57] M. J. Barnes, G. D. Wait, and I. M. Wilson, “Comparison of Field Quality in Lumped Inductance versus Transmission Line Kicker Magnets,” in *EPAC*, 1994, pp. 2–4.
- [58] M. Tawada, M. Kikuchi *et al.*, “Development of injection and extraction kickers for SUPERKEKB Damping Ring,” in *IPAC*, 2019, p. THPRB2019. doi: 10.18429/JACoW-IPAC2019-THPRB036
- [59] A. Ueda, S. Asaoka *et al.*, “Construction of the new kicker magnet systems for PF-Advanced Ring,” in *IPAC*, 2017, pp. 3401–3403. doi: 10.18429/JACoW-IPAC2017-WEPVA060
- [60] J. L. Cole, I. C. Lutz, and J. J. Muray, “High Repetition Rate Pulsers for Beam Switching Magnets,” *IEEE Trans. Nucl. Sci.*, vol. 12, no. 3, pp. 430–433, 1965. doi: 10.1109/TNS.1965.4323669
- [61] A. Dael, M. Duval, and L. Ao, “Pulsed Magnets for the Time Sharing of The GANIL beam,” *Le J. Phys. Colloq.*, vol. 45, no. C1, pp. C1–293–C1–296, jan 1984. doi: 10.1051/jphyscol:1984158
- [62] K. Okabe, M. Yoshimoto, and M. Kinsho, “Development of a Beam-Switching System with a Pulse Bending Magnet at the J-PARC,” *IEEE Trans. Appl. Supercond.*, vol. 26, no. 4, pp. 5–8, 2016. doi: 10.1109/TASC.2016.2528045
- [63] D. Anicic, M. Daum *et al.*, “A fast kicker magnet for the PSI 600 MeV proton beam to the PSI ultra-cold neutron source,” *Nucl. Instruments Methods Phys. Res. A*, vol. 541, pp. 598–609, 2005. doi: 10.1016/j.nima.2004.12.032
- [64] S. Ahmed, E. Altieri *et al.*, “Fast-switching magnet serving a spallation-driven ultracold neutron source,” *Phys. Rev. Accel. Beams*, vol. 22, no. 10, 2019. doi: 10.1103/PhysRevAccelBeams.22.102401

Bibliography

- [65] L. Sermeus, J. Borburgh *et al.*, “The Design of the Special Magnets for PIMMS/TERA,” in *EPAC*, 2004, pp. 1639–1641.
- [66] J. Borburgh, B. Balhan *et al.*, “Design and development of kickers and septa for MEDAUS-TRON,” in *IPAC*, 2010, p. THPEB032.
- [67] W. Han, X. Liu *et al.*, “Design considerations of a fast kicker system applied in a proton therapy beamline,” *Nucl. Instruments Methods Phys. Res. Sect. A Accel. Spectrometers, Detect. Assoc. Equip.*, vol. 940, pp. 199–205, oct 2019. doi: 10.1016/j.nima.2019.06.034
- [68] C. Mitsuda, T. Honiden *et al.*, “Development of the ceramic chamber integrated pulsed magnet fitting for a narrow gap,” in *IPAC*, 2015, pp. 2879–2882. doi: 10.18429/JACoW-IPAC2015-WEPMA049
- [69] C. Mitsuda, Y. Kobayashi *et al.*, “Accelerator implementing development of ceramics chamber with integrated pulsed magnet for beam test,” in *IPAC*, 2019, p. THPTS027. doi: 10.18429/JACoW-IPAC2019-THPTS027
- [70] G. Nassibian, “A scheme for improved PSB-PS beam transfer for AA filling,” Tech. Rep., 1982. [Online]. Available: <http://cds.cern.ch/record/2238436/>
- [71] M. Bai, M. Meth *et al.*, “RHIC AC dipole design and construction,” *Proc. IEEE Part. Accel. Conf.*, vol. 5, no. Id, pp. 3606–3608, 2001. doi: 10.1109/pac.2001.988193
- [72] Hyung-Suck Suh, Chun-Kil Ryu *et al.*, “Design of Switching Magnet for 20-MeV Beamlines at PEFP,” in *Proc. 2005 Part. Accel. Conf. IEEE*, 2005, pp. 1575–1577. doi: 10.1109/PAC.2005.1590840
- [73] R. B. Palmer, “Energy Scaling, Crab Crossing, and the Pair Problem,” *conf*, vol. C8806271, pp. 613–619, 1988.
- [74] D. Alesini, G. Di Pirro *et al.*, “RF deflector design and measurements for the longitudinal and transverse phase space characterization at SPARC,” *Nucl. Instruments Methods Phys. Res. Sect. A Accel. Spectrometers, Detect. Assoc. Equip.*, vol. 568, no. 2, pp. 488–502, dec 2006. doi: 10.1016/j.nima.2006.07.050
- [75] V. Shemelin and S. Belomestnykh, “RF design of the deflecting cavity for beam diagnostics in ERL injector,” in *ERL*, 2007, pp. 07–2.
- [76] Denm Li and J. Corlett, “Deflecting RF cavity design for a recirculating linac based facility for ultrafast x-ray science (LUX),” in *PAC*, vol. 2. Portland, OR, USA: IEEE, 2003, pp. 1249–1251. doi: 10.1109/PAC.2003.1289668

Bibliography

- [77] M. Bell, P. Bramham *et al.*, “RF particle separators,” in *Cern Doc. Serv.*, Dubna, Soviet Union, sep 1963, pp. 1038–1043.
- [78] A. Citron, G. Dammertz *et al.*, “The Karlsruhe — CERN superconducting rf separator,” *Nucl. Instruments Methods*, vol. 164, no. 1, pp. 31–55, aug 1979. doi: 10.1016/0029-554X(79)90432-4
- [79] J. Aggus, W. Bauer *et al.*, “Experimental investigation of a superconducting niobium X-band deflecting cavity and suggestions for the design of the deflectors for a superconducting rf beam separator at NAL,” Tech. Rep., 1973. [Online]. Available: <http://www.osti.gov/servlets/purl/4419447-rIFrIS/>
- [80] K. Akai, J. Kirchgessner *et al.*, “Development of Crab Cavity for CESK-B,” in *PAC*, IEEE, Ed., Vancouver, Canada, 1993, pp. 769–771.
- [81] K. Hosoyama, K. Hara *et al.*, “Crab Cavity for KEKB,” in *SRF*, 1995, p. SRF95F25.
- [82] K. Akai, K. Ebihara *et al.*, “Commissioning and Beam Operation of KEKB Crab RF System,” in *SRF*, 2007, p. WEP57.
- [83] Y. Funakoshi, “Operational experience with crab cavities at KEKB,” in *ICFA Mini-Workshop Beam-Beam Eff. Hadron Colliders*, 2014, pp. 27–36. doi: 10.5170/CERN-2014-004.27
- [84] B. Hall, P. K. Ambattu *et al.*, “Analysis of the four rod crab cavity for HL-LHC,” in *IPAC*, 2012, p. WEPPC032.
- [85] R. Calaga, “Crab cavity for LHC upgrade,” in *SRF*, Chicago, IL USA, 2011, p. FRIOB05.
- [86] Q. Wu, “Crab Cavities: Past, Present and Future of a Challenging Device,” in *IPAC*, 2015, p. THXB2. doi: 10.18429/JACoW-IPAC2015-THXB2
- [87] R. Calaga, “CRAB Cavities for the LHC upgrade,” in *SRF*, 2017, p. THXA03. doi: 10.18429/JACoW-SRF2017-THXA03
- [88] Q. Wu, S. Belomestnykh, and S. Brook, “Novel deflecting cavity design for eRHIC *,” in *SRF*, 2011, p. THPO007.
- [89] S. Verdu-Andres, I. Ben-Zvi *et al.*, “338 MHz Crab Cavity Design for the eRHIC Hadron Beam,” in *SRF*, Lanzhou, China, 2017, p. TUPB001. doi: 10.18429/JACoW-SRF2017-TUPB001
- [90] R. Akre, L. Bentson *et al.*, “A transverse RF deflecting structure for bunch length and phase space diagnostics,” in *PAC*, Chicago, USA, 2001, pp. 2353–2355.

Bibliography

- [91] R. Akre, L. Bentson, and P. Emma, “Bunch length measurements using a transverse RF deflecting structure in the SLAC LINAC,” in *EPAC*, no. June, 2002, pp. 1882–1884.
- [92] P. Arpaia, R. Corsini *et al.*, “Enhancing particle bunch-length measurements based on Radio Frequency Deflector by the use of focusing elements,” *Nature*, vol. 10, no. 1, p. 11457, 2020. doi: 10.1038/s41598-020-67997-1
- [93] P. Craievich, S. Member *et al.*, “Implementation of Radio-Frequency Deflecting Devices for Comprehensive High-Energy Electron Beam Diagnosis deflecting cavity structure diagnostic system for the high-energy (1.2 GeV) regime,” *IEEE Trans. Nucl. Sci.*, vol. 62, no. 1, pp. 210–220, 2015. doi: 10.1109/TNS.2014.2385155
- [94] H. Ego, H. Maesaka *et al.*, “Transverse C-band deflecting structure for longitudinal phase space diagnostics in the XFEL/SPRING-8,” in *IPAC11*, 2011, p. TUPSC092.
- [95] L. Faillace, R. Agustsson *et al.*, “Status of Radio-Frequency (RF) deflectors at RADIABEAM,” in *LINAC*, 2014, p. THPP120.
- [96] V. A. Dolgashev, G. Bowden *et al.*, “Design and application of multimegawatt X-band deflectors for femtosecond electron beam diagnostics,” *Phys. Rev. Spec. Top. - Accel. Beams*, vol. 17, no. 10, p. 102801, 2014. doi: 10.1103/PhysRevSTAB.17.102801
- [97] H. Ego, H. Maesaka *et al.*, “Transverse C-band deflecting structure for longitudinal electron-bunch-diagnosis in XFEL SACLA,” *Nucl. Inst. Methods Phys. Res. A*, vol. 795, pp. 381–388, 2015. doi: 10.1016/j.nima.2015.06.018
- [98] H. Huck, G. Asova *et al.*, “First Results of Commissioning of the Pitz Transverse Deflecting Structure,” in *FEL*, 2015, pp. 110–114. doi: 10.18429/JACoW-FEL2015-MOP039
- [99] S. Belomestnykh, I. Bazarov *et al.*, “Deflecting cavity for beam diagnostics at Cornell ERL injector,” *Nucl. Instruments Methods Phys. Res. Sect. A Accel. Spectrometers, Detect. Assoc. Equip.*, vol. 614, no. 2, pp. 179–183, mar 2010. doi: 10.1016/j.nima.2009.12.063
- [100] A. Vrielink, Y. C. Chao *et al.*, “Longitudinal Emittance Measurement System for the Ariel Electron Linac,” in *IPAC*, 2013, pp. 1139–1141.
- [101] G. Kourkafas, T. Kamps *et al.*, “Transverse Deflecting Cavity for Longitudinal Beam Diagnostics at BERLinPro,” in *Linac*, 2018, p. THPO083. doi: 10.18429/JACoW-LINAC2018-THPO083
- [102] M. Borland, “Simulation and analysis of using deflecting cavities to produce short x-ray pulses with the Advanced Photon Source,” *Phys. Rev. Spec. Top. - Accel. Beams*, vol. 8, no. 7, p. 074001, jul 2005. doi: 10.1103/PhysRevSTAB.8.074001

Bibliography

- [103] M. Conde, H. Chen *et al.*, “Commissioning of a 1.3-GHz deflecting cavity for phase space exchange at the Argonne wakefield accelerator,” in *IPAC*, 2012, pp. 3350–3352.
- [104] R. Kazim, J. Fugitt *et al.*, “Test of a new RF Separator Structure for CEBAF,” in *Linear Accel. Conf.*, aug 1992, pp. 244–246.
- [105] A. Krycuk, J. Fugitt *et al.*, “Construction of the CEBAF RF separator,” in *Int. Conf. Part. Accel.*, 1993, pp. 939–940 vol.2. doi: 10.1109/PAC.1993.308723
- [106] D. W. Storey, R. E. Laxdal *et al.*, “Feasibility of an Rf Dipole Cavity for the Ariel E-Linac SRF Separator *,” in *PAC*, 2013, p. THPBA02.
- [107] —, “Fabrication Studies of a 650 MHz Superconducting RF Deflecting Mode Cavity for the ARIEL Electron Linac,” in *IPAC’17*, Copenhagen, Denmark, 2017, p. MOPAB022.
- [108] D. W. Storey, “A superconducting RF deflecting cavity for the ARIEL e-linac separator,” Ph.D. dissertation, University of Victoria. ISBN 2013436106 2018. [Online]. Available: <https://dspace.library.uvic.ca//handle/1828/9137>
- [109] Y. Huang, H. Wang *et al.*, “Ultrafast harmonic rf kicker design and beam dynamics analysis for an energy recovery linac based electron circulator cooler ring,” *Phys. Rev. Accel. Beams*, vol. 19, no. 8, pp. 1–10, 2016. doi: 10.1103/PhysRevAccelBeams.19.084201
- [110] —, “Multiple harmonic frequencies resonant cavity design and half-scale prototype measurements for a fast kicker,” *Phys. Rev. Accel. Beams*, vol. 19, no. 12, pp. 122001–15, 2016. doi: 10.1103/PhysRevAccelBeams.19.122001
- [111] G.-T. Park, F. Fors *et al.*, “The Development of a New Fast Harmonic Kicker for the JLEIC Circulator Cooling Ring,” in *IPAC*, 2018, p. TUPAL068. doi: 10.18429/JACoW-IPAC2018-TUPAL068
- [112] D. Alesini, R. Boni *et al.*, “The RF deflectors for CTF3,” INFN - LNF, Accelerator Division, Tech. Rep., 2001. [Online]. Available: <http://www.lnf.infn.it/acceleratori/ctf3/ctff3notes/CTFF3-003.pdf>
- [113] D. Alesini and F. Marcellini, “Rf deflector design of the CLIC test facility CTF3 delay loop and beam loading effect analysis,” *Phys. Rev. Spec. Top. - Accel. Beams*, vol. 12, no. 3, 2009. doi: 10.1103/PhysRevSTAB.12.031301
- [114] J. E. Stovall, F. W. Guy *et al.*, “Beam Funneling Studies at Los Alamos,” in *Heavy Ion Inert. Fusion Work.*, 1988, pp. LA-UR-88-3277.
- [115] S. Nath, “Funneling in LANL high intensity linac designs,” in *AIP Conf. Proc.*, vol. 346, no. 1, 1995, pp. 390–396. doi: 10.1063/1.49174

Bibliography

- [116] Y. V. Senichev, “Resonant Multi-gap Funnelling And De-funneling Systems,” in *HEACC*, 2001, p. P2new06.
- [117] Y. Senichev, W. Braeutigam *et al.*, “ESS funnel device investigation accelerator,” in *EPAC*, Paris, France, 2002, pp. 2196–2198.
- [118] Y. Senichev, O. Belyaev *et al.*, “Novel H-type rf deflector,” *Phys. Rev. Spec. Top. - Accel. Beams*, vol. 9, no. 1, p. 012201, 2006. doi: 10.1103/PhysRevSTAB.9.012001
- [119] D. Alesini, S. Guiducci *et al.*, “Design and test of new fast kicker for the DAFNE collider and the ILC damping rings,” in *EPAC*, Edinburgh, Scotland, 2006, p. TUPLS009.
- [120] I. Rodríguez, L. García-Tabarés *et al.*, “Design of a strip-line extraction kicker for CTF3 combiner ring,” in *EPAC*, Edinburgh, Scotland, 2006, p. MOPLS090.
- [121] J. Holma, M. Barnes *et al.*, “Present status of development of damping ring extraction kicker system for CLIC,” in *Int. Work. Futur. Linear Colliders*, 2011, p. LCWS11.
- [122] M. E. Ajjouri, N. Hubert *et al.*, “Design of the transverse feedback kicker for ThomX,” in *IBIC*, 2016, p. TUPG08.
- [123] C. Schneider, A. Arnold *et al.*, “Characterisation and First Beam Line Tests of the Elbe Stripline Kicker,” in *IPAC*, 2019, p. MOPTS030. doi: 10.18429/JACoW-IPAC2019-MOPTS030
- [124] I. Rodríguez, E. Rodríguez *et al.*, “Detailed design, manufacturing and testing of a stripline extraction kicker for CTF3 combiner ring,” in *EPAC*, 2008, pp. 1458–1460.
- [125] G. Staats, A. Arnold *et al.*, “Kicker development at the ELBE facility,” in *IPAC*, Dresden, Germany, 2014, p. MOPME067. doi: 10.18429/JACoW-IPAC2014-MOPME067
- [126] C. Pappas, S. De Santis *et al.*, “Fast kicker systems for ALS-U,” in *IPAC*, 2014, p. MOPME083. doi: 10.18429/JACoW-IPAC2014-MOPME083
- [127] C. Pappas, S. D. Santis *et al.*, “Prototyping for ALS-U fast kickers,” in *IPAC*, 2016, p. THPMW038. doi: 10.18429/JACoW-IPAC2016-THPMW038
- [128] C. Yao, L. Morrison *et al.*, “Preliminary test results of a prototype fast kicker for APS MBA upgrade*,” in *NAPAC*, 2016, p. WEPOB24. doi: 10.18429/JACoW-NAPAC2016-WEPOB24
- [129] G. Moritz, “Eddy currents in accelerator magnets,” Tech. Rep., 2009. [Online]. Available: <http://arxiv.org/abs/1103.1800>

Bibliography

- [130] E. G. Cook, G. Akana *et al.*, “Solid-state modulators for RF and fast kickers,” in *PAC*, Knoxville, Tennessee, 2005, pp. 637–641. doi: 10.1109/PAC.2005.1590512
- [131] C. Ader, J. Wilson *et al.*, “Recent experience in the fabrication and brazing of ceramic beam tubes for kicker magnets at FNAL,” in *11th Eur. Conf. EPAC 2008*, vol. C0806233, 2008, p. WEPC139.
- [132] M. J. Barnes, W. Bartmann *et al.*, “Kicker Systems-Part 1-Introduction and Hardware,” Tech. Rep., 2017. [Online]. Available: <https://cas.web.cern.ch/sites/cas.web.cern.ch/files/lectures/erice-2017/barnesi.pdf>
- [133] C. Belver-Aguilar and M. J. Barnes, “Review of stripline beam impedance: application to the extraction kicker for the CLIC damping rings,” *J. Phys. Conf. Ser.*, vol. 874, no. 1, p. 12074, jul 2017. doi: 10.1088/1742-6596/874/1/012074
- [134] N. Wang, S. K. Tian *et al.*, “Impedance optimization and measurements of the injection stripline kicker,” *Phys. Rev. Accel. Beams*, vol. 24, no. 3, pp. 034401–10, 2021. doi: 10.1103/PhysRevAccelBeams.24.034401
- [135] H. Shi, J. H. Chen *et al.*, “Development of a 750-mm-long stripline kicker for HEPS,” *Radiat. Detect. Technol. Methods*, vol. 2, p. 47, 2018. doi: 10.1007/s41605-018-0076-9
- [136] C. Belver-Aguilar, A. Faus-Golfe *et al.*, “Stripline design for the extraction kicker of Compact Linear Collider damping rings,” *Phys. Rev. Spec. Top. - Accel. Beams*, vol. 17, no. 7, pp. 071003–14, jul 2014. doi: 10.1103/PhysRevSTAB.17.071003
- [137] C. B. Aguilar, “Development of Stripline Kickers for Low Emittance Rings : Application to the Beam Extraction Kicker for CLIC Damping Rings,” Ph.D. dissertation, Universitat de Valencia, 2015. [Online]. Available: <http://cds.cern.ch/record/2062835/files/CERN-THESIS-2015-175.pdf>
- [138] H. Shi, J. H. Chen *et al.*, “The design and test of a stripline kicker for HEPS,” in *FLS*, 2018, p. WEP2PT021. doi: 10.18429/JACoW-FLS2018-WEP2PT021
- [139] C. Yao, L. Morrison *et al.*, “Development of fast kickers for the APS MBA upgrade,” in *IPAC*, 2015, pp. 3286–3288. doi: 10.18429/JACoW-IPAC2015-WEPTY014
- [140] J. M. Cesaratto, J. D. Fox *et al.*, “SPS Wideband Transverse Feedback Kicker : Design Report,” Tech. Rep., 2013. [Online]. Available: <https://cds.cern.ch/record/1639553/files/CERN-ACC-NOTE-2013-0047.pdf>
- [141] P. Bernard, V. Vaghin, and H. Lengeler, “New disk-loaded waveguides for the CERN RF separator,” Tech. Rep., dec 1970. [Online]. Available: <http://cds.cern.ch/record/274996>

Bibliography

- [142] P. Craievich, M. Petronio *et al.*, “Implementation of radio-frequency deflecting devices for comprehensive high-energy electron beam diagnosis,” *IEEE Trans. Nucl. Sci.*, vol. 62, no. 1, pp. 210–220, 2015. doi: 10.1109/TNS.2014.2385155
- [143] H. Hahn and H. Halama, “Investigations of iris-loaded deflectors,” *Nucl. Instruments Methods*, vol. 45, no. 1, pp. 141–150, nov 1966. doi: 10.1016/0029-554X(66)90419-8
- [144] O. H. Altenmueller, R. R. Larsen, and G. A. Loew, “Investigations of traveling-wave separators for the stanford two-mile linear accelerator,” *Rev. Sci. Instrum.*, vol. 35, no. 4, pp. 438–442, 1964. doi: 10.1063/1.1718840
- [145] D. Alesini and A. Gallo, “Effects of the beam loading in the rf deflectors of the CLIC test facility CTF3 combiner ring,” *Phys. Rev. Spec. Top. - Accel. Beams*, vol. 7, no. 3, pp. 62–77, 2004. doi: 10.1103/PhysRevSTAB.7.034403
- [146] V. A. Dolgashev and J. Wang, “RF design of X-band RF deflector for femtosecond diagnostics of LCLS electron beam,” in *15th Adv. Accel. Concepts Work.*, vol. 1507, 2012, pp. 682–687. doi: 10.1063/1.4773780
- [147] T. Jian-Hao, G. G. Qiang *et al.*, “X-band deflecting cavity design for ultra-short bunch length measurement of SXFEL at SINAP,” *Nucl. Sci. Tech.*, vol. 25, no. 6, p. 60101, 2014. doi: 10.13538/j.1001-8042/nst.25.060101
- [148] A. Murokh, R. Agustsson *et al.*, “Design and fabricaiton of an X-band travelling wave deflection mode cavity for longitudinal characterization of ultra-short electron beam pulses,” in *EPAC*, Geona, Italy, 2008, p. TUPC072.
- [149] J. Shi, H. Chen *et al.*, “A 3-cell deflecting RF cavity for emittance exchange experiment at ANL,” *Nucl. Instruments Methods Phys. Res. Sect. A Accel. Spectrometers, Detect. Assoc. Equip.*, vol. 598, no. 2, pp. 388–393, jan 2009. doi: doi.org/10.1016/j.nima.2008.09.046
- [150] Y. Nishimura, K. Sakaue *et al.*, “Design of a two-cell rf-deflector cavity for ultra-short electron bunch measurement,” *Nucl. Inst. Methods Phys. Res. A*, vol. 764, pp. 291–298, 2014. doi: 10.1016/j.nima.2014.07.035
- [151] S. Jia-Ru, C. Huai-Bi *et al.*, “RF deflecting cavity design for bunch length measurement of photoinjector at Tsinghua University,” *Chinese Phys. C*, vol. 32, no. 10, pp. 837–841, oct 2008. doi: 10.1088/1674-1137/32/10/014
- [152] K. Floettmann and V. V. Paramonov, “Beam dynamics in transverse deflecting rf structures,” *Phys. Rev. Spec. Top. - Accel. Beams*, vol. 17, no. 2, p. 024001(11), 2014. doi: 10.1103/PhysRevSTAB.17.024001

Bibliography

- [153] P. Craievich, S. Biedron *et al.*, “Fermi low-energy transverse RF deflector cavity,” in *EPAC*, 2008, pp. 1239–1241.
- [154] X. Jiang, J. Shi *et al.*, “A C-band deflecting cavity design for high-precision bunch length measurement,” in *IPAC2015*, 2015, p. WEPMN014. doi: 10.18429/JACoW-IPAC2015-WEPMN014
- [155] R. J. England, B. O’Shea *et al.*, “Commissioning of the UCLA Neptune x-band deflecting cavity and applications to current profile measurement of ramped electron bunches,” in *Proc. IEEE Part. Accel. Conf.*, 2007, pp. 4135–4137. doi: 10.1109/PAC.2007.4440067
- [156] S. U. De Silva and J. R. Delayen, “Multipole Field Effects for the Superconducting Parallel-Bar Deflecting/Crabbing Cavities,” in *LINAC*, sep 2012, p. SUPB038.
- [157] T. Luo, D. Summers, and D. Li, “Design of a Normal-conducting RF-dipole Deflecting Cavity,” in *IPAC2013*, 2013, p. WEPFI091.
- [158] C. Hovater, G. Arnold *et al.*, “The CEBAF RF separator system,” in *Int. Linear Accel. Conf.*, dec 1996, pp. 77–79.
- [159] R. Kazimi, H. Wang *et al.*, “Source and extraction for simultaneous four-hall beam delivery system at CEBAF,” in *IPAC*, 2013, pp. 2896–2898.
- [160] M. Stefani and G. T. Park, “Double quarter wave deflector cavity design and simulation,” in *IPAC*, 2019, p. WEPGW109. doi: 10.18429/JACoW-IPAC2019-WEPGW109
- [161] A. Arnold, P. Michel, and U. Lehnert, “Personal correspondence,” 2017.
- [162] U. Lehnert, “Personal correspondence,” 2018.
- [163] P. Emma, “Spatial Chirp Limitations of Deflecting Cavity Kickers,” Tech. Rep., 2012.
- [164] C. Emma, “High Efficiency, High Brightness X-Ray Free Electron Laser Pulses via Fresh Bunch Self-Seeding and Undulator Tapering,” Ph.D. dissertation, 2017. [Online]. Available: <https://escholarship.org/uc/item/65p5d7h6>
- [165] B. Hall, G. Burt *et al.*, “Design and testing of a four rod crab cavity for High Luminosity LHC,” *Phys. Rev. Accel. Beams*, vol. 20, no. 1, p. 012001, jan 2017. doi: 10.1103/PhysRevAccelBeams.20.012001
- [166] S. U. De Silva and J. R. Delayen, “Design evolution and properties of superconducting parallel-bar rf-dipole deflecting and crabbing cavities,” *Phys. Rev. Spec. Top. - Accel. Beams*, vol. 16, no. 1, p. 012004, jan 2013. doi: 10.1103/PhysRevSTAB.16.012004

Bibliography

- [167] R. Calaga, S. Belomestnykh *et al.*, “A double quarter-wave deflecting cavity for the LHC,” in *IPAC*, 2013, pp. 2408–2410.
- [168] D. Gavela, J. Calero *et al.*, “Calculation and design of a RF cavity for a novel compact superconducting cyclotron for radioisotope production,” in *IPAC*, 2015, p. WEPMN057. doi: 10.18429/JACoW-IPAC2015-WEPMN057
- [169] J. R. Delayen and H. Wang, “New compact TEM-type deflecting and crabbing rf structure,” *Phys. Rev. Spec. Top. - Accel. Beams*, vol. 12, no. 6, p. 062002, dec 2009. doi: 10.1103/PhysRevSTAB.12.062002
- [170] A. Castilla, I. Ben-Zvi *et al.*, “First rf performance results for the DQW crab cavities to be tested in the CERN SPS,” in *IPAC*, Copenhagen, Denmark, 2017, p. MOPVA095.
- [171] B. Xiao, L. Alberty *et al.*, “Design, prototyping, and testing of a compact superconducting double quarter wave crab cavity,” *Phys. Rev. Spec. Top. - Accel. Beams*, vol. 18, no. 4, p. 041004, 2015. doi: 10.1103/PhysRevSTAB.18.041004.f5
- [172] R. Calaga, E. Jensen *et al.*, “Crab Cavity Development,” in *Adv. Ser. Direct. High Energy Phys.*, oct 2015, vol. 24, pp. 137–156. [Online]. Available: https://doi.org/10.1142/9789814675475_0007
- [173] B. Markert, “Weak or Strong: On Coupled problems In Continuum Mechanics,” Habilitation, University of Stuttgart, 2010.
- [174] S. Reitzinger, M. Wabro, and S. Zaglmayr, *Sensitivity Analysis for Maxwell Eigenvalue Problems in Industrial Applications*. Springer, 2013. ISBN 978-3-642-30316-6
- [175] K. Brackebusch and U. Van Rienen, “Investigation of Geometric Variations for Multicell Cavities Using Perturbative Methods,” *IEEE Trans. Magn.*, vol. 52, no. 3, mar 2016. doi: 10.1109/TMAG.2015.2487542
- [176] L. C. Maier and J. C. Slater, “Field strength measurements in resonant cavities,” *J. Appl. Phys.*, vol. 23, no. 1, pp. 68–77, 1952. doi: 10.1063/1.1701980
- [177] V. Baglin, J. Bojko *et al.*, “The Secondary Electron Yield of Technical Materials and Its Variation With Surface Treatments,” in *EPAC*, 2000, pp. 217–221.
- [178] A. Wagner, M. Butterling *et al.*, “Positron Annihilation Studies using a Superconducting Electron LINAC,” in *AIP Conf. Proc.*, vol. 1970, 2018, p. 40003. doi: 10.1063/1.5040215
- [179] E. Hammerstad and O. Jensen, “Accurate Models for Microstrip Computer-Aided Design,” in *MTT-S Int. Microw. Symp. Dig.*, vol. 80. MTT006, 1980, pp. 407–409. doi: 10.1109/MWSYM.1980.1124303

Bibliography

- [180] E.O. Hammerstad and F. Bekkadal, *Microstrip handbook*, Norwegian Institute of Technology: Norway, Ed., Trondheim, 1975.
- [181] M. Navarro-Tapia and R. Calaga, “Bead-Pull Measurements of the Main Deflecting Mode of the Double-Quarter-Wave Cavity for the HL-LHC,” in *SRF*, BC, Canada, 2015, p. THPB019. doi: 10.18429/JACoW-SRF2015-THPB019
- [182] L. C. Maier and J. C. Slater, “Determination of field strength in a linear accelerator cavity,” *J. Appl. Phys.*, vol. 23, no. 1, pp. 78–83, 1952. doi: 10.1063/1.1701982
- [183] U. van Rienen, *Numerical Methods in Computational Electrodynamics - Linear Systems in Practical Applications.*, ser. Lecture Notes in Computational Science and Engineering. Springer, 2001, vol. 12. ISBN 978-3-642-56802-2
- [184] R. Schuhmann and T. Weiland, “Conservation of discrete energy and related laws in the Finite Integration Technique,” *Prog. Electromagn. Res. PIER*, vol. 32, pp. 301–316, 2001.

Declaration of authorship

I, Gowrishankar Thalagavadi Hallilingaiah hereby declare that i have written this document independently and all the sources of information and aid have been acknowledged to the best of my knowledge. This document has not been submitted previously for any other qualification at any other universities or institutions. This thesis is based on the work done by myself under the guidance of my supervisors.

Dresden, 30 November 2022

Gowrishankar Thalagavadi Hallilingaiah

Curriculum Vitae

Personal information

Name / Surname	Hallilingaiah, Gowrishankar Thalagavadi
Address	Kamenzer Straße-26, 01099 Dresden
Telephone	+49 17634359665
Personal Email	gowrish@web.de, g.hallilingaiah@hzdr.de
Nationality	Indian
Date of birth	29.09.1985
Gender	Male

Work experience

Dates	June 2022 to present
Occupation	Wissenschaftlicher Mitarbeiter
Main responsibility	Conditioning of the 1.3 GHz deflecting cavity used for bunch length measurement.
Employer	Helmholtz Zentrum Dresden-Rossendorf Innovation GmbH, Bautzner Straße 400, 01328 Dresden
Dates	March 2022 to December 2022
Occupation	Wissenschaftlicher Mitarbeiter
Main responsibility	Conditioning of the RF power couplers in a resonator ring.
Employer	Helmholtz Zentrum Dresden-Rossendorf Innovation GmbH, Bautzner Straße 400, 01328 Dresden
Dates	September 2016 to February 2022
Occupation	Wissenschaftlicher Mitarbeiter
Main activities and responsibilities	Electromagnetic and multiphysics simulations of RF cavities, fabrication and high-power testing of the normal conducting deflecting cavity.
Employer	University of Rostock, Rostock, Germany
Dates	October 2015 to December 2015
Occupation	Tutor
Main activities and responsibilities	Conducted tutorial classes of "Introduction to Numerical Mathematics" for Computational Science and Engineering students.
Employer	University of Rostock, Rostock, Germany
Dates	April 2015 to July 2015
Position held	Wissenschaftliche Hilfskraft
Main activities and responsibilities	Integrating of the open source software, SALOME and FEniCS.
Employer	University of Rostock, Rostock, Germany
Dates	September 2009 to August 2014
Position held	Scientific Officer / D
Main activity	Design and development of technologies required for safe handling, containment, and long term storage of the high level radioactive liquid waste.
Employer	Bhabha Atomic Research Centre (BARC), Mumbai, India

Education

Dates	September 2016 – June 2023
Title of qualification	PhD
Topic of PhD	Development of a transverse deflecting cavity as a beam separator for ELBE
Description of the project	Currently, in the electron accelerator, ELBE at HZDR, only a single secondary source can be driven at any given time. An RF kicker is being developed under the joint project between HZDR and the University of Rostock to overcome this limitation. The transverse deflecting cavity separates the bunches from the main beam into multiple beamlines to drive different secondary sources simultaneously, thereby significantly enhancing the capabilities of the ELBE accelerator.
University	University of Rostock, Rostock, Germany
Dates	October 2014 to July 2016
Title of qualification awarded	Masters in Computational Engineering
Principal subjects	Computational Electromagnetics, Numerical Mathematics and I, and Sensors & Actuators.
Description of the project	A 2.5D eigenmode solver was developed using the open-source FEM package, and the code was validated with the literature values. Further, the rotational-symmetric superconducting cavity was optimized using particle swarm optimization technique.
University	University of Rostock, Germany
Dates	September 2008 to August 2009
Title of qualification awarded	Post Graduate Diploma in Electronics Engineering spec. in Nuclear Engineering
Principal subjects	Accelerator physics, radioactivity measurement techniques, and instrumentation & control systems specific to nuclear facilities.
Institute	Homi Bhabha National Institute, Mumbai, India
Dates	2003-2007
Title of qualification awarded	Bachelor of Engineering in Electronics and Communication engineering.
Institute and University	Bangalore Institute of Technology affiliated to Visvesvaraya Technological University, Karnataka, India

Publications

Conference proceedings	[1] G. T. Hallilingaiah, A. Arnold, U. Lehnert, P. Michel, and U. van Rienen, "Numerical Studies of Normal Conducting Deflecting Cavity Designs for the ELBE Accelerator," in IPAC, 2018, pp. 3824–3827, doi: 10.18429/JACoW-IPAC2018-THPAL074. [2] G. T. Hallilingaiah, A. Arnold, S. Köppen, P. Michel, and U. Van Rienen, "Fabrication, field measurement, and testing of a compact RF deflecting cavity for ELBE," in IPAC, 2022, p. MOPORI20, doi: 10.18429/JACoW-LINAC2022-MOPORI20.
------------------------	---